HOOSHIAR ZOLFAGHARNASAB

Toward a 3D Planning Approach for Breast Conserving Surgery

Ph.D. Thesis

FACULDADE DE ENGENHARIA DA UNIVERSIDADE DO PORTO
June 2018

FACULDADE DE ENGENHARIA DA UNIVERSIDADE DO PORTO

Toward a 3D Planning Approach for Breast Conserving Surgery

Hooshiar Zolfagharnasab

Programa Doutoral em Engenharia Eletrotécnica e de Computadores

Supervisor: Hélder Filipe Pinto de Oliveira (PhD)

Co-supervisor: Jaime dos Santos Cardoso (PhD)

June 2018

Resumo

O cancro da mama é a forma mais comum de cancro de entre as mulheres, contabilizando menos de um terço de todos os diagnósticos e um oitavo das mortes relacionados com cancro. A excisão do tumor via cirurgia apresenta-se como a forma mais tradicional de tratamento. Sendo um cancro curável, o sucesso do tratamento depende do estágio de diagnostico, características do tumor e da fisiologia do paciente.

Como inegável símbolo de feminidade, a deformação da mama causada pelo tratamento tem graves consequências na qualidade de vida do paciente, com um terço dos pacientes em fase de tratamento a mostrar desconforto em relação ao aspeto da mama após a excisão do tumor. A razão principal para tal desconforto, está relacionado com a diferença entre as expectativas criadas pelo paciente e as restrições cirúrgicas. Assim, a necessidade de uma nova forma de abordar o tratamento assume um papel importante. Usando informação do próprio paciente, acompanhados por um modelo simulado, os cirurgiões poderão ter a capacidade de discutir os diferentes resultados de diferentes intervenções e os pacientes poderiam ter uma melhor noção do resultado após tratamento. Usando este modelo, os pacientes podem participar diretamente no processo de decisão e assim as suas expectativas corresponder às capacidades cirúrgicas da equipa medica. Por outras palavras, tal modelo é requerido para uma melhor comunicação entre o paciente e o médico, almejando um melhor conhecimento por parte do paciente dos possíveis resultados da cirurgia, bem como para fornecer uma melhor plataforma que permita à equipa medica melhorar as suas capacidades, resultando assim num tratamento com menor deformação da mama.

Para desenvolver tal plataforma, quatro obstáculos têm de ser superados. Primeiro, o modelo 3D do paciente deve ser obtido com a máxima precisão e de encontro com os requisitos médicos. O custo e a possibilidade de uma metodologia de reconstrução fiável são também necessidades importantes. Segundo, os modelos reconstruídos devem ser segmentados para a zona de interesse apenas. O estado da arte sugere que a deteção completa da região da mama é uma tarefa desafiante sem consenso médico em relação as fronteiras exatas da mama, como por exemplo a sua fronteira superior. Terceiro, com vista a facilitar a interação médico-paciente, os modelos segmentados devem ser matematicamente refinados de forma a serem interativos. Quarto, de forma a ter uma noção da forma da mama após cirurgia, o resultado deve ser previsto com base nas características do tumor e da fisiologia do paciente.

Na literatura relacionada com o tema de cirurgia mamária, as principais tecnologias para apoio ao planeamento, são maioritariamente associadas a aumento/mamoplastia ou outras formas de cirurgia plástica. Embora o procedimento de reconstrução dos modelos do paciente intersecte com as varias opções de tratamento, eles diferem fundamentalmente em termos de aplicação. Dos métodos já existentes, estes requerem instalações bastante específicas, de modo a fornecer os modelos e realizar o seu processamento (dispendiosas) ou requerem pessoal altamente especializado. Com vista a solucionar estas dificuldades e tendo em conta a grande prevalência do cancro da mama, aqui é proposta uma forma de baixo custo e eficiente de planeamento que pode ser usada na clínica; de baixo custo (em relação a preço, instalações, e pessoal especializado) e eficiente para

ir de encontro a todas as exigências acima mencionadas. Finalmente, a abordagem proposta é apresentada como uma ferramenta de planeamento, implementada para ser usada como um sistema de apoio à decisão, tanto no planeamento de cirurgias como no treino de estudantes de medicina.

Abstract

Breast cancer is the most common cancer among females, accounting for less than a third of diagnosed instances as well as one-eighth of cancer-related death in women. Considering treatment, which mostly encompasses tumor excision via surgery, breast cancer is known as curable cancer; however, the success of the treatment depends on cancer diagnosing stage and tumor characteristics, as well as patient physiology.

While breasts are an undeniable symbol of the feminine, the imposed deformation caused by surgery influences patients' quality of life. This is justified by reports stating that almost one-third of patients being treated is not satisfied with the aesthetic shape of their breast after the tumor excision surgery. The main reason may probably lie upon the gap between patients' expectations from the surgery in one side, and the surgical constraints on the other side. Here, the necessity of an approach to plan breast cancer treatment is highlighted. By using patient's own breast model, accompanied by a simulated model, surgeons could discuss the outcome of different surgical options, and patients could imagine their breasts' shape after the treatment. With this scheme, patients can directly participate in the procedure of treatment decision, and therefore they can align their expectations with the expertise of the medical treatment team. In other words, such planning approach is intended to improve the communication between patients and physicians, aiming to elevate patients' understandings of surgical aesthetic outcomes, as well as proving a framework for surgeons to improve their expertise to perform surgeries resulting in treatments with less deformation.

To provide a planning approach based on the aforesaid objective, 4 main challenges have to be overcome. First, patients' 3D model should be obtained with an accuracy which fulfills medical requirements. Not only the accuracy, but also the cost, and the availability of reconstruction methodology play important roles. Second, the reconstructed 3D models must be segmented to only have patient's breast as the region of interest. Note that a concise study of the state-of-the-art methodologies indicates an incomplete detection of breast region. Therefore, detecting complete breast region is a challenging task since there is no medical consensus on the breast exact boundaries in some regions, such as breast upper boundary. Third, to facilitate the aforementioned interaction between patients and physicians, the segmented breast models must be mathematically redefined such that they can be deformed interactively. And finally forth, to have an overview of the breast shape after surgery, the breast shape can be predicted with respect to both the tumor characteristics and patient's physiology.

By reviewing literature in the scope of breast surgery, it is observed that most of the proposed planning approaches were suggested for augmentation/mammoplasty, or breast pose transformation. Although the procedure of reconstructing patients' 3D model intersects with current planning approaches, their rest differs fundamentally in terms of application. The few ones targeting breast cancer treatment, either require powerful facilities to provide models and perform the biomechanical processing (that takes longer than expectation) or they require expert personnel to configure them. In this regard, considering the large-scale worldwide prevalence of breast cancer, we aimed to propose an affordable and efficient planning approach to be employed in clinics widespread;

affordable (in terms of cost, facility and required personnel) to be used clinics, and efficient to fulfill the aforementioned demands. Finally, the proposed approach is presented as a planning tool, implemented to be used as a decision support system for breast cancer, either in planning surgeries or in training medical students.

Acknowledgments

First and foremost I offer my sincerest gratitude to my supervisor, Professor Hélder Filipe Pinto de Oliveira, who has supported me throughout my dissertation with his patience and knowledge whilst allowing me the room to work in my own way. I attribute the level of my Ph.D. degree to his encouragement and effort and without him, this dissertation, too, would not have been completed and written. One simply could not wish for a better and friendlier supervisor.

Furthermore, I would like to thank my co-supervisor, Professor Jaime dos Santos Cardoso. He supported me greatly, enthusiastically motivated me to carry out the research, and taught me to be steady in this way. I could not complete my work without his invaluable assistance. He was always available when I needed. The words cannot express my sincere gratitude.

The members of the VCMI (Visual Computing and Machine Intelligence) group have contributed immensely to my personal and professional time at INESCTEC. The group has been a source of friendship as well as good advice and collaboration. I am especially grateful to João P. Monteiro, João P. Teixiera, Silvía Bessa, Sara Pires Oliveira, Ana Rebelo, Samaneh Khoshrou, A. Filipa Sequeira, and Inês Domingues. They supported me greatly and were always willing to help me.

A very special thank INESCTEC, for all the work conditions, infrastructure and technical support are given to my Ph.D. dissertation and for the other challenges, I worked in.

And I would like to thank my dearest friends who assisted me revising my dissertation grammatically; Beth Hirsch, Ali Azarian, Mohammad-Ali Fotouhi-Ghazvini, Hadi Honarvar Nazari, and Pouya Asrar, and Tiago Ramos.

I also want to thank the students that contributed to this thesis who officially and non-officially, I supervised: Pedro Faria and Pedro Costa. Thank you all, for helping me to improve.

In addition, I would like to thank FCT – Fundaçãopara a Ciência e a Tecnologia (Portuguese Foundation for Science and Technology) for helping and providing the funding within Ph.D grant number SFRH/BD/97698/2013, and from the European Community's Seventh Framework Programme [grant number FP7600948], as well as BCCT.plan project funded by Portugal Operational Programme (Portugal 2020) – NORTE-01-0247-FEDER-017688, and 3d BCT financed by FCT (PTDC/SAU-ENB/114951/2009).

Last but not least, I would like to express my sincerest gratitude to my parents, baba Amjad and maman Nastaran for all their love, encouragement and infinite support throughout everything. You provided me all the opportunities from the very first day of my life, I hope that this work makes you proud. And to my sweetheart, Malihe who loved, supported, encouraged, and helped me get through these years, in good times and in bad, in sickness and in health.

Hooshiar Zolfagharnasab

"A complex system that works
is invariably found to have evolved from a simple system that works."

John Gaule

Contents

List of Figures

List of Tables

Acronyms

2D	Two-dimensional
2.5D	Depth data
3D	Three-dimensional
ACR	American College of Radiologists
API	Application Programming Interface
BAT	Breast Analyzing Tool
BCCT	Breast Cancer Conservative Treatment
BCCT.core	Breast Cancer Conservative Treatment.cosmetic result
BCE	Binary Cross Entropy
BCS	Breast Cancer Surgery
BCT	Breast Cancer Treatment
BI-RADS	Breast Imaging Reporting and Data System
BRA	Breast Retraction Assessment
BSI	Breast Symmetry Index
CIE	Commission on Illumination
DCT	Discrete Cosine Transform
DT	Delaunay Triangulation
FE	Finite Elements
FEM	Finite Element Modeling
FFD	Free Form Deformation
FoV	Field of View
GBR	Gradient Boosting Regression
GCV	Generalized Cross Validation
GMM	Gaussian Mixture Model
GUI	Graphical User Interface
HKS	Heat Kernel Signature
HM	Heuristic Model

IBM	Image-based Modeling
IBR	Image-based Rendering
ICP	Iterative Closest Points
IG	Information Gain
IMF	Infra-Mammary Fold
IR	Infra-Red
JND	Just Noticeable Difference
LBL	Lower Breast Line
LIQ	Lower-Inner Quadrant
LOPO	Leave One Patient Out
LOQ	Lower-Inner Quadrant
MIMO	Multiple Input Multiple Output
MISO	Multiple Input Single Output
ML	Machine Learning
MOR	Multi-Output Regression
MRI	Magnetic Resonance Image
MSE	Mean Square Error
NBL	Nipple Base Line
OF	Objective Function
p2p	Point-wise Distance
PCA	Principal Component Analysis
PCL	Pointcloud
PDE	Partial Differential Equation
QoL	Quality of Life
RANSAC	Random Sample Consensus
RBM	Range-based Modeling
RBL	Redundant Bent Layer
REM	Radial Element Method
RF	Random Forests
RMS	Root Mean Square
RoI	Region-of-Interest
RSS	Residual Sum of Squares
SCAPE	Shape Completion and Animation for People
SDK	Software Development Kit
SIM	Similarity
SVD	Singular Value Decomposition

ToF	Time-of-Flight
UBL	upper Breast Line
UIQ	Upper-Inner Quadrant
UOQ	Upper-Outer Quadrant

To My Family
My love for you shall live forever.

Chapter 1

Introduction

Breast cancer is a widely known disease that mostly affects women around the world. With prevalence near to 29% of all cancers and nearly 14% of cancer deaths in women, breast cancer was the most common cancer amongst females in 2016 [171]. Nevertheless, with one of the highest incidence rates of female disease, breast cancer is curable if it is diagnosed in early stages [8]. It has been shown that with a correct diagnosis and early treatment, more than 90% percent of patients can live longer than 5 years after the treatment [54]. Based on diagnosing time, there are two groups of treatments used by specialists: invasive and noninvasive. In early-stage diagnosis, noninvasive methods, such as hormone therapy, radiotherapy, and chemotherapy, can be employed while in situations when the disease is diagnosed later, the invasive method such as surgery is strictly recommended [142].

Considering invasive treatment, mainly two surgical approaches are performed; Mastectomy, and Lumpectomy [142, 198]. Not only the characteristics of the tumor (benign or malignant), but also patient's physiological characteristic, and even the opinion of both surgeon and patient are taken into account for deciding the appropriate treatment [142]. In the mastectomy, almost the entire breast tissue is excised to remove the tumor, and also to reduce the recurrence of cancer. In the other approach, that is also known as Breast Conserving Surgery (BCS), it is attempted to remove only the tumor and preserve the breast tissue; however, to reduce the chance of redevelopment of cancer, a thin layer of healthy tissue surrounding the tumor is removed as well. Additional post-surgery treatments, such as radiotherapy, are recommended as adjuvant therapies to assure that the suspicious remaining cancerous cells are removed completely [4].

Although less suspicious cells are left after performing the mastectomy, similar survival rates have been reported for both invasive approaches [31, 142]. Thus, with the similar survival rates, surgeons and patients normally prefer to carry out surgeries with less breast deformation; having better aesthetic outcomes [29, 142]. It should be noted that the amount of breast deformation depends on not only the amount of the removed tissue, but also the surgeon's expertise to perform the incision [142], and the adjuvant therapies carried out after the primary treatment [17]. Although treatments have progressed to have lower secondary effects, breast cancer surgery is still a reality for most patients.

1.1 Motivation

Breast is one of the feminine symbols; therefore, any imposed deformations through surgical treatments impress patients' Quality of Life (QoL) significantly. Considering the performed type of the invasive treatment, patients are reported to experience different QoL [91]. Still, despite the smaller deformation after BCS, studies have shown that up to 30% of patients are dissatisfied with their post-operative appearance [82]. Therefore, alongside the survival rate and the success of the treatment, more attention should be paid to the aesthetic outcome of the BCS [29, 142].

Several studies have shown that the final aesthetic outcome of breast surgery can be affected by different variables, from different surgical practices and expertise to some breast specific characteristics, such as volume, density, size and location of the tumor. The aforementioned factors complicate the prediction of breast shape and thus influence patient/surgeon communication about surgical procedure results. Even though this is an important step, regarding the acceptance of the final outcome and the contribution of breasts to the sense of femininity and beauty of most women, in fact, follow-up studies after breast cancer treatment show the harmful impact of poor aesthetic results on the psychosocial health of women, who describe loss of self-esteem [74], sexual impairment [1] and dislike towards their bodies after treatment [101]. On the other hand, physicians have been recognizing the value of support decision systems for planning BCS, to compare the outcome of different surgical options and facilitate surgeon/patient communication [190, 197]. The value of such systems is further supported by studies confirming that women are more willing to deal with the aesthetic results when they are included in the decision process [190].

The development of a planning/simulation system for surgery demands the creation of three dimensional (3D) models of the breast that can be deformable in a realistic fashion, to reproduce known deformations imposed by surgery. Such deformable models can provide an appropriate scheme for physicians to interactively consult about possible treatment procedures with patients. Not only the patients, but also the medical team can benefit from such planning system as they can improve their skill by sharing the experiences via an interactive framework, or they can use it for training purposes in education.

A brief literature review reveals that yet, there has not been any proposed planning/simulation system aligned with the requirement of BCS. Mostly, state-of-the-art approaches concentrated on performing the aesthetic evaluation of breast shape after surgeries. An aesthetic evaluation tool intends to determine the treated breast deformation level in Harris *et al.* scale [79]. Tools such as Breast Analyzing Tool (BAT) which were proposed in 2007 by Fitzal *et al.* [60] focused on performing breast aesthetic evaluation by comparing the treated breast with the collateral breast to detect the asymmetry level between them. Independently in the same year, Cardoso *et al.* [29] proposed a methodology to extract features from frontal images and perform the evaluation by using Machine Learning (ML) techniques.

Breast Cancer Conservative Treatment Cosmetic Results (BCCT.core) [29], attempted to evaluate the deformation of the breast using images of the treated breast. A later improvement was proposed in 2014 by Oliveira *et al.* [143] to elevate the performance of the aforementioned tool by

employing depth maps to extract more depth features with the aim of performing a more robust evaluation of the breast aesthetics. A general look at these tools highlights that they cannot be identified as a complete planning tool before BCS since they have been designed to evaluate the shape of the breast after treatment.

In literature, strategies to model breast deformations are abundant and designed to different applications: estimate pose transformation [57, 77, 154], assist registration tasks among different radiological imaging modalities [84, 86, 130], model breast deformation [13, 170, 175], guided surgery [34, 35], predict the healing process of the breast after tumor removal [66, 197]. The aforementioned applications use either biomechanical models or fitting approaches to predict deformations that, due to some inherent limitations, are not the most suitable approach to include in a tool designed to be used in the daily clinical practice. First, the computational process for most algorithms might take hours or days, depending on the complexity of the models. Such delay in producing simulated surgery outcomes complicates patient/physician communication during consultations. Second, most models are simple representations of the breast biomechanics, using unverified parameters, posing fidelity concerns on the predictions. Third, the characterization of individual-specific parameters to create personalized models of the breast, alongside with precise representation of loading and boundary constraints during different clinical procedures, is still an unsolved challenge [155]. The aforesaid methodologies intend to provide patient-specific treatment solutions. Thus, the model parameters should be easily personalized with respect to patient and tumor characterizations during the consultations. Alternative strategies to model breast deformations could encompass the fitting of parametric models [16, 64, 113, 149, 162], physical equations to describe known breast deformations [38], user-intuitive parameters to change breast shape [63, 169] or dataset of known cases to simulate breast surgery outcomes [102]. These strategies model the breast with a limited number of parameters and produce results in a timely manner more adequate to clinical practice, but the modeling of breast deformations has yet to be improved for clinical surgery planning applications.

Despite some tools are already available [142], to the best of our knowledge, there is currently no tool, other than surgical experience and clinical judgment, to predict the impact of BCS on the shape and deformation of the treated breast [68]. In fact, the available solutions usually rely on generic models, are mainly targeted to plastic surgery (namely breast augmentation) which is a different topic in terms of planning. Moreover, they usually demand expensive and large equipment to scan patient's torso for generating the 3D model and require expertise to handle those scans [51].

Now, more than ever, a tool to provide the framework to plan for BCS is needed. Such tool should be capable to predict patient's breast model prior to the surgery in a reasonable time, apart from the available complicated ones which either require expensive facilities, or powerful computers or complicated to be configured in daily usages in clinics.

1.2 Objectives

We aim to enhance the communication between patients and physicians with the intention of improving patient's QoL who have undergone BCS. In this way, a planning tool for BCS will be proposed that it is designed to benefit patients by providing an outlook of their breast shape to assist them to overcome the concerns of the aesthetic outcome of their breast after the surgery. Not only the patients but also the medical team can benefit from the proposed planning approach since they can improve their skills to carry out surgeries which impose less deformation to the natural shape of the breast.

The designing of the aforementioned planning tool poses several challenges, as listed in the following:

Providing patient's 3D model First, the provision of the patient's 3D model is mandatory to fulfill the requirement of proposing patient-specific treatment solution. While the commercial solutions to generate 3D models are known to be expensive and complicated for clinical usages, it is intended to use low-cost devices to carry out the 3D model reconstruction.

Segmenting breast region from patient's 3D model The second challenge is defined with respect to the segmentation of the breast from the reconstructed torso. The segmentation is intended to provide patient's specific breast in order to be used either in parametric model generation or breast shape prediction. To facilitate the preparation of 3D breast models in clinics, automatic methodologies should be taken into consideration.

Generating patient's specific parametric model of breast To provide a breast model which can be deformed naturally through interaction, it is essential to generate a mathematical model of the breast. Presenting the patient's own breast in the form of the parametric model assists physicians to deform the breast easily to explain the possible post-surgery outcomes.

Predicting patient's breast shape after BCS The final challenge is defined by predicting the shape of patient's breast before performing the BCS. The prediction encompasses the correlation between the imposed deformation and the clinical characteristics of patient's breast and the tumor properties.

1.3 Contributions

The contributions of this dissertation, 3D reconstruction methods for breast surgery planning, are listed as follows:

1. 3D reconstruction of patient's torso using Microsoft Kinect as a low-cost device; proposing a coarse rigid registration, improving ICP-based non-rigid registration, enhancing the color of reconstructed model

2. Proposing a multi-modal methodology to segment complete contour of breast from 3D data
3. Improving Free Form Deformation (FFD) methodology by proposing new initial models for fitting breast data
4. Proposing a ML model to predict breast shape after BCS, creating a synthetic dataset comprising the 3D pointclouds of pre- and post-surgical models and extending the dataset by varying clinical features (breast density, tumor size, tumor location)

List of Publications Related to the dissertation

The work related with this dissertation resulted in the publication of the listed journal papers:

- H. Zolfagharnasab, S. Bessa, S. P. Oliveira, P. Faria, J. F. Teixeira, J. S. Cardoso, and H. P. Oliveira, *A regression model for predicting shape deformation after breast conserving surgery*, Sensors, 18(1), pages 167–196, 2018

From this dissertation, the following international conference papers were published:

- H. Zolfagharnasab, J. P. Monteiro, J. F. Teixeira, F. Borlinhas, and H. P. Oliveira, *Multi-modal complete breast segmentation*, In Proceedings of the Iberian Conference on Pattern Recognition and Image Analysis, pages 519–527, 2017
- H. Zolfagharnasab, J. S. Cardoso, and H. P. Oliveira, *Fitting of breast data using free form deformation technique*, In Proceedings of the international conference of image analysis and recognition, pages 608–615, 2016
- P. Costa, H. Zolfagharnasab, J. P. Monteiro, J. S. Cardoso, and H. P. Oliveira, *3D reconstruction of body parts using RGB-D sensors: Challenges from a biomedical perspective*, In Proceedings of the 5^{th} International conference on 3D Body Scanning Technologies, pages 378–389, 2014
- P. Costa, J. P. Monteiro, H. Zolfagharnasab, and H. P. Oliveira, *Tessellation-based coarse registration method for 3D reconstruction of the female torso*, In Proceedings of IEEE international conference on bioinformatics and biomedicine (BIBM), pages 301–306, 2014

I also participated in national conferences with the following papers:

- H. Zolfagharnasab, J. P. Monteiro, J. F. Teixeira, f. Borlinhas, and H. P. Oliveira, *Automatic segmentation of breast complete contour using multi-modal data*, In Proceeding of 26^{th} Portuguese Conference on Pattern Recognition, pages 50–51, 2017

- H. Zolfagharnasab, J. S. Cardoso, H. P. Oliveira, *Parametric modeling of breast data using free form deformation*, In Proceeding of 25^{th} Portuguese Conference on Pattern Recognition, pages 49–50, 2016
- H. Zolfagharnasab, J. S. Cardoso, H. P. Oliveira, *A 3D parametric model for breast data*, In Proceeding of 24^{th} Portuguese Conference on Pattern Recognition, pages 40–41, 2015
- H. Zolfagharnasab, H. P. Oliveira, *Non-rigid registration of point clouds regularized by NURBS*, In Proceeding of 23^{rd} Portuguese Conference on Pattern Recognition, pages 76–77, 2014
- H. Zolfagharnasab, J. S. Cardoso, H. P. Oliveira, *3D breast parametric model for surgery planning – A technical review*, In Proceeding of 22^{nd} Portuguese Conference on Pattern Recognition, pages 85–86, 2013

1.4 Document Structure

This dissertation is organized into 8 chapters, each one comprising a study related to the challenges to design the BCS planning tool. While the motivation, the objective, and the contributions have been discussed in the first chapter, the remaining presents the description of the dissertation structure.

In the second chapter, the literature review of the BCS is described first, including anatomy of the female breast, breast cancer facts and figures, and treatment and its consequences. Then the focus will change from medical descriptions to the breast aesthetic evaluation since it motivates the demands for a pre-operative planning tool. The evolution of the methodologies using 2D data (such as images) to 3D data is then studied, as well. While the aesthetic evaluation methodologies are designed with post-operative purposes, they are not aligned directly with the objectives of the current research. Statement of demands will be followed by briefly reviewing state-of-the-art approaches used to either predict, or plan the breast surgeries, including BCS, and breast augmentation surgery.

In the third chapter, there will be a literature review on sensors and methodologies to reconstruct the 3D models of patients. Concerning both the medical requirement and the cost of equipment, a low-cost sensor is chosen and a methodology is developed in order to carry out the 3D reconstruction of patient's torso within two registration steps: rigid and non-rigid. The reconstructed results indicated the demand for color enhancement techniques, which has been studied as well. The 3D reconstruction pipeline is then adapted to generate a dataset comprising 3D models of the patients which will be used in the following research.

Since the concentration of the current research is focused on proposing a planning approach for the BCS, it is required to segment the breasts as the Region of Interest (RoI). In this way, an automatic multi-modal methodology is proposed in Chapter 4 to detect the breast complete contour first, and then segment it from the reconstructed torso. The complete breast contour includes the

exterior contour, detected from the 3D surface model, and the interior one which is the pectoral muscle annotated from MRI data and automatically registered to the 3D surface data.

The segmented breast is presented as a cloud of points; therefore, further interacting by a physician during the consultation, will not result in natural deformation of the 3D model in whole. This is despite the fact that it is preferable for both physicians and patients to track the deformation of the breast shape entirely, as changes are imposed to the breast interactively. Such behavior of breast models is feasible through generating a parametric model from the 3D segmented breast data which is detailed in Chapter 5.

In Chapter 6, the prediction of breast shape will be studied. Following the investigation of current methodologies, which are mostly time-consuming, or require high-end computers, or complicated for clinical usages, a solution will be proposed to exploit ML techniques to overcome not only the aforesaid drawbacks but also the requirement of creating a patient-specific predicted breast model. Additional studies have been carried out to determine the impression of clinical features, including tumor size, tumor region, and breast density (adipose to fibroglandular ratio) on the deformation of the breast after BCS. The conducted studies assisted in generating a dataset by varying the clinical feature in order to train the ML model to predict the breast shape.

In Chapter 7, the technical implementation of the planning demonstration is presented in 3 stages: 3D torso reconstruction and breast complete contour segmentation, parametric model generation, and breast shape prediction after BCS.

Finally, the conclusion is wrapped up in the Chapter 8, together with future lines of research.

Chapter 2

Literature Review

Investigating on breast cancer without knowing the structure of breast is impossible. Therefore, in this chapter, first, it is aimed to review the anatomy of a breast. Skimming briefly to the causes of breast cancer, common treatments will be reviewed. Introducing imposed deformation resulted from surgeries, a discussion will be conducted to determine the necessity of surgeries which result in less breast deformation. Then, by inspecting the influences of breast deformation on patient's QoL, the importance of patient/physician communication through consultations will be argued. The discussion will be followed by explaining the demands for a planning/simulation approach suited for pre-operation breast surgeries.

Investigation of state-of-the-art approaches related to planning/simulation approaches requires introducing the methodologies for breast aesthetic evaluation. Although most of them utilize 2D images, the trend has been shifted to employ 3D models; therefore, the advantageous and of using 3D models will be appraised, as well. Finally, to comply the objectives of pre-surgical planning approach, a literature review will be conducted to fulfill the objectives of planning/simulation. Additional investigations are performed in nearby scopes, including breast shape simulation approaches for breast reconstruction surgeries, to motivate the demands and requirements of planning/simulation approach.

2.1 A Brief Review of Breast Cancer and the Treatment

Breasts are important organs in women's body, whose primary role is related to not only sexual attraction but also the production of milk to nourish children. As highly deformable organs, they are located on the anterior and lateral parts of the chest, overlying the *pectoralis major* and *minor* muscles. Having a heterogeneous structure (see Figure 2.1), consisting of mammary glands (fibroglandular tissue) and adipose tissues (fat), breasts are firmly attached to the skin and underlying structures by fibrous bands referred to as Cooper's ligaments. These suspensory ligaments provide the function of support, hold the breasts in place and contribute to determine the shape and contour of the breasts [156]. Adipose tissue is fat-storing loose connective tissue, which determines the size of the breast, and mammary glands are modified sweat glands responsible for

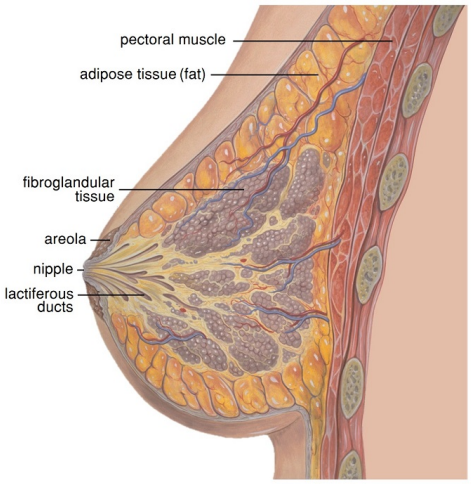

Figure 2.1: Breast anatomy: fibroglandular and fat tissues, which have distinct mechanical properties, compose most of the breast - adopted from[1].

milk production. The relative distribution of fibroglandular and fat tissues varies significantly depending on patient's age, menstrual cycle, pregnancy/lactancy, hormone therapy and menopause, which affects the structure and morphology of the breast [156, 189]. The ratio of these two types of tissue defines the breast density, which among other factors, can be related to the risk of developing breast cancer. In fact, women with a higher mammography breast density, are more likely to develop breast cancer [92].

While the reason is still unknown to the medical community, a normal fibroglanduar cell becomes cancerous due to the mutation of its DNA, when proto-oncogenes, responsible for cell division, are modified. The mutation affects the number of the cells to grow up unrestrainedly, originating a mass of cancerous cells, called a tumor. Initiated from different cells, breast cancer is categorized into different types. The ductal carcinoma in situ is the most common benign breast cancer tumor that begins from a duct cell. Since the tumor is reluctant to spread, it is a highly curable cancer. Unlike the ductal carcinoma in situ, the malignant tumor from invasive ductal carcinoma is known to spread to surrounding tissue, causing around 80% of total diagnosed cancers [135]. Not only duct but also lobe cells can be mutated to grow uncontrollably, causing another type of cancer, called invasive lobular carcinoma, as the second most incidence of malignant tumors.

The breast cancer treatment comprises invasive and non-invasive approaches. Whilst in invasive treatment, it is attempted to remove cancerous cell through surgery, non-invasive treatment, such as chemotherapy, radiotherapy, and hormone therapy, are pursued to eliminate the tumor without surgery. Non-invasive surgery is followed mostly when cancer is diagnosed in early stages, or the physiology of patient is not appropriate for surgery [8]. When the tumor is spread to neighboring tissue, or there might be the risk of remaining suspicious cell after surgery, a combination of invasive and non-invasive treatments is taken into consideration.

[1] https://commons.wikimedia.org/

Focusing on the invasive treatment, two common surgeries are carried out for tumor resection: Mastectomy and Lumpectomy [142]. Illustrated in Figure 2.2, mastectomy comprises the removal of entire breast tissue, although there might exist tissue which is not affected by cancerous cells. In other words, it is attempted to abandon the redevelopment of cancer in the treated breast via removing total breast tissue through the mastectomy. With respect to the diagnosing stage, and the location of the tumor, five types of mastectomy are performed: simple (or total), radical, modified radical, partial, and subcutaneous mastectomy.

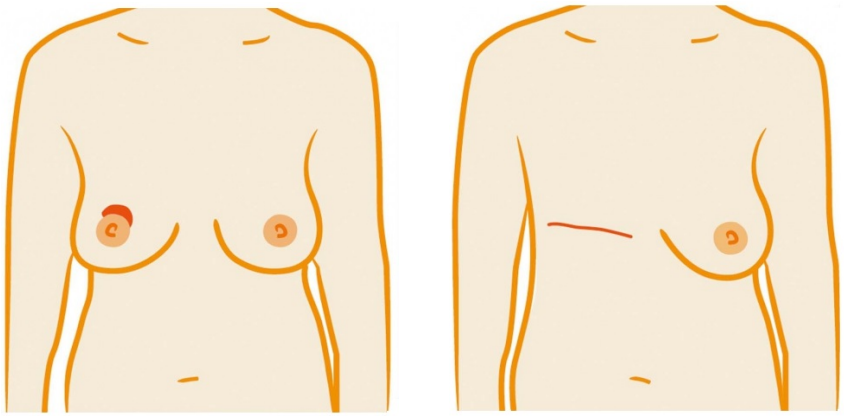

(a) (b)

Figure 2.2: Illustration of a breast with the position of (a) tumor, and (b) the position of scar resulted after mastectomy. The images are adopted from[1].

For decades, mastectomy was prescribed for almost every breast cancer cases, contributing with a high rate of success for removing the tumor; however, this surgical option has a profound impact on the aesthetic appearance of the breast by deforming the torso shape intensively.

With widespread mammography screening, the average size of detected tumors has been decreased and therefore, such treatment which imposes large deformation on the breast, is not preferred by surgeons and patients [33]. Instead, treatments in which more healthy tissue is preserved, have drawn the attention of medical society. Known as Breast Conservative Treatment (BCT), it includes several stages, first to remove the tumor, and then to ensure that no more cancerous cell remains.

Breast Conserving Surgery (BCS) is an important stage during BCT which is intended to excise the tumor plus a margin of healthy tissue. However, to decrease the chance of cancer redevelopment, and also to assure the removal of cancerous cells completely, adjuvant therapies, such as radiotherapy or chemotherapy are followed up after the primary treatment. Excision of less tissue (comparing with mastectomy) makes BCS an appropriate surgical option for most of the patients (50% - 75%) with breast cancer diagnosed at early stages [33]. Although BCS is similar to partial mastectomy, the amount of removed tissue disarticulates the two surgeries from

[1] https://www.breastcancercare.org.uk/

each other [142]. Figure 2.3 depicts a scenario in which a tumor is lactated inside the breast and then removed via BCT.

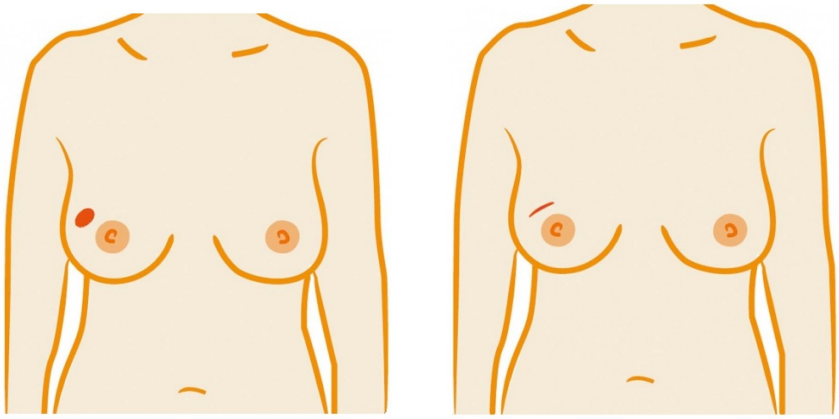

(a) (b)

Figure 2.3: Illustration of a breast with (a) the position of the tumor, and (b) the position of scar resulted after lumpectomy. The images are adopted from [1].

Besides better aesthetic results, several studies have shown that BCT presents almost the same survival rate as mastectomy; therefore, it is the most preferred invasive surgical approach pursued by medical community [33]. However, the treatment plan, including necessary surgical approaches, and adjuvant therapies, is always tailored based on both medical and patient choices. This emphasizes the importance of communication between the medical team, and the patient in the duration of making decisions, alongside the correct working practice, in order to improve the surgery strategies resulting in a satisfactory aesthetic outcome.

2.2 Importance of Planning for BCS

Since breasts are a symbol of the feminine, imposing any deformation resulted from BCS, impacts patients' QoL significantly. Researchers have reported that near to 30% of patients are dissatisfied with the aesthetic outcome of their breast after the treatment [82]. Nevertheless, cosmetic evaluation indicated that only up to 6% of surgeries resulted in poor aesthetic outcome [61]. This fact indicates that although preserving more tissue during the invasive treatment can result in a better cosmetic outcome, other factors are involved either directly or indirectly in the formation of breast new shape after the surgery.

First, surgery-related factors such as surgical approach, the placement of incisions [41, 45, 184, 199], the volume of excised tissue or surgeon expertise might lead to different extents of breast shape deformations [33]. Second, patient-related physiological characteristics are involved, as well. These factors include breast size [45, 119, 157, 199], body mass index, the age of first

[1] https://www.breastcancercare.org.uk/

pregnancy, and menopause situation [142]. Finally, the third group of factors to determine breast shape after treatment, are dependent on the tumor size [52], volume [184], and location [176].

In fact, follow-up studies after breast cancer treatment showed the harmful impact of breast deformation on the psychosocial health of women, who described the loss of self-esteem [74], sexual impairment [1] and disliked towards their bodies after treatment [101].

Patients are usually involved in the decision process regarding their surgery, but most of the time surgeons lack the means to provide visual clues about the post-surgery results of different alternatives. Previously, surgeons have to use inconvenient ways, such as drawing on paper, to explain the visual outcome of surgery [173]. Although it is an inefficient way to draw the 3D shape of the breast on 2D paper, it improves the surgeon/patient communication and involve patients more in the process of treatment decision. Such contribution leads to acceptance of the final outcome patients. Therefore, physicians have been recognizing the value of support decision systems for planning BCS, to compare the outcome of different surgical options and facilitate the aforesaid communication. The value of such systems is further supported by studies confirming that women are more willing to deal with the aesthetic results when they are included in the decision process [190]. By reviewing literature, it is revealed that a comprehensive planning tool to cover the requirements of both patients and physicians has not been proposed yet; although there are methodologies and further developed tools performing the post-operative planning to perform breast aesthetic evaluation.

Since the attempts to propose a planning tool for BCS surgeries was originated from post-operative tools (to evaluate breast shape), first, a brief investigation will be carried out to study the methodologies proposed for breast aesthetic evaluation. Then, inspired by the aforementioned reviews, pre-operative tools will be studied, as well, to design a framework to perform the planning prior to surgery.

2.3 Breast Aesthetic Evaluation after BCS

Since breast mostly consists of adipose tissue, behaving like deformable organs, they can be extremely impressed by either external or internal forces. Putting this fact besides the triple factors influencing breast shape after surgery studied in Section 2.2, it can be concluded that quantifying the level of deformation demands geometrical analysis of breast, surrounding regions. In this section, the available aesthetic scale, accompanied by the most prominent methodologies are studied in the field of breast shape evaluation.

2.3.1 Scale of Assessment

Originally proposed by Harris in 1979 [79], Harris scale is the most widespread aesthetic evaluation metric nowadays [31, 142]. The classification in Harris scale consists of four level; Excellent (treated breast is identical to untreated one), Good (there are some slight differences between treated and untreated breasts), Fair (treated breast is completely discernible from untreated one) and Poor (treated breast is completely distorted).

2.3.2 Breast Aesthetic Evaluation Methodologies

Perhaps the easiest method to evaluate breast shape is to ask patients to evaluate themselves based on their perception [5]. Conversely to its availability, this method is not reproducible due to lack of expertise in the process of treatment, as they usually underestimate, or overestimate the real situation [32, 41, 118, 142]. Either in questionnaire or via email, most patients feel unpleasant to criticize their breast shape after BCS, hence they would tend to reflect better aesthetic outcomes compared to reality [141].

Other evaluation methods, such as peer evaluation with a panel of observers, might not result in a concrete decision, since, observers evaluate differently based on their own background. Besides, there is not a meaningful relationship between the number of patients and time required for evaluation, even using fast communication methods such as electronic mail. However, there are significant concerns subjecting the privacy patients, since it is hard to keep privacy during evaluation.

In contrast with subjective evaluation, objective methods present comprehensive producible results based on constant knowledge. Formulating aesthetic evaluation, Penzer *et al.* [150] published the first objective methodology, Breast Retraction Assessment (BRA), in which could measure cosmetic results based on breast asymmetry using frontal views [151]. To have an aesthetic evaluation, they compared treated breast to untreated one by calculating upward and inward retractions. Such measurement resulted in asymmetry calculation that led to extract BRA value, which indeed was different from the Harris scales.

In 2007, a new generation of aesthetic evaluation methodology was proposed to automate the process of parameter measurement. Fitzal *et al.* [60] suggested using Breast Symmetry Index (BSI) to evaluate asymmetry by measuring the difference between both breasts. Followed by an application known as BAT (as in Figure 2.4), they evaluated the cosmetic result of BCS, by taking into account distances from nipple to sternum, differences in breast contours and differences in size between breasts.

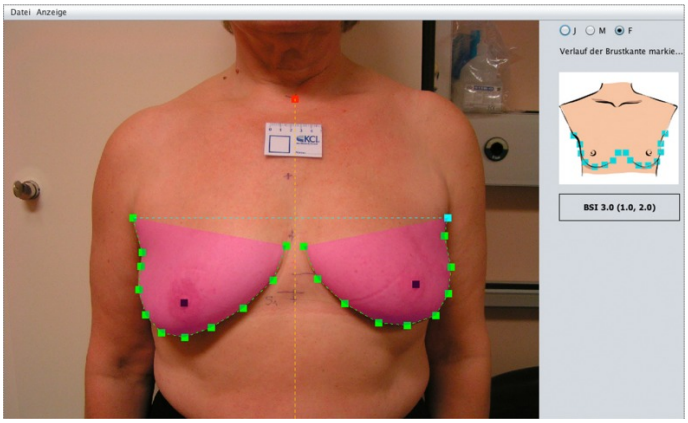

Figure 2.4: Aesthetic evaluation with BAT [60]; The image is adopted from [107].

Although their method seemed to depend on manual annotation of breast landmarks to calculate the BSI (such as the sternum), they demonstrated that the same results could be obtained by annotations from either experts or non-experts. Besides, they provided clues to show there was no correlation between patient's view (in the image) and BSI measurements. Though, discerning between good and fair evaluations (in the Harris scale), their methodology was unable to discriminate excellent and good or fair and poor.

Simultaneously in 2007, Cardoso and Cardoso [29] proposed a method, called BCCT.core (Breast Cancer Conservative Treatment Cosmetic Results) to extract a set of measurements and then perform the aesthetic evaluation. Using color, scar visibility and asymmetry obtained from frontal images, BCCT.core could categorize results precisely and present the final aesthetic score in Harris scale. A preview of the BCCT.core software is depicted in Figure 2.5.

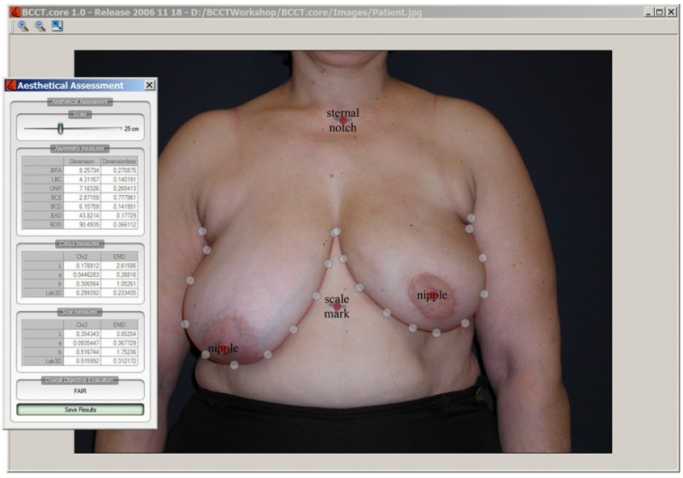

Figure 2.5: BCCT.core while evaluating breast frontal images; fiducial points are in red [29, 142]; The image is adopted from [141].

Distinguishing color dissimilarity, BCCT.core extracted color contents of each breast by a color histogram. Comparing the color locally and sector by sector, the method was able to find color changes related to scars. Following the color dissimilarity, it then searched to find fiducial points (nipple complex, breast contour and sternum notch) which were critical in detecting inframammary contour demanded to measure asymmetry. The result of the performed measurements was presented as breast aesthetic features, and were fed to a ML classifier to evaluate them and produce the final result in Harris scale. This method successfully classified the breast shape up to 70% of correctness comparing to subjective method performed by experts [31].

2.4 Toward Using 3D representation of Female Breast

The discussed methodologies in Section 2.3.2 evaluated aesthetic assessment via only 2D images. The drawback of using only 2D frontal images of breast was highlighted especially when it was tried to measure 3D features. While 2D images were incapable to represent the depth and

volumetric information of the breast, the trend changed toward using data with more dimensionalities, including 2.5D data (also known as depth-map), or 3D models. A recent investigation by O'Connell in 2017, substantiated the positive potentials in using 3D models to overcome the deficiencies of not only 2D images but also subjective evaluations [140].

Using Moiré topographic camera, Noguchi *et al.* [139] presented a method to measure differences between breast curves to obtain asymmetry. This research was the first work among others to utilize the depth information in the aesthetic evaluation. However, the final score was measured as the combination of subjective (for color and scar) and objective (asymmetry) evaluations.

In 2005, oncoplastic surgery concentrated on breast reconstruction to improve some of the poor scale surgeries [11]. This motivation drew the attention of researchers to evaluate breast cosmetics via 3D methodologies. Although a comprehensive evaluation has been performed using only frontal images, some researchers showed that using 3D images can improve the precision of correct measurements [10].

Losken *et al.* [121, 122] and Moyer *et al.* [133] proposed a method to extract asymmetry using arrays of 3D cameras. Arranged in 3 different planes, while cameras were all focused on manubrium, patients were scanned in two different positions; sitting with arms at their sides and on their hips. Followed by Root Mean Square calculation, the software bisects the reconstructed 3D model from thorax and put the mirrored left part on the right part. Using this technique, the software (shown in Figure 2.6) was able to compare level of asymmetry between breasts, ignoring skin color measurements.

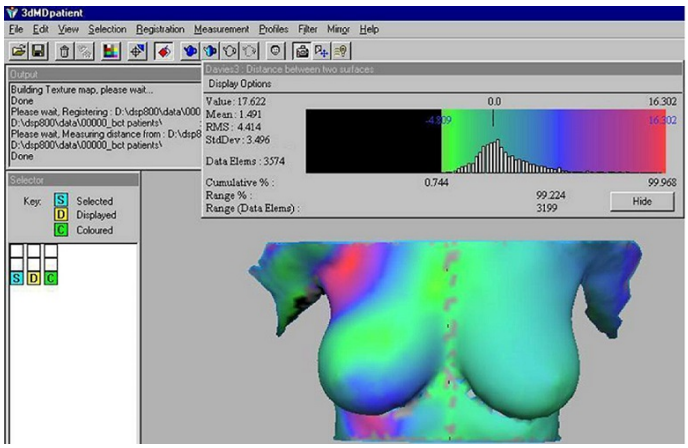

Figure 2.6: Software output showing symmetry score (root mean square or RMS) and the color histogram by Moyer *et al.* [133].

Bert *et al.* [19] introduced a 3D stereophotogrammetry system to capture 3D surface data to measure volumetric information. Registering daily patient's surface model to referenced model, they assured that the calculation of breast volume was reproducible, and accurate disregarding the patient position. To perform registration, their methodology determined the rigid body transformation which minimizes the distance between treated and reference model. Experimental results showed that since both deviation and constructed models error were sub-millimeters, the accuracy

acceptable to be used in clinics. However, specific facilities (shown in Figure 2.7) needed to be installed to obtain 3D models which made this methodology difficult for most clinics to replicate.

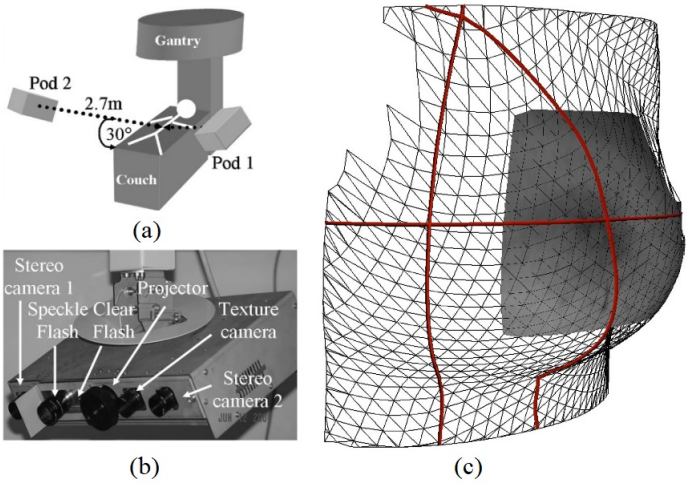

Figure 2.7: The 3D modeling system proposed by Bert *et al.* [19]; (a) the 3D stereo-photogrammetry system, (b) the sensors installed on each pod, (c) and the triangulated 3D model with a small part with overlaid texture. The images are adopted from [19].

Concerning the application of 3D laser scanners, a research was carried out by Kovacs *et al.* [103–105] to measure breast volume of a 3D dummy model. Evaluating the method's precision, they studied the optimization of the imaging technology in mammary regions, as well. In this research, they studied scanner related factors and tested the most favorable imaging technologies on dummy models, to guarantee that the method is reproducible. Finally, they were successful to present an application with an acceptable accuracy and reproducibility. Figure 2.8 illustrates an example of segmenting breast from the torso and computing its volume.

Tepper *et al.* [185, 186] proposed a method to exploit 3D models for breast reconstruction surgeries. Utilizing their method, surgeons were able to obtain volumetric information, breast size, breast shape and even contour by quantitative breast measurement and volumetric calculations. Followed by a research in 2010, Tepper *et al.* [187] introduced a new application called Mammometrics, providing a standard system for breast analysis. They showed that surgeons can benefit using post-operative planning and objectively evaluate surgical results. Also, the authors confirmed the usefulness of current research in various clinical areas such as autologous breast reconstruction, prosthetic breast reconstruction, reduction mammoplasty, and augmentation mammoplasty. Moreover, they claimed that using 3D imaging technology can lead to represent and extract some new features which had never been used before. Figure 2.9 demonstrates an output of reported measurements from Mammometrics.

In 2011, Sun *et al.* [179] carried out a research with the goal of proposing a user-friendly system to provide data and image files of breast extend region with proper layouts for the planning and post-operative evaluation. Shown in Figure 2.10, pre-operative plannings and post-operative images were compared for visual validation of proposed methodology.

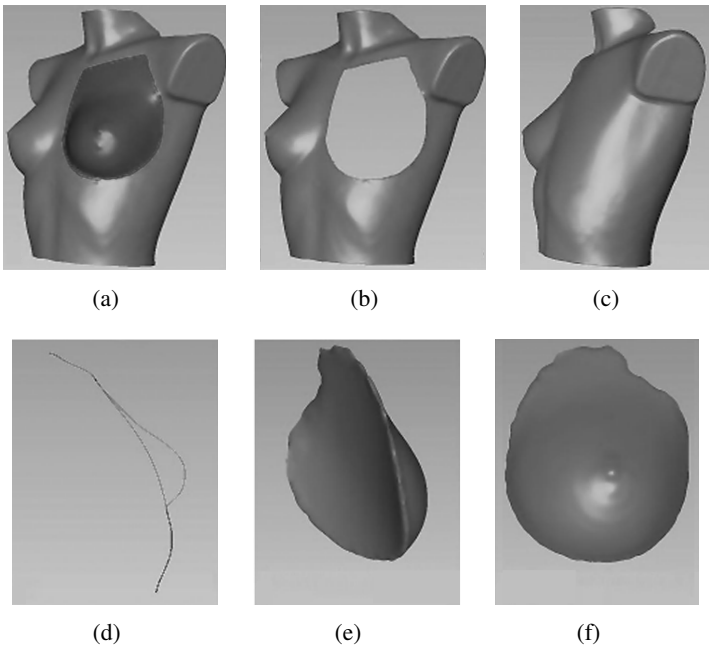

Figure 2.8: The procedure to compute breast volume by Kovacs *et al.* [103]: (a) annotating breast region, (b) segmenting the breast, (c) interpolating chest wall, (d) sagittal section of the chest torso, chest wall and breast (e) and (f), measuring breast volume (306 *cc* for the shown example). The images are adopted from [103].

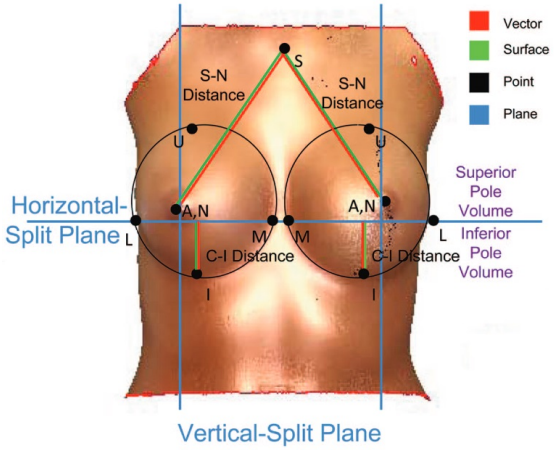

Figure 2.9: Measurement resulted from Mammometrics by Tepper *et al.* [187]. An overview of a single 3D image summarizing standard points, planes, distances, and volumes. S, sternal notch; N, nipple point; A, anteriormost point; M, medial inframammary fold point; L, lateral inframammary fold point; C, chest wall; I, inferior-most point; U, upper-most point. The image is adopted from [187].

They introduced a 3D scanning system accompanied by breast region measurement methods to parameterize the breast pocket region. Using parameters such as UBL (upper breast line), NBL (nipple baseline) and LBL (lower breast line); they tried to define the breast implant picket region in preoperative planning. Also, postoperative scanning and evaluation have been performed

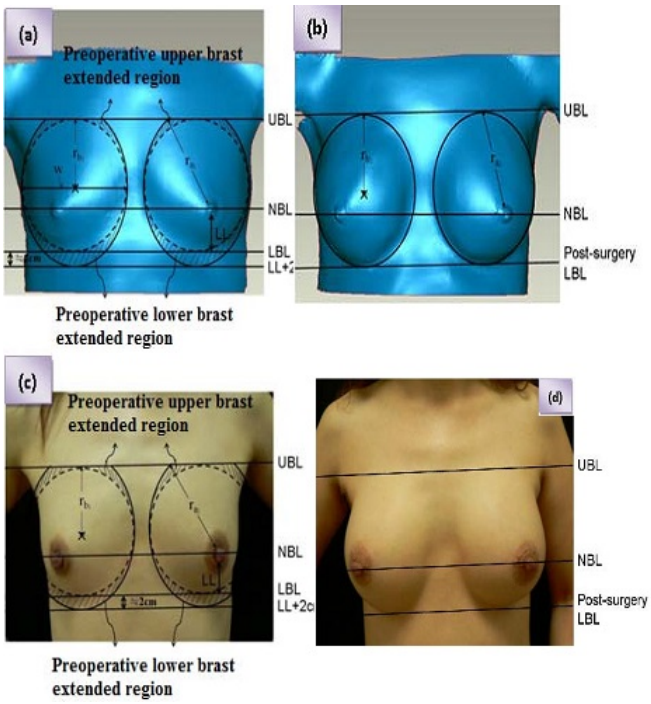

Figure 2.10: The comparison of breast implant pocket region for preoperative planning and post-operative image, suggested by Sun *et al.* [179]

to record the shape of the breast right after the surgery to 24 weeks after, with the duration of two weeks. Authors claimed that in studied cases, the breast cup size and implant pocket extend indicator for planning and post-surgery were matched under reasonable condition. Albeit, their suggestion is not conceived as a planning tool based on the defined objectives of the current research.

Henseler *et al.* [80] proposed to use a multiple stereo camera systems to reconstruct breast model without human interaction. Using a stereophotogrammetry system consisting of 8 cameras located on 4 pods two by two (depicted in Figure 2.11(a)), they constructed breast models from dummy torso (Figure 2.11(b), and Figure 2.11(c)). Following reconstruction, they evaluated the reconstructed models using the software BAT proposed in [60], stating satisfactory results of the evaluation. However, evaluation obtained by measurements from the real breast was much more accurate since the conical shape of breast causes an over immersion on the chest during scanning. Also, misdetection of the chest wall and breast boundaries impressed distance measurement negatively, leading to inaccurate feature detection. The aforesaid drawback made their methodology irreproducible [142].

In 2012, Oliveira *et al.* [143] proposed to use Microsoft Kinect, as a low-cost sensor, to obtain depth-map of the breast. Using depth-map shown in Figure 2.12, they extracted new depth and volumetric features [142, 144]. Finally, they reinforced the methodology for breast aesthetic evaluation proposed in [29] by combining the new features with the old ones in [29]. This research showed that unlike the previous methodologies, patient's 3D breast models can be obtained via low-cost devices.

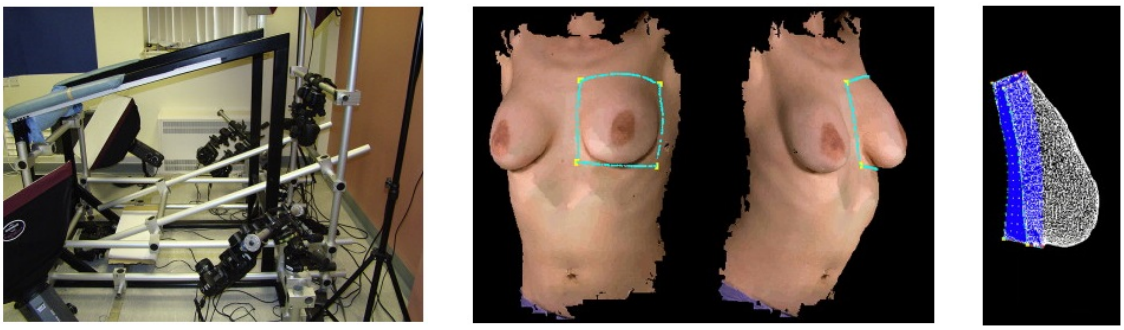

(a) (b) (c)

Figure 2.11: Application by Henseler *et al.* [80]: stereophotogrammetry (a), segmented breast on the 3D model (b), and segmented breast and chest wall (c). The images are adopted from [80].

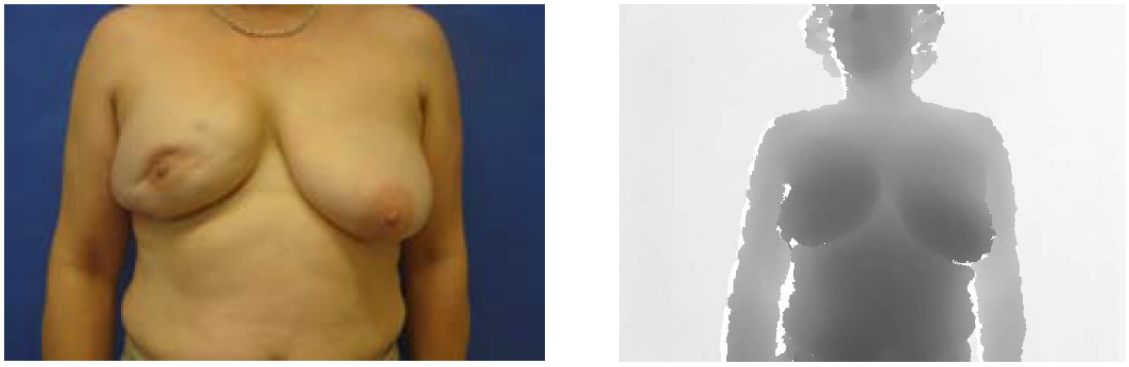

(a) (b)

Figure 2.12: Patient's frontal breast image and b) Kinect generated disparity map [141]

In a research carried out by Lancher *et al.* [110, 111] in 2015, the aforementioned low-cost sensor used by Oliveira *et al.* [143], was studied in detail to verify its applicability in medical application. Besides, they proposed a framework reconstruct patients' torso to be used in breast evaluation and planning tools. Comparing the 3D reconstructed models from the suggested framework with models obtained from a stereophotogrammetry 3D scanner, they reported the reconstruction quality in the range of 2 – 4 *mm* of mean absolute error.

In a recent study by Li *et al.* [115] in 2016, 3D models were used to measure breast ptosis. To achieve the aim, they reconstructed the 3D torso of patients using stereophotogrammetry systems followed by manual annotation of breast region. Employing Gaussian curvature, the surface curvature of each region was obtained, as well as surface orientation in which reflects the normal direction of each triangle of the mesh. For each of the aforesaid 3D features, histogram templates were generated with respect to the four ptosis grades. Training a model with histogram matching-based prediction methodology, they could classify the level of ptosis for a new test case. Finally, they concluded that the 3D measurement of curvature combined with the orientation of

breast surface resulted in a more accurate classification of breast ptosis, comparing to common 2D subjective evaluations.

2.5 From Post-operative Evaluation to Pre-treatment Planning

The idea of using 3D breast models opened a new line of research in the development of new methodologies to identify the cosmetic outcome of BCS; however, the suggested methodologies still lacked to represent breast deformation before performing BCS. In other words, there was still a gap between the decision of the treatment and the evaluation of the performed surgery. This was the Achilles heel of the post-operative tools aiming only to improve surgeon's expertise for future surgeries, instead of planning for current ones. In the recent years, there have been some attempts pointing to fulfill the requirement of a planning tool for BCS aligned with pre-operative purposes; although, they were mostly proposed to plan breast augmentation surgeries, instead.

In 2000, Chen *et al.* proposed a methodology to model and estimate aspects of a virtual reality system for reconstructive breast surgery [38]. Their suggestion comprised two stages in which first a parametric model was generated using superquadrics as the primitive shape of a breast, and then, fitted to the 3D data of patient's breast acquired by a 3D scanner. Totally 23 parameters were employed to resemble breast shape and deformation. Finally, in order to take the deformations into account, they used Lagrangian mechanics, proposed by Terzoloulos and Metaxas in [188], to convert multiple parameters into a generalized coordinate with a dynamic degree of freedom; however, further evaluations in [149] showed that the fitting stage resulted in an unstable and time-consuming fitting. Figure 2.13(b) demonstrates an example of a breast model developed by a physician to model the female breast depicted in Figure 2.13(a).

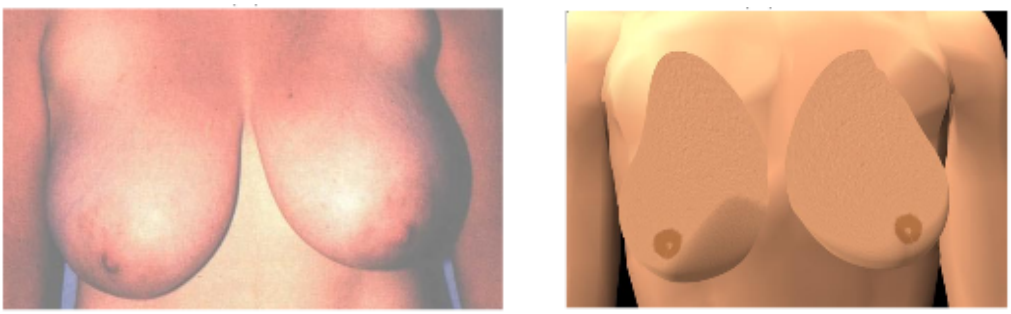

(a) (b)

Figure 2.13: The method proposed by Chen *et al.* [38]; (a) the reference image is used by physicians to develop (b) the parametric model.

Highlighting the necessity of a tool for both surgeons and patients to predict outcome result of the surgery, Balaniuk *et al.* [15] combined both virtual reality approaches and soft tissue modeling methods to simulate augmentation surgeries. To obtain 3D models, they used generic 3D torso, including body surface, fat tissue, lobes and breast muscles, and equipped it with parameters to fit

it into patient's body. The soft tissue simulation which deals with the deformation of the breast was conducted with Radial Element Method (REM), that is conceived for the real-time, physically based, dynamic simulation of deformable objects. Not only the internal forces imposed from the inserted implant, they considered gravity force in their equation, resulting in the estimation of breast models in patient's different poses. Figure 2.14 depicts the deformation of a simulated breast resulted after inserting an implant in the breast tissue.

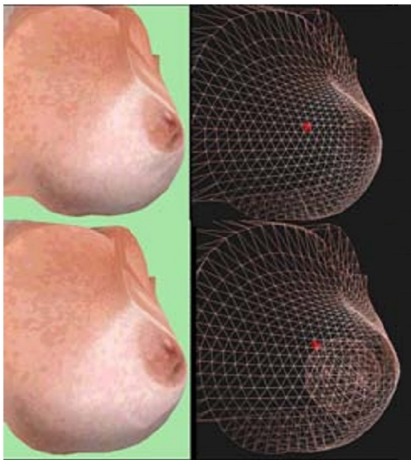

Figure 2.14: Blaniuk *et al.* [15] virtual reality approach

In 2007, a methodology was proposed by Jiang *et al.* [94,95] in order to plan brachytherapy for breast cancer treatment, that is a type of adjuvant therapy in which a radioactive seed is inserted inside the cancerous tissue. Aiming to eliminate miscalculations to insert the radioactive seed, they measured the volume of the breast, and the tumor as well, to identify an adequate dose of the radioisotope, and to ensure a uniform dose distribution avoiding hot/cold spots. Via their application called *Vision*, they processed CT images of patients lain in the supine position to a construct 3D view of thorax, while providing a simulated needle to embed the seed into the tissue. After the evaluation, they indicated that the proposed application achieved 99.73% of accuracy in estimating the measured volume against the true volume, outperforming the commercial competitors.

On the same year, Haung *et al.* [87] proposed an approach to plan breast reconstruction surgery. They calculated shape, area, volume and depth of both skin and muscle of patient's healthy breast to use them for reconstruction treatment. In the other words, the reconstruction is planned for the treated breast based on measurements over the healthy breast, within four steps. In the first step, they used Magnetic Resonance Imaging (MRI) to acquire the breast model of the patient. Using balloon segmentation, they obtained the healthy breast and generated its triangular mesh through the second step. Deformable models were used in the third step to flatten the mesh of the breast so that they could measure the volume and shape of the demanded flap for breast reconstruction. Figure 2.15(a) depicts the process of flattening. Finally, through the fourth step, they could calculate the approximate curve shape of the flap. In Figure 2.15(b), both real and virtual calculated flaps are depicted for visual comparison.

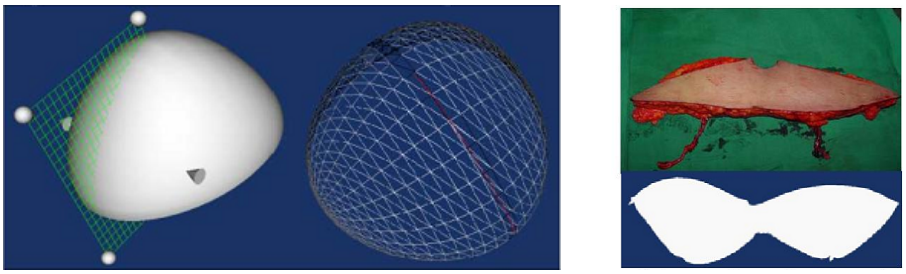

(a) (b)

Figure 2.15: The method proposed by Haung *et al.*; (a) the triangulated mesh resulted from processing MRI acquisition, and (b) the real flap used for breast reconstruction vs the virtual calculated one; images are adopted from [87]).

The authors claimed that the proposed approach has been evaluated by experienced plastic surgeons and furthermore it was accepted as a dependable directive design for real surgeries. It should be noted that there has not been any qualitative or quantitative evaluation to prove the effectiveness of the proposed planning scheme.

The research performed by Pérez del Palomar *et al.* [53] focused on prediction of breast shape in both supine and upright positions. Highlighting the direct connection between the breast shape and gravitational forces, they stated the breast shape simulation with respect to applying forces (such as gravity), would have significant importance in planning plastic surgeries. They first carried out an investigation to correlate the spatial features of patient's breast in both supine and upright position. Then, constructing patient-specific 3D models from CT images, they proposed to use Finite Element Modeling (FEM) to deform the breast shape in the aforementioned positions. Finally, as depicted in Figure 2.16, they evaluated the imposed deformation from gravity through the comparison with the landmarks which were annotated manually on 3D scanner images. Overall evaluations expressed that the FEM approximated the deformation of the breast reasonably well regarding gravity forces.

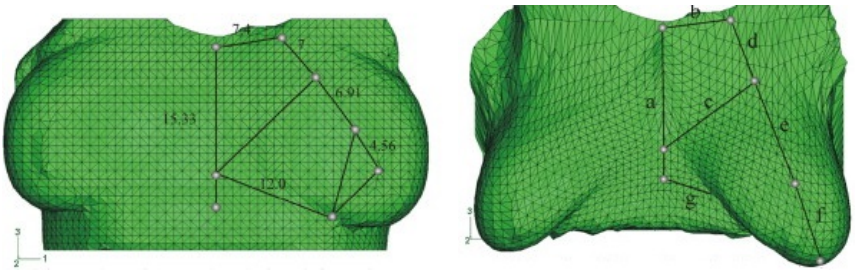

(a) (b)

Figure 2.16: Breast represented in the supine (a), and the result of imposing gravity to simulated up-right (b). The images are adopted from [53].

In further investigations, as in [112], they extended the work by predicting the imposed deformation during prosthesis insertion. To achieve this goal, they used finite elasticity theory to model patient's breast shape during augmentation mammoplasty. Comparing the results together, shown in Figure 2.17, were performed by two different procedures in which the first one comprised a quantitative verification using the procedure reported by Chung *et al.* [43], and the second one consisted of local comparisons by measuring the deviation of the Euclidean distance of manually annotated landmarks. In this regard, the first verification was done by reporting the most deviation around 11 *mm*, and the second one ended with the deviation less than 9 *mm*.

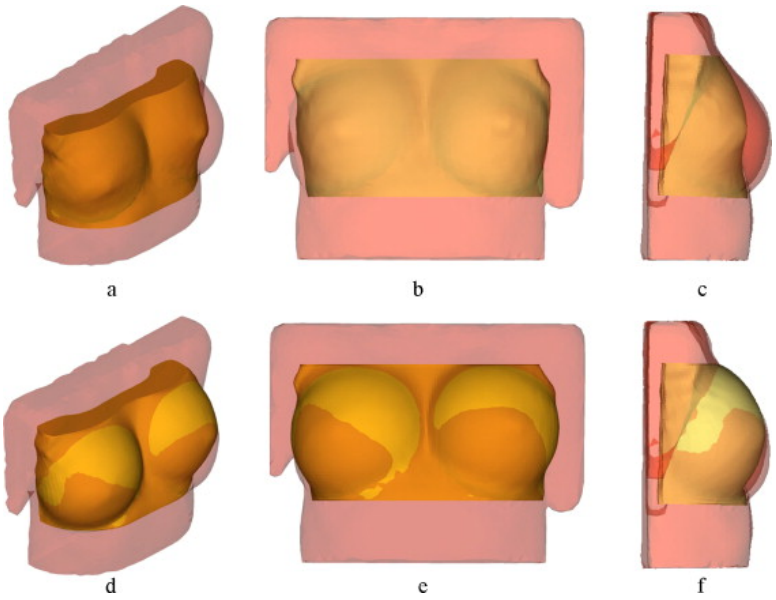

Figure 2.17: The deformed model (yellow) superimposed over the geometric model of the patient before the performing augmentation surgery (red): (a)–(c) before simulation; (d)–(f) after simulation (Figure is adopted from [112]).

Aligned with the requirement of a planning tool for breast augmentation surgery, Ciechomski and colleagues [51] proposed a web-based tool, called Crisalix, to predict the breast shape after augmentation surgeries. It was implemented to perform the planning via patient's specific 3D models, hence, to reconstruct the 3D model, it demanded 3 images (two lateral and a frontal, as in Figure 2.18(a)), together with two physical distance measurements of the patient's anatomy such as nipple-to-nipple and nipple-to-inframammary fold (shown in Figure 2.18(b)). Following the definition of the implant position and diameter, Tissue Elastic Modeling (resembling biomechanical modeling), is then exploited to apply the deformation on the breast. The authors evaluated their methodology in two different aspects: evaluating the 3D reconstruction and evaluating post-operative outcomes. Concerning the 3D model, and comparing to the 3D models resulted from the 3D scanner, they stated the mean reconstruction error between 2 and 4 *mm* with a maximum outlier error of 16 *mm*. On the other hand, the qualitative evaluations of the simulation outcome were indicated to be satisfactory based on the analyses from plastic surgeons (Figure 2.19).

Using the same basis of FEM, Garbey *et al.* [67] proposed an approach to predict breast 3D

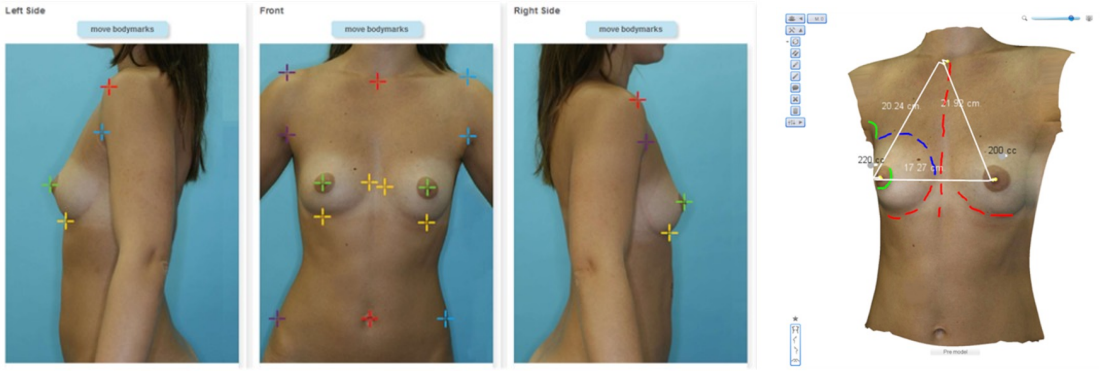

(a) (b)

Figure 2.18: The three provided images (a) used for 3D model reconstruction (b). The colorful annotated points in (a) assist the reconstruction algorithm to register the images in a 3D coordinate. The images are adopted from [51].

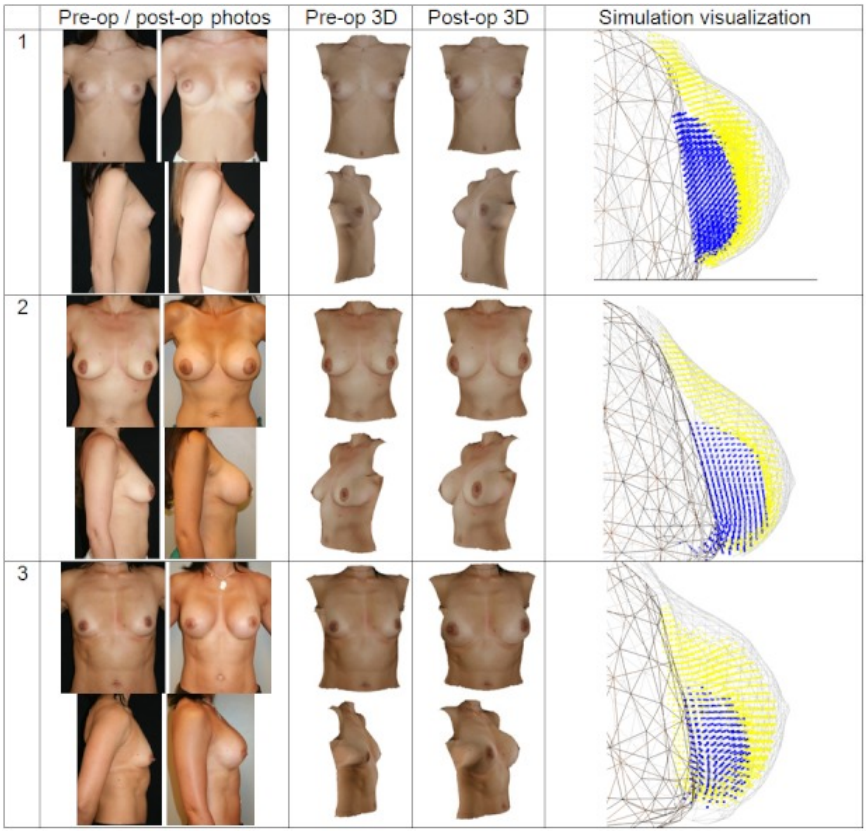

Figure 2.19: Three examples of planning for augmentation surgery with Crisalix tool, proposed by Ciechomski *et al.* [51]; The second column depicts the pre- and post-images while the third column comprises the 3D simulation of pre- and post-treatment models. The last column denoted the location of the implant. The image is adopted from [51].

shape (obtained from MRI data) after breast cancer treatment via coupling mechanical and biolog-

ical models with a multi-scale framework. While the implemented timescale for biomechanical FEM was set in the scale of seconds, the biological models were applied with the timescale of a week. The two biomechanical and biological frameworks were designed to deal with the patient pose simulation (supine to upright), and wound healing, respectively. It should be noted that the stop criterion of both frameworks was set until the incision location was completely filled by regenerated tissue. Figure 2.20 depicts the cross-section profile of the tetrahedral breast model (Figure 2.20(a)), and comparison between initial and deformed breast model resulted from the simulation (Figure 2.20(b)).

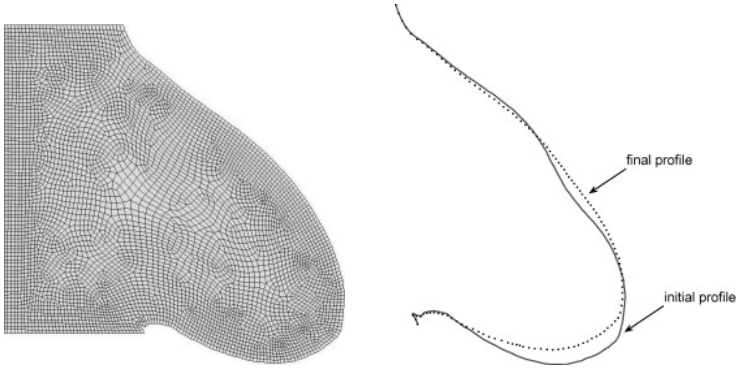

Figure 2.20: Cross section profile of tetrahedral Breast model (a), and the final breast shape compared with initial one resulted from multi-scale framework proposed by Garbey *et al.* (b). The images are adopted from [67].

Regardless of the required simulation time Although the methodology of FEM is known to perform the simulation in a time longer than medical expectation, Georgii *et al.* [72] suggested a FEM-based solution which benefited from highly efficient numerical solvers to predict breast shape for augmentation mammaplasty. Although the FEM itself is known to perform the simulation very slowly, Georgii *et al.* enhanced it through the redefinition of the required parameters. As an instance, to speed up the processing of the imposed displacement resulted from insertion of the implant, they applied pre-defined the internal body forces the implant would cause. Starting from a patient 3D model obtained by laser scanners, they first detected the breast contour via a semi-automatic methodology, and then segmented it. The procedure was followed by filling the hole imposed by the segmentation to resemble the rear wall behind the breast. In the next step, the rear wall was shifted toward the back, accounting the thickness of the skin and pectoral muscle. Finally, the breast and the rear wall were cut along with 4 boundary planes to determine the breast volume. The aforesaid procedures are depicted in Figure 2.22.

By employing proper parameters to control over implant placement and its rigid shape, they could overcome the challenge of controlling both the placement and the rigid shape of the implant. The key contribution in the implant insertion was based on the strategy in which the implant was blown up through the mesh, instead of cutting the tetrahedral connection. This strategy avoided

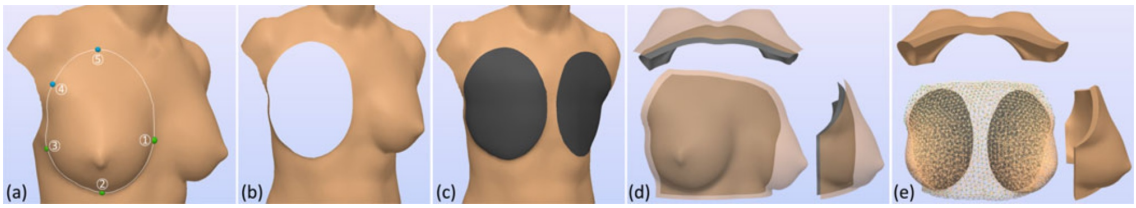

Figure 2.21: The pipeline to detect the breast frontal contour via a semi-automatic methodology (a), and segment the breast (b), filling the whole with the rear wall (c), shifting the tissue into the torso until it reaches the rear wall (d), and finally forming a closed volume by cutting the whole set along with 4 boundary planes. The images are adopted from [72].

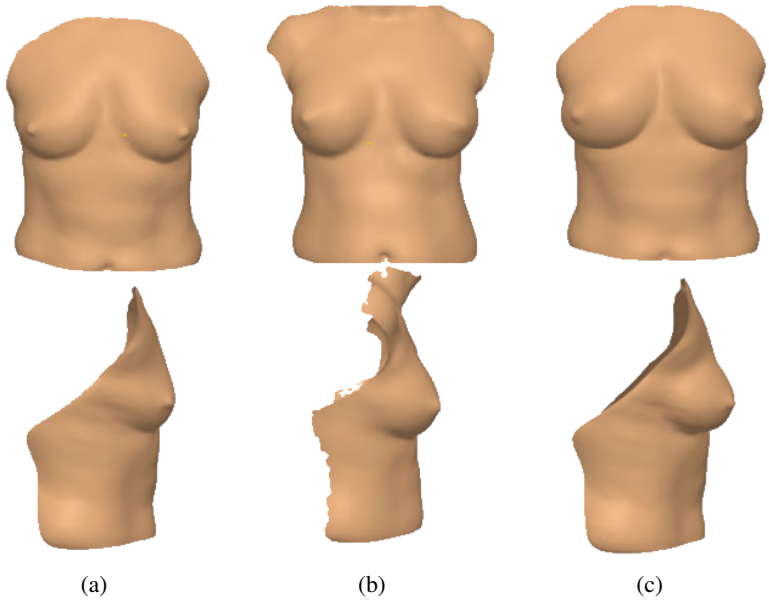

Figure 2.22: Visual comparison of the pre-operative 3D model (a), the post-operative after 6 weeks (b), and the outcome of the simulation (c) of the methodology proposed by Georgii *et al.*. The images are adopted from [72].

the recalculation of the mesh after inserting the implant, resulted in faster computation; however, the current strategy led to deformation of the implant, which was not studied. Finally, applying boundary condition to avoid displacement of the rear wall, and considering the weight of both breast tissue and the implant, they stressed the mesh with gravity and internal forces (from the implant) to obtain the predicted shape of the breast. Figure 2.22 illustrates the graphical outcome of the proposed solution. The validation of the methodology was performed via two aspects: evaluation of 3D model by measuring the distance of predefined landmark, and evaluation of the breast volume estimation after the surgery. Using two patients, totally 4 breasts were considered in the evaluations, and the reported comparisons between the prediction and the post-operative 3D model showed a close to reality predictions (Figure 2.23); although the authors stated that more evaluations were needed to validate the suggested solution before using it widely in clinics.

Aligned with the objective of the current research, Vavourakis *et al.* [197] conducted a similar

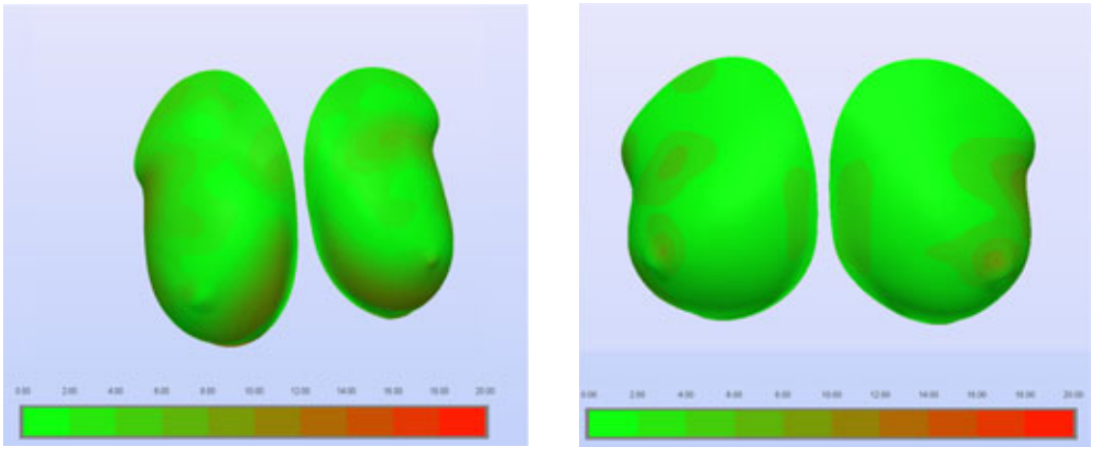

(a) (b)

Figure 2.23: The numerical distance between simulated and post-operative breast shapes for the two patients used for evaluation. The RMS is measured 3.3 *mm* and 2.1 *mm* for the shapes depicted in left and right, respectively. The images are adopted from [72].

research which resulted in a 3D surgical simulator to predict patient-specific breast shape, taking the wound healing process after BCS into account. In brief, the authors modeled the 3D post-surgical shape of the breast by coupling a physiological model of tissue recovery with a biomechanical model of pose estimation. The formerly predicted breast contraction caused by wound healing while the latter used a Mooney-Rivlin biomechanical model of the breast to simulate the breast shape in different patient poses as a function of the tissue mass density and the body force vector. The final shape of the breast was then predicted as an integration of both models. The three main stages of the surgery simulation comprised the construction of a patient-specific Finite Element (FE) model of the breast, the definition of the tumor, and the wound healing simulation itself, which used the multi-scale biomechanical model of wound healing described above. Considering that, each of these stages was carried out with the patient in different positions - MRI was acquired with the torso facing down (prone), surgery planning was made with the patient facing up (supine) and the simulation occurs in a stage where there was no stress force on the breast model, called unloading stage; hence pose transformations were also required in between the simulation, putting additional calculations which resulted in the overall performance that was longer for medical expectations. The evaluation was carried out with respect to the surface distance between the simulated models and acquired follow-up 3D scans (3 months after treatment) via a high accuracy 3dMD commercial imaging system. The measurements between the deformed breast after the simulation and the 3D models of follow-up scans were reported between 2.8 and 4.1 *mm*, indicating an excellent simulation accuracy. Figure 2.24 demonstrates the comparison between follow-up scan and the simulated breast shape in the same pose for one of the patients in the example list of the conducted research.

Besides the challenges in designing the methodologies, the demanded equipment also has

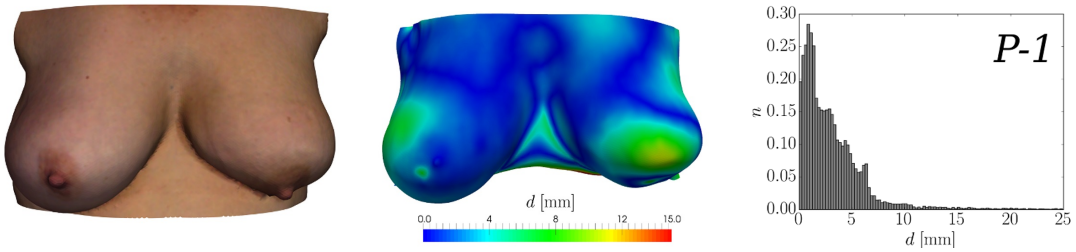

(a) (b) (c)

Figure 2.24: Comparison of (a) the breast models obtained from the 3D laser scanner, and (b) the biomechanical simulation pipeline proposed by Vavourakis *et al.* [197]. The histogram of distances in reported in (c). The images are adopted from [197].

impressed the development of breast surgery related methodologies; hence the trend has been shifted from using high-cost and complicated facilities to the low-cost and hands-free solution. The studies carried out by Henseler *et al.* [81], Oliveira *et al.* [143], and O'Connell *et al.* [140], highlights the potential of a low-cost sensor, such as Microsoft Kinect, in the reconstruction of patient's 3D model.

2.6 Summary

Nowadays, breast cancer treatment mostly involves removal of the tumor with a thin layer of healthy surrounding tissue, known as BCS; however, since breast is a symbol of the feminine, the imposed deformation impacts the QoL of patients significantly. Studies have shown that involving patients in the procedure of decision making for treatment, improve their outlook on the treated breast shape, resulting in more satisfaction about the treatment. Therefore, the importance of a tool facilitating the interaction between patients and physician before BCS is being highlighted in the medical community. This demand inspires from post-operative tools which were designed to evaluate the aesthetic shape of the breast after BCS. Widely using frontal images, aesthetic evaluation tools extract required features for conducting their task.

Considering availability of sensors and methodologies to obtain 3D models, the trend shifted from using 2D data to 3D models representing patient's breast. This motivated the creation of pre-operative tools to predict the shape of the breast before the primary treatment, instead of evaluating it after the surgery.

Concerning 3D models, a variety of sensors have been used to reconstruct patient's torso. Not only 3D laser scanners but also data from medical scanners such as MRI and CT can be processed to generate patient's breast model. Yet, there has not been an individual study aiming to correlate the 3D models obtained from different modalities. Considering the cost of equipment, the methodologies demanding low-cost sensors, and processing facilities are more in the center of attention. The term low-cost devices should not be confused with 3D outcomes which have not

been qualified for medical applications, while conducted investigations have shown the proficiency of those devices in generating 3D models for medical purposes.

In terms of requirement for expert personnel, most of the reviewed methodologies are difficult to be followed by the medical team, as there might be specific protocols for scanning, or difficult approaches to prepare the 3D models. As an instance, the FEM requires preparing tetrahedral meshes that demand basic knowledge of mechanics. Or another example can be pointed to methodologies which need manual annotation of breast contour. Since there is no common consensus about the breast contour, different solutions may be obtained while different operators prepare 3D initial models.

Apart from the 3D model generation, techniques to perform breast shape simulation consist of mainly two solutions, including fitting, and FEM, each demanding different computational requirement. In one side, application of fitting resulted in solutions which were efficient in computation, but inaccurate in modeling the breast, and hence the overall prediction. On the other side, FEM showed a powerful representation of simulation, although it demanded powerful computation facilities. There have been investigations targeting to reduce the demanded computation power of FEM by putting constraints on generating or regenerating 3D models; however, the constraints ought to be considered in which the total performance of the simulator is not influenced.

Last but not least, most of the conducted studies comprised approaches to suited for reconstruction mammaplasty surgeries, that is indeed out of the scope of the objectives of this study. Although there have been few types of research concerning the pre-operative planning tools for BCS, they are not appropriate for daily clinical use because of the computational, and expert personnel requirement.

Chapter 3

Reconstruction of Patient's 3D Model*

In recent years, the development of 3D scanning technologies has influenced a variety of areas of knowledge, including those related to biomedical research and the development of applications for healthcare. The importance of patient-specific 3D reconstructed models is highlighted when they are aimed to be utilized in the proposing BCS planning approaches to facilitate patient/surgeon communications. In presence of patient's own reconstructed models, medical consultations before surgery can be more beneficial for both patients and medical team.

Forasmuch as the 3D representations are to be used for the purposes of planning proper treatment, it is required to use devices and methods to reconstruct 3D models with adequate accuracy to fulfill the medical requirement. Besides, the affordability and reliability of the employed devices and the employed methodologies are signified with the consideration of the widespread application of the purposed planning approach. In this regard, to accomplish the requirement of the purposed planning approach.

In this chapter, we intend to study the reconstruction of 3D models of patients. In this way, first the acquisition methodologies will be studied as well as sensors. Such study is intended to find a low-cost solution suitable for medical application. The acquired data will be than registered within two stages; rigid, and non-rigid registration. Finally, and additional color enhancement stage is proposed to improve the visualization of the 3D reconstructed model.

3.1 Reviewing 3D Reconstruction Methodologies

Reconstruction of a 3D model is an interconnected process depending on both sensors and methodologies. Reconstructing an acceptable 3D model fulfilling the requirements of medical expectations (in terms of similarly to the scanned object, and the presence of fine details) demands a deep investigation of available methodologies, as well as sensors. In this way, further studies are carried out to investigate the details of reconstruction methodologies, covering the aspects of the acquisition of input data, registration of the data, and enhancement of the final 3D reconstruction.

*Some parts of this Chapter appeared in [48, 49, 132]

3.1.1 Methodologies

Regardless of employed technique, the 3D reconstruction methodologies can be categorized into 3 groups: Image-based Rendering (IBR), Image-based Modeling (IBM), and Range-based Modeling (RBM); however, the combination of image and range based modeling is also reported as an unofficial 4^{th} group to carry out the reconstruction of 3D models. In the following, each of the aforesaid methodologies is studied in details.

3.1.1.1 Image-based Rendering

IBR is a technique to reconstruct a continuous 3D scene instead of creating a complete 3D model. IBR methodologies mainly create an intermediate data structure by processing a set of images. The created data structure can be used later to render new images of the scene or object which had not been captured [129]. Using stereo matching techniques, IBR is mostly used to create continuous scenes via close cameras around the object; hence not only the position of cameras is important for a smooth reconstruction, but also large numbers of closely images are required to estimate the position of the reconstructed object [159].

Unfortunately, reconstructed scenes by IBR are deeply affected by discontinuities, making it an inappropriate methodology to reconstruct models with occlusions. Besides, performing an incomplete reconstruction makes the IBR based methods an inappropriate option in cases either the 3D model is needed to be spanned entirely, or volumetric information is demanded to be computed from the model [159, 172].

An example of reconstruction using IBR is illustrated in Figure 3.1. As it is shown, multiple views have been captured from different angles to reconstruct the 3D model. But, since cameras are presented only in specific locations, the whole model cannot represent a complete reconstruction encompassing the details of the camera backward.

Figure 3.1: Image-based Rendering of Buildings near each other; the location of cameras are depicted with white and green colors (image is adopted from [195]).

3.1.1.2 Image-based Modeling

IBM is widely used in 3D reconstruction based on perspective geometric information of an object (obtained by texture, contour, shading or specularity), or perspective camera model. IBM methodologies can be set up with RGB images, which make the whole method versatile, and low-cost enough to use inputs from RGB cameras. Besides, IBM's accuracy of reconstruction is also enhanced by using interactive methods [159]. However, to raise the degree of freedom in spanning the reconstructed model, a large number of images from different views are required, as well as the positions of each camera to identify the perspective geometric information.

3.1.1.3 Range-based Modeling

RBM is mostly performed via specific sensors emitting artificial lights and capture the projected patterns. The captured data from these sensors (known as active sensors, which will be covered in Section 3.2.2) are used to reconstruct the object directly from input data [159]. In addition, while the aforesaid sensors cannot directly capture color information, either color is ignored or additional facilities (such as a camera) are demanded to capture RGB information from the reconstructing scene. In this situation, an extra registration phase must be carried out to calibrate the main sensor used for 3D reconstruction with the sensor which is employed to get capture color [159].

Reflecting patterns to capture the depth information of an object makes RBM sensitive to intrusion sources caused by either reflective surfaces, or emitter sources working in similar wavelength as the reconstruction sensor does. Therefore, additional care ought to be taken while setting up the devices for scanning an object.

The distance of sensor to the reconstructing object defines the number of details the 3D model presents. As an instance, in the reconstruction of large objects which the reconstruction sensor is located far, the output is mostly imperfect and the edges are smoothed with poor quality and blurred angels. In such situations, employing techniques such as acquiring multiple scans and fusing them into a single model can improve the overall quality of the reconstruction.

Comparing to the aforementioned reconstruction methodologies, RBM can be considered as an expensive reconstruction method since it requires specific range cameras. In case of reconstructing the model with color, additional sensors must be provided, as well as additional computation step to align the captured color on the 3D model.

3.1.1.4 Combination of Image and Range based Modeling

Since none of the explained methodologies reconstruct perfect 3D models, a combination of them can lead to better outcomes. As it was discussed, RBM outperforms in small ranges but lacks in presenting color information. In contrast, IBM performs better to reconstruct basic colorful models. As it is expected, the combination will result in a methodology which can reconstruct colorful 3D models using IBM, and then refine them by employing RBM. However, since ranged-based reconstruction does not provide accurate models in sharp details, application of IBR can enhance the fine details [24].

3.2 Acquisition Methods

The sensors which are used to create 3D reconstructed models are mostly categorized into two groups of passive and active sensors, with respect to their performance in capturing object's depth information. While passive sensors rely on available wavelength in the environment to capture data (in RGB camera, the visible wavelength), active sensors use their own dedicated sources of light to emit patterns and use the reflection to capture objects' depth information.

3.2.1 Acquisition with Passive Sensors

Passive sensors usually use unprocessed images to estimate the geometric relations for generating 3D objects. Images from different views are compared with respect to geometric algorithms (such as triangulation) to find correspondences between them to be used for reconstruction [134].

Being able to process the depth information using simply available sensors (such as cameras), passive sensors are categorized amongst inexpensive devices. Instead, methodologies supporting passive sensors require more computation during 3D modeling. Performing reconstruction with more details is possible by either using high-quality cameras or capturing images from multiple views. Nevertheless, the quality of the 3D reconstructed models is tightly dependent on the quality of captured images.

3.2.1.1 Multi-view Reconstruction

Reconstruction with multi-view images is a common methodology using cameras as passive sensors. As shown in Figure 3.2, multiple cameras are located around the object to be reconstructed to capture multi-view scenes.

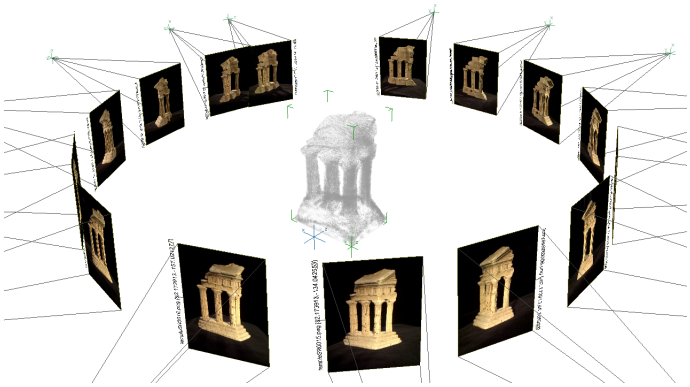

Figure 3.2: Multi-view reconstruction cameras; The image is adopted from [145].

Knowing the position of each camera, corresponding features among images are found, resulting in computation of the disparity map. Hence, the depth of the object can be obtained using triangulation geometry which leads to reconstruct the model [83]. Shown in Figure 3.3, using matched features in images C_1 and C_2 captured in two different views, disparity can be calculated via binocular disparity geometry, and the depth of the black spot can be estimated as well,

to reconstruct it. It is interesting to mention that the same process is performed in human vision system [153].

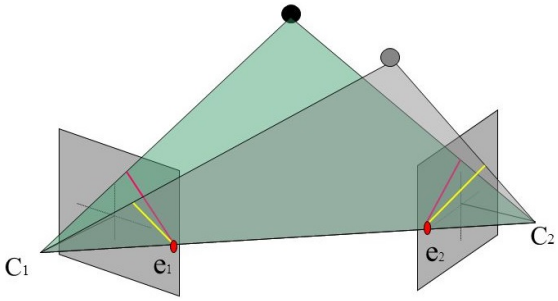

Figure 3.3: Binocular disparity geometry

3.2.1.2 Reconstruction Using Shadows

In this methodology, 3D model of an object is reconstructed using the shadow while the light source is moving [22]. Though being low-cost, the method cannot guarantee to provide detailed 3D models [166]. Figure 3.4 illustrates the deformed shadow on the model and the result of the performed reconstruction from two different views.

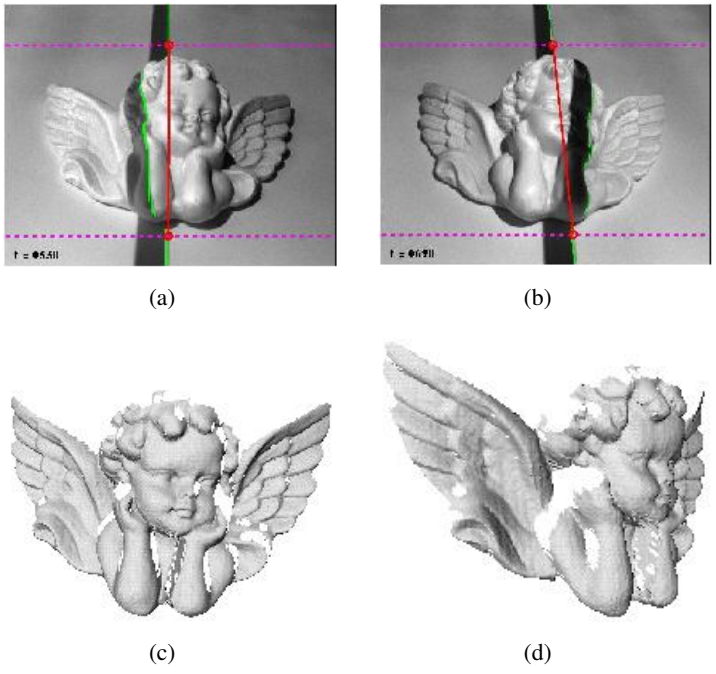

(a) (b)

(c) (d)

Figure 3.4: 3D reconstruction using shadow; (a) and (b) are moving shadows, (c) and (d) are 3D reconstructed model from different views. The images are adopted from [22].

3.2.1.3 Reconstruction Using Focusing

Not only the images with sharp edges but also out of focus photos can assist to find the depth of multiple objects. This methodology demands to know camera focal length of the lens capturing the scene. The amount of blurring is proportional to the distance of the object from the camera; hence by focusing step by step, different depth fields are sharpened, leading to know the depth of the object located in that region. While the object itself occludes the scene, employing this technique will result in an incomplete 3D model. Also, the number of details presented in the reconstructed model depends on the amount of lens movement in each step. Finally, it should be noted that objects which are not aligned perpendicularly to the optical axis or having depth dimension larger than the depth of view, will appear in different ranges in each step, making the analysis more complicated [136].

3.2.2 Acquisition with Active Sensors

Active sensors in 3D reconstruction are those using specific patterns emitted from their own source of light. Therefore, these sensors are mostly a combination of an emitter, and a receiver calibrated together. The employed technology accompanied with the reconstruction methodology in some of the active sensors are briefly studied in the through this section.

3.2.2.1 Time of Flight

Time of Flight (ToF) is a group of technologies which can be used to find the depth of different objects by employing a variety of spectra, from ultrasound to light. In the simplest implementation, sensor's emitter sends pulses toward an object. Then the receiver collects the pulses reflected by the surface of an object located in front of the sensor. The time delays between the reflected pulses determine the object's depth, which is essential for 3D reconstruction. Figure 3.5 depicts both emitted and reflected pulses. The delay which is named t_D is used to calculate the depth of the object.

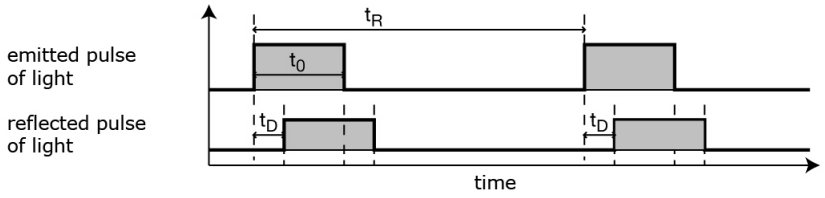

Figure 3.5: ToF emitted and reflected pulses; The image is adopted from[1].

ToF sensors are sensitive to environmental noise especially when working spectra are close to visible light. Besides, sensors which are working near to each other may cause interference, although it can be alleviated by multiplexing them. Additionally, ToF sensors can be influenced by

[1] http://upload.wikimedia.org/wikipedia/commons/0/05/TOF-camera-principle.jpg with modification

surfaces with multiple reflections, or the objects with complicated geometrical surfaces, reporting overestimated or underestimated depth due to different reflected pulses [208].

3.2.2.2 Structured Light

Structured light sensors are one of the most accurate devices among active sensors. In this sensors, a specific pattern is projected to an object, and then a receiver captures the reflections. Similar to the concept of binocular disparity measurement, the depth of the scanned object is measured followed by reconstructing it. Shown in Figure 3.6, the process is depicted for more clarification [39].

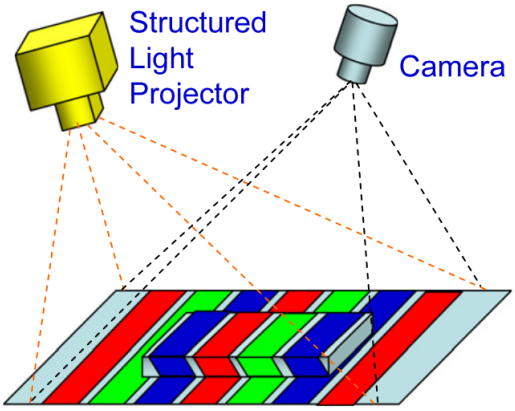

Figure 3.6: Active sensor patterns, from [70]

To have colorful reconstruction, some devices use extra RGB camera placed beside depth camera to capture color information. Knowing exact position of depth and RGB camera (the calibration data), the reconstructed model can be aligned with color image [65]. Figure 3.7 depicts a sensor based on structured pattern to reconstruct a model.

3.2.3 Summery of 3D Reconstruction Methods

Although passive sensors and methodologies are more available with less expense (comparing to active sensors), their performance is abandoned by technical difficulties. First, it is required to find strong correspondences to align the captured views to each other, which is known as an ill-posed problem with respect to the captured angle, the distance to object, and the number of presented details in the captured image. The situation gets worst in uncontrolled light conditions since employed reconstruction methodology has to be robust to the changes in the illumination intensity. And second, using multiple sensors, or defining a specific protocol to use a single sensor increases the complexity of model reconstruction, as well as additional calibration stage between the cameras, is required [39].

On the other hand, in contrast with their cost, active sensors capture data with lower resolution compared with passive sensors. Besides, though being robust to acquisition conditions (such as light), they present poor performance comparing to passive sensors, in the reconstruction of

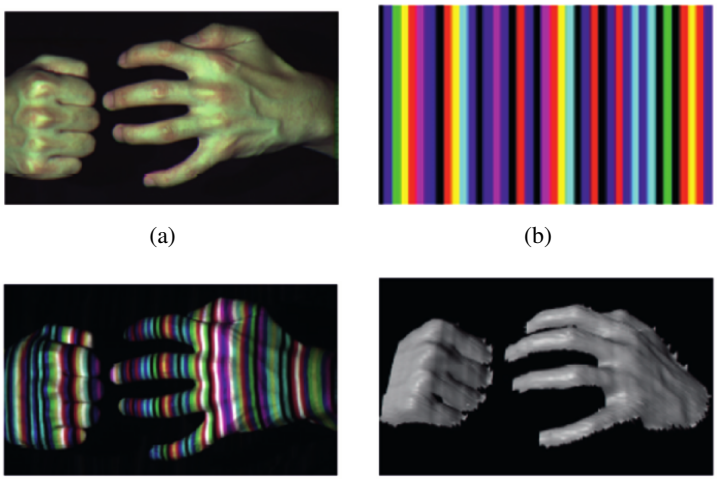

(a) (b)

(c) (d)

Figure 3.7: 3D reconstruction of a fist (a), the structured pattern (b), the emitted pattern on the fist (c), and the 3D reconstructed model. The images are adopted from [39].

textured objects. Moreover, they reconstruct colorless models or represent pseudo colors, hence additional sensors must be considered when colorful reconstruction is intended.

The comparisons reported in Table 3.1 expresses briefly the difference of reviewed types of sensors in terms of resolution and robustness to texture.

Table 3.1: Comparing active and passive sensors with respect to resolution and robustness to texture

Sensors	**Resolution**	**Textured Objects**	**Non-textured Objects**
Passive	High	Robust	Not-robust
Active	low	Not-robust	Robust

Reportedly, in terms of fine details of the reconstructed model, active sensors typically are incapable of detecting the detailed depth of textured objects(for instance, the fur of a fabric), leading to reconstruction which is not robust to the aforesaid details. In the way around, they can capture robust input data to be used in the reconstruction of non-textured objects, since they represent fewer depth details. Contrarily, passive sensors show different behavior, since they can detect robust correspondences in textured objects to use them in 3D reconstruction; however, they mainly carry out poor reconstruction, comparing to the models created by active sensors. Finally, the choice of sensor and technology is delimited by application, cost, the number of details required to be presented in the reconstructed 3D model.

3.2.4 Microsoft Kinect: Introduced for Gaming, Employed for Reconstruction

In recent years, emerging of new and low-cost devices have drawn the attention of researchers to use active sensors for 3D reconstructions. Not so far in 2010, Microsoft Kinect showed itself as a capable, low-cost, and mid-resolution active sensor to be used in data acquisition for 3D reconstruction. Using structured light pattern and machine learning techniques to output RGB-D data [100], Kinect has been proved to be accurate enough to be used as a medical acquisition device in particular contexts [140, 152, 205]; however, it is not compromised free. In this section, first, the device structure and performance will be reviewed. Considering the medical application of human body reconstruction, the choice of Microsoft Kinect results in multiple challenges which will be explained in further.

3.2.4.1 Microsoft Kinect

Developed by PrimeSense and introduced by Microsoft, Kinect had an evolutionary entrance in the world of games in 2010. Shown in Figure 3.8, it was originally designed to remove the demand of wired controllers, but soon it was adopted in different research projects since it is a low-cost sensor with available drivers for different platforms to provide a stable data communication.

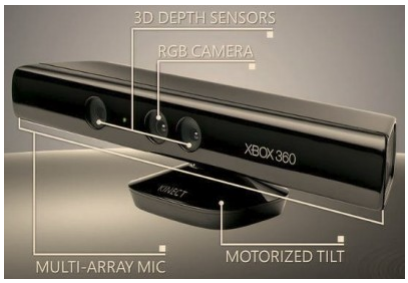

Figure 3.8: Microsoft Kinect (image is adopted from[1])

The original introduced Kinect produces depth maps with 640×480 pixels by employing an active sensor in which near to infra-red (IR) speckle patterns are projected to the object and reflections are captured by a standard CMOS sensor. Each block of speckle-pattern consists of 211 horizontal and 165 vertical spots distinguished with a bright spot in the middle. Blocks are repeated 3 times vertically and horizontally to cover the RoI, totally projecting 633×495 spots. With such pattern, the sensor is able to perform in the range of 0.8 m to 3.5 m with an accuracy of 3 mm in both height and width, and the accuracy of 1 cm for depth in the range of 2 m. Blocks and spots emitted by Kinect are depicted in Figure 3.9.

Additionally, Kinect is equipped with an RGB sensor resolving images in 1280×1024 pixels at most. With multi-array embedded microphones, Kinect is also able to process environmental sounds.

[1] https://www.generationrobots.com/img/cms/Kinect-sensor.png
[1] http://www.futurepicture.org/Kinect_Hacking/Powershot_IR_Mod/Powershot_IR_Mod_IMG_0017.JPG

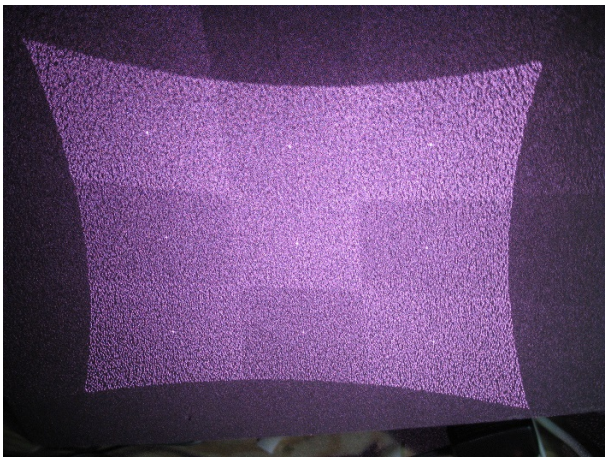

Figure 3.9: Kinect emitting structured light (image is adopted from[1])

In 2012, Microsoft announced a modified version of Kinect to be utilized directly via PC platforms, called Windows Kinect. Although there were not any functional differences between two versions, Microsoft improved the *near detection* mode, enabling the depth sensor to see objects as close as 40 *cm*. Thus, it communicates more information about depth values outside of the range. There was also improvements for the 10-joint skeletal system to track the head, and a full frame Application Programming Interface (API). Besides, new methodologies such as *KinectFusion* [90] were featured in the Software Development Kit (SDK) presented with the device.

For depth maps, the sensor produces a 2D array with a representation of 11 bits per entry consisting of depth information of each projected point to the frontal region. Unlike RGB camera, the output of depth sensor cannot be used directly, because information from depth-map does not correspond to real-world distances. Thus, it is required to convert pseudo-distances to the real world through pre-processing. Unfortunately, depth-maps resulted from Kinect are not aligned with the RGB image, as far as resolutions are not the same; hence a transformation stage is necessary if colorful reconstruction is intended. Since the specific transformation relation has not been revealed by the developer, experimental relations have been suggested to perform the transformation. Reviewing literature, some of them are listed as follows:

$$d_m = \left(\frac{d_r}{2048}\right)^3 \times 9216,^{[2]} \tag{3.1}$$

in which d_r denotes the row data from Kinect and d_m represents the transformed (or real) distance.

$$d_m = K_a + \tan\left(\frac{d_r}{K_2} + K_1\right),^{[3]} \tag{3.2}$$

[2] http://groups.google.com/group/openkinect/browse_thread/thread/31351846fd33c78/e98a94ac605b9f21?lnk=gst&q=stephane&pli=1

[3] http://groups.google.com/group/openkinect/browse_thread/thread/31351846fd33c78/e98a94ac605b9f21?lnk=gst&q=stephane&pli=1

where $K_1 = 1.1863$, $K_2 = 2842.5$ and $K_a = 0.1236$.

$$d_m = \frac{1}{d_r \times K_1 + K_2}, \quad (3.3)$$

[1]

by consideration of $K_1 = -0.0030711016$, and $K_2 = 3.3309495161$.

As long as the resolution of the depth map is low (640×480) and contains high levels of noise, including missing points, outliers, and Gaussian noise, it is essential to improve depth map quality either by reducing noise or increasing resolution. Applying a bilateral filter [192] on the Kinect's depth-map, Newcombe *et al.* [137] tried to obtain a discontinuity preserved depth-map with reduced noise. Increasing of the Kinect's resolution was studied by Schuon *et al.* [168] and developed by Cui *et al.* [50] to obtain super-resolution depth maps.

3.2.4.2 Challenges of Using Microsoft Kinect in 3D Reconstruction of Body Parts

Over the past few years, different research groups worked on the reconstruction of body parts using the Microsoft Kinect and were able to identify and overcome some of the existing challenges. Such previously identified challenges are related to calibration parameters, noise, acquisition, and reconstruction software.

Solutions that modify predefined silhouettes of the body while scanning, similar to the one suggested in [204], have been proposed. Alternatively, the usage of multiple Kinect devices [193] has been tested. But interference between devices has been observed [126], as well as an increase in the computational cost and a decrease in the portability. Nonetheless, it is possible to define a set of constraints, similarly to Tong *et al.* [193] in their three-Kinect scanning system.

Whilst Kinect's manufacturing calibration data stored in the device's memory, alternative methods have been proposed by Zhang *et al.* [206] and Herreca *et al.* [27] to configure the calibration parameters experimentally. Han *et al.* [76] recognized a valuable contribution of such works on the Kinect calibration since the precision of the pointcloud generation increased. Nonetheless, newer versions of the SDK already addressed such calibration related issues. The usage of factory supplied parameters avoids additional calibration procedures, thus improving usability and reducing the need for further intervention. However, due to possible structural changes in the device body, either by manufacturing tolerances and/or small structural changes that affect the Kinect components over time, there is still the necessity of re-calibration procedures.

Besides the accuracy of the calibration parameters, different sources of noise affect the Kinect data. Mallick *et al.* [126] recently presented a review paper systematizing Kinect noise-related work. In that regard, they highlighted the fact that Kinect's depth sensor relies on the comparison of a known pattern against each new frame retrieved from its IR camera. Since it is an active sensor, not only multiple devices can interfere with the measurements of each other, but also other sources of IR light, like halogen operating room lights [174] or even direct sunlight, can degrade

[1] http://nicolas.burrus.name/index.php/research/kinectcalibration

the reconstructed depth maps. The noise resulted from the IR interference of multiple Kinects are shown in Figure 3.10.

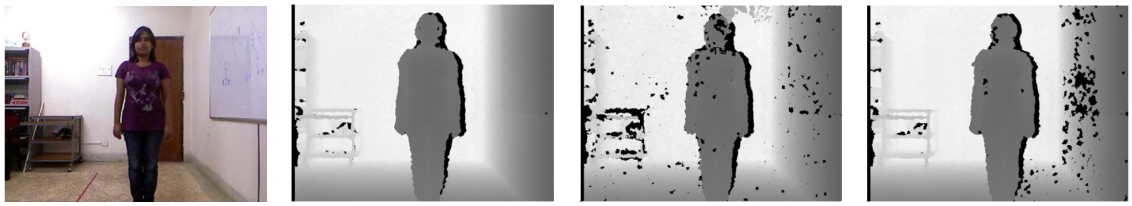

(a) (b) (c) (d)

Figure 3.10: Experiment using multiple Kinects capturing views in the same operational region conducted by Mallick *et al.* [126]; (a) room and human, (b) single Kinect, (c) Two parallel Kinects (180°), (d) Perpendicular (90°) Kinects

The same experiment was performed to investigate the effects of scanning reflective and transparent surfaces. They concluded that using of the aforementioned objects must be avoided since they greatly affect the projected dot pattern and are prone to introduce noise in the data, as illustrated in Figure 3.11 and Figure 3.12 for reflective and transparent surfaces, respectively [126].

(a) (b)

Figure 3.11: An experiment conducted by Mallick *et al.* [126] using Kinect to capture views with reflective objects; (a) RGB image with two mirrors as reflective objects, (b) Kinect fails to report the mirror itself; however the rear side of the person is estimated with a lot of holes.

Concerning the usage of a single Kinect, the gold standard reconstruction methodology is KinectFusion [90, 137], developed by the homonymous Microsoft research group. It merges iteratively the incoming depth-maps into a single reconstructed model. Note that the reconstruction is only accurate for rigid objects, presenting a high computational cost. The sensor trajectory and the result of the reconstruction are demonstrated in Figure 3.13.

The human body itself is a non-rigid model since patient breathes or (may) move unexpectedly during the acquisition, imposing slight deformation between the scanned views. To overcome the non-rigidity of views, the solution proposed by Li *et al.* in [116] was focused on utilizing non-rigid registration methods. They proposed a reconstruction pipeline in which it benefited from a non-rigid algorithm for alignment of captured views to result in a smooth output. Though presenting accurate reconstruction results, but their solution requires manual intervention of an expert to select proper views; therefore, it can be referred as a limitation within the medical context. The

(a) (b)

Figure 3.12: An experiment conducted by Mallick *et al.* [126] using Kinect to capture views with transparent objects; (a) RGB image with four transparent objects, (b) Kinect fails to report the transparent parts; however the if they are filled with opaque contents, or they have labels, the depth estimations are reported.

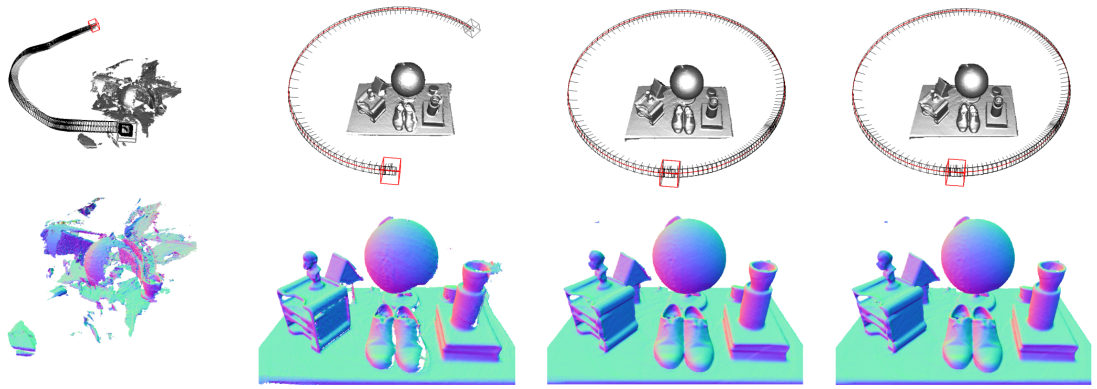

(a) (b) (c) (d)

Figure 3.13: Experiment of KinectFusion to reconstruct an object [137]; (a) frame-to-frame reconstruction, (b) reconstruction with more than $\frac{2}{3}$ of a complete loop, (c) reconstruction after a complete loop, (d) reconstruction after 4 complete loops. The images are adopted from [137].

authors claimed to perform the registration with eight selected views; nonetheless in medical applications, neither patients nor clinic operators are expert enough to select appropriate views. The used pipeline is depicted in Figure 3.14.

3.2.4.3 Summary of the Challenges for 3D Reconstruction of Body Parts Using Kinect

The previously discussed challenges related to the application of reconstruction methods within the biomedical context are listed in Table 3.2. In one side, KinectFusion which proposed in [90, 137] was shown to perform an accumulative 3D reconstruction, but it demands heavy computation. Also, assuming the only rigid motion between views, in the presence of non-rigid motion it either fails to conduct the registration or the deformed views are accumulated as outliers to the 3D

(a) (b) (c) (d) (e) (f)

Figure 3.14: The reconstruction pipeline proposed by Li *et al.* in [116]; (a) capturing near to 150 frames and selecting 8 manually, (b) fusing the views, (c) registering them rigidly in a cumulative fashion, (d) registering them non-rigidly registration to align the view completely, (e) aligning surfaces into a single watertight surface, (f) fusing the captured texture to the reconstruction output

reconstructed models. In other words, KinectFusion suits for rigid reconstruction scenarios. On the other side, the proposed methodology by Li *et al.* [116] benefits from compensating non-rigid motions between the views, however, it required manual intervention to select only 8 views out of 150 captured data. Such intervention demands specific expertise to select suitable views, or correct the selected ones, therefore, this methodology is not an appropriate option to overcome the challenges of patient torso reconstruction. The reconstruction methodologies by Herrera *et al.* [27] and Tong *et al.* [193] deal with similar drawbacks, either in acquisition set-up or intervention of experts.

Table 3.2: Comparing methods and identified challenges within medical context

Methods	Heavy computation cost	Reconstruct only rigid objects	Restrictive acquisition set-up	Additional intervention necessary	Description
Tong *et al.*, [193]			×		Requires 3 Kinects to be installed in predetermined positions;
Izadi *et al.* [90]	×	×			Need GPU processing due to heavy computation; remove moving objects;
Li *et al.* [116]				×	Requires expert personnel to select appropriate views
Herrera *et al.* [27]				×	Depth map quality improved trough calibration procedure

3.2.5 Methodologies for Rigid Registration of Multiple Views Acquired by Kinect

A brief review of the available literature reveals that 3D representation of an object can be obtained by either of the strategies listed as follows:

- Merging the views directly, without any pre-processing,
- Detecting robust keypoints which provide a representative description of the pointclouds and aligning the views bases on the transformation that aligns the keypoints,

- Aligning the views first, and then performing the registration,

In reconstruction scenarios when Kinect is employed, aligning the captured views is mandatory since each view represents specific coordinate which was defined regardless of the sensor's position. Thus, first, the captured data should be transformed in a single coordinate through alignment stage. The alignment stage is also known as coarse registration and aims at computing an initial estimation of the rigid motion between the views. It is then followed by a fine registration stage, which looks for the most accurate solution possible to aligns the views. The pointcloud registration process, together with different reconstruction approaches have been comprehensively studied by Salvi *et al.* in [165].

Concerning keypoint extraction methodologies needed for coarse registration stage, Spin images [96] and curvedness [97] (illustrated in Figure 3.15 and Figure 3.16, respectively) are two commonly used descriptors, correspondingly related with distances between points and planes, and with bending energy of surfaces.

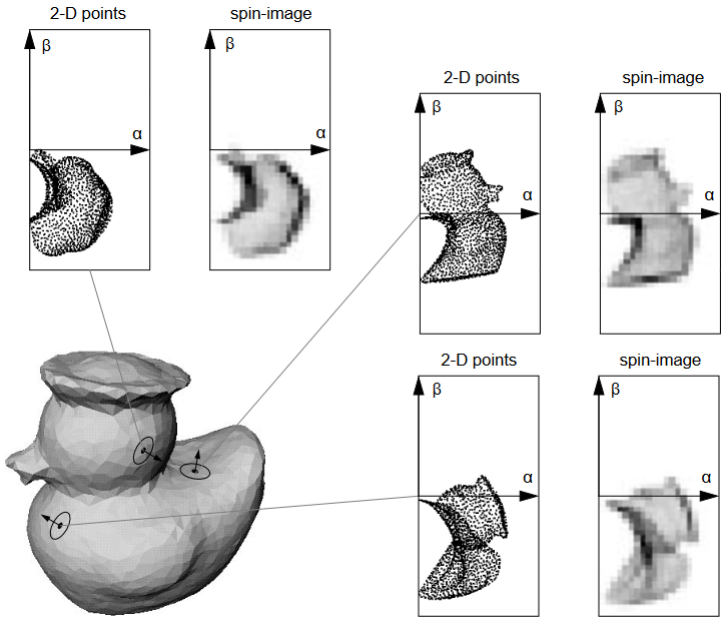

Figure 3.15: The spin images for three oriented points on the surface of a toy example model. The 3D position of vertices in the mesh is mapped into 2D using the spin map for each oriented point basis. By accumulating 2D points in discrete bins, spin-images are generated [96].

Spin images, although low discriminative and time consuming, provide invariant local shape descriptors of the pointcloud to guide the coarse alignment. Both descriptors assume that the points are uniformly distributed across the surface (or pointcloud), which cannot be assured in case of utilizing Kinect.

The Principal Components Analysis (PCA) uses the 3 main spatial orientations of a pointcloud to align it to another but requires similar and overlapping input views. But there are other methods, like the detection of corresponding co-planar sets of points [2] and matching between histograms [164], as well as others based on the calculation of curvature indices. It can be concluded

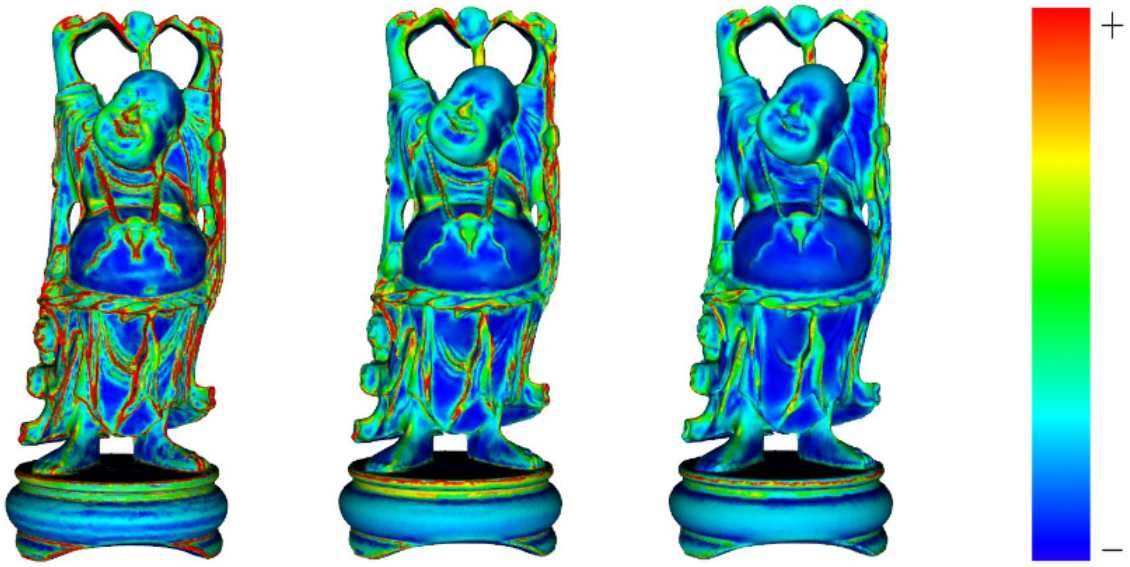

Figure 3.16: The curvedness of the Buddha model estimated at different scale levels r_k; (a) $r_k = 2$,(a) $r_k = 5$,(a) $r_k = 7$. Note that increasing the scale is similar to applying a smoothing filter to the 3D surface before calculating the surface curvature [97].

that these methodologies are often incapable of proposing a correct coarse alignment between the pointclouds. This is especially true when dealing with highly misaligned views, making these methods unsuitable to be used in a 3D reconstruction of bare body parts, also because of their high computational cost and infeasible response time.

Although PCA [42,165] is expected to perform well for coarse registration, since it is sensitive to the presence of noise and outliers, the extracted keypoints are not robust enough especially when views are captured from a noise sensitive sensor such as Kinect.

Other solutions include the use of silhouette information [204], multiple Kinect solutions [193] and articulated part-based cylindrical body models [202]. These solutions, though being versatile, do not fulfill the requirements to be used in for medical purposes [48]. A different multi-view registration methodology, for the medical environment, specifically designed to be embedded in a low-cost system is required.

The discussed rigid registration methodologies deal only with rotation and translation of the views to align them, thus, the residual distance between the views maintains in the same range albeit the number of iteration increases. More diminution of the residual distance is accessible through applying the deformation to one of them in order to fit align it on the overlapped region; however, the applied deformation must keep the geometrical attributes of the deforming view. In the scope of image processing, it is called non-rigid registration. A brief literature review In this regard will be carried out to investigate possible solutions to perform non-rigid registration.

3.2.6 Methodologies for Non-rigid Registration of Multiple Views

A challenging step to perform non-rigid registration is determining correspondences. Contrarily to rigid registration where the correspondences would maintain changeless among multiple sections, they may deform or change shape completely through non-rigid motions. To create strong correspondences in legacy methodologies, as in [196], multiple markers which were clamped on the surface of the scanned object, were adopted to determine references points used in registration. Such simple solution is not appropriate since it increases the acquisition complexity (to identify a suitable location for markers). In addition, it decreases the portability of methodology to use specific correspondences.

The application of static markers was to ensure the presence of correspondences. Recently, studies have shown that isometric and rotation invariant features can lead to finding points which can be used instead of physical markers. As an instance, Sun *et al.* [178] proposed the *Heat Kernel Signature (HKS)* as a feature which captures local information about the neighborhood of a point by reflecting the distribution of heat from that point onto the rest of the shape over time. Since heat diffuses to larger neighborhoods, the recording time scale provides a specific signature for each point to describe the surrounding shape. Consideration of short time scale (for heat diffusion) will lead to reflect the details in small a neighborhood while the behavior of heat diffusion over longer time reveals the summaries of the shape in a larger region. Since the heat diffusion is a function of geodesic distance over the surface of the shape, it is invariant to rotation and isometric deformation.

Studying HKS at multiple time intervals provides specific signatures for each point which can be used to identify the corresponding points. Figure 3.17 demonstrate the HKS signatures for the different timescale of different regions of a deformable model. In Figure 3.17(b), and Figure 3.17(c), the matched regions are compared due to the different time scales of capturing HKS.

Although the discussed signature shows a robust behavior with respect to disturbance, rotation, scale, and isometric deformation, it demands complex computations to calculate the signature of each point. This denotes that HKS is better for validating previously found correspondences, rather than searching in the solution space (all the correspondences) to find a correct match.

HKS is not the only feature used for non-rigid registration. As in [37], Chang *et al.* adopted spin images to identify the required correspondences. In the aforesaid research, first, they detected features of articulated objects, where the difference between the source and the get pointclouds consists of a few rigid motions. Then for each cluster of rigid motion, they computed the spin images, a feature descriptor to find the corresponding points between the two registering sets, and, a rigid transformation was generated for each correspondence. Finally, using a cost function for each cluster, the transformation that results in less distance between the source and target sets in each cluster was selected. Figure 3.18 depicts the discussed approach.

The proposed methodology of Chang *et al.* performs well in situations the total motions of the model can be clustered into a few rigid movements. In this situations, each rigidly registered

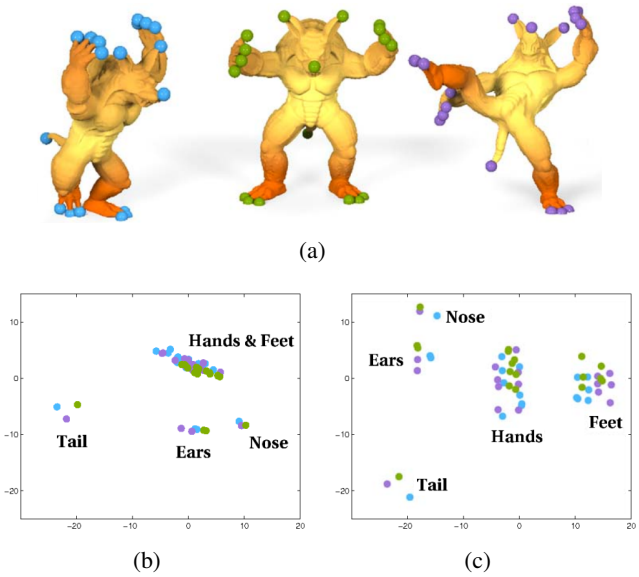

(a) (b) (c)

Figure 3.17: Visualization of HKS features with respect to different time scales; (a) Feature points on three poses of the Armadillo model; Classical multi-dimensional scaling embedding of the feature points based on their HKS at (b) $t = [0.1, 4]$, and (c) $t = [0.1, 80]$. The color of each point corresponds to the pose from which it is taken. Images and 3D models are adopted from [178].

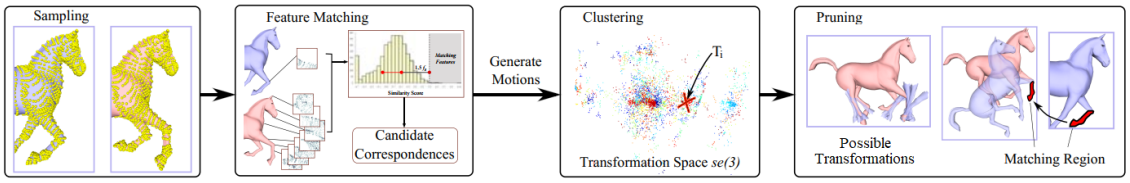

Figure 3.18: Example of a non-rigid registration from Chang *et al.* [37]. After computing coordinate frames and feature descriptors, the pointclouds are sampled and candidate correspondences are found by comparing spin images between the shapes. Then, a rigid transformation for each correspondence is generated and clustered the resulting set of candidate transformations to obtain the final set of transformations. Finally, unnecessary transformations are pruned based on matching regions. The image is adopted from [37].

clusters are connected through joints (the boundaries between clusters). As Conceivably, the joints where the non-rigid motions are highlighted, might not be registered well. One may suggest generating smaller clusters of rigid motions to ensure smooth representation of the registered model; however, the more clusters exist, the more time to compute the transformations.

While the found correspondences might not provide a correct clue, some researchers have proposed to prune unreliable ones. As an example, Huang *et al.* [88] proposed a two-step methodology to certify the correctness of the found corresponding points:

1. The isometric consistency (the difference of the geodesic distance between the correspondences);

2. The similarity of two points (the difference of the principal curvature in the location of the correspondences);

They proposed to create an affinity matrix of the correspondences, followed by computing its principal eigenvector. The computed vector denotes the confidence value of each point to belong to coherent cluster on the target pointcloud.

The certified correspondences were then used to formulate the non-rigid registration to an optimization problem. With a strategy similar to [177], they minimized the sum of a correspondence energy and a local rigidity preserving energy between the corresponding clusters of the source and the target pointclouds. Figure 3.19 illustrates the registration of the source pointcloud on the target one.

(a) (b) (c) (d)

Figure 3.19: An example of a non-rigid registered data from Huang *et al.* [88]; (a) source + target, (b)sampled point on source, (c) certified correspondences, (d) registration result

Another set of solutions were proposed to use a template to simplify the problem of part-to-part solution into part-to-whole. As in [180, 200, 201], a template of the human face was used to identify the missing regions and fill them using available data from other scans in the same sequence. This solution is a well-known approach to the human face and body [182]; however one may criticize the availability of template for medical limb reconstruction. In this way, the authors proposed to compute the required an a priori template (called *urshape*) on the fly during the optimization. Defining the shape and the motion of the acquired object, The urshapes are constructed from initial input frames. Then, by computing smooth deformation fields for each sequence, and they are merged in the sequential order of the input frames, resulting in an updated urshape. This cycle iterates until a global urshape and its deformation is obtained. An example of computing urshape from a sequence of input data is depicted in Figure 3.20.

The obtained on the fly template is then fed to reconstruction pipeline to be used in as the target model through the non-rigid registration. Although construction of a template can assist the procedure of registration, in the situation when the captured input data present large amount of deformation, neither a template nor a complete fitting is achievable. Evaluation (which have been done only with respect to total computation time) reports that the methodology is much slower than competitive, including Iterative Closest Points (ICP) algorithm [20], and hence it requires powerful machines to reconstruct 3D model in medically expected times.

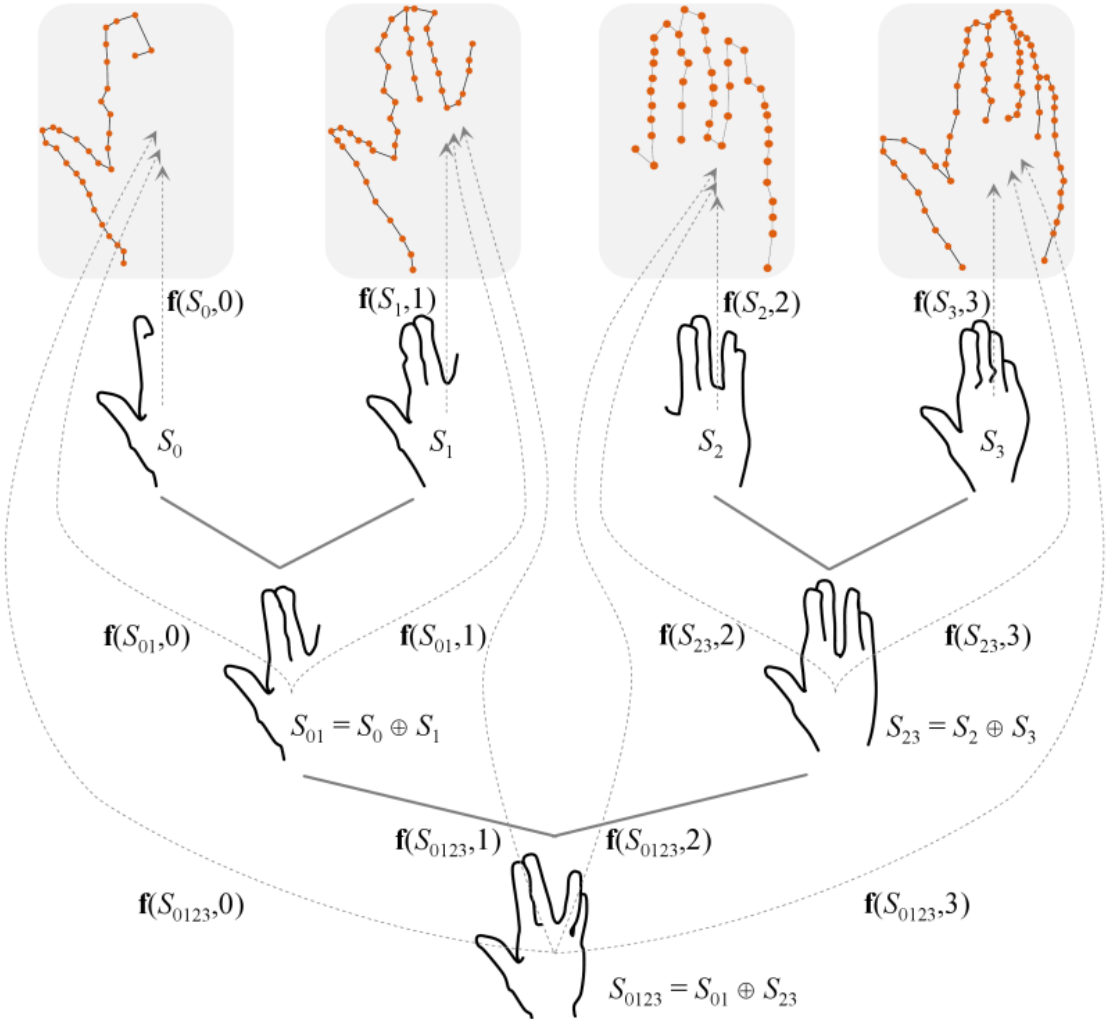

Figure 3.20: The hierarchical merging of urshapes (S) until a final urshape and a deformation (f) is obtained. The image is adopted from [200].

In the research detailed in [124], Ma *et al.* formulated non-rigid registration as the estimation of a mixture of densities. They fitted a Gaussian Mixture Model (GMM) to the source set by constraining the center of GMM to coincide with the GMM's of the target set. Besides, they benefited from local features to assign the membership probabilities of the mixture model in order to preserve both local and global structures of the source model. Further evaluation during the registration and for assessment of the models was performed using the formula reported in Equation 3.4.

$$\varepsilon = \sqrt{\frac{1}{|S|}\sum_{a}^{b} || T(x_n) - y_m ||^2} \tag{3.4}$$

Originally, they proposed their methodology to deal with the non-rigid registration of 2D point sets; however, evaluation of their methodology using 3D pointclouds showed promising results, in

which the registration error between the two 3D pointclouds was measured to be less than 0.92 *mm* in the worst case even when an occlusion exists in registering models.

The non-rigid registration methodology (called NR-ICP) proposed by Amberg *et al.* [7] is developed over the work proposed by Allen *et al.* [6] in which considered the use of affine transformation. To find the required parameters of transformation, it uses a pair of corresponding points which was found through ICP. In other research, Allen *et al.* [6] proposed a modified ICP registration not only to carry out Euclidean but also affine transformation as well; howsoever, using a single correspondence would not lead in a unique affine transformation. To solve the issue, Amberg *et al.* [7] proposed to assign constraints to limit the number of computed affine transformations up to one by adding a regularization term in the cost function.

Considering $S = (v, \varepsilon)$ as the source model set of n vertices (v) and m edges (ε), and also a target model T, it is aimed to find parameters X describing a set of displaced source vertices $v(X)$. To perform the non-rigid registration, the source model is deformed locally only on regions where corresponding regions exist on the target model. The proposed parameters is an affine 3×4 matrix (X_i) defined per source vertices ($i \in [1, n]$).

To decrease the distance between the two registering sets, local affine transformations are found and then applied to the source model by minimizing the cost function reported in Equation 3.5.

$$E(X) := E_d(X) + E_s(X) + E_l(X) \tag{3.5}$$

The first term $E_d(X)$, formulated mathematically in 3.6, expresses the distance between the deformed template and the target. Ideally, it should converge to zero to allow fitting the registering set completely on each other.

$$E_d(X) := \sum_{v \in V_i} \omega_i ||T, X_i v_i||^2 \tag{3.6}$$

To allow matrix production, source vertices are defined as $v_i = [x, y, z, 1]^t$. While $||.||$ denotes the Euclidean distance between a point such as v and its closest point on the target model, the reliability of the match is weighted by ω_i. The weights are set to zero for vertices which no correspondences can be found, and 1 for others. Since the search space for the nearest point to each vector increases the complexity of the methodology up to $O(n^2)$, it was proposed to limit the search space within the sphere including the triangulated face. Although the adapted strategy decreases the complexity from $O(n^2)$ to $O(\log_2 n)$, it imposes a prior condition which requires the initial models to be very close to each other in order to find the correspondences.

The second term of $E(X)$ appeared in 3.7, is related to the stiffness of the deforming vertices. The weighted difference of the neighbouring vertices transformations are penalized under the Frobenius norm $||.|| + F$ using the weights $G = diag(1, 1, 1, \gamma)$.

$$E_s(X) := \alpha \sum_{i,j \in \varepsilon} ||(X_i - X_j)G||_F^2 \tag{3.7}$$

γ highlights the skew and rotational differences of the source local region to be registered, that is chosen depending on the units of data and the type of deformation to be applied. In situations where the registering sets are on the same scale between $[-1,1]^3$, it can be set to 1. α is a weight in which regulates the flexibility of the source.

The third term of $E(X)$ is introduced in 3.8, which is a simple landmark term used both for initialization and guidance of the registration. Having determined a set of landmarks (or known correspondences) $L = \{(v_{i_1}, l_1), \ldots, (v_{i_l}, l_l)\}$, this term can be denoted as:

$$E_l(X) := \beta \sum_{(v_i,l)\in L} ||X_i v_i - l||^2 \tag{3.8}$$

In case no landmark is determined, the cost function is minimized globally, that physically means the source model collapses into a point on the target pointcloud. To avoid it, landmarks are automatically chosen locally with respect to the closest point on the registering sets when they are not initially determined. Finally, β is used to fade out the importance of noisy landmarks in noisy pointcloud.

Having constructed the cost function (formulated in 3.5), it is minimized efficiently using ICP algorithm stated in Algorithm 1.

Algorithm 1 Procedure to register two non-rigid sets

1: **procedure** NON-RIGID OPTIMAL STEP ICP(S, T)
2: Initialize X^0
3: For each stiffness $\alpha^i \in \{\alpha^1, \alpha^2, \ldots, \alpha^n\}, \alpha^i > \alpha^{i+1}$
4: Until $||X^j - X^{j-1}|| < \varepsilon$
5: Find preliminary correspondences for $v(X^{j-1})$
6: Determine X^j as the optimal deformation
7: **end procedure**

The stated algorithm minimizes $E(X)$ within two loops. Starting with large α (accounting for stiff deformation), the outer loop aims to apply a global deformation to the source model. Decreasing the stiffness weight step by step, more local deformations are applied to the source pointcloud.

While the outer loop was responsible to regulate the deformation based on the iterative decrease of the stiffness, the inner loop is used to find deformation for each stiffness. Optimal transformations are computed based on the preliminary correspondences found using the closest points. Considering the fixed stiffness which regulated the movement of the point, the found transformation is constrained to deform the vertices parallel to the target surface, instead of moving them directly toward correspondences. The old source model is then replaced by the new deformed one, and the iteration continues until a distance criterion is satisfied. Through the next iteration of the outer loop, lower stiffness is found and the search for new correspondences continues. Figure 3.21 depicts an intermediate step of the registration.

To briefly summarize, in non-rigid registration methodologies, it is aimed to minimize the distance between the views by deforming one of the views, while the other one is kept rigid. While

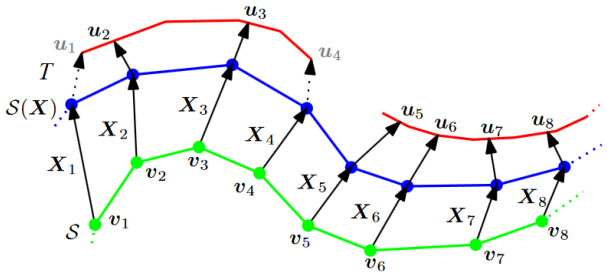

Figure 3.21: The source model (S in green) is deformed ($S(X)$ in blue) by locally affine transformation (X_i) to fit on the target model (T in red). u_i shows the correspondences (the closest points), while u_1 and u_4 are ignored since they lie on the boundary of the model. The image is adopted from [7].

these discussed methodologies were shown to successfully decrease the remained residual distance between views and provide a smooth reconstruction in terms of alignment of the views, but they ignore the possible color differences between the views. This issue appears especially when the pairwise registration of unorganized colored pointclouds is carried out in case the views are captured under different illumination conditions. Since the discussed registration methodologies provide no strategies to handle different color changes of the overlapped regions, the 3D models are reconstructed with a mixture of colors within the aforesaid regions, showing an inconsistent color quality.

Therefore, the purpose is to improve the visual quality of the 3D reconstructions of multiple views by exploring the approaches to repair the surface color, avoiding the presence of too distracting color artifacts.

3.2.7 A Brief Review on Current 3D Inpainting Methodologies

Different issues can be formulated as interpolation problems aiming at computing new values for missing data in coherence with a set of known data. Motivated by applications such as image restoration, object removal or disocclusion in IBR [75] different inpainting techniques have recently thrived in the related fields of computer vision. Furthermore, inpainting can be recognized as an ill-posed inverse problem that typically implies the use of local or global priors, based on the assumption that statistical properties or geometrical structures are in some way common to both known and unknown elements of data. For the case of image inpainting, its purpose refers not only to the recovery of missing or damaged parts in an image but also to the pursuit of a resulting image looking as natural as possible [25].

In 2013, Lozes *et al.* [123] proposed a new way to use the framework of PDEs to perform graph-based morphological operators directly on raw discrete data, such as pointclouds. Using this framework, they could perform the processing required for filtering and interpolating for patches for pointclouds. Figure 3.22 illustrates the color inpainting of a 3D vase model.

Recently, several PDE-based methods have been proposed for the problem of inpainting on images, pointclouds [58] (depicted in Figure 3.23) or manifold-valued images [14].

(a) (b)

Figure 3.22: Inpainting a 3D model by the methodology proposed by Lozes *et al.* [123]; (a) original + RoI, and (b)inpainted models; the images are adopted from [123].

(a) (b) (c)

Figure 3.23: Inpainting a 3D model by the methodology proposed by Elmoataz *et al.* [58]; (a) original, (b)RoI, and (c)inpainted models; the images are adopted from [58].

In a related line of research Garcia *et al.* [69, 203] proposed to perform the estimation of missing data by exploiting Discrete Cosine Transform (DCT) to obtain the required regression equation. Although recognizing the regression equation vulnerable to the Residual Sum of Squares (RSS) amongst the data (both available and estimated ones), Garcia *et al.* proposed a smoothing coefficient to be used as compensation, to be selected by a Generalized Cross Validation (GCV) methodology is applied iteratively to find the best smoothing coefficient due to the RSS amongst the data. Their methodology can deal with either missing or corrupted data in data presented with any dimensionality. In Figure 3.24, 3D data with voxels presentation are smoothed.

3.2.8 Reviewing Color Evaluation Methods

Color evaluation is considered as an open problem, since commonly used color spaces, including RGB and HSV, represent non-uniform distributions of color where the color difference correlate

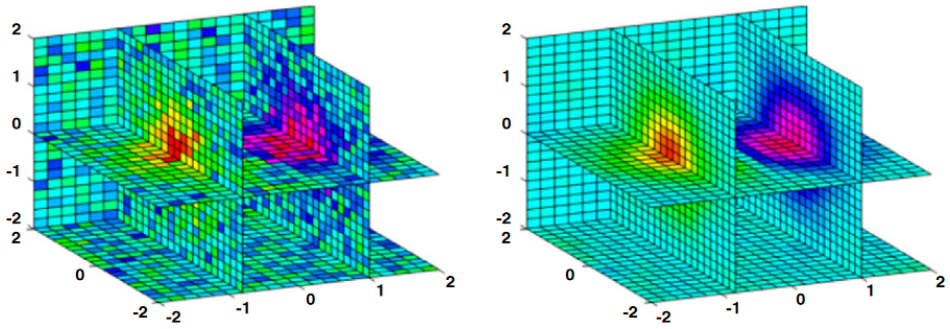

(a) (b)

Figure 3.24: Inpainting a 3D data with voxel representation by the methodology proposed by Garcia *et al.* [69,203]; (a) data with corrupted values, and (b) restored data; the images are adopted from [69].

poorly with human perception. In other words, there are different colors with the same numerical distances from each other, in which they seem to represent the same information, but they are perceived subjectively different. This problem gets more complicated when changes of the illumination are taken into consideration.

3.2.8.1 Pixel-based Color Evaluation Methodologies

Proposed by International Commission on Illumination (CIE), ΔE is a metric to show the difference between two perceived colors with a single scaler [98]. Computation of ΔE is performed in *Lab* color space. Unlike *RGB* and *CMYK*, *Lab* color space is designed according to human vision models. Mathematically, the metric was designed to express $\Delta E = 1$ as Just Noticeable Difference (JND); however, empirically, it was shown that the minimum color differences which human vision can perceive are $\Delta E \approx 2.3$ [125]. The most recent modification of the aforementioned metric is $\Delta E2000$ which puts more weight on the lightness of the color, therefore even in the situations when color is affected by low light, the metric can reflect the difference between the colors better. [46] proposed a modification to ΔE, called $\Delta E_{CMC(l:c)}$ to use manipulated brightness and saturation coefficient, thus the color space was represented in an elliptical space rather than original spherical. The added feature could be used to define more accurate color differences. More details on the metric can be found in the work of [120]. Figure 3.25 illustrates the difference of ΔE for a for a set of colors with close spectra.

Reflecting only the average of individual color differences amongst a comparing set, ΔE is not capable to lead in a concrete deduction about the overall color in a region. This is in contrast with the human vision which perceives a mixture of colors in a region, instead of individual pigments. In this regard, a fair evaluation may include the assessment of color changes in the regions where the human vision is attracted. This approach opens a line of research, called saliency estimation to locate the regions where observers' attention is drawn.

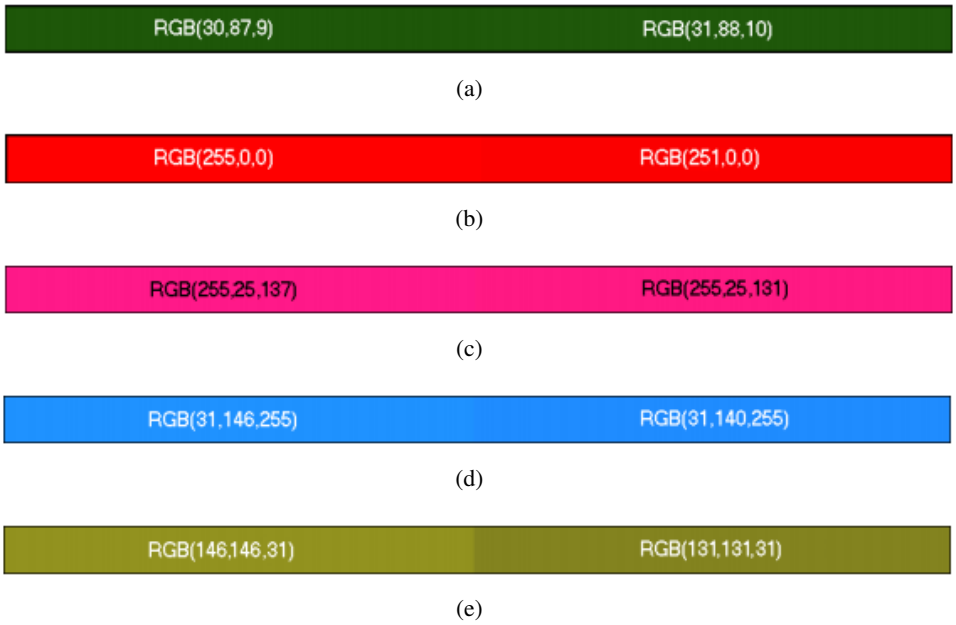

Figure 3.25: The calculated ΔE for colors with close spectra: (a) $\Delta E2000 = 0.321896$, and $\Delta E_{CMC(1:1)} = 0.482114$, (b) $\Delta E2000 = 0.835821$, and $\Delta E_{CMC(1:1)} = 0.817270$, (c) $\Delta E2000 = 1.322063$, and $\Delta E_{CMC(1:1)} = 1.600799$, (d) $\Delta E2000 = 2.121094$, and $\Delta E_{CMC(1:1)} = 2.634044$, (e) $\Delta E2000 = 5.518652$, and $\Delta E_{CMC(1:1)} = 5.481823$. The images are adopted from [131].

3.2.8.2 Saliency Map Estimation

Salient regions in an image are determined based on the locations where an observer looks at them as soon as the images are visualized. Having a variety of applications, saliency maps can track the individuals' behavior in marketing, or provide soft-attention guidance maps. Traditionally, saliency maps are obtained using eye-trackers, mouse clicks [93] or webcams [106]. However, in situations when the required facilities are not provided, several methodologies have been proposed to estimate saliency maps. As an instance, the methodology suggested by Itti *et al.* [89] focused on estimating saliency maps by considering low-level features at multiple scales, followed by combining them.

Another approach, which is called *iSEEL*, was proposed by Tavakoli *et al.* [183]. They predicted saliency maps considering two stages in which through the first stage, image features are extracted to generate a pool of features. Using the generated pool, in the second stage, similar images stored in the scene bank are found. These images are later used to retrieves the trained predictors in order to facilitate the formation of the ensemble of saliency estimators. The architecture of their methodology is depicted in Figure 3.26.

Another recent research carried out by Pan *et al.* [146] was intended to estimate saliency maps, as well. Their proposed saliency generator, called *SalGAN* consists of two stages in which is the first stage, it uses a deep convolutional neural network which was initially trained with a Binary Cross Entropy (BCE) loss over downsampled versions of the saliency maps. The second stage is followed by refining the predicted saliency by a discriminator network trained to solve a binary

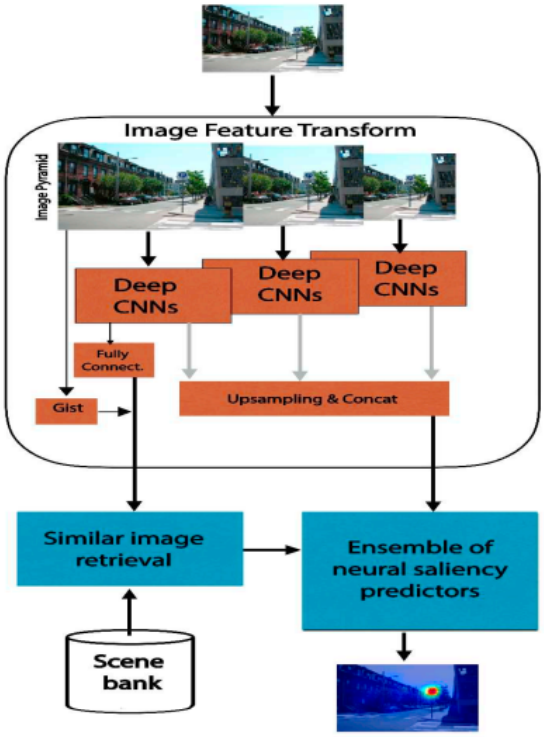

Figure 3.26: The iSEEL pipeline to estimate saliency map proposed by Tavakoli *et al.* [183]

classification task between the saliency maps generated by the first stage and the ground-truth ones. Figure 3.27 illustrates two images and the estimated saliency maps by SalGAN methodology.

Figure 3.27: Qualitative results of SalGAN on the two image: the left column represents the image while the middle and the right column illustrates the fixation maps (ground-truth), and the estimated saliency maps, respectively. The images are adopted from [146].

3.3 3D Reconstruction of Patient's Torso Using Kinect

While Kinect is chosen as the acquisition sensor in this research, it is mandatory to define a protocol to scan patients. Having defined the protocol in the first stage, secondly, it is important to select the target views to be registered.

3.3.1 Acquisition Protocol and System Overview

The acquisition of raw RGB-D data from the Kinect follows the protocol established within the context of the PICTURE Project[1], depicted in Figure 3.28. The Kinect is placed on a tripod at 90 *cm* from the subject being scanned. The images are taken consecutively at 15 frames per second while the subject performs a 180° rotation, with hands on the hips, in front of a homogeneous blue background.

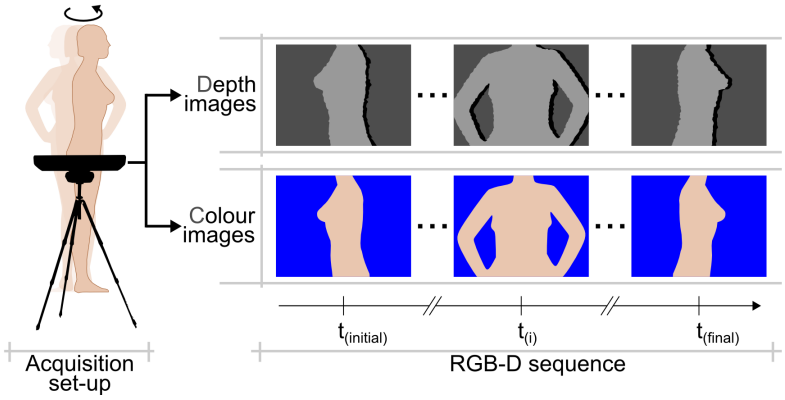

Figure 3.28: Overview of the acquisition protocol; illustration of resulting RGB–D sequence and colored pointcloud generation.

Note that the mapping between different coordinate systems was carried out by the device-specific manufacturing calibration data provided within the Kinect SDK.

3.3.2 Pre-processing of Raw Depth and Color Images

Arises from the acquisition protocol that the scene observed by the Kinect is composed of elements with different apparent motions, the object of interest (closer to Kinect) rotating around itself and the surrounding environment. The raw depth maps are segmented to retain only information respective to the object of interest. Given the possibility of some variations during acquisition, namely the relative size of the foreground with respect to the background, a discontinuity based approach was considered. Firstly, the gradient of the depth map was obtained by using Gabor filters. Then, the Otsu's segmentation method applied over that result, followed by a connected components computation stage. Subsequently, the closest region, with respect to the camera, was labeled as foreground.

[1] http://vph-picture.eu/

The depth map filtering aims at removing untrustworthy noisy points on the edge of the foreground silhouette in the depth map. Similarly to Schmeing *et al.* [167], it was considered that, given a single object of interest, both color(I_{color}) and depth (I_{depth}) images are a set of two disjoint regions. Thus, each set is recognized as $S = F \cup B, F \cap B = \varnothing$, being F the set of pixels on the depth map that belongs to the foreground, and B the set of pixels belonging to the background. Given the aforementioned acquisition protocol, intra-similarity of such disjoints sets were assumed, both in the depth and color spaces.

Schmeing *et al.* [167] also pointed out that, if the edges in the color image and in the depth-map perfectly align, then the two sets S_{depth} and S_{color} must be the same. On the other hand, it was also assumed that, since depth-maps are more noise prone than RGB images, the correct edge information can be found on the color frame. Hereupon, depth map filtering step is performed by:

1. The color image is mapped to the depth space;
2. The binary mask obtained for depth map segmentation is used as the initial foreground/background estimate for the GrabCut Algorithm [160], which performs the segmentation of the RGB data;
3. Every F depth element that belongs to B color is label as invalid.

Such approach guarantees that all the potential foreground pixels of the depth map are discarded. Apparently, the information about the object of interest on this process might be lost. Nevertheless, by using a multi-view approach, it was assured that, at least in one of the subsequent views, such information will appear in the foreground.

3.3.3 Rigid Registration of Multiple Views Captured by Kinect

Besides the limitations related to inevitable tolerances in the manufacturing process of Kinect, its own characteristics (such as field of view, resolution, acquisition rate and working range) and different sources of noise affect acquired views, make it impossible to retrieve the 3D shape using only a single depth map. In that way, it is often desirable to merge different views into a richer and more complete 3D representation of body parts. This process is called multi-view registration and can be carried out in several ways as depicted in Figure 3.29.

Assuming patient's torso as a rigid object within the rigid registration, the captured views can be registered by solving a minimization problem with 6 degrees of freedom, including translation and rotation in the 3D coordinate. But since the captured Kinect views are not initially in the same coordinate, it is necessary to coarsely align them. Known as coarse registration, this task can be carried out using the methodology proposed by Costa *et al.* [48], via choosing the keypoints with respect to the Delaunay Triangulation (DT) principle. This principle states that for a set P of 3D points, there exists a triangulation $DT(P)$ such that no point in P is inside a circumsphere defined by any triangle in $DT(P)$ [71]. The adjacent triangles contained in the DT of a pointcloud can be grouped to form tetrahedrons. Those triangles which belong only to one tetrahedron and also

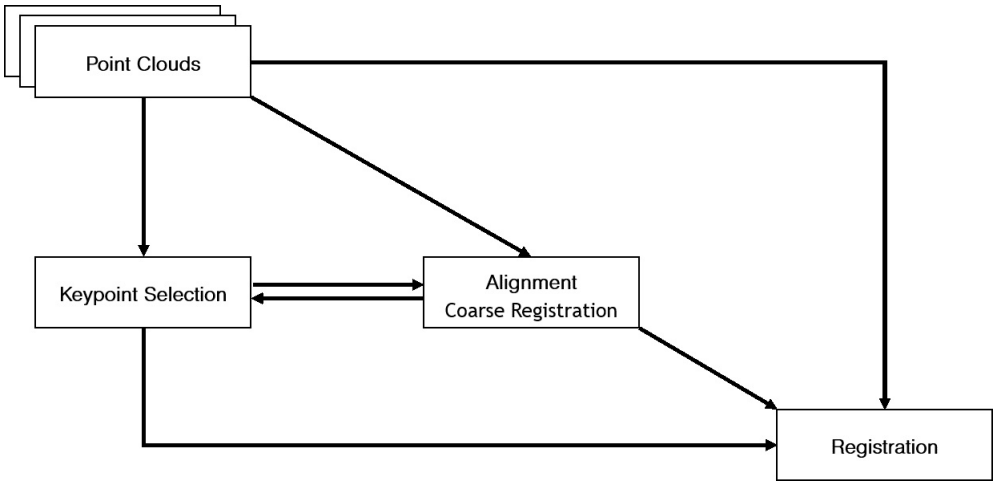

Figure 3.29: The different possible approaches (including coarse and fine) for multi-view registration

belong to the external surface are selected as the free boundaries triangles. Then, the vertices of the selected free boundary triangles are chosen as keypoints to compute the Euclidean transformation parameters (including rotation and translation) between two consecutive views and align them with each other.

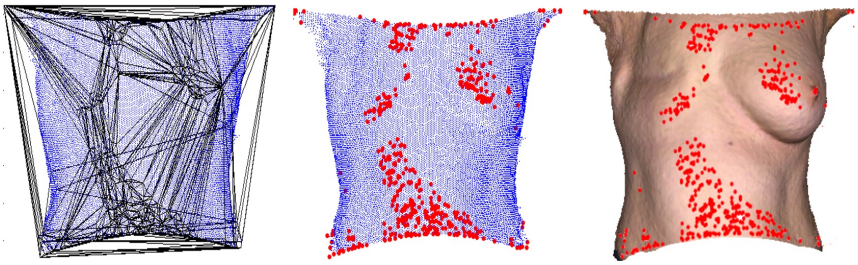

Figure 3.30: The keypoints are the vertices (red dots) of the free boundary triangles of the Delaunay Triangulation of the pointcloud. It is possible to see that the distinctive structures of the breast are correctly detected.

For the fine registration stage, the Global Procrustes ICP [191] was used, which uses the Generalized Procrustes Analysis to achieve the minimization of the cost function. While the stop criterion of the original algorithm was based on the number of iterations, it was changed slightly to represent both error-based and finite iteration stop criterion. New conditions are presented as follows:

- The pointclouds being registered remain almost unchanged in two consecutive iterations (the mean square error between consecutive poses of the pointclouds is below $1 \times 10^{-5}\ m$); or, if the first condition is not met;
- A maximum of 300 iterations has been reached;

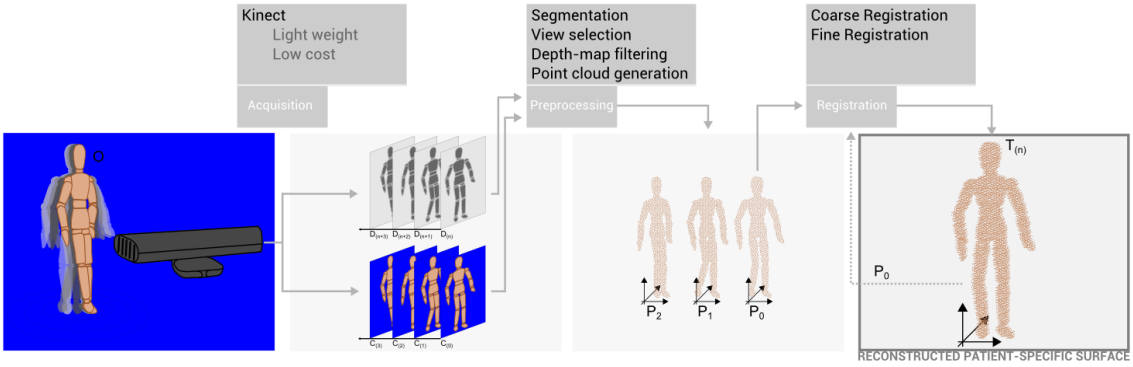

Figure 3.31: The general workflow in order to reconstruct patient's 3D model. On the left, multiple views of a patient (O) were taken using a Microsoft Kinect. The depth ($D(i)$) and color ($C(i)$) data is used to create pointclouds $S(i)$ of the model (I) that are then merged iteratively (II) towards a reconstructed model T

As a summary, pointclouds are generated from the filtered depth map data acquired by Kinect. Then, multiple selected views are iteratively registered into the same coordinate basis independently, meaning that each lateral view was independently registered with the frontal. Figure 3.31 briefly depicts the rigid registration pipeline.

3.3.4 Non-rigid Registration via Improved NR-ICP

Considering the cost function proposed by Amberg *et al.* [7], the distance between the deformed source and target was reflected in the first term that is regulated by ω_i. While the search for the closest point was bounded within the sphere including the triangulated vertex, the selection of the wrong correspondence produces an overestimated value for the aforesaid term. To avoid such circumstance, a small modification is proposed based on Equation 3.9 to assign the weight proportional to the distance between the correspondences.

$$\omega_i = \begin{cases} 0 & \textit{no correspondences in the sphere} \\ \frac{dist(T,X_i v_i)}{\max(dist(T,X_{i_j} v_{i_j}))} & j \in \textit{points inside the sphere} \end{cases} \tag{3.9}$$

In other words, the weights for a triple pair of points inside the sphere, are computed based on the maximum distance between them. In situations when the pairs don't resemble (because of deformation), the distance term is tuned to be larger. Contrarily, when the tipple pairs of points are located in the same distance of each other, ω_i is selected closer to 0.

Figure 3.32 depicts two scenarios in which the proper weight is defined based on Equation for a set of 3 correspondences 3.9. In situation that the points are located near to each other (Figure 3.32(a)), the term ω_i approaches to o since d_1 is very smaller compared to d_{max}. Contrariwise, when correspondences are far from each other (as in Figure 3.32(b)), or there exists skew between them, d_1 increases compared to d_{max}, and hence ω_i approaches to 1.

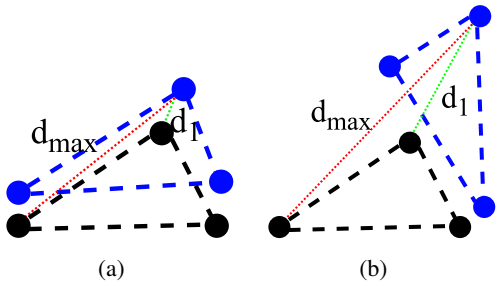

Figure 3.32: Simple illustration of weight assignment with respect to the distance between correspondences; (a) in scenario when points are close to each other, ω_i approaches to 0 since $d_1 << d_{max}$, and (b) when the point is further or there is skew between them, although $d_1 < d_{max}$, ω_i approaches to larger value comparing to the previous scenario. Note that the target and source models are colored with black and blue, respectively.

As it was previously discussed, current non-rigid registration methodologies in multi-view scenarios consider no strategies to provide smooth color changes in overlapping regions. Taking the acquisition protocol in mind (that was discussed in Section 3.3.1), the captured views are shaded differently by reason of patient rotation while the illumination source was fixed. Nevertheless, the reconstructed models, in some contexts, hampered by less than naturally looking reconstructions that greatly impact the visual inspection.

3.3.5 Enhancing Color of Patient's 3D Point-Clouds

It is proposed to tackle the enhancement of model's visualization by using a geometry-based approach to estimate erroneously the assigned color of a reconstructed surface. For this purpose, a reconstruction pipeline previously discussed is hereafter considered. Such approach provides multiple, artifact-contaminated, scattered pointclouds aligned to a common reference, and is, thereby, the baseline scenario to evaluate the proposed method (Figure 3.33).

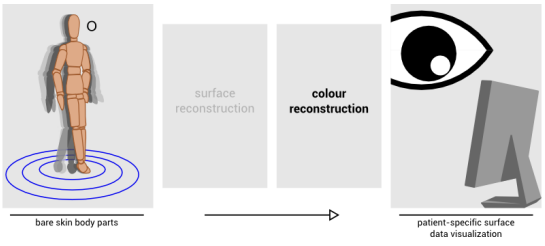

Figure 3.33: Framework overview of the considered

3.3.5.1 Geometry-based Color Correction

An overview of the three-folded procedure is schematized in Figure 3.34. The reasoning behind this strategy is that the input data contains enough information to allow a naive reconstruction

approach, based on the smooth continuity of the local structure's color, and, that such approach could rival with a more traditional inductive, data-intensive learning one.

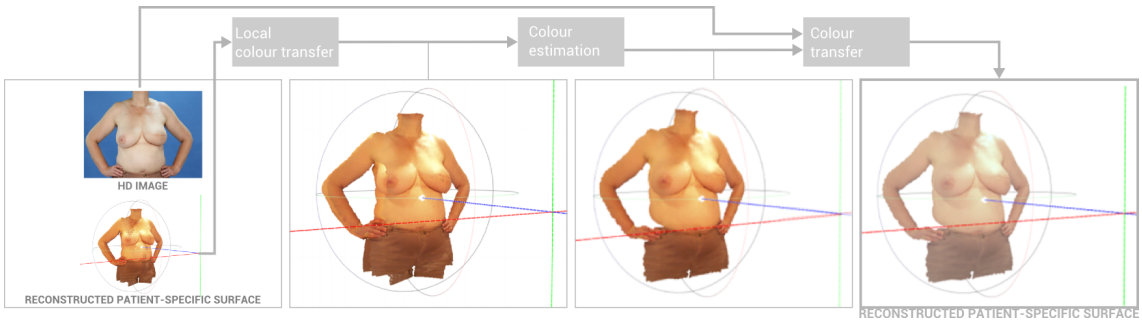

Figure 3.34: Overview of the color inconsistency correction method.

3.3.5.2 Local Color Transfer

Considering multiple pointclouds (corresponding to multiple views) relating to body surface regions that partially overlap (one frontal and two laterals) registered by the aforementioned surface reconstruction method, the first step of the proposed method is a straightforward proximity-based local color transfer approach.

Pertaining to the pointcloud from the frontal pose as the target reference appearance, point correspondences to each lateral view are computed by the closest point search. The distance between two pointclouds, for instance, P and Q, is, in this matter, defined as their point-wise Euclidean minimum distance ($dist(P,Q) = min_{p\in P, q\in Q} dist(p,q)$). Then, each point belonging to any of the lateral pointclouds which distance to its nearest neighbor in the frontal pointcloud is smaller than a small neighborhood threshold value ($< 3\ mm$) is assigned the color of the corresponding frontal point. As a result of this step, the appearance of points in overlapping regions will be uniform, and color information from frontal pose pointcloud prevail. Notwithstanding, transitions between non-overlapping regions will be accentuated.

3.3.5.3 Color Estimation

The new color of the points in the lateral views is found based on a radial interpolation approach, taking as reference the points from the frontal views in the same radius range. To do so, a given pointcloud $P = \{p_i \in \mathbb{R}^3\}_{i=1}^{n}$, with n points, is projected on a Mercator image by converting to spherical coordinates (r,θ,φ) each p_i with (x,y,z) coordinates (Figure 3.35), considering the origin of the coordinate system at the central position of the nipple-areola complex (O'').

It follows the color estimation on the Mercator projection space, using the following equation:

$$f_C(\theta) = C_L + (C_H - C_L)\frac{exp(\alpha(\theta - min_\theta)) - 1}{exp(\alpha(max_\theta - min(\theta))) - 1} \tag{3.10}$$

where C_L and C_H are the color at the extremities of the strip in the frontal view; θ is the angle of the region where the color is to be estimated; min_θ and max_θ are, respectively, the minimum and

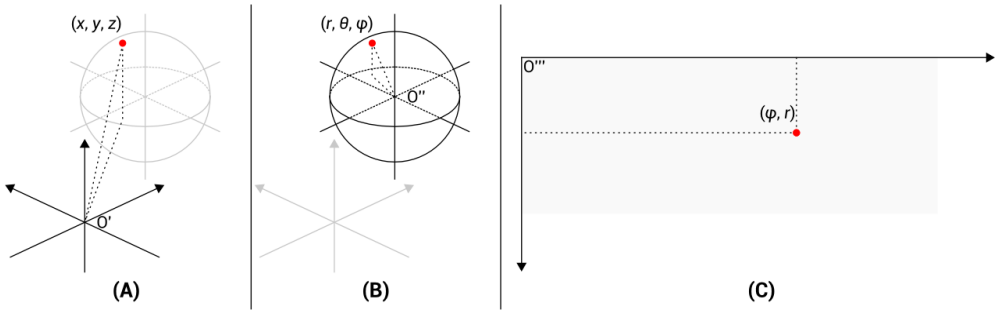

Figure 3.35: Generation of Mercator image.

maximum angles of the region to be estimated; α is the parameter that controls the propagation of the color between extremities, and, $f_C(\theta)$ is the new color at a given angle θ.

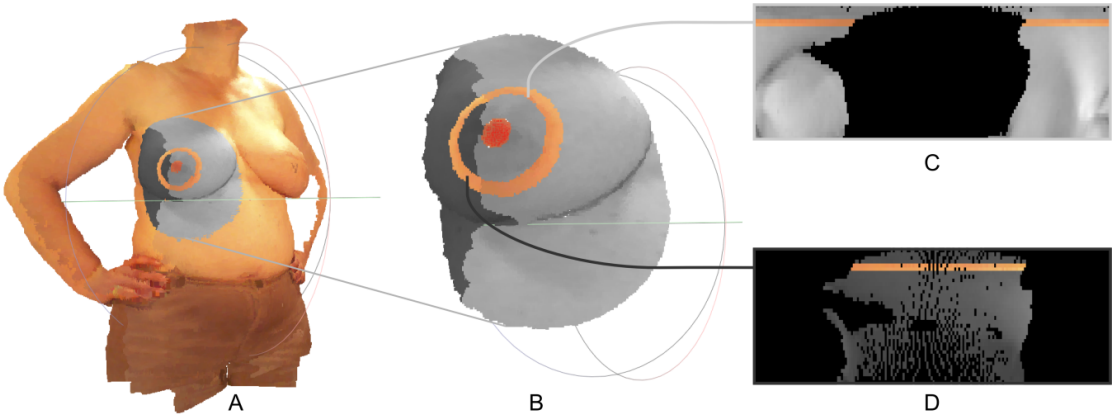

Figure 3.36: Geometry-based skin-color estimation method.

3.3.5.4 Color Transfer

For the final step, the information from the 2D HD images are used as a reference to change and improve the color appearance of the 3D pointclouds, considering the following equation [158]:

$$f_C(x) = \frac{\sigma_{2D}}{\sigma_k}(x - \mu_k) + \mu_{2D}, \tag{3.11}$$

where σ_k and μ_k are respectively the mean and standard deviation of the source image (Kinect data) and σ_{2D} and μ_{2D} the same for the target image (2D HD data).

3.4 Evaluation of the 3D Reconstruction of Patient's Torso Using Kinect

3.4.1 Dataset

To evaluate the performance of the detailed 3D reconstruction methodology, 43 patient models were used. Patients were scanned with both Kinect and a dedicated scanning system based on active multi-view stereo-photogrammetry provided by the company 3dMD, at Royal Free Hospital in London. The 3dMD sensor was used because of its high-accuracy in the reconstruction of 3D models, and providing colors near to the reality. Note that the experiment over Kinect data was conducted using down-sampled pointclouds from approximately $90k$ points to $16k$ points, to accelerate the performance of the proposed reconstruction pipeline.

3.4.1.1 Dataset of 3D Reconstructed Models for Registration

The proposed 3D reconstruction pipeline was used to generate 3D models from the data provided by Kinect and evaluate the accuracy of the proposed registration methodologies. Besides, the models generated by 3dMD were all used as ground-truth data. It should be noted that all the 43 3D models were considered though evaluation of registration methodologies.

3.4.1.2 Dataset of 3D Reconstructed Models for Inpainting

A subset of 24 models among the 3D reconstructions of 3dMD data was selected as the ground-truth data for inpainting. The models were annotated such that the lateral color information is mostly missing. An illustrative example is presented in Figure 3.37.

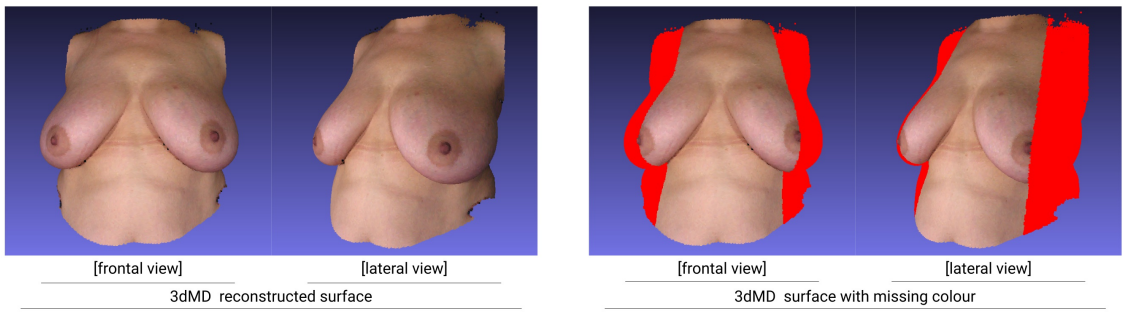

Figure 3.37: Example data to be inpainted

3.4.2 Evaluation Metrics

3.4.2.1 Registration Metrics

The most commonly used approach is to calculate Euclidean Distance measure between the 3dMD models and the reconstructed pointclouds, for instance the Hausdorff Distance or Root Mean

Square Error-related metrics, where the lower is the value of the metric the better is the reconstruction. To obtain an accurate evaluation using these Euclidean metrics, it is mandatory to have both pointclouds aligned in the same coordinate system.

This requires a preliminary alignment stage using a standard registration methodology. In order to be more accurate as possible, a software called CloudCompare was used for this purpose. Since the Field of View (FoV) of Kinect and 3dMD are generally different, the two pointclouds were segmented manually while the Kinect data is always a sub-space of the 3dMD data (see Figure 3.38). With this, it was guaranteed that the comparison is fair and only the 3D information is taking into account to the value of the metric.

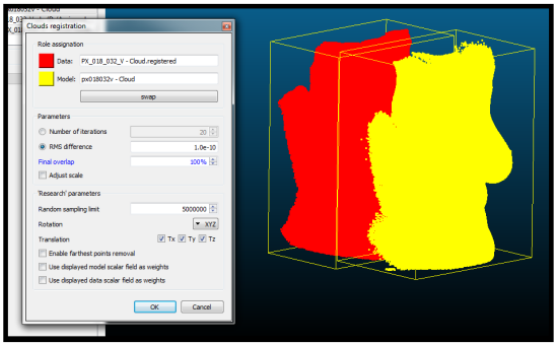

(a)

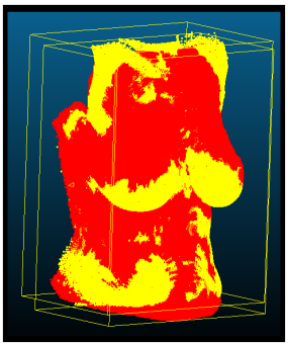

(b)

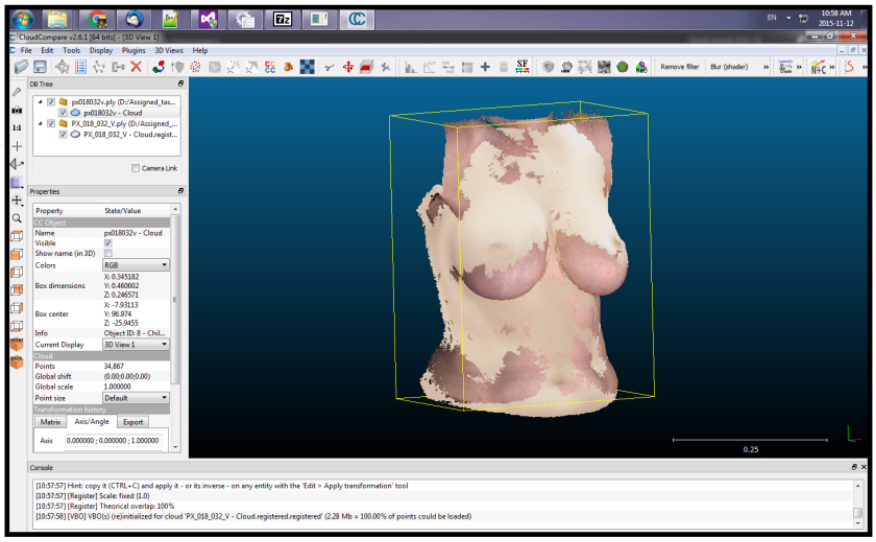

(c)

Figure 3.38: The process to perform numerical evaluation using CloudCompare; (a) both models, the 3D reconstructed and 3dMD models are segmented to have the same FoV, (b) the reconstructed and the 3dMD models are aligned, and (c) the residual distance between them is obtained in terms of Root Mean Square Euclidean distance.

3.4.2.2 Color Inpainting Metrics

The briefly conducted review by Section 3.2.8 revealed that the color comparison can be carried in two fashions: individual comparison of pixels, or grouped analysis of color changes. While the first one focuses on the average of individual distances between color pigments, the second one reflects the color differences being perceived by the human vision. The two metrics being discussed in this section, are intended to scrutinize the two aforesaid fashions.

CIE–ΔE Metric In the present work, the metric $\Delta E_{CMC(l:c)}$ is to be computed between estimated colors and original colors from 3dMD models for the corresponding points that were annotated as missing. Then, the missing lateral sides were colored with both the referenced and the proposed inpainting methodologies, and finally, they were compared with the models with real colors from ground-truth models.

Saliency-based Metrics Information Gain (IG) is an information theoretic metric introduced by Kummerer *et al.* [108, 109], to measure saliency model performance beyond systematic bias. In mathematical notation, it is calculated in bits per fixation via Equation 3.12.

$$IG(P,Q^B) = \frac{1}{N}\sum_i [\log_2(\varepsilon + P_i) - \log_2(\varepsilon + B_i)], \tag{3.12}$$

where Q^B, P, and B are fixations, saliency map, and baseline map. Besides, i indicates the i^{th} pixel, N represents the total number of fixated points, and ε is for regularization. The IG measures the average information gain of a saliency map compared with the baseline with respect to the fixation map [26]; hence the positive IG scores denotes the saliency map predicts the fixated locations better than the baseline map, as the negative scores mean contrariwise.

The second metric studied alongside the IG is Similarity (SIM) which is intended to measure the similarity between two distributions [161, 181]. Considering the histogram of the distribution of saliency, it can be obtained as the sum of the minimum values at each pixel, after normalizing the input maps, using Equation 3.13.

$$SIM(P,Q^D) = \sum_i \min(P_i, Q_i^D) \; where \; \sum_i P_i = \sum_i Q_i^D = 1 \tag{3.13}$$

While P is an estimated saliency map, and Q^D denotes a continuous fixation map iterating over discrete pixel locations i. The SIM is a continues value in the range of $[0,1]$ in which 1 corresponds to the same saliency distributions, and 0 means no overlap between them.

3.4.3 Evaluation of the Rigid Registered Models

The numerical results for the Hausdorff Distance or Root Mean Square Error-related metrics are reported in Table 3.3.

Reconstructed models were compared with the 3D ground-truth data. The quantitative and qualitative analysis shows the methodology is accurate enough with an average error of 2.63 *mm*

Table 3.3: Numerical results of the evaluation of rigid registration of Kinect 3D reconstruction performed in 43 cases; μ stands for average and σ denotes standard deviation.

Euclidean Distance (mm)		Hausdorff Distance (mm)		Time (s)
μ	σ	μ	σ	μ
2.63	0.51	20.97	11.67	188.9

for 43 patients. Results are very promising, however, some of the reconstructed models present small local misalignment. Since Kinect and 3dMD data have not been acquired at the same time, these artifacts are originated by the undesired motion of the patient being scanned during the acquisition protocol. This kind of motion, obviously between the two different acquisitions creates misalignment in which increases the measured distance during the conducted evaluation.

Not only numerical, but also visual evaluation is performed to validate the reconstructed model. As in Figure 3.39, the reconstructed models of three patients are illustrated.

A detailed investigation of the visual results reveals that the views are not completely aligned in the overlapped regions, being demonstrated in Figure 3.40 in which the registered view are shown in pseudo-color. As it was expected, since the patient was rotating during the acquisition, nonlinear movement have influenced patient's torso, therefore, the scanned views are slightly different in overlapped regions. In addition to nonlinear motion caused during rotation, respiration artifacts are expected to influence the scanned views. These motions are known as the main sources which influence the rigidity of the scanned object in the current application.

3.4.4 Evaluation of Non-rigid Registered Models

To set up the methodology parameters, the vector of stiffness weights (α) is initialized with 100, and with a step of 0.5, it is decreased up to 1. The aforesaid decreasing trend assures the views are approached each other such that reliable correspondences can be established between them. Then, as the stiffness decreases step by step, the influence of the affine transformation appears more in deforming the source view toward the target pointcloud.

Also, since the views are acquired in the same scale (as the distance between the sensor and the patient was maintained constant), γ is set to 1. Finally, in the absence of the predefined landmarks, β is set to 0. The same 43 models which had been evaluated in rigid registration were considered in the current experiment, as well as the configuration of the used machine. Table 3.4 reports the bidirectional measurements in the scale of millimeters.

Table 3.4: Numerical results of the evaluation of non-rigid registration of Kinect 3D reconstruction performed in 43 cases; μ stands for average and σ denotes standard deviation.

Registration Methodology	Euclidean Distance (mm)		Hausdorff Distance (mm)		Time (s)
	μ	σ	μ	σ	μ
Original ICP-NR	2.21	0.49	20.56	11.50	232.8
Improved ICP-NR	2.18	0.50	19.97	11.52	233.4

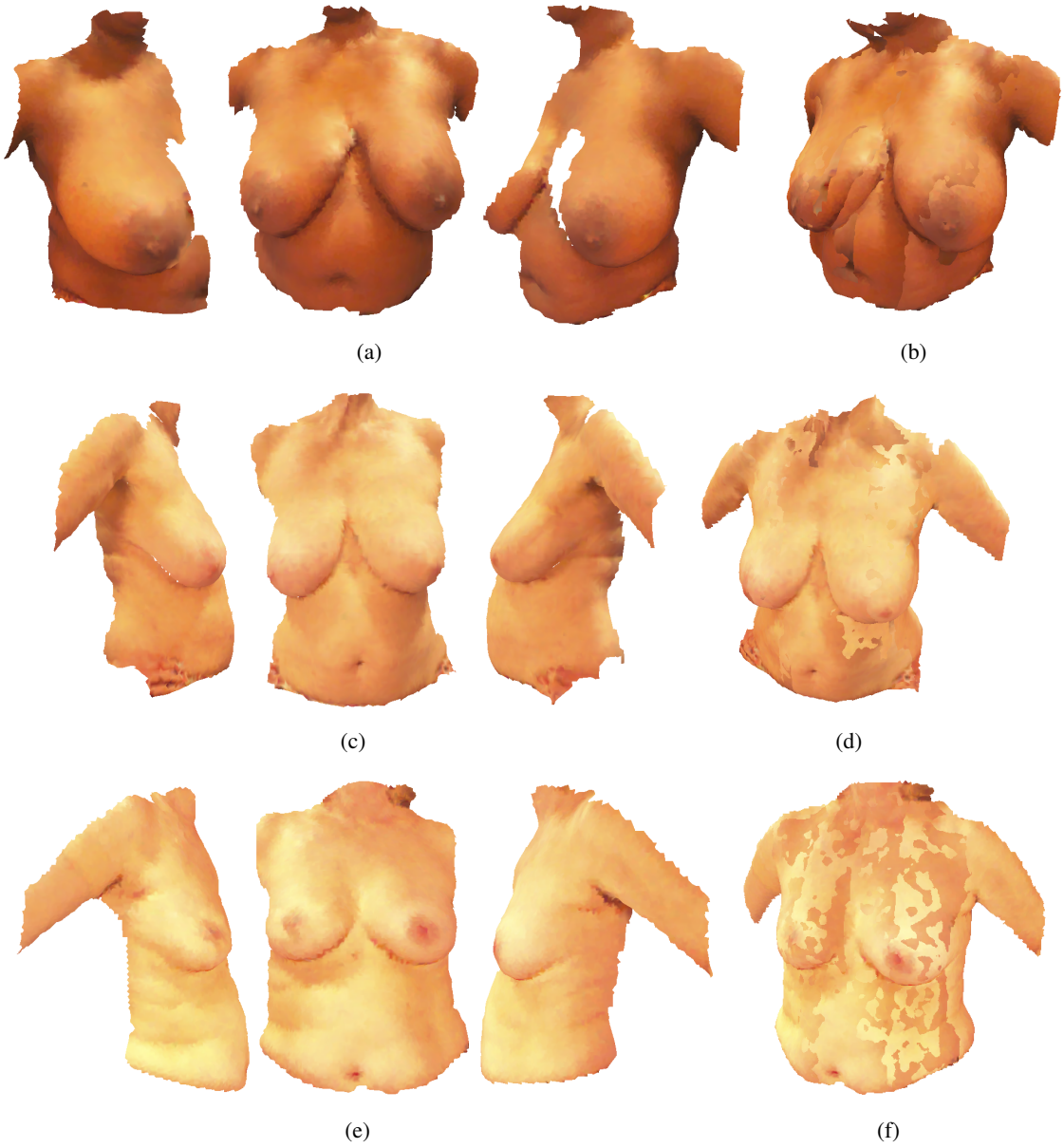

Figure 3.39: The results of reconstructing 3D models of three patients using the proposed pipeline; the first column illustrates the automatically selected views, and the second column shows the rigidly registered 3D models.

By evaluating the numerical results from both non-rigid registration methodologies with the results of Table 3.3, it is shown that distance between the reconstructed models and the ground-truth data is decreased less than 0.5 *mm*. Despite the small deformation between the comparing sets (since the ground-truth data and the views for 3D reconstruction were not acquired in the same moment of time), the distance error between them is decreased, indicating that the lateral views are deformed to compensate the sources of the motions discussed before.

Besides the numerical evaluation, visual comparisons are conducted to verify the performance of the registration methodology. Figure 3.41 visualizes the 3D reconstructed model of a patient

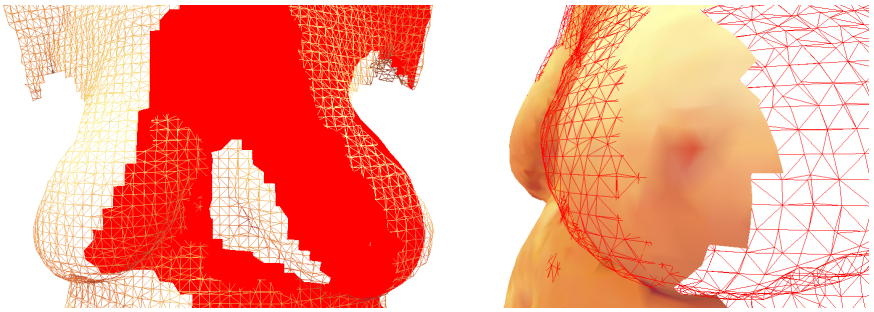

(a) (b)

Figure 3.40: The frontal and the perspective overview of the rigidly registered views; the lateral view is shown with pseudo color.

in pseudo color in which two reconstructed pointclouds, including a rigidly registered and a non-rigidly registered model, are compared.

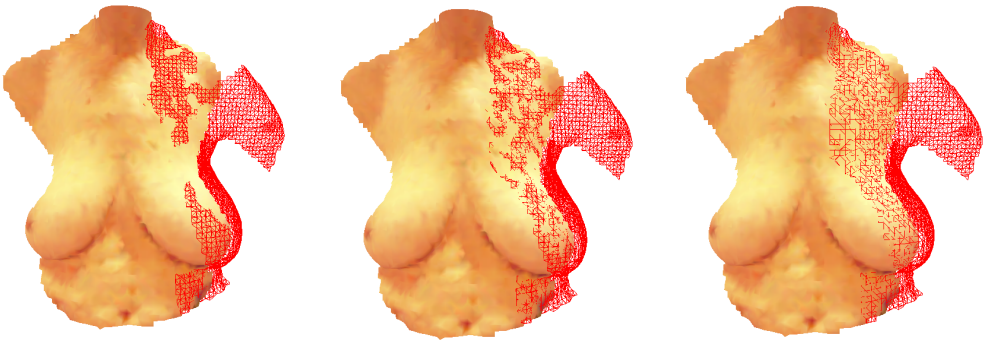

(a) (b) (c)

Figure 3.41: Visual comparison of 3D models resulted from (a) rigid registration, (b) non-rigid registration with ICP-NR, and (c) non-rigid registration with improved ICP-NR

As it is anticipated, the modification of the weights due to their distances to the nearest points has improved the performance of the non-rigid registration method in terms of decreasing the distance between the 3D reconstructed model and ground-truth. Such slight improvement (less than 0.03 *mm*) is obtained by giving more weights to more confident correspondences. More details are depicted in Figure 3.42, in both true color pseudo color models. In the overlapped regions, the improved non-rigid registration is shown to carry out a slightly better alignment.

Unlike the numerical analysis of the 3D model, which showed promising results, the reconstruction pipeline presents poor outcomes regarding the models' color. The phenomenon is fed by two main reasons; the acquisition protocol, and the reconstruction pipeline itself.

First, it is worth to go back to the scanning protocol. Data acquisition was performed while patients were rotating around their height axis in front of Kinect. Since the environmental light sources were fixed, the motion of the patients changes the shading direction on the torso. Hence, the scanned views presented pointclouds with slightly different color information. As the second

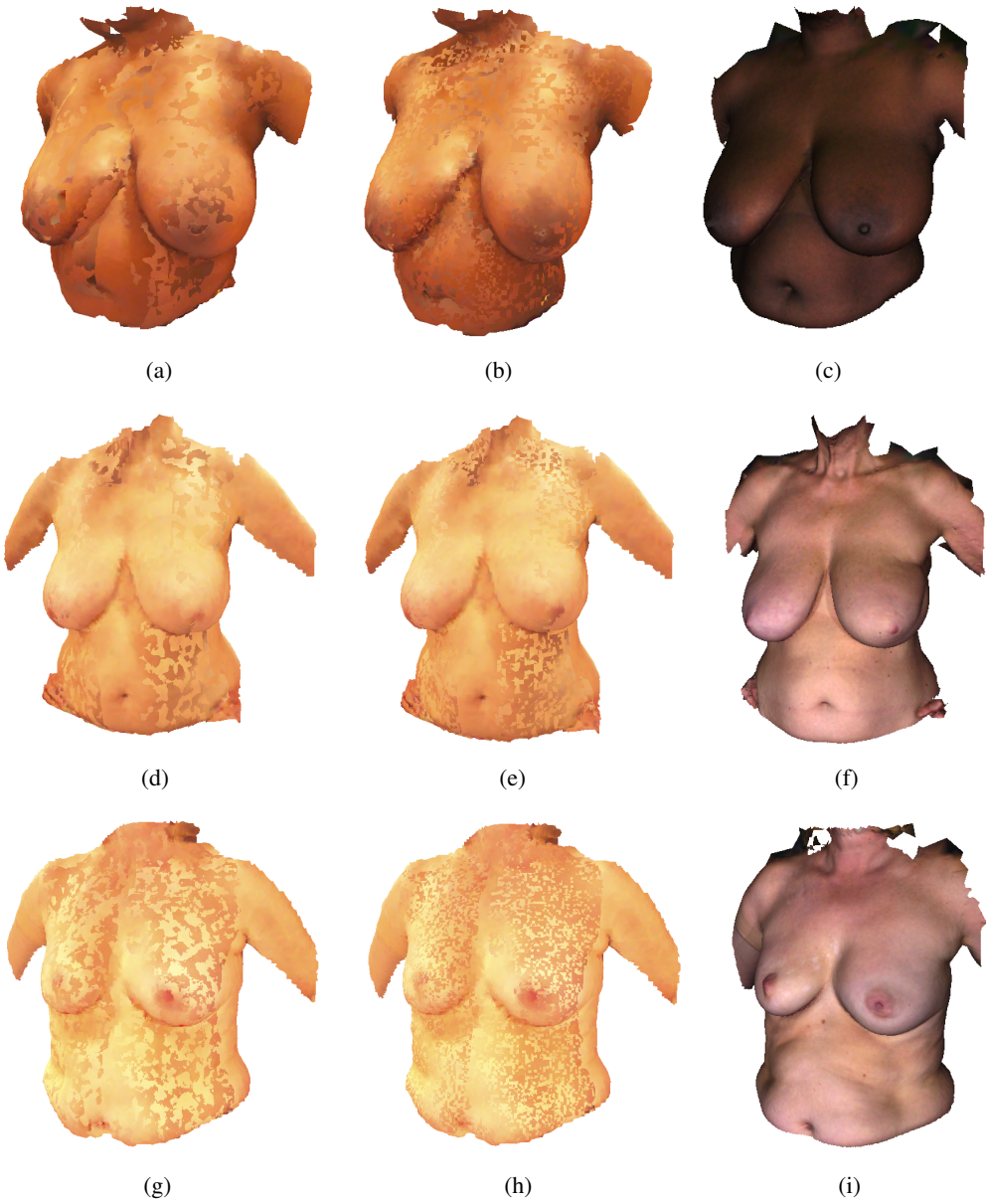

Figure 3.42: Visual evaluation of the non-rigid registration of 3 patients; the first and the second columns are the original non-rigid registration method proposed by Amberg *et al.* [7], and the improved non-rigid registration method, respectively. The third column illustrates the ground-truth data acquired by 3dMD.

reason, the 3D reconstruction methodology contains no strategy to consider the color of each view. Therefore, as it was shown in Figure 3.42, each reconstructed model is shown with a mixture of colors belonging to either lateral and frontal views. Especially after non-rigid registration, since the overlapped regions are almost fully aligned, the colors of the registered views are mixed more.

Table 3.5: Performance comparison of inpainting methods on the breast cancer patients dataset. 24 cases with both laterals annotated as missing are used to evaluate both methods with the estimation of $\Delta E_{CMC(l:c)}$ against ground-truth colors.

Inpainting Methodology	μ	σ.	min	max
Proposed	12.6	2.6	5.5 [case 6]	16.2 [case 22]
Referenced	10.5	2.9	5.1 [case 6]	17.0 [case 22]

3.4.5 Evaluation of Inpainting via Saliency Maps

An experiment was conducted to evaluate the performance of the proposed geometry-based estimation method against the reference inpainting methodology by Garcia *et al.* [69, 203].

A previously available MATLAB implementation of the reference method by Garcia *et al.* [69, 203] was used. Differently, from the original work, a pre-processing step was introduced that converts each pointcloud to a voxel representation. The size of voxel was experimentally selected to be 2 *mm*. In this regard, each voxel represents the average color of the points which are within the same datum, though voxels that contain a point with missing color are tagged to be inpainted.

The inpainting is performed to estimate the missing color in each channel individually. The missing points are given the color which has been assigned to their voxel via inpainting. Lastly, a median filter is used to smooth the color change within the boundaries of the inpainted region in order to improve the visual outcome.

First, the effectiveness of the proposed inpainting method is illustrated by the quantitative assessment using ΔE metric is presented in Table 3.5.

The difference between methods around 2.160, is not only lower than both standard deviations, as well as, on the lower limit of human ability to perceive a color difference (starting from 2.3 up according to [125]). Nevertheless, it should be noted that according to the color difference metric $\Delta E_{CMC(l:c)}$ the average estimated color by the reference method of Garcia *et al.* [69, 203] is closer, though not significantly, to the ground-truth color, than the proposed geometry-based color estimation.

Notwithstanding numerical results, a few cases of the resulting inpainted pointclouds are rendered against the original data and presented in Figure 3.43. By visual inspection of the results, a few questions were raised with respect to depth perception and presence of artifacts. On Figure 3.43 the best and worst cases identified in Table 3.5 are presented, as well as, case 8 that happened to be the example that verified the biggest difference in performance among the proposed and the reference methods. For the later case, the mean $\Delta E_{CMC(l:c)}$ was 14.529 for the proposed method and 7.816 for the reference. Despite artifacts being noticeable in both methods, reference tends to be consistently smoothed out, hence the aforementioned questions.

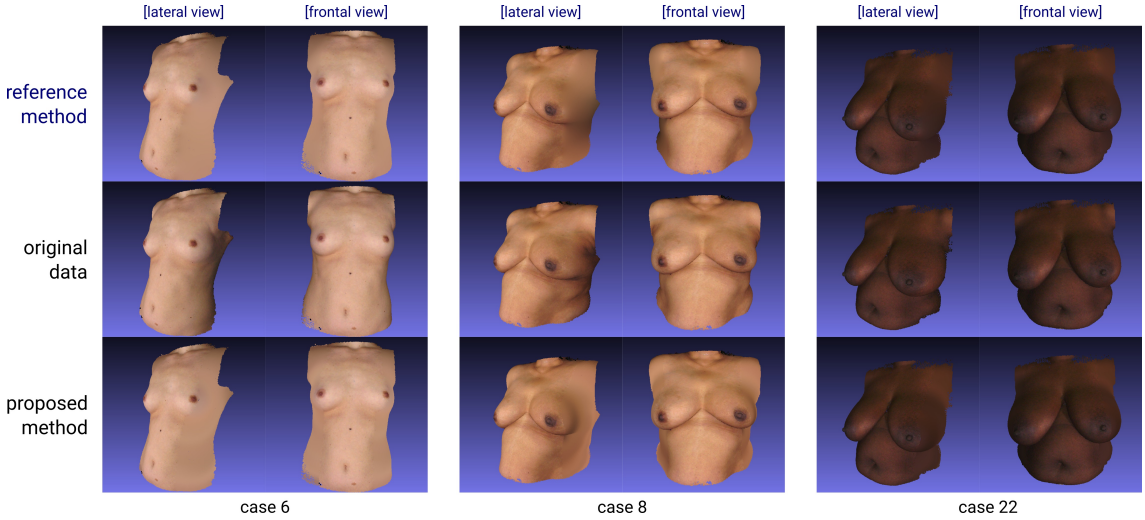

Figure 3.43: Visualization of example results for the geometry-based skin color estimation for bare torso surface reconstruction

In this regard, an additional evaluation was planned to assess the referenced and the proposed methodologies with respect to similarities to the ground-truth data. In order to employ the discussed saliency estimation methodologies for each of the 3D pointclouds (both the inpainted models and the ground-truth), 7 snapshots were taken; one view of frontal, and 3 views of lateral sides, respectively with 20, 40, and 60 degrees. The snapshots were represented as 2D images, with gray background, as it is illustrated in Figure 3.44.

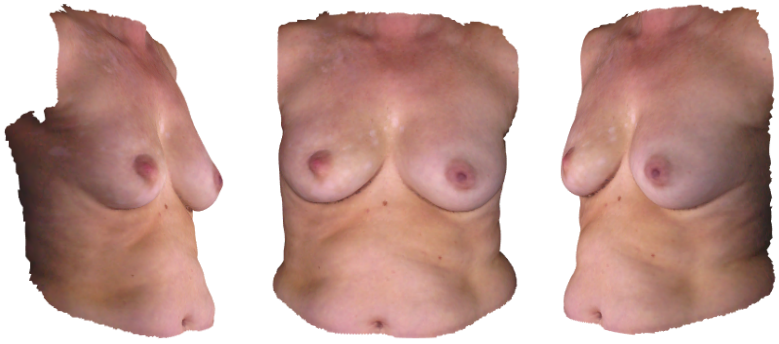

Figure 3.44: Rotating the 3D models to take snapshots in 7 angles; (a) 60° of the lateral right side, (b) frontal (0°), and (c) 40° of the lateral left side

Then, the two discussed methodologies were used to obtain saliency maps for each snapshot, as well as the calculation of IG and SIM. Note that the calculation of IG and SIM was carried out in order to determine whether the color enhancement with the referenced inpainting method, or the color enhancement with the proposed inpainting method provides closer colors to the ground-truth data. Back to the scope of the IG, the comparison was intended to determine whether the gained information from the snapshots taken from reference enhanced models or the snapshots

taken from the proposed enhanced models are positive. The same intention was pursued SIM, as well. Figure 3.45 illustrates an example of the estimated saliency maps for the three saliency maps obtained from the two inpainting method and the ground-truth data.

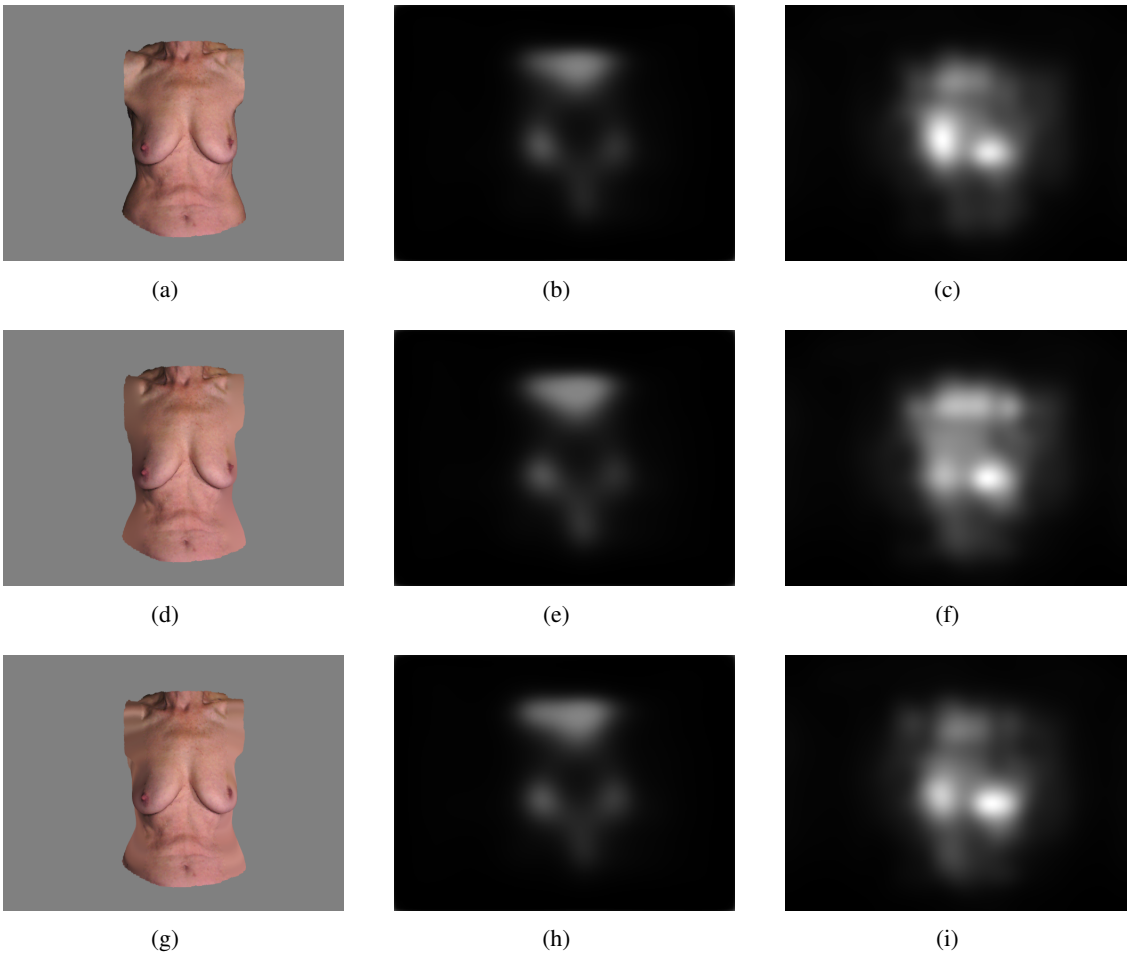

(a) (b) (c)

(d) (e) (f)

(g) (h) (i)

Figure 3.45: Visual comparison of performed experiments on same input data; (a) torso with the original color; (b) SalGAN of the original; (c) iSEEL of original; (d) torso with the referenced inpainted color (e) SalGAN of Referenced inpainted; (f) iSEEL of Referenced inpainted; (g) torso color enhanced by the proposed method
(h) SalGAN of Our inpainted; (i) iSEEL of Our inpainted

Table 3.6 reports the of positive incidences of IG and SIM in the 7 taken snapshots.

Regarding the IG score, the proposed inpainting methodology is evaluated to contain more information in 4 snapshots (2 for each lateral sides) comparing to the models inpainted with the referenced method. Inasmuch as the inpainting methodology was intended to estimate the missing colors of the lateral sides, it can be claimed that the taken snapshots contain more information of the inpainted regions. Nevertheless, since the IG is evaluated to be positive in more lateral views, it can be concluded that more information can be gained in case the 3D models are inpainted with the proposed methodology.

Table 3.6: Evaluation of the inpainting methodologies via saliency maps generated with SalGAN [146] and iSEEL [183]. Note that the evaluation is performed based on the counting positive scores of both IG and SIM metrics.

Metric	# of positive cases		Total number of cases per model
	SalGAN	iSEEL	
IG	4	4	7
SIM	4	6	7

Considering the SIM metric, the same argument can be discussed to conclude that the distribution of the saliency maps generated from the 3D models inpainted with the proposed methodology is evaluated to resemble more to the distribution of the saliency maps generated from the ground-truth data. Finally, overall evaluation certifies the correctness of the proposed inpainting methodology.

Having certified the correctness of the proposed inpainting methodology on the ground-truth data, the same experiment was carried out again, but instead, the 3D reconstructed models were inpainted instead. Figure 3.46 demonstrates three patients before and after color enhancement. As it is expected, the proposed inpainting methodology alleviated the shading issue and provided a smooth color distribution on the model, as well as the overall similarity with the ground-truth data.

The color enhanced models (second column of Figure 3.46) not only present smoother distribution of color, comparing the results after registration (first column of Figure 3.46), but also resembles more to the ground-truth data (third column of Figure 3.46). The same output can be observed in the models illustrated in the second and the third rows of Figure 3.46).

3.5 Summary

This chapter comprises the discussion about 3D reconstruction methodologies. Initially, a brief literature review was conducted on the 3D scanning sensors, as well as 3D registration methodologies. Three views were selected automatically with respect to the defined acquisition protocol, and they were rigidly registered throughout coarse and fine steps. The coarse registration was intended to roughly align the lateral views in correct position regarding the frontal view. The fine stage was proceeded to approach the lateral views to the frontal through an iterative scheme.

Although the output of rigid registration showed promising reconstructed models, the lateral views were not aligned well on the frontal one due to the non-linear motion of the patient imposed through the data acquisition. While such motions cannot be compensated via rigid methodologies, non-rigid registration was considered as the main solution to decrease the remained distance between the views.

Finally, an in-house color enhancement methodology was proposed to improve the color quality of the 3D reconstructed models in two consecutive stages. First, putting the attention on the frontal view, it was tried to propagate the frontal color in a radial order on the lateral views to have a smooth distribution of colors, especially on the overlapped regions. Then, by using an image

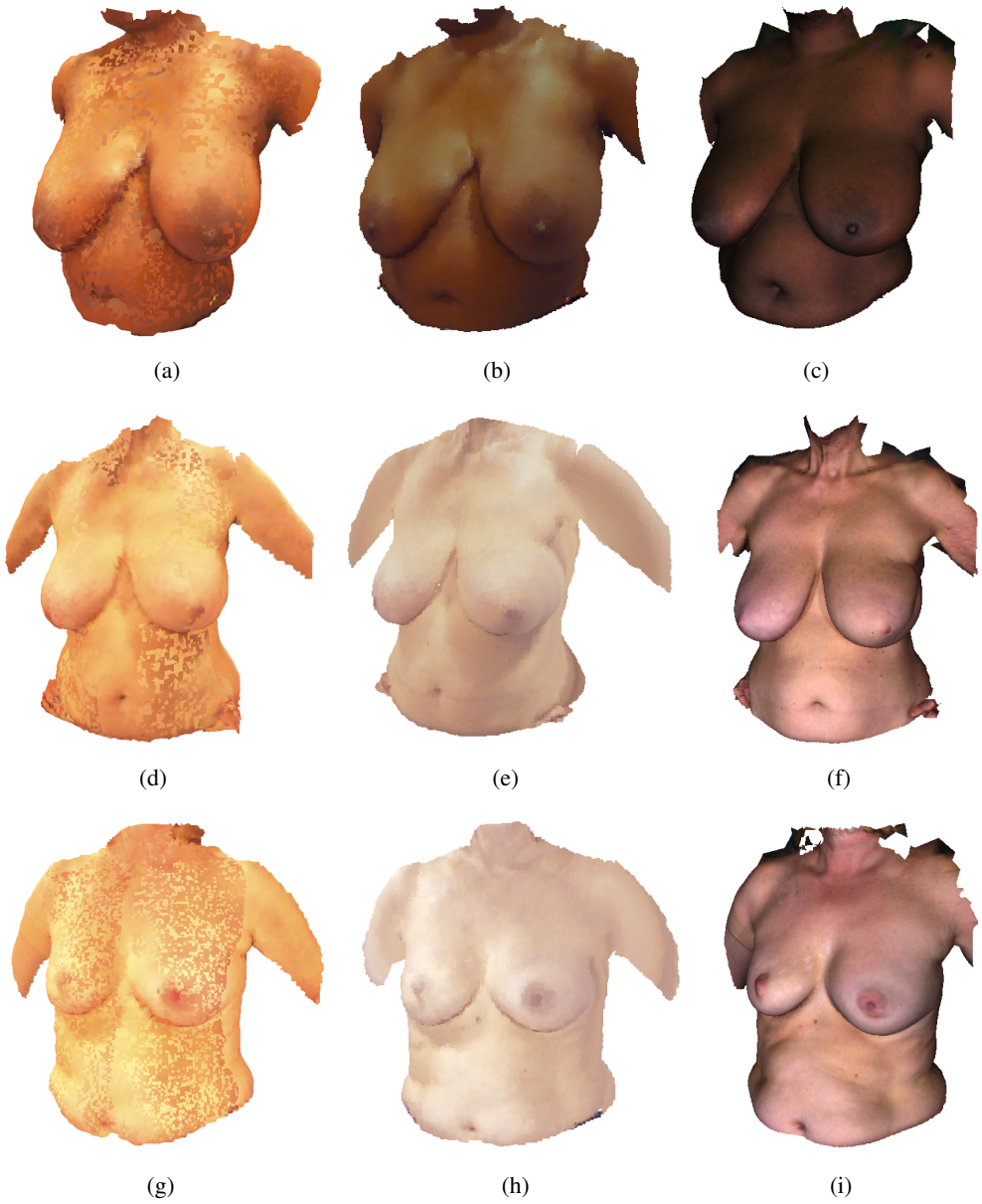

Figure 3.46: Visual comparison of 3D models before and after color enhancement with the models generated from 3dMD data. The first column depicts the 3D models of patients after non-rigid registration stage. The second column is the color enhanced model, and the third column shows the models reconstructed from 3dMD sensor.

taken with a high-quality camera which was mounted over Kinect, the histogram of the 3D reconstructed model was transferred toward the histogram of the high-quality image. The proposed mechanism was evaluated using color distance measurement alongside a competitive inpainting methodology. Although the competitive methodology was slightly better in numerical evaluations, our suggested method was evaluated better visually.

Chapter 4

Breast Complete Contour Segmentation*

Automatic segmentation of breast is an important step in the context of providing the input for further steps in the planning tool for BCT. As an instance, the segmented breast can be utilized to generate a parametric model (that will be discussed in Chapter 5) which can be deformed interactively. Current methodologies for breast segmentation require user interaction to select contour endpoints [28], or to perform an incomplete detection of breast region [114, 143]. Considering the inferior breast contour, most of the available methodologies detect the contour in a medically acceptable range; however, since there is no medical consensus on the actual location of breast upper contour, the aforesaid studies ignored the detection of the contour in that region and considered simple approaches to model it. As an instance, in [143], it was suggested to use a straight line to resemble the upper contour.

In the current chapter, beginning with the demands and requirements of detecting breast contour, the state-of-the-art methodologies are reviewed. Following the investigation of the drawbacks of current known methodologies, a new approach is proposed to detect complete breast contour. The proposed approach encompasses three methodologies to detect both the exterior and the interior contour of breast via multi-modal solution. While the exterior contour comprises both upper and inferior contour visible from frontal 3D reconstructed models, the interior contour is obtained via 3D models obtained from MRI data. Finally, the proposed approach will be evaluated quantitatively and qualitatively, and further discussion will be conducted through the comparison of the detected breast contour with the ground-truth contour obtained via BCCT.core.

4.1 A Brief History on Breast Region Segmentation

Breast region segmentation is being studied for many years both in 2D and 3D data. Previous studies have been widely focused on finding the inferior contour, which outlines the lower half of the breast up to the sternum in one side and in the vicinity of the axilla in the other side. In

*Some parts of this Chapter appeared in [211]

the research performed by Cardoso *et al.* [28] the breast contour detection was performed using frontal RGB images. This approach was formulated by computing the shortest path between the endpoints of the breast contour, after transforming the image as a weighted graph using gradient information. This was based on a semi-automatic approach since some key points were manually identified: breast contour endpoints and nipples position. Figure 4.1 illustrates a given frontal image, the computed gradient to find the shortest path between the annotated endpoints, and the detected contour.

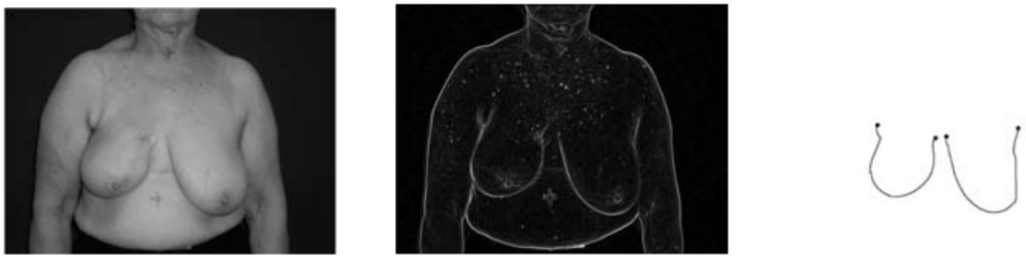

(a) (b) (c)

Figure 4.1: Detected contour by the methodology proposed by Cardoso and Cardoso [28]; (a) is the input frontal image, (b) represents the gradient map, and (c) denotes the detected contour by finding the shortest path connecting manually annotated endpoint within the gradient map. The images are adopted from [28].

Subsequently, improvements to the methodology were performed for the complete automation and correct detection of the contour [30]. Anatomically, the contour is approximately circular and centered on the nipple. This fact inspired the authors to solve the shortest path problem in polar coordinate; thus, a cost map is generated by converting the Cartesian coordinate to polar, centered in the nipple position. However, it is generally accepted that using only RGB images is difficult to find a generalized method for breast contour delimitation since it is characterized as too sensitive to changes of the gradient [114].

In another research, Lee *et al.* [114] studied active contours with shape constraints to detect the breast contour. They initiated the active contour with a catenary curve which has been proved not only to capture the overall shape of breast contour but also to quantify the breast morphology. An optimized catenary curve was rotated to fit the orientation of the breast, and then it was inflated with proper balloon force to prevent the active contour from collapsing in a unique point. Their evaluations showed that the proposed constraint for the active contour maintained the typical shape of the breast; however, since their initial model was an open curve, the superior contour was ignored. Figure 4.2 illustrates the detection of inferior contour via the methodology proposed by Lee *et al.* [114].

In another approach, Oliveira *et al.* [143] proposed a methodology using depth data acquired with a Microsoft Kinect device. In the top-down view, their proposal employs two main stages; a template matching to find the fiducial points followed by the shortest path approach. Because of the tear shape of the breast, they suggested finding the shortest path in polar coordinates. Whereas

Figure 4.2: Detection of breast (inferior) contour via the methodology proposed by Lee *et al.* [114]

the nipple was not visually distinguishable in the depth image, breast peak point was selected alternatively as the center of the associated polar coordinate space. Breast peak points were found based on gradient vector field information associated with convergence filter theory. Although this was a totally automatic approach, similar to the other methodologies described, only the lower contour was found, mostly due to the lack of discontinuities in the upper part of the breast. In this way, the upper part of the breast was defined as the horizontal line connecting the two contour endpoints. The output of the aforesaid methodology is depicted in Figure 4.3.

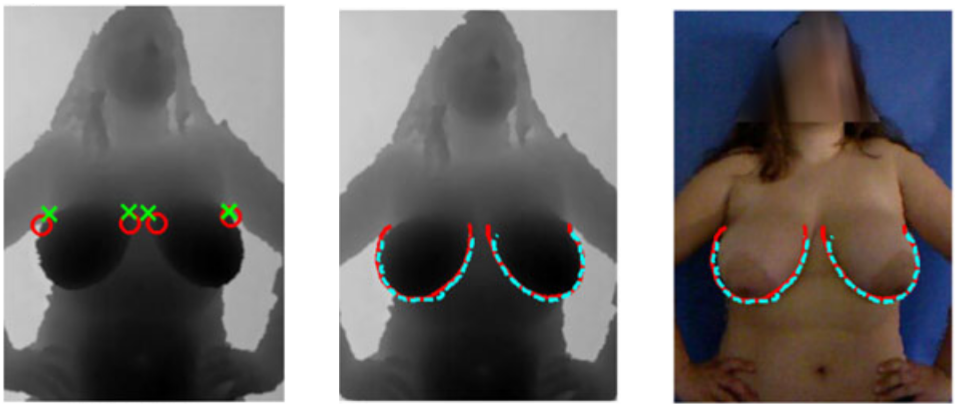

(a) (b) (c)

Figure 4.3: Automatic detection of endpoints and breast contours via RGB-D data, proposed by Oliveira *et al.* [143];(a) detected endpoints (red circles) comparing with ground truth endpoints (red cross) over the depth map; (b) visual comparison of the detected contour (dashed cyan) with ground truth (solid red) over the depth data; (c) the contours are overlaid RGB frontal image for better visualization.

Breast contour detection has also been used for segmenting breast in thermogram images. Kamath *et al.* [99] used both horizontal and vertical projection profile to locate lower and upper borders of the breast as RoI. Then the infra-mammary fold and the axilla are detected by analyzing the horizontal gradient of RoI. Visual evaluation of their method indicated that the right and left contours of breast were well detected, but the infra-mammary and superior contours were flattened due to strict upper and lower borders. Figure 4.4 depicts the obtained mask and the detected contour of the breast. Similarly to previous methodologies, their approach could not detect the upper contour; hence they considered it as a straight line connecting the two upper endpoints.

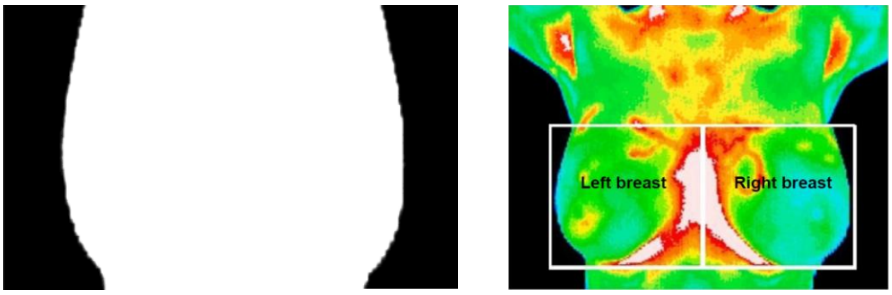

(a) (b)

Figure 4.4: The output of the approach to detect breast contour proposed by Kamath *et al.* [99]; (a) Segmented binary image of the top and bottom part of the breast, (b) Breast thermogram image with highlighted upper, lower, left, right and central borders

In another work, Núñez-Benjumea *et al.* [138] performed the detection of the breast landmarks first, and then by applying a slightly modified algorithm of Cardoso *et al.* [28], they find the infra-mammary contour. Using 2D frontal images, they benefited from different color channels to detect the jugular notch, armpit, and nipple via the changes in the illumination, and morphological operators. In Figure 4.5, their automatic detection of the prominent points are depicted in the two sets of best, and worst.

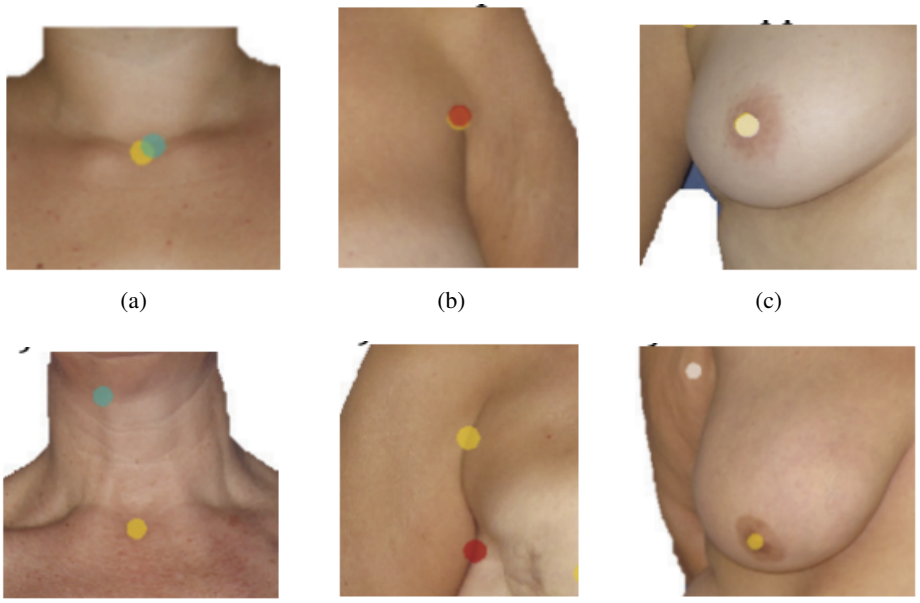

(a) (b) (c)

(d) (e) (f)

Figure 4.5: The result of automatically detecting the prominent points by the methodology proposed by Núñez-Benjumea *et al.* [138]; the first row illustrates best detection cases, and the second denotes the worst detected ones. Yellow spots are ground-truth while the colored dots are detected ones. The images are adopted from [138].

The research presented in [207] was focused on detecting inferior breast-chest contour in 3D data. They developed an algorithm based on the curvature of the model to find inferior contour candidates through points of the concave regions, where the minimum principal curvature was less than the average curvature of the model. To remove false positive candidates, a reference point was determined near to the peak point of the breast where the breast surface slopes down toward the chest wall. Possible contour points lie upon the location where the mesh curvature changes. Figure 4.6 shows the selection of points and the output of the discussed approach.

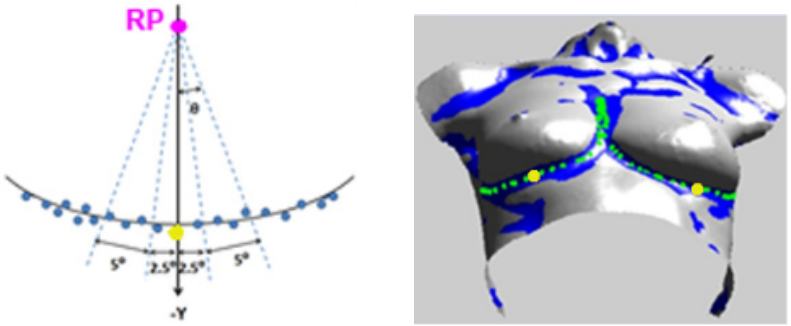

(a) (b)

Figure 4.6: The output of methodology proposed by Zhao *et al.* [207]; (a) Set of possible contour points (blue) divided into different 5-degree sector regions, (b) Set of possible contour points (blue) and detected points along the breast contours (green) displayed on the surface. The images are adopted from [207].

An advantage of their approach is that they could detect the inferior contour directly using patient 3D torso. However, the total performance of their approach is influenced by the quality of reconstruction, as in presence of noise or outlier, wrong candidates can be selected as the breast contour. Besides, their approach requires complete 3D reconstruction of the female torso. The 3D models reconstructed by the low-cost methodology discussed in Chapter 3 could not be used for the discussed methodology because of the absence of points in the inframammary region.

In summary, from the literature review, it can be concluded that existing approaches lack on automation or do not detect the correct delimitation of breast shape, mainly on the upper part of the breast contour, and also they disregard the pectoral muscle limit.

4.2 Multi-modal Breast Segmentation

Since the 3D complete breast contour (including both interior and exterior contours) are not available in registered surface data, a multi-modal scenario is required, in which the exterior contour was obtained using 3D surface models integrating the 3D reconstruction pipeline discussed in Chapter 3 (Figure 4.7(a)). The pectoral muscle information is obtained from MRI images manually annotated by experts (Figure 4.7(b)). The work of Oliveira *et al.* [143] was used as the basis

for the framework proposed in this chapter. The proposed algorithm can be implemented as a sequence of a few high-level operations, as presented in Figure 4.8.

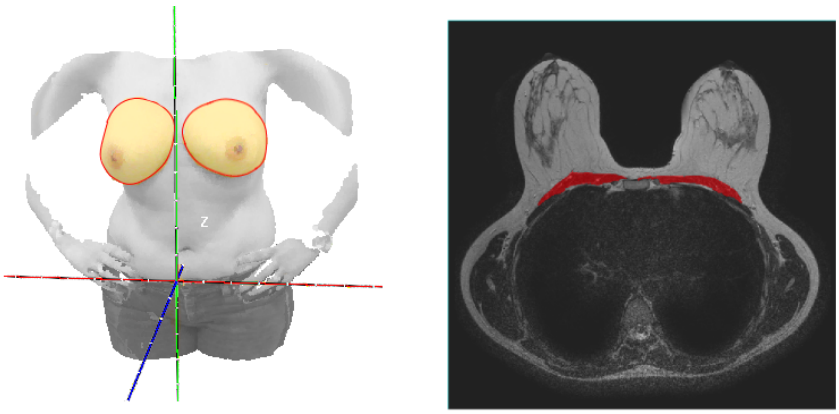

(a) (b)

Figure 4.7: Input data: (a) RGB-D reconstructed data – breast region delimited by the red contour, and (b) MRI slice data – pectoral muscle delimited by the red region

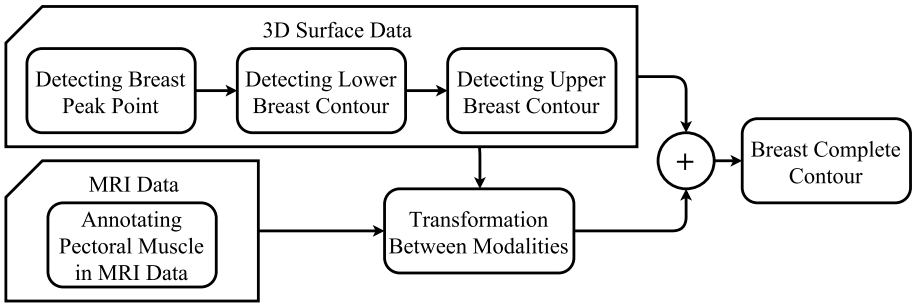

Figure 4.8: Algorithm flowchart

4.2.1 Breast Exterior Contour Segmentation

Instead of using depth data (2.5D) which has been employed by the baseline methodology [143], it is suggested to use 3D reconstructed torso. To facilitate the detection of contour, first, the 3D data is projected into the coronal plane in order to convert the depth map. To assure that the projected data (patient body) is parallel to the acquisition device, the projection is carried out with respect to the largest PCA component of data.

As in the baseline method, the breast contour is modeled as a shortest path in a graph whose nodes are the pixels of the image, and the edges are the connection of neighboring pixels. The breast contour corresponds to a low-cost path through edge pixels, with the appropriate weight function. Intuitively, breast contour is characterized by a difference in the pixel's grey-level values, which originate an edge in the image. The breast contour is approximately circular; thus, the computation is more naturally performed by adopting polar coordinates. Each column in the

polar image corresponds to the gradient along each radial line in the original space, computed using a 3-point numerical differentiation. The center of the polar coordinates is defined as *breast peak*, which corresponds to the point in the breast where disparity attains the lowest value. The typically round shape of breast leads to a distinctive pattern in the gradient vector field where the gradient diverges in all directions. The peak is detected using a Convergence Index Filter with a divergent radial vector field template. Finally, the breast contour is found by taking the endpoints as the reference, that is automatically obtained by measuring the 'strength' of vertical edges in the external boundary of the breast. This was always a drawback in the proposed methodology by [143], in this sense, a new methodology is proposed based on template matching.

Although the exact location of breast contour endpoints has not been consensually defined in the medical community, it can be assumed that the external, and internal end-points are in the vicinity of the axilla, and below the sternum, respectively. In this regard, the kernel depicted in Figure 4.9(a) has been designed in order to detect external end-point of the patient's left breast contour. The size of the kernel has been experimentally tuned to 17 pixels[1]. This is performed in a RoI delimited taken into account the position of *breast peak* point. The external end-point is defined as the topmost extremity of the response to the template matching, after applying a threshold defined as the average of candidates' intensity value. Figure 4.9(b) depicts the candidates for external endpoint. The one which is closest to the breast peak is chosen as the external endpoint (the point labeled c_5 in Figure 4.9(b)). Note that the template matching procedure can be enhanced by applying only on the breast region above the mean line of the depth map.

The internal endpoint is located on the opposite side but at the same distance of the breast vertical median plane defined by the *breast peak* point. In Figure 4.9(c), it is possible to visualize all previously mentioned details. Similarly, the detection of the external end-point in the right breast can be performed by flipping horizontally the kernel presented in Figure 4.9(a).

One of the contributions of this research is related to the definition of the upper breast contour, which to the best of our knowledge there is no other work performing this task. After detecting the lower breast contour as explained previously [143], the filter which is mathematically described in Equation 4.1 is performed. The region where upper breast contour exists is characterized as an edge-less region, thus, the use of an approach similar to the one applied to the lower breast contour would lead to a wrong detection. To solve this, the values of the cost map are rectified by element-wise multiplication in $\alpha_{r,c}$.

$$\alpha_{r,c} = \begin{cases} 1 & r - w \leq a \times c + b \leq r + w \\ 0 & otherwise \end{cases} \tag{4.1}$$

where r, c are rows and columns of cost map (in polar coordinates) respectively, and $a \times c + b$ is the line which connects the endpoints in cost map (a and b are line coefficients and c is variable in 2D coordinate). This multiplication imposes a tunnel with the initial width of $w = 1$ pixel between the end-points where the upper contour lies upon. With this approach, a more natural

[1] Note that the aforesaid size is selected for the depth map resolution equal to 640×480.

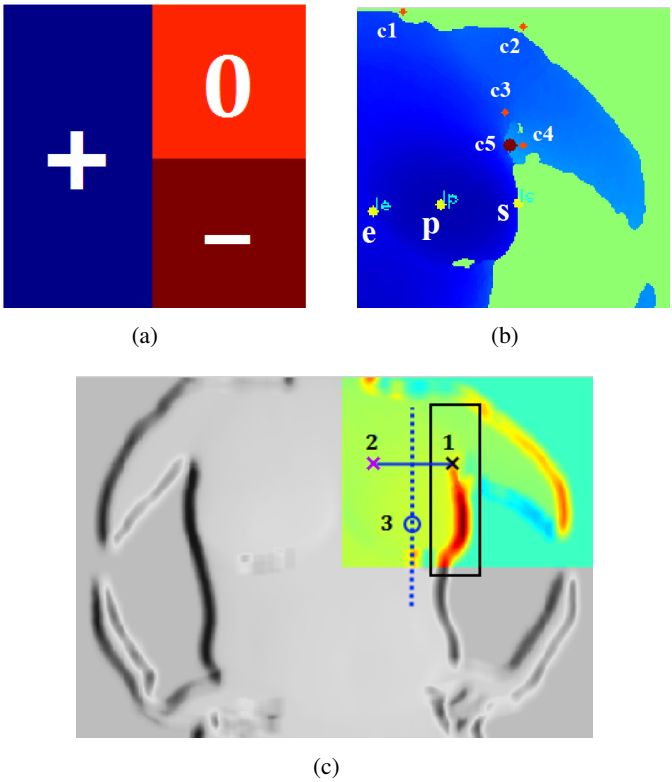

(a) (b)

(c)

Figure 4.9: (a) Suggested template for detection of left external endpoint, (b) the candidate external points $c_{1\rightarrow5}$; e and s are ending and starting point of inframammary contour; p denotes breast peak; fianlly c_5 is selected as it is closet candidate to p, (c) response of the template matching on the left breast RoI is shown colorful. The external endpoint (labeled 1, or $s_{beginning}$) is used together with breast peak point (labeled 3) to locate the internal endpoint (labeled 2, or s_{ending}).

segmented breast shape is obtained (see Figure 4.11). Once the tunnel is constructed, the upper contour is detected via finding the shortest path connecting the mentioned endpoints through the tunnel. Since the initial width of the tunnel may not be sufficient for finding the shortest path, w is increased iteratively until the upper contour is discovered.

The Cartesian and polar representation of the breast RoI (centered at breast peak point), the cost-map with the found shortest path to connect the two endpoint, and the finally the detected breast exterior contour are illustrated in Figure 4.10.

4.2.2 Breast Interior Contour Segmentation

The breast interior contour (also known as pectoral muscle,) cannot be detected from RGB-D data since it is not visible in this type of data. An option to define the pectoral muscle location is via MRI data. However, in order to combine the information from the two modalities (RGB-D and MRI) a transformation must be performed, since RGB-D is acquired in upright and MRI in the supine position. Besides the differences in scanning position, a slight side flatness is observed in

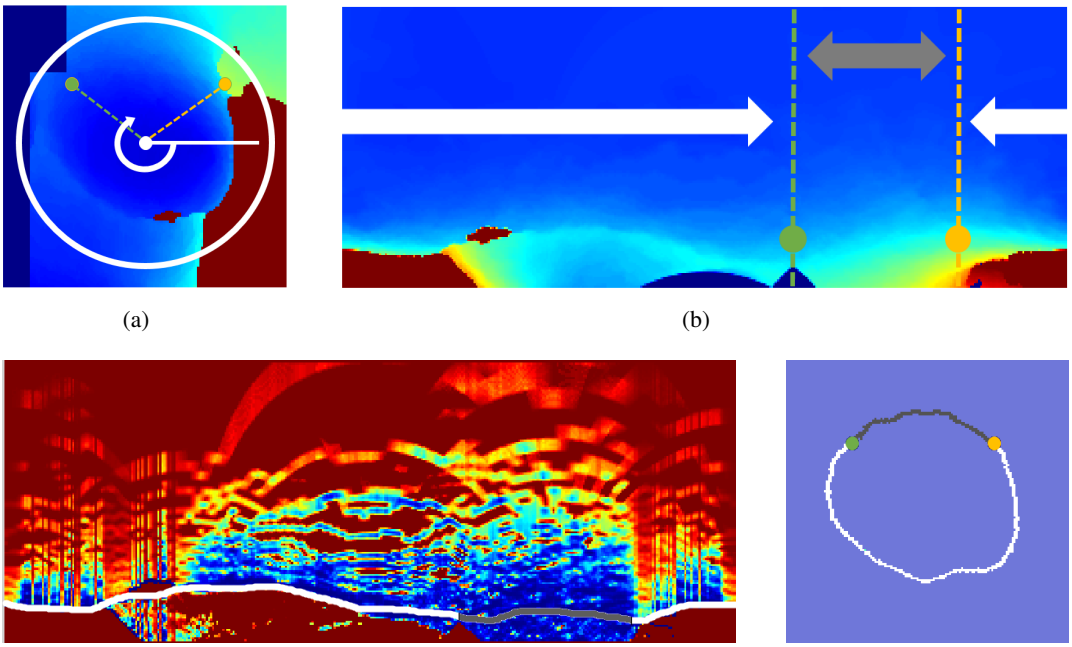

(a) (b)

(c) (d)

Figure 4.10: Visual presentation of detecting breast exterior contour; (a) the RoI containing the breast cantered at breast peak point (while circle in the), and exterior and interior endpoints (shown in yellow and green), (b) polar representation of the RoI; the regions containing the inferior and the upper contours are colored in white and gray, (c) computation of cost map, and finding the shortest path connecting the endpoints. Note that the contour is dilated for better visualization; (d) the detected contour in the Cartesian representation

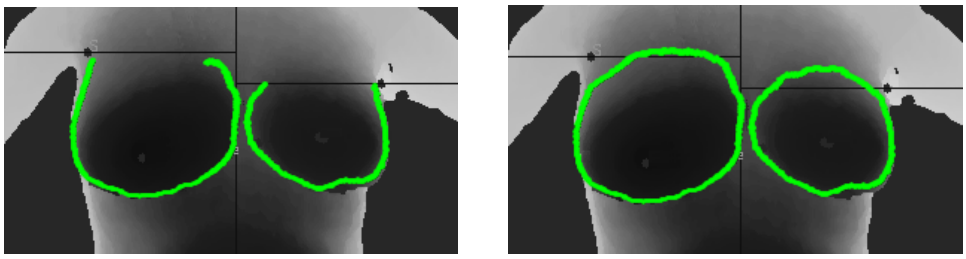

(a) (b)

Figure 4.11: Detecting breast exterior contour; (a) lower contour, and (b) lower contour together with upper contour obtained by the described procedure

MRI due to the stabilization padding and in some cases whenever breast is larger than the table's depth a considerable frontal deformation.

To simplify the problem, it is assumed that unlike the breast tissue, the pectoral muscle is not deformed, or changed its shape while the MRI is taken. Also, it should be adjudged that changing in the patient position (from upright to prone) has no effect on the rigidity of breast model. Besides, the pectoral muscle keeps its relative position with respect to the skin (sternum region) in both acquisitions. The aforementioned assumptions provide a strategy to define a framework for the

required transformation. In this way, two solutions are proposed, which require the definition of 4 fiducial points, in both data, which are assumed to be in the same locations on the patient's torso. Detection of the aforementioned fiducial points is automatically feasible through the following steps:

- Finding the value ranges of segmented breast in each dimension
- Considering 4 quadrants around the center of mass of the segmented breast
- Finding the furthest point in each quadrant to the center of mass

4.2.2.1 Fitting planes to the corresponding fiducial points

In this solution, 4 planes are fitted to the regions defined by the 4 fiducial points in the RGB-D space. These planes serve as a guide for the correct positioning of the pectoral muscle, by an iterative process. Figure 4.12(a), depicts the first and last iteration of navigating the pectoral muscle in the suggested solution.

4.2.2.2 Semi-rigid transformation of MRI data

Inspiring from the ICP methodology, this solution transforms pectoral muscle obtained from MRI data to RGB-D space in an iterative process by coarsely matching of the fiducial points. During the iterative process, the required parameters for rotation, translation, and scaling are determined, which are consecutively applied to MRI data until the average distance between transformed models in consecutive iterations becomes less than 0.1 millimeters (see Figure 4.12(b) and Figure 4.12(c)).

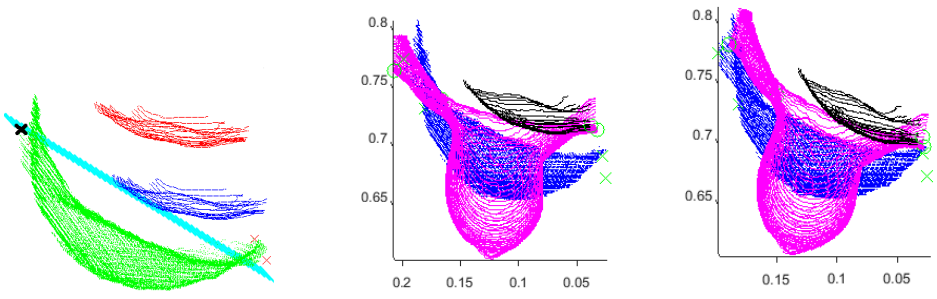

(a) (b) (c)

Figure 4.12: (a) First (red) and last (blue) iteration of navigating the pectoral muscle to the transformed fitting plane (cyan) of the fiducial points (black). (b) is MRI data before the first iteration, and (c) is after final iteration of the semi-rigid transformation of MRI data. Fiducial points of MRI and RGB-D torso are denoted by green circle and cross, respectively.

4.3 Results and Discussion

The proposed methodology is evaluated both in a quantitative and qualitative way. Ground-truth annotation was performed on depth data regarding the limitation of breast region (exterior breast contour).

4.3.1 Database

A database consisting of 32 patients was used for the evaluation. Each patient 3D reconstructed model was obtained using the methodology discussed in Chapter 3. Besides, pectoral muscle information was obtained from MRI slices manually annotated by an expert. It should be noted that the ground-truth data for breast inferior contour have been obtained using the methodology proposed in [29].

4.3.2 Exterior Breast Contour Segmentation

Evaluation is performed using the Hausdorff and the average distance between the ground-truth contour and the contour obtained from the proposed methodology (see Table 4.1). The Hausdorff distance between point sets A and B is defined as in Equation 4.2:

$$h(A,B) = \underset{a\in A}{max}\ \underset{b\in B}{min}\ \| a-b \| \tag{4.2}$$

Table 4.1: Breast contour detection error (in mm).

		Detected → Ground-truth		Ground-truth → Detected	
		Euclidean	Hausdorff	Euclidean	Hausdorff
Proposed Method	Mean (±std)	3.84 (1.41)	11.51 (4.77)	2.64 (0.95)	9.00 (3.92)
	[Min, Max]	[1.69, 7.23]	[5.45, 23.08]	[1.02, 5.54]	[3.84, 20.18]
Baseline Method	Mean (±std)	3.22 (1.97)	13.32 (10.35)	2.87 (1.88)	14.23 (9.51)
	[Min, Max]	[0.93, 17.87]	[2.91, 55.73]	[0.76, 16.24]	[2.29, 62.30]

where $\| . \|$ is the Euclidean distance. The motivation for using this metric is to represent the worst case scenario. The average error of 3.84 *mm* from detected contour to the ground-truth indicates that the exterior contour has been found in a reasonable region. Though representing lower average compared to the baseline methodology, the standard deviation for the proposed contour detection shows less deviations from the average. Mathematically, it means the detection range of the both methodologies are too near to each other.

Beside the head to head competition concerning the average Euclidean distances, the proposed method presents not only lower Hausdorff distances, but also smaller maximum and minimum range. it highlight the proposed methodology resulted in contour with less deviation from the ground-truth data, compared to the baseline methodology.

As long as the visual evaluation of inferior contour indicates a competitive detection comparing with the ground-truth, there is a small visible gap between the discovered superior contour of the manually annotated one (see Figure 4.13(a)). Although the presence of this gap influences the numerical evaluation, the detected contour is still found in the consensually accepted region that is also certified by the Hausdorff metric. Comparisons of the inferior contour with the baseline methodology ([143]) shows the same results, as both methodologies use the same approach to detect the contour.

4.3.3 Interior Breast Contour Segmentation

The lack of ground-truth for the interior contour makes it possible to perform only a qualitative evaluation, through the visualization of pectoral muscle position against the location of the breast. It has been shown that the pectoral muscle is located in an accepted anatomical location toward both the breast tissue and sternum bone, mainly using the second approach (Semi-rigid transformation of MRI data). Figure. 4.13(b), Figure 4.13(c) and Figure 4.13(d) depict the visual output for one of the patients of the database.

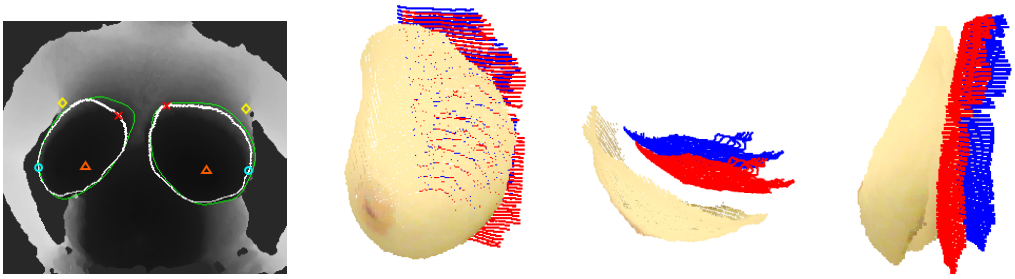

(a) (b) (c) (d)

Figure 4.13: (a) Visual evaluation of contour detection; detected contour (white) ,and ground-truth (green), breast peaks (triangle), infra-mammary endpoint (blue circle), internal endpoints (red cross), and external endpoints (yellow diamond) (b) perspective view, (c) top view, and (d) lateral view of pectoral muscle transforming suggestions; the suggestion powered by fitting planes is shown in blue while the output of semi-rigid transformation solution is shown in red.

4.4 Summary

In this chapter, an automatic methodology has been proposed for the complete segmentation of breast region using a multi-modal approach. The contributions are related to the correct delimitation of the breast region including the upper part and the inclusion of the interior breast contour (pectoral muscle). Quantitative and visual inspections of the results indicate a good performance and robustness for a wide variety of patients. Future work will focus on the use of these results incorporated in the planning tool, which will permit the improvement of the interaction between

patients and physicians, allowing patients participate in the decision process and be more informed about the consequences of the treatment.

Chapter 5

Parametric Modeling*

In Chapter 3, a low-cost methodology to reconstruct 3D models of patient torso was studied, and in the following investigations (Chapter 4), a new automatic approach was proposed to segment breast completely, including exterior contour (corresponding to frontal surface), and the interior one (that is pectoral muscle). Considering the objective of a planning tool, the reconstructed 3D breast must be presented such that it can be interactively deformed. The aforesaid aim is achievable if the breast model is represented as a mathematical model which is suitable for manipulation. The procedure in which breast model is represented as a mathematical model is called parametric modeling.

This chapter begins with reviewing current state-of-the-art methodologies to generate parametric models from 3D input data. Then, concentrating on Free Form Deformation (FFD) as our baseline methodology, an investigation will be conducted to create deformable models from input data. Finally, confirmed by a quantitative analysis, we proposed two simplified versions of FFD to increase model similarity to the input data while decreasing required fitting time.

5.1 A Brief Study of State-of-the-Art Methodologies

Parametric modeling is the process of transforming specific data to mathematical models; however, in the mathematical scope, it is called fitting instead of modeling. In the early 1990s, Terzoloulos and Metaxas [188] proposed a methodology to fit complex 3D shapes via dynamic models which can be deformed either locally or globally. They developed a new family of modeling primitives to cover the following requirements of fitting: Free-Form and parametric geometry, local and global deformations, physics and dynamics of the objects, applied forces and internal tensions, and finally determining details and abstractions of the input data. Besides the experiments using both 2D and 3D data, they stated the benefits of using superquadrics to satisfy the requirements of fitting, and they reported to obtain satisfactory results to deal with conflicting demands of shape reconstruction and shape recognition. Figure 5.1 depicts the output of their proposed model, fitted to the sparsely sampled 3D data from upper hemisphere of an egg.

*Some parts of this Chapter appeared in [210]

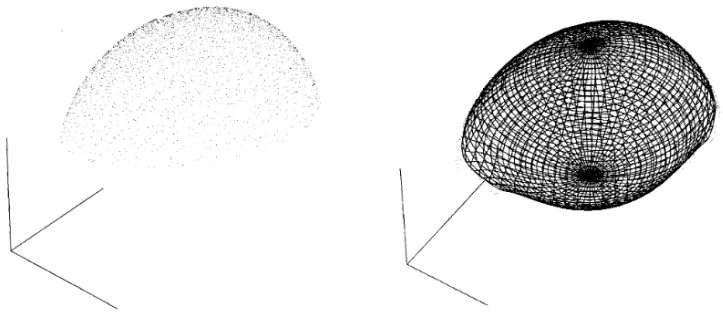

(a) (b)

Figure 5.1: Illustration of the parametric model fitted to the sparsely sampled 3D data from upper hemisphere of an egg; (a) the scattered points, (b) and the fitted model. The images are adopted from [188].

The methodology proposed by Chen *et al.* [38] to model the breast was equipped with a parametric model that used a superquadric surface as the primitive shape. While the primitive function defined the breast general shape, features to deform the whole shape, such as gravity (resembling ptosis) are applied via additive or multiplicative matrices to generate a new shape. Briefly reviewed, breast shape was defined via 5 parameters, 6 parameters were used for rigid transformation (rotation and translation) of the model on the patient's torso, and finally, 12 parameters were used to control the deformations. All 23 parameters were fitted to the manually annotated breast data obtained by a 3D scanner, using the methodology of Terzoloulos and Metaxas [188]. Figure 5.2 shows the frontal and lateral view of the primitive model they employed in their work.

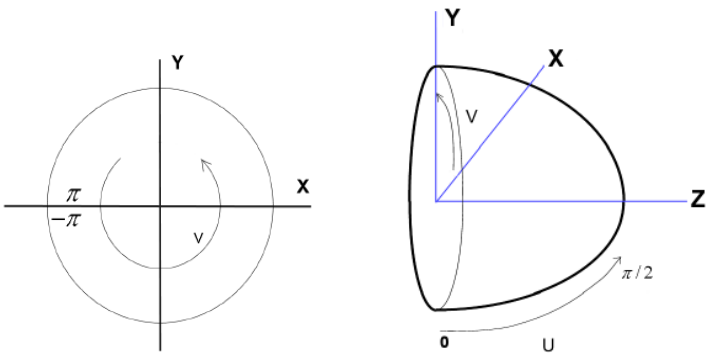

(a) (b)

Figure 5.2: The primitive shape of a breast in (a) frontal view, and (b) lateral view, proposed by Chen *et al.* [38].

Later in 2014, Pernes *et al.* [149] developed a methodology on top of Chen's suggestion to pull the implicitly defined parametric model towards the input data points by computing attracting forces exerted on the model points, using Gauss-Newton iterative fitting method. The conducted

research targeted to find optimum values for Chen's model parameters to decrease the Euclidean distances between the parametric model, and the input data. They evaluated their methodology by using two sets of breast data, obtaining 3D segmented breasts from a high precision 3D scanner, and 3D reconstructed breasts from a low-cost depth sensor, Microsoft Kinect. Overall evaluations reported a distance error around 1 *cm* and 2.8 *cm* for data obtained by a 3D scanner, and Kinect respectively. Figure 5.3 illustrate the input data and the fitted model generated by the proposed methodology.

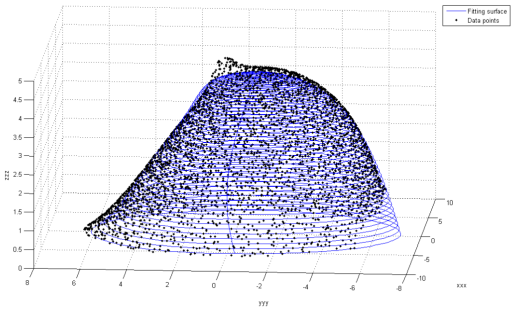

Figure 5.3: The parametric model (blue lines) of the input breast data (black points) using the methodology proposed by Pernes *et al.*. The breast data is obtained by a precise 3D scanner. The images are adopted from [149].

Considering the application of parametric modeling of the human body, Weiss *et al.* [204] proposed a novel methodology to reconstruct human shape from noisy monocular range data. Combining low resolution image silhouettes with coarse range data obtained by a depth sensor, they generated a estimated parametric model for the body, and then by fitting the parameters of SCAPE (Shape Completion and Animation for PEople [9]) predefined models to the estimated silhouettes, they could accurately find human pose, and generate the body parametric model. In their work, models were used with 15 body parts connected in a kinematic tree with 3 degrees of freedom between each part. The captured data, the processed point clouds, the fitted parametric model, and finally the recovered body in new pose are depicted in Figure 5.4(a), Figure 5.4(b), Figure 5.4(c), and Figure 5.4(d), respectively.

Similarly, Aitpayev and Gaber [3] used predefined models to reconstruct human avatar (male, female and child), using three types of avatars including male, female and child equipped with additional scaling parameters to generate outcomes regardless the scale of predefined models.

The method proposed by Ruiz *et al.* [163] is an example that creates a fitted surface to the input data by satisfying the Nyquist-Shannon criteria. Then, the minimization problem (which is defined based on the residual distance between the surface and the input data) is solved by the Gauss-Newton iterative method to approach the surface to the data iteratively.

In a different application using bi-planar CT data, Aubert *et al.* [12] proposed a methodology to reconstruct 3D rib cage employing a statistical parametric model approach. In this way, they defined 3 simplified parametric models for rib cage, rib mid-line, and rib surface. The mid-line of each rib was modeled by connecting the center of 30 ellipsoids estimating the cross-section of

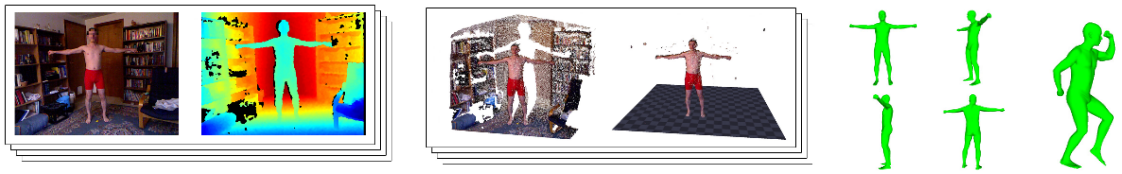

(a) (b) (c) (d)

Figure 5.4: The pipeline of generating human body parametric model by fitting the parametric models of SCAPE dataset to the point clouds obtained from Kinect; (a) shows the RGB-D captured data of 4 frames, (b) illustrates the point cloud generated from RGB-D data, (c) denoted the fitted model to acquired data in loaded 4 frames, and (d) shows the obtained parametric model in different pose. The images are adopted from [204].

each rib, following a manual correction stage to improve the matching between the found model and the data. In a hierarchical order, the ellipsoids represented both the model of rib surface, and the rib mid-line, and finally, the whole rib cage was modeled using the estimated rib mid-lines.

As a summary, the aforesaid methodologies performed the fitting via two main solutions; physical and non-physical. Concerning the physical solution, the fitting is pursued by optimizing only the model's parameters in order to approach the parametric models to the input data. However, via non-physical solutions, additional parameters which were not originally in the definition of the initial model, are considered take the fitting into account. The reviewed methods in [38, 149, 188] were proposed based on implicit solutions, while application of FFD in the research carried out by Bardinet *et al.* [16] can be categorized as a non-physical solution. In the following, more details of the FFD approach, that is the basis of this work will be presented, using the work of Bardinet *et al.* [16].

5.1.1 Free-Form Deformation

The methodology proposed in [16] used an algorithm to perform parametric fitting in two steps. Starting from an initial model, they tried to find the best parameters to fit it to the data in the first step. Then, they added a set of points to deform the fitted initial model and approach it the input data. In this regard, they reformulated the fitting problem as a minimization issue in which the control points are linked locally to the fitted model and then they are moved to minimize the distance between the fitted model and the input data.

Having a brief review of the mathematical properties of superellipsoid, Bardinet *et al.* proposed to use it as the initial model. With 5 parameters, superellipsoid can generate a variety of geometrical shape, as they are illustrated in Figure 5.5. They selected superellipsoid since they wanted to model a convex object which resembled the chosen initial model.

Within the procedure of the two-step fitting, first, they fitted a superellipsoid to input data by changing its parameters of in order to minimize the Euclidean distance (also called distance error)

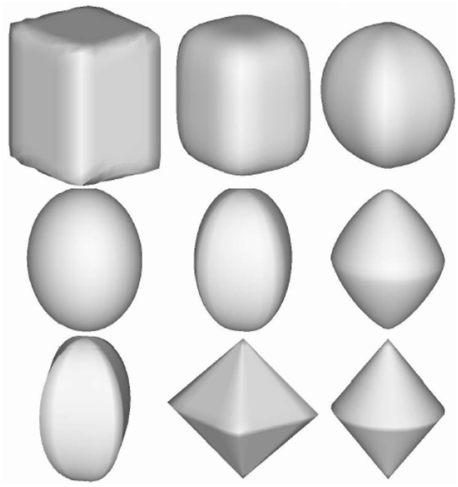

Figure 5.5: Examples of the shapes generated from superquadrics. The images are adopted from [16].

between the input data and the initial model. The second step was proceeded by initiating a 3D parallelepipedic grid of points, called grid of control points, that surrounded the fitted superellipsoid (Figure 5.6).

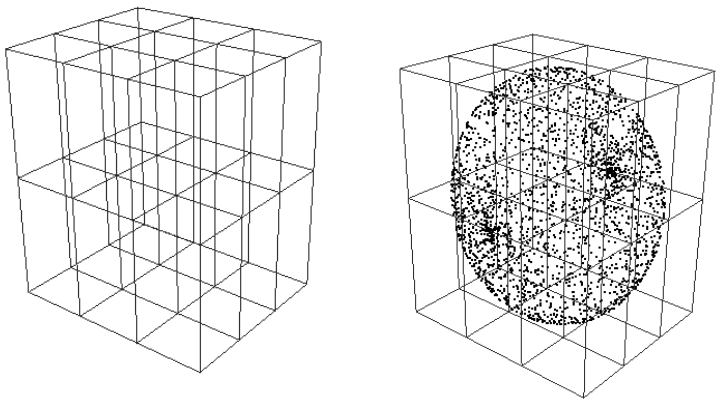

(a) (b)

Figure 5.6: Illustration of (a) the grid of control points, and (b) the initial model

The dimensions and orientation of the grid are defined by radial parameters of the superellipsoid. Containing $(l+1).(m+1).(n+1)$ points, the grid is linked to the fitted superellipsoid using a tensor product of tri-variants Bernstein's polynomials:

$$X = \sum_{i=0}^{l} \sum_{j=0}^{m} \sum_{k=0}^{n} C_l^i C_m^j C_n^k (1-s)^{l-i} s^i (1-t)^{m-j} t^j .(1-u)^{n-k} u^k P_{ijk} \tag{5.1}$$

The parametric model is defined as X, while P is a matrix containing the points of the control

grid. Besides, s, t, and u are used to denote local coordinate of each model point regarding its corresponding control point in continuous domain, and m, n, and l are the number of control points in each dimension. Compacting the summations, Equation 5.1 can be rewritten, as:

$$X = BP \tag{5.2}$$

X is a matrix containing the points of the deformed model with the size of $NP \times 3$, P is a matrix including the coordinate of the control points with size of $NC \times 3$ where $NC = (m+1) \times (n+1) \times (l+1)$, and finally B is called the deformation matrix with size of $NP \times NC$. Considering δX as the displacement field between input data and superellipsoid, Equation 5.2 can be rewritten regarding to linear equation system:

$$\delta X = B\delta P \tag{5.3}$$

The superellipsoid is then deformed through relocating the control points of the grid. Within iterative steps, the points on the superellipsoid are approached to the input data by solving the following minimization equation:

$$min_p||BP - X||^2 := min_{\delta P}||B\delta P - \delta X||^2 + \alpha \sum_{j=1}^{NP} \sum_{j'} ||P_j - P_{j'}||^2 \tag{5.4}$$

In the second term, j' corresponds to the neighbors of P in the position of j and NP stands for the number of control points. In other words, the second term is an internal energy corresponding to the insertion of zero-length spring between control points, that is being regularized by the weight of α. The equation can be solved using Singular Value Decomposition (SVD) of the matrix B.

Visual evaluation shown in Figure 5.7, as well as the numerical evaluations certifies the fitting. Evaluation of required fitting time indicates that the total procedure can be performed in a reasonable time, considering a cube of control points consisting of 64 points. Increasing the number of control points will indeed minimize the residual distance error, but increases the computation complexity, and the required time.

Although the discussed methodology using superellipsoid as initial model generated medically expected parametric models, the choice of the initial model can influence the fitting outcomes. As an instance, using superellipsoid is not recommended for data that represent concavities. In the following section, a detailed investigation will be conducted targeting the use of different initial models in generating parametric models for breast data.

5.2 Moving Towards Better and Faster Breast Fitting using FFD

A preliminary analysis of the FFD approach (Section 5.1.1) on 3D breast data was performed and the result is depicted in Figure 5.8. Deep investigation into the generated model reveals the drawback of using superellipsoid for a convex-concave 3D model of a breast (models with one

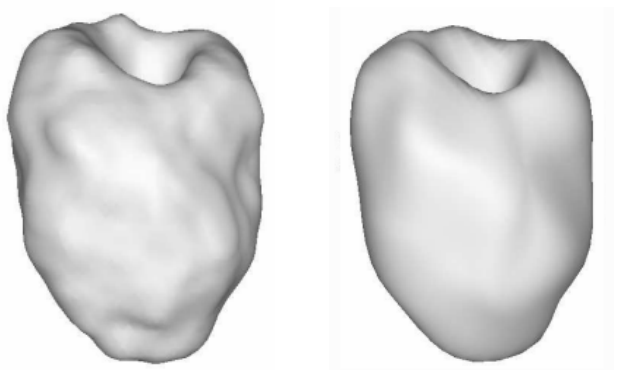

(a) (b)

Figure 5.7: The parametric model generated for ventricle data; (a) input ventricle model, (b) generated parametric model from Bardinet *et al.* [16]

side open, and the other side closed). An issue which is called Redundant Bent Layer (RBL) affected the performance of modeling negatively by increasing distance amongst the model and input data. The misalignments of the RBL points (depicted in Figure 5.8(b)) is the main reason for the decrease in the similarity between the parametric model and input data. RBL occurs when both closed sides of the initial model (both hemispheres of the fitted superellipsoid) are pulled to the closed side of breast data. Since the control points are arranged in a 3D formation, the two pulled sides of the initial model cannot be overlaid completely. Therefore, a gap is imposed between two sides of the deformed model. This gap is responsible for producing wrong fitted surface which increases the distance between parametric model and input data. In order to eliminate the RBL on the parametric model, two solutions can be taken into consideration by modifying either the initial model or the arrangement of the control points.

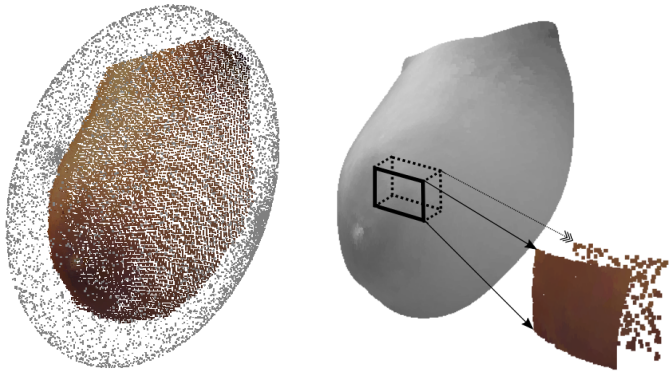

(a) (b)

Figure 5.8: Generating parametric model of a breast using superellipsoid proposed as the initial model; (a) the input data and the initial superellipsoid, (b) the fitted superellipsoid. The breast surface consists of two layers; a frontal layer and an RBL which is located in the back.

5.2.1 Modifying the Initial Model

The Achilles heel of the RBL is the definition of the initial model; therefore, replacing it with an open-sided object could overcome the issue. Two initial models are proposed in this research: a finite boundary plane and a superquadric model based on a superparaboloid similar to the one proposed in [149]. Figure 5.9 illustrates the proposed initial models.

The first solution suggests in using a finite boundary plane to fulfills both the requirements of using an open-sidedness and flexibility (in any direction) whilst the second solution suggests using a superparaboloid which was previously introduced in [149]. It not only aims to satisfy the requirement of open-sidedness of the initial model but also performs the fitting process with fewer iterations, since the primitive shape is similar to the objects (breast) to fit. Finally, it is recommended to set up both suggested initial models to be orthogonal to the largest principle direction of data. This assures that the model is initiated in a correct place where can overlay the input data completely. For this purpose, we used a PCA-based approach.

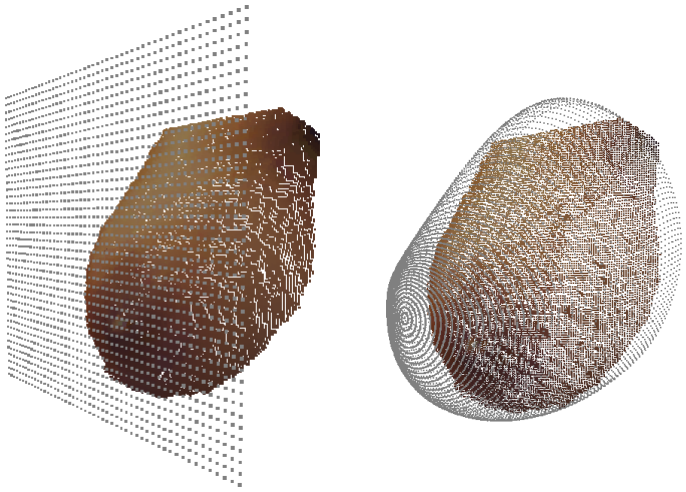

(a) (b)

Figure 5.9: The proposed initial models: (a) plane, (b) superparaboloid

5.2.2 Modifying the Arrangement of Control Points

Previously discussed, the FFD carries out the deformation of initial model by relocating the control points. In [16], it was suggested to use control points arranged in a 3D grid. As discussed before, referring to an open-side breast data, the control points located in the open-side of the model provide a circumstance in which RBL has emerged. Additionally, their participation in the calculating new location of model points imposes additional computation (and time) costs to the algorithm. Therefore, we propose to remove ineffective control points by reducing the dimensions of the control grid from 3D to 2D.

Dimension reduction should be carried out with regard to the presentation of input data. In other words, the dimension in which less data is presented can be a suitable candidate to be removed. Common methodologies to perform PCA can lead to obtaining the best removal candidate. Assuming the third dimension as the candidate of removal, the proposed dimension reduction of control points simplifies the nested summations used to relocate control points in Equation 5.1:

$$X_{new} = \sum_{i=0}^{l} \sum_{j=0}^{m} C_l^i C_m^j (1-s)^{l-i} s^i (1-t)^{m-j} t^j P_{ij} \tag{5.5}$$

X_{new} denotes the points of the parametric model. The fewer control points are considered in the computation, less time for fitting is required. Figure 5.10 shows the difference between a 3D grid of control points (originally suggested in [16]) and proposed 2D grid.

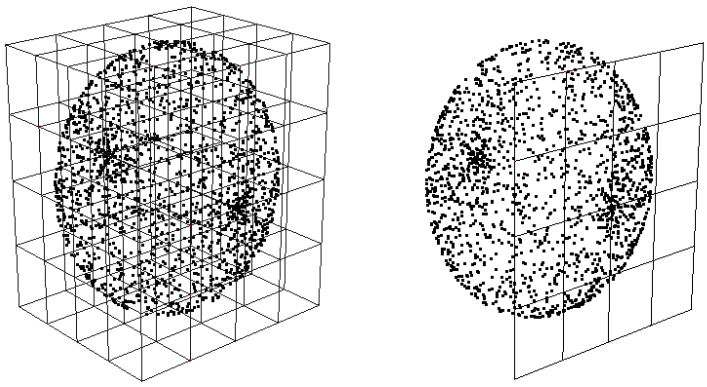

(a) (b)

Figure 5.10: (a) 3D cube of control points, (b) 2D grid of control points with the initial model of superellipsoid; the dimension reduction has been taken place by PCA to find the one which represents fewer data.

5.3 Implementation and Results

The original methodology discussed in [16] together with proposed methodologies were implemented using C++ and Mathworks MATLAB R2015a respectively, and evaluated on a 3.40 GHz machine equipped with 8 GB of memory.

The iterative modality of the studied algorithms requires defining a stop criterion. Such criterion is defined in relation to the Euclidean distance between the models being generated in every two consecutive steps. Furthermore, as far as the average distance between two consecutive generated model exceeds 1.50*mm*, the algorithm continues iterative fitting.

Two metrics are considered for the evaluation of the explained methodologies; distance error and computation time. Distance error stands for the average of Euclidean distance between the input data and the generated parametric model. Not only Euclidean, but also Hausdorff distance

is calculated. The smaller the distance error is, the more similar the two sets will be. Besides, the computation time is also a key advantage in comparisons. Aligned to the expectations, faster methodologies are more preferable.

The evaluated dataset includes 70 breast models. Each 3D model in the dataset was obtained by scanning a patient with Microsoft Kinect and reconstruct via the 3D reconstruction algorithm proposed in Chapter 3. Table 5.1 presents the results obtained by the different methodologies in terms of average fitting errors (Euclidean and Hausdorff) together with standard deviation. It is important to notice that bi-directional distances (from model to data and from data to model) are reported since there might be differences in the number of points between the two comparing pointclouds. Also, the average number of required iterations to reach to stop criterion are reported. Inasmuch as superparaboloid methodologies have been implemented in a different compiler, time comparison cannot lead to mere deduction; however, a comparison can be carried out with respect to the number of iterations, since it is compiler independent. Besides the numerical analysis, visual comparisons are depicted in Figure 5.11.

Table 5.1: Reported results to compare proposed methodologies of FFD

	Methodology		Euclidean (M→GT) (mm)	Euclidean (GT→M) (mm)	Hausdorff (M→GT) (mm)	Hausdorff (GT→M) (mm)	Time (s)	Mean No. Itr
MATLAB	Superparaboloid + FFD (3D)	μ	1.57	2.28	11.02	26.28	1955	**3.60**
		σ	0.25	0.48	3.93	7.84	273	
	Superparaboloid + FFD (2D)	μ	1.60	3.03	7.14	29.62	324	10.42
		σ	0.25	0.81	1.76	7.62	41	
C++	Superellipsoid + FFD (3D)	μ	**1.31**	1.70	7.63	13.43	3001	10.42
		σ	0.08	0.25	1.52	4.83	1445	
	Superellipsoid + FFD (2D)	μ	**1.21**	2.71	5.62	24.27	64	5.33
		σ	0.11	0.52	1.33	7.49	21	
	Plane (2D) + FFD (2D)	μ	**1.25**	2.78	6.27	23.67	45	**3.83**
		σ	0.11	0.52	1.71	8.23	24	

The smallest average Euclidean error from parametric model to input data was 1.21*mm* which is obtained by the superellipsoid and a 2D FFD. The methodology of using a plane with a 2D FFD takes the second rank with an average Euclidean error of 1.25 *mm*, and finally, the superellipsoid with 3D FFD stands in the third rank by obtaining an error of 1.31*mm*. With respect to the error from input data to model, the smallest distance error was obtained by using the methodology of superellipsoid deformed by a 3D FFD with an error of 1.70 *mm*. And in the following rank, superparaboloid deformed by 3D FFD stands with the error of 2.28 *mm*. The third rank belongs to the methodology which uses a superellipsoid and a 2D FFD presenting an error of 2.71 *mm*. A brief look at the Table 5.1 and the requirements of the fitting stage reveal that the methodologies based on FFD superellipsoid and plane generate more precise parametric models than superparaboloid. Considering Model to ground-truth Euclidean distance, the suggested improvement of the 2D arrangement of control points surpasses another method since it eliminates the RBL phenomena.

With a small gap, the methodology of using the plane with 2D FFD stands in the second rank since using the plane as the initial model cannot present the boundaries of breast better than superellipsoid. On the other hand, methodologies using superparaboloid generate parametric models with more distance errors. Although using predefined initial model can accelerate the convergence, the shrinkage of the parametric model in the boundaries emerges additional distance error. Such shrinkage is visible in generated models depicted in Figure 5.11(e) and Figure 5.11(f).

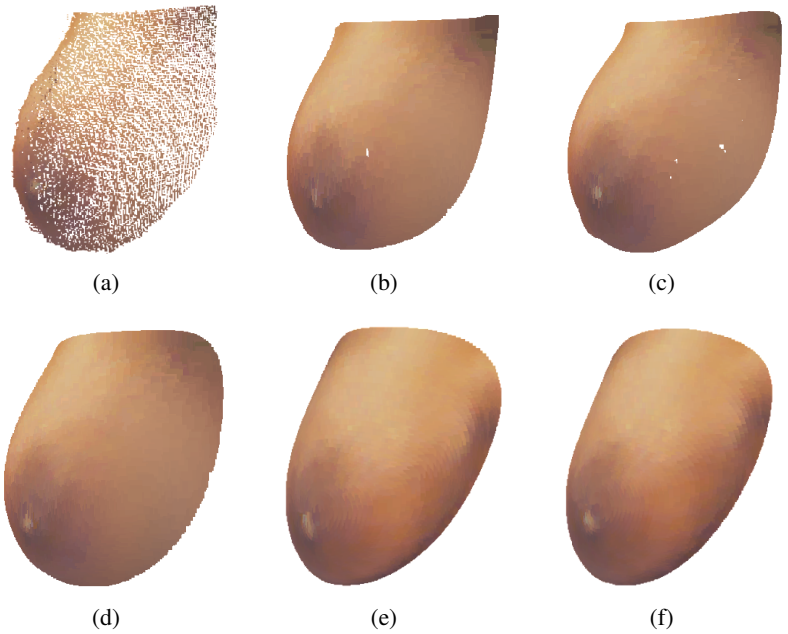

Figure 5.11: Visual comparison of performed experiments on same input data; (a) original patient breast; (b) Plane + FFD (2D); (c) Superellipsoid + FFD (2D); (d) Superellipsoid + FFD (3D); (e) Superparaboloid + FFD (2D); (f) Superparaboloid + FFD (3D)

Also, investigating the arrangement of the control points admits the advantage of using 2D grid instead of 3D. Eliminating excess control points leads to both the increase in the efficiency of the remained control points and decreasing time complexity of the algorithm. Additionally, the proposed improvements demonstrated smaller error in comparison to the original methodology and also in fitting time.

5.4 Summary

Putting all together, parametric modeling is a technique which converts input data into a mathematical model. Mentioning the importance of a parametric modeling in a planning tool, methodologies of FFD have been studied and two improvements were proposed to enhance it; improvement of the initial model and modification of control points arrangements. Quantitative analysis indicated the proposed approach improves the performance of FFD methodology by decreasing the average distance error. Visual analysis accompanied with quantitative results indicate that the proposed

methodologies suffer from model shrinkage in the boundaries. Since the mentioned shrinkage is responsible for the increase of the distance between input data and model, possible future work will be concentrated to generate parametric models with less shrinkage which leads to less distance error.

Chapter 6

Prediction of Breast Shape after BCS*

Breast cancer treatments can have a negative impact on the breast aesthetics, in the case when the surgical procedure is intended to intersect the tumor. For many years, mastectomy was the only surgical option, but more recently Breast Conserving Surgery (BCS) has been promoted as a reliable alternative to treat cancer while preserving most part of the breast. However, as it was discussed in Chapter 1, there is still a significant number of BCS intervened patients who are unpleasant with the result of the treatment, which leads to self-image issues and emotional overloads. Therefore, surgeons recognize the value of a tool to predict the breast shape after BCS more and more each day; but, the creation of such models is a challenging task due to the deformable characteristics of the breast, the lack of landmarks to define its shape and the complex nature of the deformations imposed by the surgery.

In this chapter, we propose a methodology for predicting the imposed deformation after BCS by using Machine Learning (ML) techniques. Nonetheless, there is no appropriate dataset containing breast data before and after surgery in order to train a learning model. Therefore, an in-house semi-synthetic dataset is proposed to fulfill the requirement of this research.

6.1 A Review of Current Planning Methodologies for Breast Surgeries

By reviewing literature, it is revealed that methodologies to predict/simulate breast deformation are specifically designed for different applications. A detailed investigation of the methodologies targeting breast shape simulation/prediction has been done through Chapter 2. Here, it is aimed to draw the reader's attention toward the methodologies based on biomechanical simulation.

Rajagopal *et al.* [154] proposed the Lagrangian iterative scheme to evaluates a 3D model in the unloaded state, with the purpose of fitting MRI 3D data on the 3D surface model. They formulated a solution based on a standard forward finite deformation approach, to find the reference state. In this approach, an estimated reference state was stressed with force vector and the residual of the unbalanced forces was evaluated repeatedly until convergence is achieved. They finally evaluated

*Some parts of this Chapter appeared in [59, 209]

their FE methodology with an analytic solution and verified their predictions with experimental results on phantom geometries. Figure 6.1 depicts the models before and after fitting with Root Mean Square (RMS) error of 1.18 *mm*.

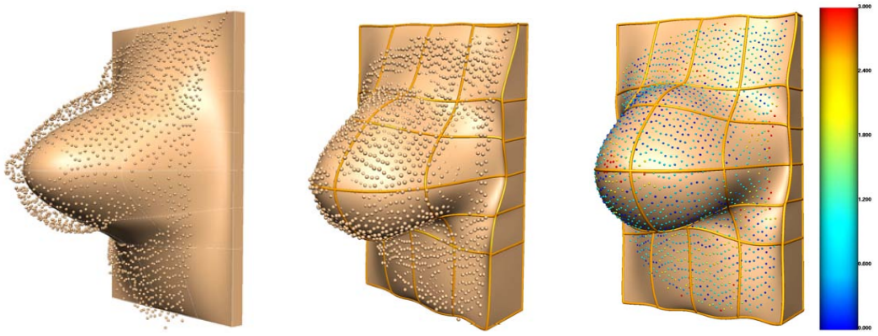

(a) (b) (c)

Figure 6.1: Fitting results from the work by Rajagopal *et al.* [154]. (a) and (b) showing the mesh before and after fitting the MRI data to the 3D surface model. (c) final fitting with an error of 1.18 *mm* reported for the current model. The colored points represent the skin 3D surface model showing the individual error magnitude, in millimeters.

The study performed by Garbey *et al.* [66] suggested a multi-scale modeling of breast deformation prediction after tumor resection. In that work, they joined FE biomechanical modeling and cellular automata, to simulate the breast shape outcome not only for minutes after the surgery but also in long-term wound healing. Their suggested methodology was further used applied in the research by Garbey *et al.* [67], that has been discussed in Chapter 2. Their proposed workflow is demonstrated in Figure 6.2.

Eiben *et al.* [57] studied breast pose estimation via biomechanical modeling in order to register breast MRI models captured in different poses. Considering breast shape being acquired in two different positions (prone and supine), they proposed to use patient-specific biomechanical models to provide an initial deformation of the breast. By removing the gravity stress, they obtained breast biomechanical model in zero gravity in both positions, and then they performed the required registration between the two mentioned position, as it is depicted in Figure 6.3.

They finally evaluated the registration by annotating some landmarks and finding the drift between the known landmarks in the registered model. By reporting the average distance less than 5.7 *mm*, they concluded that the proposed methodology performed in a medically accepted error range.

Aiming to combine MRI data with 3D surface data, Eder *et al.* [56] proposed a similar iterative approach to obtain the unloaded state from a breast in prone position acquired from MRI data. To overcome the challenges of different patient poses, they had to convert the MRI data from prone to upright and then combine it with 3D surface data. In their research, they applied the force vector that arises when the re-loaded configuration is displaced to the ground-truth position, instead of using the displacement vectors directly to update the zero gravity state estimate. These vectors

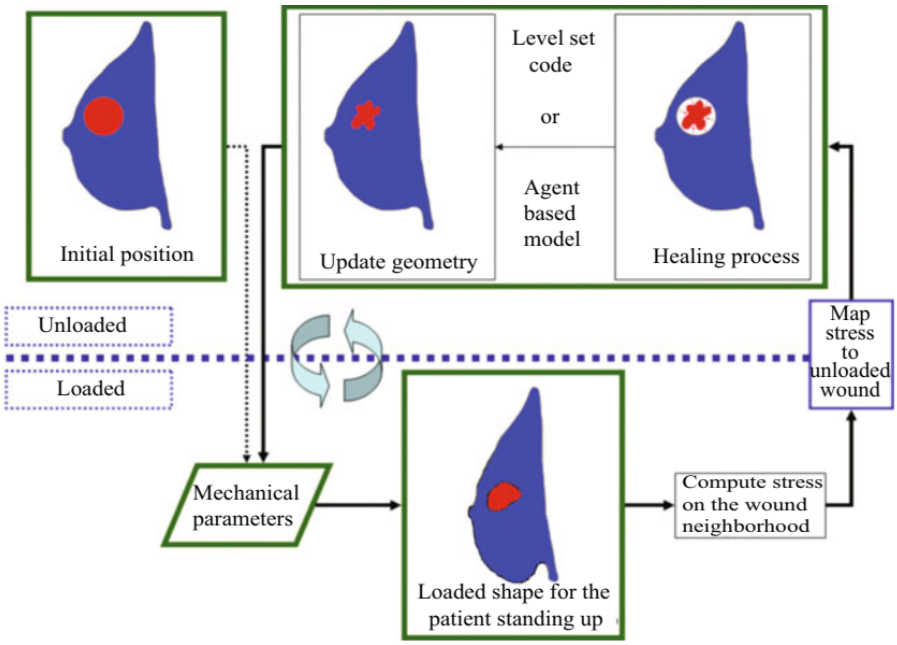

Figure 6.2: The proposed workflow used in the research by Garbey *et al.* [66]

were then used in the unloaded position to calculate the corresponding node update. Figure 6.4 shows the pipeline they followed to convert patient poses to each other.

In another attempt, Patete *et al.* [147] modeled breast tissue deformation via a mass-spring approach, where they initially estimated the spring's rest length and stiffness. Further simulations were performed to deform the uncompressed breast model to reach the real compressed one. Figure 6.5 illustrates the outcomes of their methodology.

In a very recent study by Martínez-Martínez *et al.* [127], ML techniques were employed to predict the deformation of the breast through compressing it by two parallel plates. Through the simulation stage, they provided the input data from 10 real breasts, and the used FEM was configured with 4 types of material, including adipose, fibroglandular, muscle and tumor tissue. For prediction, the performance of 3 regression models was investigated: decision tree, extremely randomized trees, and random forest. The evaluation was carried out due to the mean Euclidean distance between the predicted breasts and the data simulated by the FEM, indicating that the extremely randomized trees outperformed the other two models with an error less than 2 *mm* in average. The visual output of FEM before and after the simulation is demonstrated in Figure 6.6.

In particular, the work of Vavourakis *et al.* [197] is highlighted which proposed a 3D surgical simulator to predict a patient-specific outcome after BCS. This framework predicts the breast shape after surgery taking the wound healing process into account. The simulator relies on a coupled multi-scale FE numerical procedure to solve two mathematical models: a biochemical model for wound healing and angiogenesis, and a biomechanical model for soft tissues and poses estimation. The first considers both wound healing biochemical process and the formation of new blood vessels, while the second predicts the breast shape as a function of the breast tissues mass density and the body force vector. The final shape of the breast is then predicted as an integration

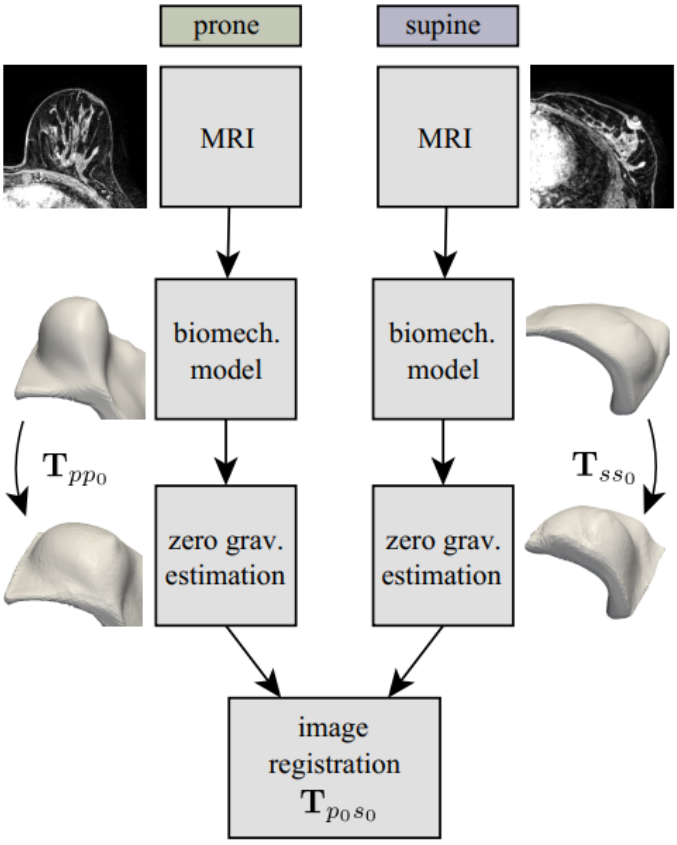

Figure 6.3: Overview of the workflow proposed by Eiben *et al.* [57] to align prone and supine models. They employed biomechanical simulation followed by image registration.

of both models. More details will be discussed either Chapter 2.

6.2 Dataset for Learning Breast Healing Deformations

Historically, several factors have been identified to have a significant impact on the shape deformations caused by BCS, which can be grouped into the patient, the tumor, and the surgery-related factors [33]. Hence, any model designed to predict breast deformations should take into account the influence of those characteristics. Since the main goal of this study is to learn the influence of different combinations of those factors, a large number of 3D data of patient's breast before and after surgery ($\approx$ 1 year) is mandatory. However, there is no available dataset that satisfies such requirements. As consequence, an in-house dataset was constructed, taking advantage of available MRI data, acquired before surgery and having some anatomical structures of interest annotated. Due to the lack of post-surgery data, the wound healing process was simulated using the BCS simulator proposed by Vavourakis *et al.* [197], which made the source code available for the scientific community.

In this Section the framework designed by Vavourakis *et al.* [197] used to simulate BCS results is explained and the construction of the dataset used to develop the proposed methodology is

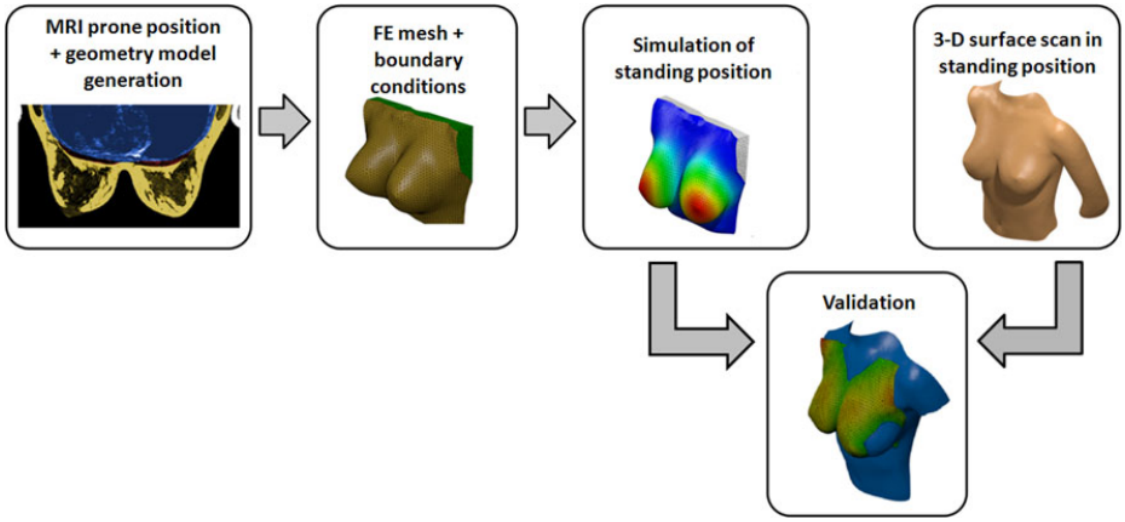

Figure 6.4: The workflow has started with the MRI data acquisition and segmentation of the relevant anatomical components from MRI prone position. Then realistic model geometry is generated over the FE mesh and boundary conditions are defined as well.The simulation of upright position is performed in the next step. Finally, the simulated model is verified by comparing it with the 3D surface data by finding the displacement to the real breast geometry. The image is adopted from [56].

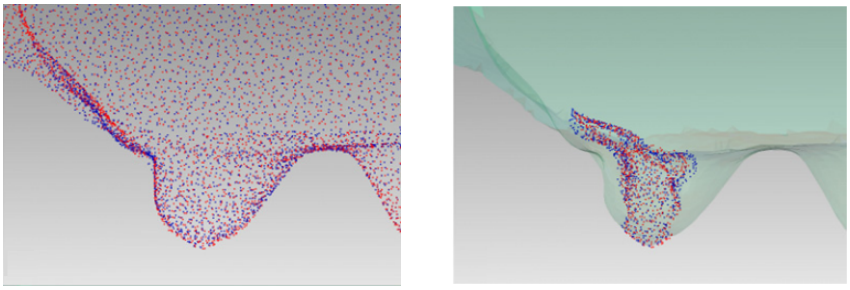

(a) (b)

Figure 6.5: Superimposition of (a) a deformed compressed with (b) an uncompressed ground-truth model form the approach proposed by Patete *et al.* [147].

detailed.

6.2.1 Wound Healing Simulator

Vavourakis *et al.* [197] proposed a BCS simulator that models the 3D post-surgical shape of the breast by coupling a physiological model of tissue recovery with a biomechanical model of pose estimation. The former predicts breast contraction caused by wound healing while the latter uses a Mooney-Rivlin biomechanical model of the breast to simulate deformations for different patient's positions. The main stages of the surgery simulation (Figure 6.7) comprise the construction of a patient-specific FE model of the breast, the definition of the tumor and the wound healing simulation itself, which uses the multi-scale biomechanical model of wound healing described above.

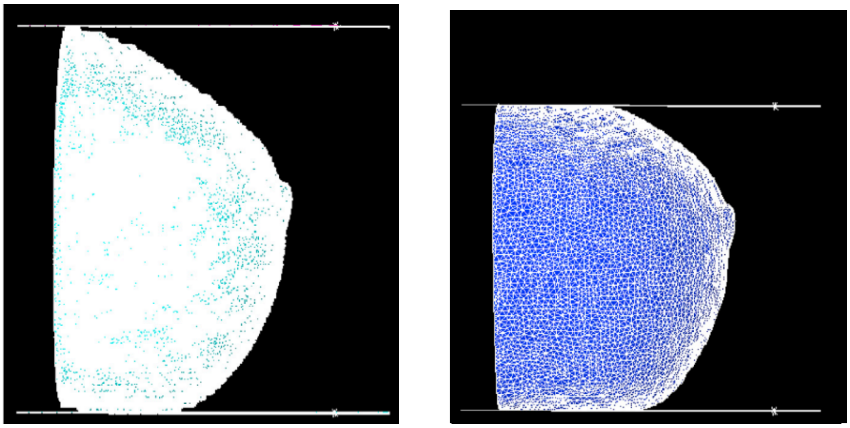

(a) (b)

Figure 6.6: Sagittal view of a breast (a) before and (b) after the compression simulated in the approach proposed by Martínez-Martínez *et al.* [127].

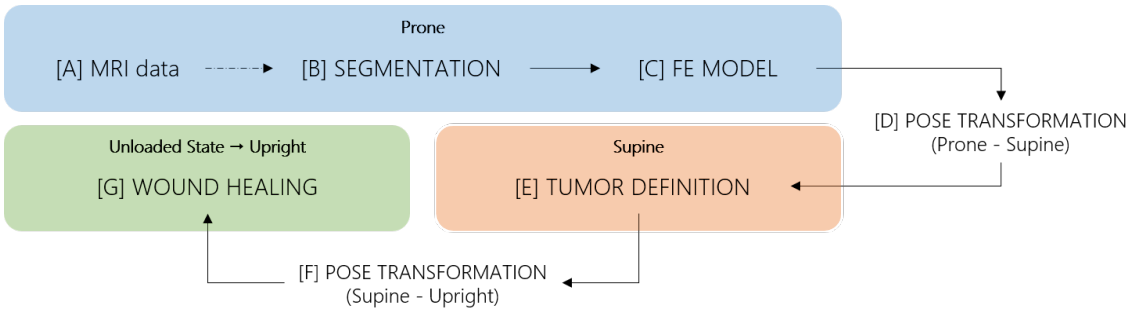

Figure 6.7: BCS simulation followed pipeline, as proposed by Vavourakis *et al.* [197].

Each of the wound healing pipeline stages is carried out with the patient in different positions and thus, some pose transformations are also accounted for (Figure 6.8). In fact, MRI is acquired with the torso facing down (prone position), surgery is performed with the patient facing up (supine position), the simulation occurs in an unloaded stage and surgery results are evaluated in the upright position.

6.2.1.1 Finite Element Model

According to Vavourakis *et al.* [197], a 3D patient-specific biomechanical FEM of the breast can be created from MRI data (Figure 6.7, [A]), that is segmented to delineate breast and background (Figure 6.7, [B]). Fat and fibroglandular tissues can also be differentiated to create a more detailed FEM, in which distinct mechanical properties are assigned to elements according to the breast tissues they represent. Upon the segmentation of the structures of interest, a 2D surface mesh of FE that represents skin and a 3D mesh representing the interior of the breast shall be generated (Figure 6.7, [C]).

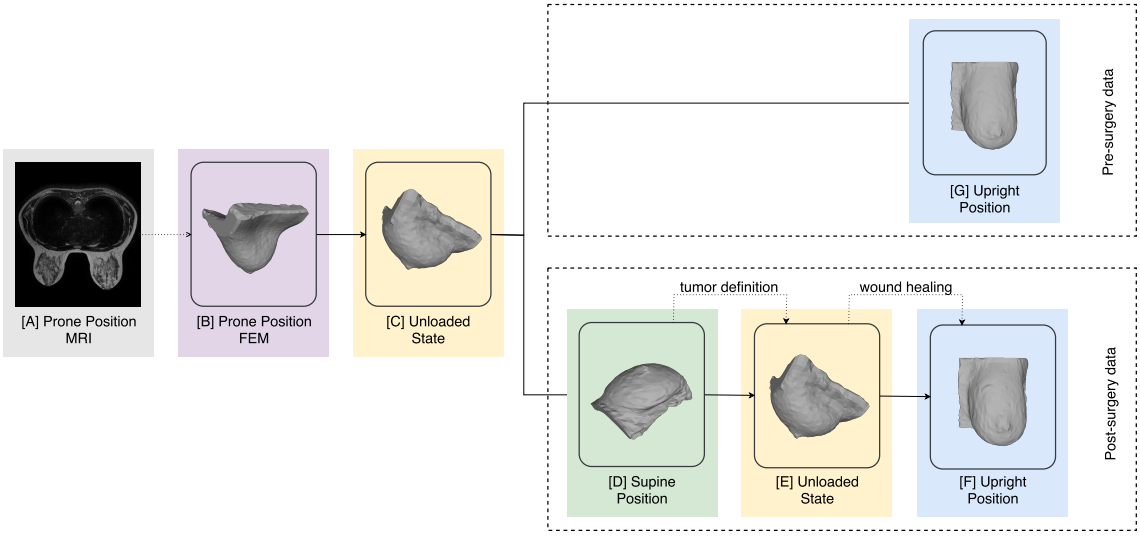

Figure 6.8: Pose transformation pipeline, as proposed by Vavourakis *et al.* [197].

6.2.1.2 Pose Transformation

The FEM generated from MRI data represents the breast in the prone position because it assumes the configuration of the patient during MRI acquisition. Yet, during the surgery simulation workflow, some stages require the model to represent the patient in different positions. As consequence, two explicit pose transformations occur ((Figure 6.7, [D] and [F])), and a third one takes place during the wound healing step (Figure 6.7, [G]). In detail, MRI data is acquired with the patient lying in the prone position (Figure 6.8, [A]), but the upright position (Figure 6.8, [G]) is the most suitable pose to evaluate the natural shape of the breast and, consequently, its deformations. Thus, wound healing results are outputted in the upright position (Figure 6.8, [F]). On the other hand, BCS is performed with the patient lying in the supine position (Figure 6.8, [D]), implying that any surgical planning activity, such as the definition of tumor characteristics and the volume to excise, should be done in this position. The multi-scale model used for surgery simulation can estimate pose transformations by computing the unloaded state (a gravity-free reference state) and re-applying gravity stress in the desired direction. As result, the FEM, constructed in prone position, is converted to an unloaded state (Figure 6.8, [C]), from which both supine (Figure 6.8, [D]) and pre-surgery upright position (Figure 6.8, [G]) can be estimated. The tumor is defined in the supine position (Figure 6.8, [D]) and the FEM is again converted from supine to the unloaded state (Figure 6.8, [E]), where the wound healing simulation is carried out. The simulation result (post-surgery data) is returned in upright position (Figure 6.8, [F]). With this pose transformation pipeline, both pre- and post-surgery data are represented in the upright position and can be directly compared to predicting shape deformations caused by BCS.

6.2.1.3 Tumor Definition

The multi-scale biomechanical model proposed by Vavourakis *et al.* [197] simulates the wound healing process taking as input the volume excised during surgery. This volume depends on the tumor position and size, and therefore, a virtual surgery has to occur in which all FE inside the volume to excise are re-labeled as damaged and assigned with different physiological and mechanical parameters. In [197], this virtual surgery is simulated in the supine position: the surgeon identifies the tumor position, defines the incision lines and outlines the incision path inside the breast. The excision volume is then approximated by a cylinder that contains the lesion and whose axis is perpendicular to the chest-wall, extending from the skin to the pectoral muscle. All FE contained inside this cylinder are assigned with damaged tissue properties.

6.2.2 Dataset Construction

To create the dataset, a subset of MRI data from the PICTURE project[1] was used. In detail, T1-weighted MRI image sets were used, containing approximately 60 axial slices each, with an average voxel resolution of $0.59 \times 0.59 \times 3mm$, ($x$, y and z axes, respectively). Taking advantage of the manually annotated structures, 3D point clouds (PCLs) of patient's torsos were created using the breast contour, *Latissimus Dorsi* muscles, and the pectoral muscle, as frontal, lateral and posterior boundaries, respectively. However, considering that the computational cost of the wound healing simulation is decreased if performed for each breast individually, instead of using the entire torso as done by Vavourakis *et al.* [197], the torso point cloud (PCL) was vertically divided with a plane defined along the sternum. Performing this division, individual breasts PCLs were obtained, which provide breast shape variability in the dataset. Any breast PCL holding visible MRI coil compression are discarded from the simulation because the deformation is not reversible with the multi-scale biomechanical model.

After segmentation, each resulting breast PCL ($\approx$ 1900 surface points) was converted to a $3D$ triangulated surface mesh to model the skin, using the Ball-Pivoting algorithm [18], in MeshLab [44]. The breast volume was next meshed in Gmsh [73], by inserting uniformly distributed points inside the object ($\approx$ 2500 volume points), subsequently connecting them with tetrahedrons elements. To complete the creation of the FEM, distinct boundary conditions and material properties were assigned to the surface mesh - frontal surface, pectoral muscle (back surface), lateral limits, and top and bottom boundaries were defined - following the strategy proposed by Vavourakis *et al.* [197].

For the purpose of data augmentation, the number of dataset instances was increased by varying some input parameters related to breast and tumor characteristics, namely the breast density, and the tumor size and position, known to influence the aesthetic result after BCS.

To represent all categories of breast densities in the dataset, it was necessary to model other ratios of tissues than the ones represented in original MRI data, by varying the number of FE that

[1] http://www.vph-picture.eu/

are assigned with mechanical properties of fibroglandular and fat tissues. To avoid a segmentation step, the approach proposed by Del Palomar *et al.* [53] was used to simplify the structural complexity of the breast, by assigning a weighted average value of the mechanical properties of each tissue type to all elements of the model. Hence, the ratios defined by the American College of Radiologists (ACR) classification system - the Breast Imaging Reporting and Data System (BI-RADS®) [55] - can be considered for weighting the material property values described in [197], and represent several breast densities. This reporting system identifies 4 categories of breast density (A, B, C, and D), which are described in Table 6.1. Following this strategy, the fibroglandular/fat ratios: A - 10/90, B - 35/65, C - 60/40, D - 85/15, were used to average material properties of each category, as detailed in Table 6.2.

Table 6.1: BI-RADS® breast density description [55].

Density Categories	% Fibroglandular Tissue	Description
A	$< 25\%$	Almost entirely fatty breast
B	$25 - 50\%$	Scattered areas of fibroglandular density
C	$50 - 75\%$	Heterogeneously dense breast
D	$> 75\%$	Extremely dense breast

Table 6.2: Combination of tissues biomechanical properties for each density category. c_1 and c_2 are parameters of the Mooney-Rivlin biomechanical model, and ρ_0 is the material density. The reference values from Vavourakis *et al.* [197] were used.

BI-RADS®	Biomechanical Properties		
	c_1 (Pa)	c_2 (Pa)	ρ_0 (Kg.m^{-3})
A	0.1 x 120 + 0.9 x 80 = 84	0	0.1 x 1020 + 0.9 x 910 = 921
B	0.35 x 120 + 0.65 x 80 = 94	0	0.35 x 1020 + 0.65 x 910 = 948.5
C	0.6 x 120 + 0.4 x 80 = 104	0	0.6 x 1020 + 0.4 x 910 = 976
D	0.85 x 120 + 0.15 x 80 = 114	0	0.85 x 1020 + 0.15 x 910 = 1003.5

Besides the breast shape and composition, it is also important to characterize the tumor location and size. Since the relationship between tumor position and the aesthetical outcome is generally defined using breast quadrants to discretize tumor locations, tumors are randomly positioned inside each quadrant instead of choosing any position inside the breast, which assures the representativeness of the dataset by guarantying that there are instances of tumors in every quadrant. There are 4 quadrants defined by a vertical and horizontal division of the breast through the nipple and in the upright position (Figure 6.9): Upper-Outer or superolateral Quadrant (UOQ), Upper-Inner or superomedial Quadrant (UIQ), Lower-Outer or inferolateral Quadrant (LOQ), Lower-Inner or inferomedial Quadrant (LIQ) [78].

[1] https://commons.wikimedia.org/

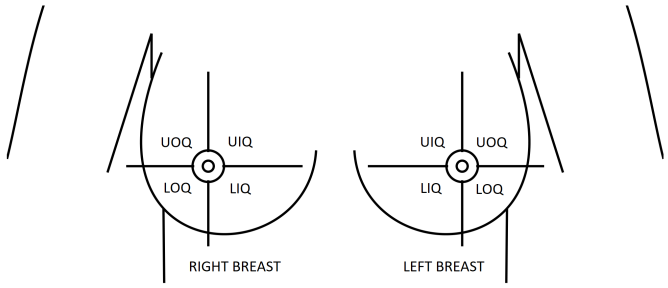

Figure 6.9: Breast quadrants definition: Upper-Outer (UOQ), Upper-Inner (UIQ), Lower-Outer (LOQ), Lower-Inner (LIQ) quadrants - adapted from [1].

The breast quadrants division is established in the upright position. However, according to the surgery simulator pipeline (Figure 6.7), the tumor is defined in the supine position. Therefore, in an attempt to define quadrants in the horizontal position which correctly correspond the upright ones, the nipple position (manually annotated) is used as a reference point to compute the vertical and horizontal planes that define the quadrants boundaries. Three main planes are then sequentially defined, as seen in Figure 6.10. The first plane corresponds to the one along the pectoral muscle (Figure 6.10(a)) and is defined by its normal which is computed by the cross product of two vectors, defined by three corner points of the pectoral muscle (two on the top and one on the bottom). The second plane sets the superior-inferior boundary (the red plane in Figure 6.10(b)) and is defined as parallel to the XY-plane (taking into account that the direction of the MRI acquisition is perpendicular to this plane), crossing the nipple. Finally, the third plane sets the lateral-medial boundary (the green plane in Figure 6.10(c)), being perpendicular to the pectoral plane and crossing the nipple too.

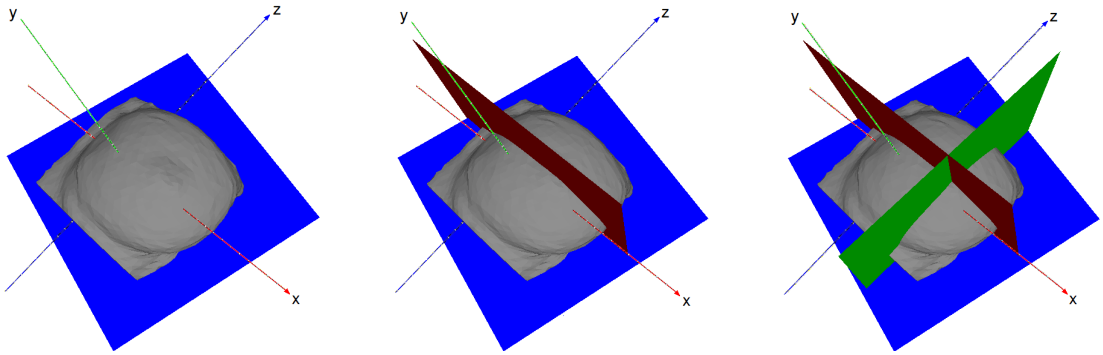

(a) (b) (c)

Figure 6.10: Definition of breast quadrants planes in supine position; (a) Pectoral plane, (b) Superior-Inferior plane (red), and (c) Lateral-Medial plane (green)

Having defined the quadrants, the tumor position is then randomly selected inside each quadrant – 3 spatial coordinates (x, y and z) are used to set the center of the tumor - and the excision

volume is computed. Briefly, the line between the nearest point of the pectoral muscle and the tumor position sets the normal vector to the muscle, and a predefined cylinder (with a known radius, height and, consequently, volume) is aligned through this direction (Figure 6.11). Different tumor sizes (volumes) can then be modeled by varying the ratio between the cylinder and breast volumes. Once the BCS protocol states that a breast tumor is eligible for BCS only if its removal does not require excision volumes higher than 20% of breast volume [47], cylinder volumes need to be limited to respect this threshold. In this study, excision volumes of 5%, 7.5% and 10% of the total breast volume were simulated, corresponding to three size categories: small, medium and large tumors, respectively (Figure 6.12(a) - 6.12(c)).

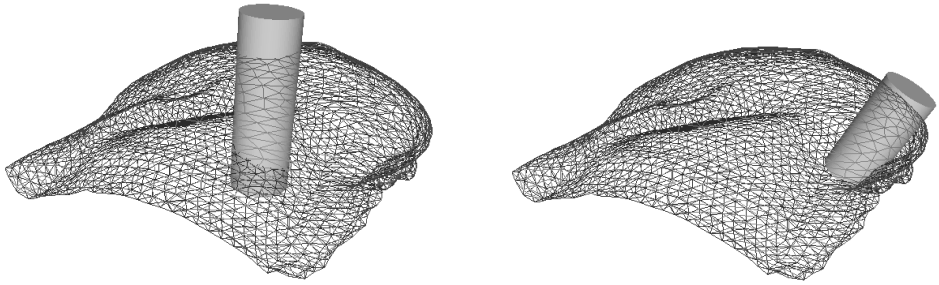

(a) (b)

Figure 6.11: The alignment of a predefined cylinder (a) through the direction given by pectoral normal, in relation to the tumor location (b).

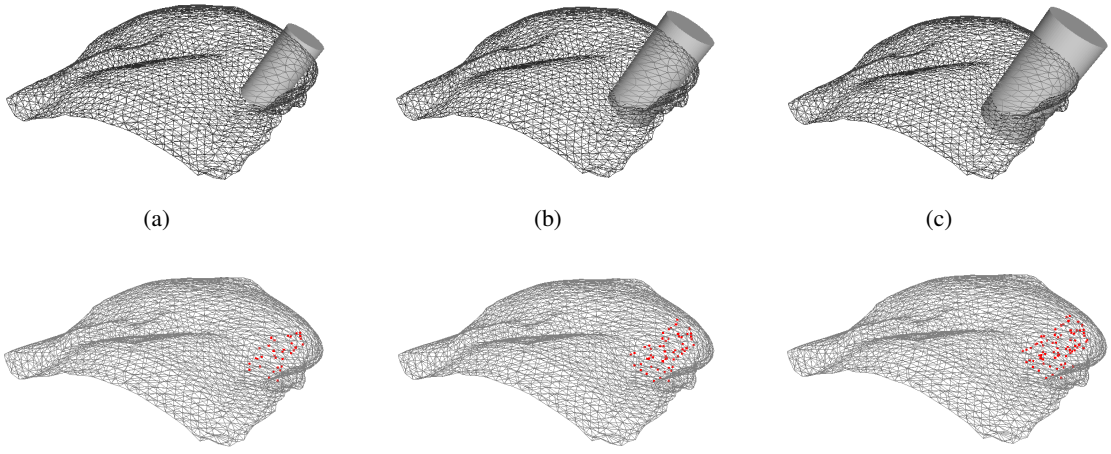

(a) (b) (c)

(d) (e) (f)

Figure 6.12: Definition of the cylinder to excise and the correspondent points labelled as damaged: small (a and d), medium (b and e) and large tumor sizes (c and f).

Once the cylinder is defined, the FE inside it is set as damaged (Figure 6.12(d) - 6.12(f)), and assigned the correspondent biomechanical and biochemical properties used by Vavourakis *et al.* [197].

Figure 6.13 shows the main considerations made in the conception of the dataset. This dataset was built using 6 breast PCLs (obtained from MRI data), taking into account a uniform distribution of breast volume (2 small, 2 medium and 2 big breasts) and breast laterality (3 left and 3 right breasts), as described in Table 6.3. Dataset instances were created by sequentially defining 4 different breast densities for each breast selected before, according to BI-RADS® reporting system ($4 \times 6 = 24$ cases), then different quadrants for the tumor location ($4 \times 24 = 96$ cases) and, finally, 3 different tumor sizes for each location ($3 \times 96 = 288$ cases). In the end, the dataset sums up to a total of 288 cases representing all the possible combinations of the most prominent clinical factors reported to affect breast shape after BCS.

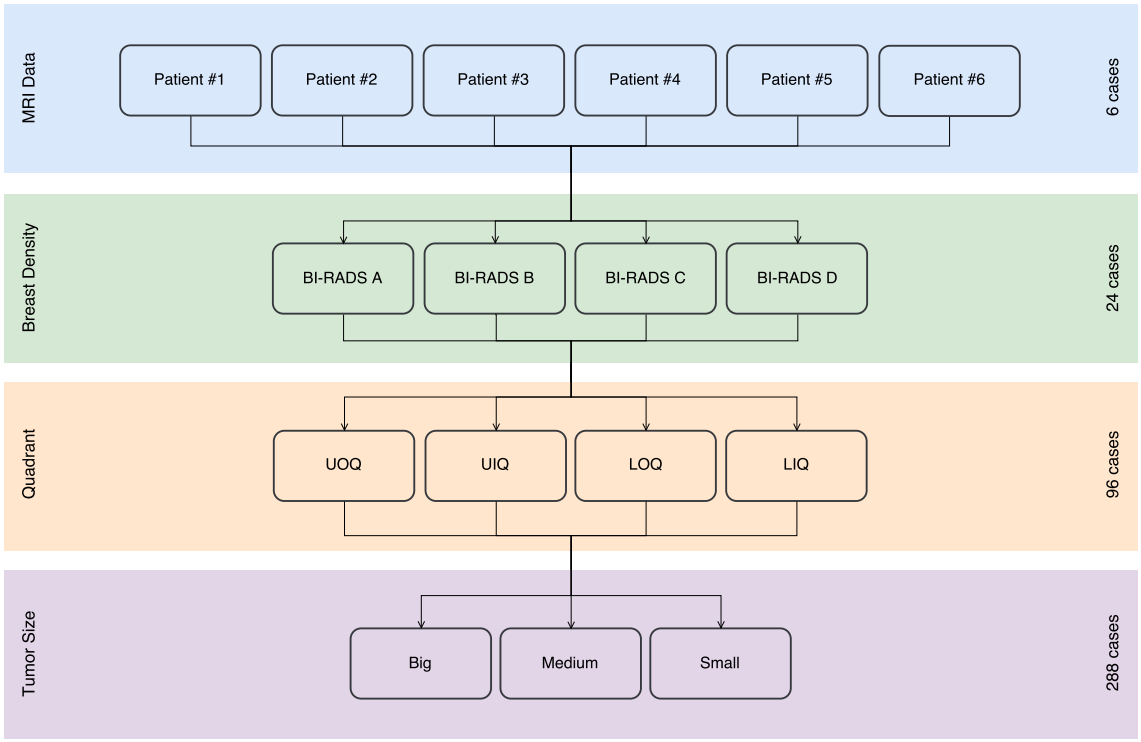

Figure 6.13: Sequential features combination used in dataset construction.

Table 6.3: Characterization of breast MRI data used for data augmentation: size, volume, and laterality.

Breast characteristics	**Patient #1**	**Patient #2**	**Patient #3**	**Patient #4**	**Patient #5**	**Patient #6**
Size	Small	Medium	Large	Medium	Large	Small
Volume (mm^3)	495,948	802,661	1,314,990	1,052,500	1,202,500	559,677
Laterality	Left	Left	Right	Left	Right	Right

6.3 Methodology

The prediction of the post-surgery shape of the breast after surgical intervention is a complex task that requires modeling the influence of several factors on the aesthetic outcome of surgery. Approaches to model these deformations are typically based on biomechanical models. However, FEM takes longer than expectations, from hours on high-end machines, up to some days on normal computers used in clinics. In this work, an alternative strategy based on ML techniques is proposed which overcomes the timing demands of biomechanical simulation, keeping most of the properties and characteristics of the breast.

6.3.1 Features

Feature extraction and representation is an important step in any ML task. Although clinical evidence suggests that a prediction model for breast deformation after BCS should take breast shape (laterality), volume and density into account, considering tumor characteristics such as quadrant (position) or size as inputs, such factors should be inspected in a more systematic way to confirm their influence and effects. Moreover, such analysis is important to suggest the best-suited ML algorithms to model the problem at hand. For visual purposes, the feature investigation was constrained only to the breast surface.

6.3.1.1 Breast Characteristics

Regarding breast characteristics, both density and shape are known to affect the extent of breast points displacements. Figure 6.14 shows the superposition of pre- and post-surgical breasts of the same patient when different densities are modeled. The resulting plots show that breast density impacts the magnitude of points displacements: the magnitude of displacements decreases as the breast density increases. In fact, this was the expected behavior, because denser breasts have a higher fraction of glandular tissue, which is less deformable than fat.

As for breast laterality, the mirroring of displacements can be seen when right and left breasts are compared (Figure 6.15). Although the magnitude of displacements is similar, the direction changes according to the breast laterality.

6.3.1.2 Tumor Characteristics

Figure 6.16 shows the effect of the tumor position on the displacements between pre- and post-surgical data. An interesting effect can be noticed: the distribution of displacements on the breast is dependent on the breast quadrant where the tumor is positioned. Larger displacements are centered around the tumor, vanishing as the distance to the tumor center increases. Hence, a feature space transformation might be helpful to describe the displacements distribution as a function of the tumor position. In the alternative, Euclidean and polar distance to tumor could benefit the modeling of the points displacements.

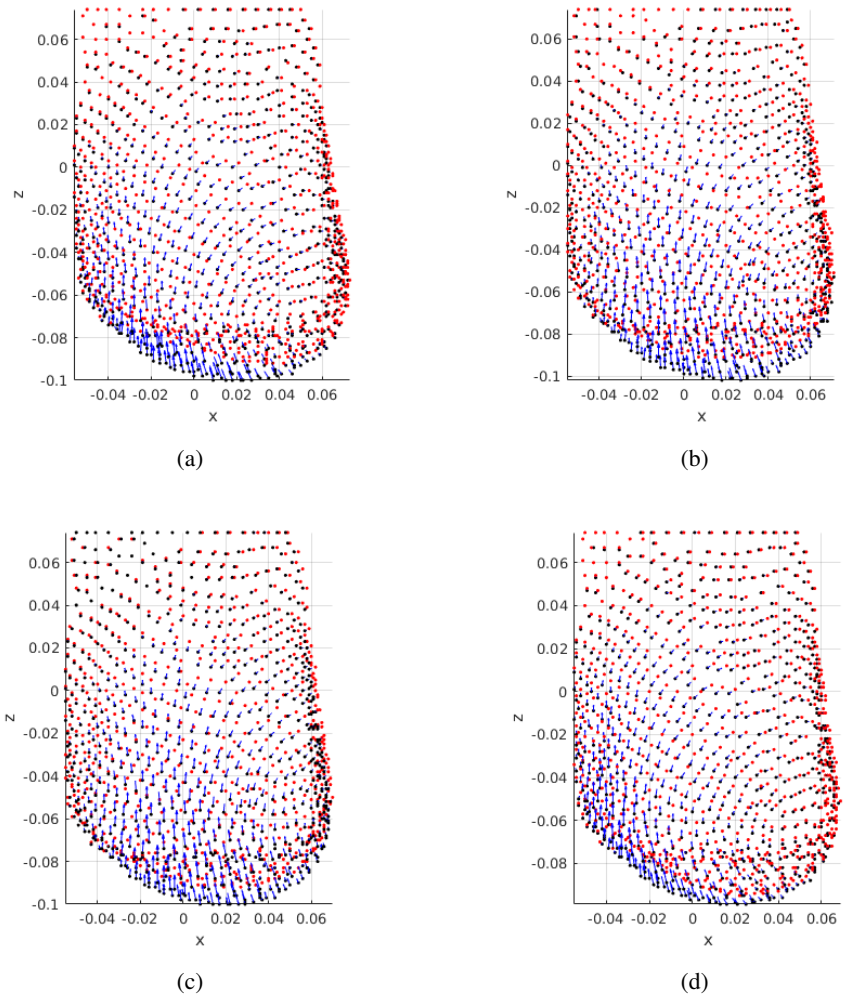

(a) (b)

(c) (d)

Figure 6.14: Influence of breast density on deformations: PCLs are shown for the same patient with variable breast density and fixed tumor position (UOQ) and size (small). Pre and post-surgical data on black and red, respectively. Blue arrows indicate displacement direction and magnitude; (a) BI-RADS A, (b) BI-RADS B, (c) BI-RADS C, (d) BI-RADS D

Finally, the influence of the tumor size on the magnitude of breast displacement is shown in Figure 6.17. Results evidence that larger tumors cause larger breast displacements after surgery wound healing. In fact, this was the expected behavior: after tumor removal, the remaining breast tissues adapt to fill the left void. This results in breast contraction, which is a function of the excised volume.

6.3.1.3 Feature Engineering

A brief look to Figures 6.14 to 6.17 denotes how different breast and tumor characteristics influence breast deformations after BCS and respective wound healing process. Breast density and tumor size have a particular impact on the magnitude of the displacements, while the quadrant where the tumor is positioned and the breast laterality influences the distribution of that displacement.

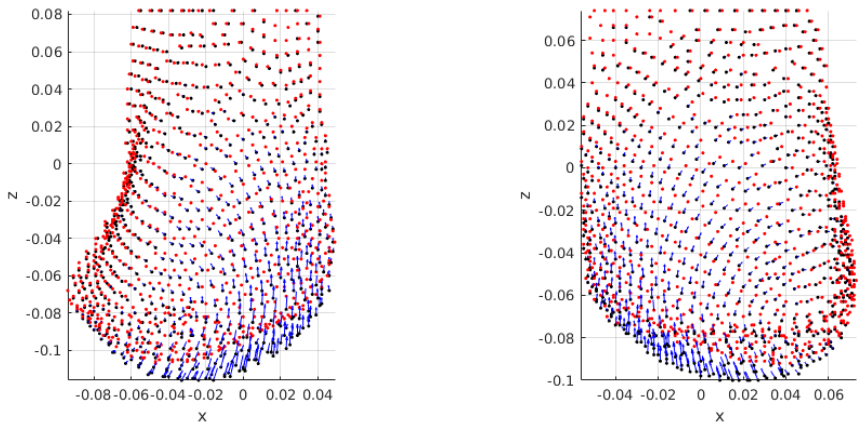

(a) (b)

Figure 6.15: Influence of breast shape/laterality: PCLs are shown for two patients with BI-RADS A and the largest tumor positioned on UOQ. Pre- and post-surgical data on black and red, respectively. Blue arrows indicate displacement direction and magnitude; (a) Patient's right breast, and (b) Patient's left breast

Therefore, one can expect that breast deformations can be modelled using the spatial coordinates of points, the distance of each point to the tumor position (the distance from a point perpendicular to the tumor cylinder), while accounting for categorical features such as breast density, tumor region, breast laterality and tumor size, as described in Table 6.4. Despite being appointed as an important clinical factor influencing the aesthetics of breasts after BCS, the volume of the breast is not explicitly listed. However, that information is implicitly covered due to the categorization of tumor sizes (expected excision volumes) which are defined as a percentage of the breast volume.

Definition of the features has been conducted aligned with the aforesaid expectations. The constructed feature list comprises three data attributes: points' coordinates, points' difference to the excised cylinder (both Euclidean and polar) and points' distance to the excised cylinder as quantitative continuous, tumor size and breast density with a categorical ordinal, and breast laterality and tumor region with a categorical nominal attribute. The point coordinates simply express the location of each point in the 3D coordinate system, while the points' coordinate difference feature reflects the difference between healthy points and the excised cylinder in each axis of the coordinate system. While the distance to the excised cylinder highlights the Euclidean distance from each healthy point, the polar distance to the excised cylinder expresses the same distance, but in polar notation. It is important to note that the coordinate difference and distance features for damaged points (inside the excised cylinder) are considered to be zero.

6.3.2 Regression Models

In this section, it will be explored the solution taken into consideration the feature analysis above. The intention of exploiting ML in breast shape prediction is to estimate points' coordinate after surgery healing, taking as input the points positions before surgery, as well as breast and tumor

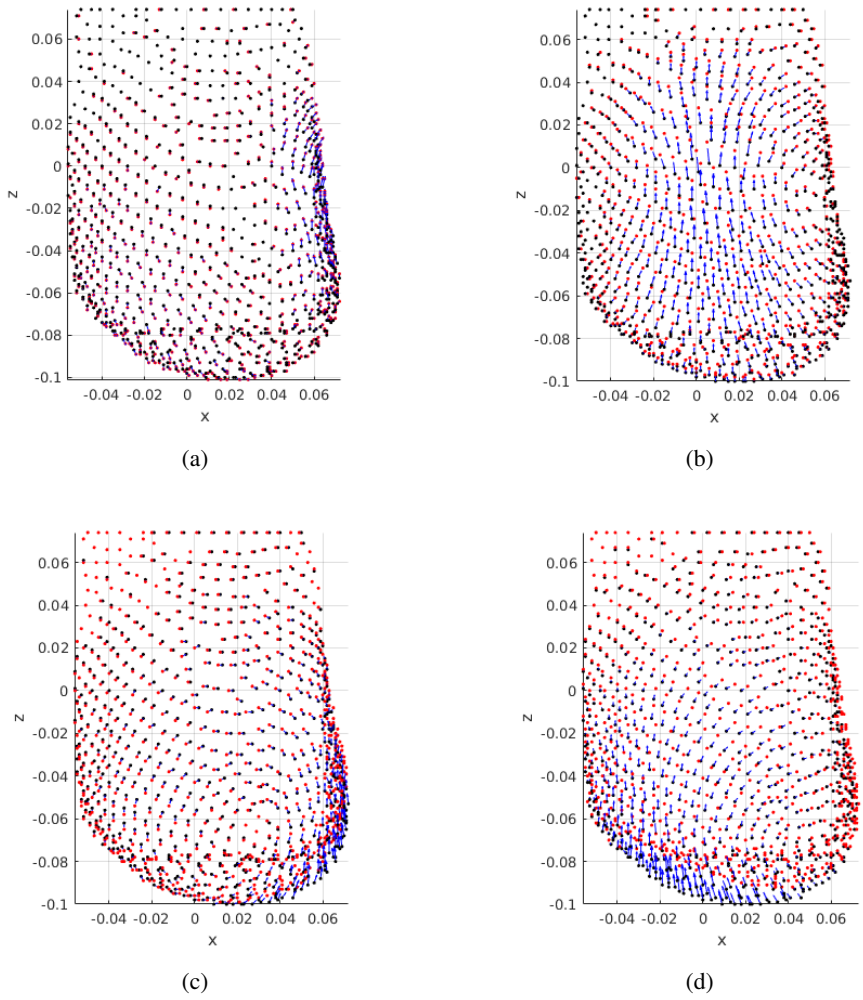

(a) (b)

(c) (d)

Figure 6.16: Influence of tumor position on deformations: PCLs are shown for the same patient with the tumor positioned in different breast quadrants/regions. Largest tumors are shown for BI-RADS A. Pre- and post-surgical data on black and red, respectively. Blue arrows indicate displacement direction and magnitude; (a) UIQ, (b) UOQ, (c) LIQ, and (d) LOQ

characteristics. Since the points' coordinate is a continuous variable in 3D space, learning techniques providing regression methodologies are taken into consideration; however, prediction of the point coordinates poses a challenge to transfer breasts with different laterality or size, into the same coordinate system. Such circumstance can be prevented by re-formulating the demanded output from the regression. Instead of predicting the exact point coordinates, required displacement to translate a pre-surgery point to its post-surgery location can be predicted, alternatively. The post-surgery PCL is then attainable by applying predicted displacement on the pre-surgery PCL. Described in mathematical notation, the regression model can be expressed as in Equation 6.1:

$$\begin{bmatrix} P^{pre} & F \\ \vdots & \vdots \end{bmatrix} \xrightarrow{f} \begin{bmatrix} disp^{pre \rightarrow post} \\ \vdots \end{bmatrix}, \tag{6.1}$$

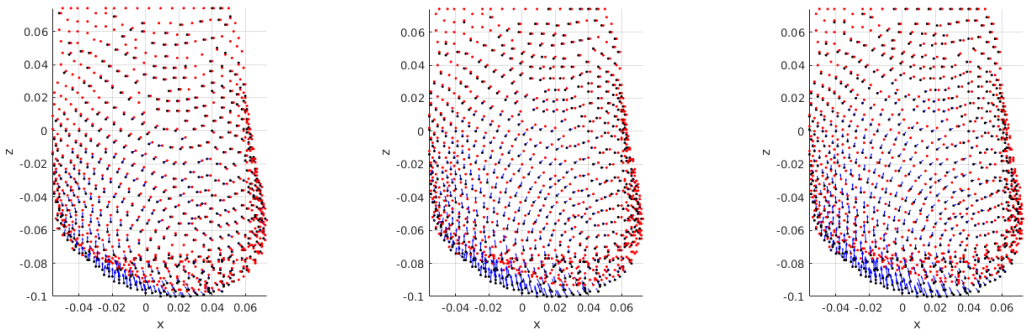

(a) (b) (c)

Figure 6.17: Influence of tumor size: PCLs are shown for the same patient with BI-RADS A, and tumor on region UOQ. Pre- and post-surgical data on black and red, respectively. Blue arrows indicate displacement direction and magnitude; (a) small, (b) medium, and (c) large

Table 6.4: Description of features to be used in the prediction of breast deformations after BCS

Features	**ID**	**Type**	**Space**	**Description**
Point's coordinate	p_x p_y p_z	Quantitative Continuous	$\in \mathbb{R}^3$	Breast points coordinate in 3D space. The center of geometry of PCLs should be translated to the origin.
Coordinate difference to the excised cylinder	$disp_x$ $disp_y$ $disp_z$	Quantitative Continuous	$\in \mathbb{R}^3$	Difference of each healthy point (signed) of pre-surgery PCL to the excised cylinder
Distance to the excised cylinder	$d_{x,y,z}$	Quantitative Continuous	$\in \mathbb{R}$	Euclidean distance of each point of pre-surgery PCL to the excised cylinder
Polar distance to the excised cylinder	ρ ϕ z	Quantitative Continuous	$\in \mathbb{R}^3$	Polar difference of each healthy point (signed) of pre-surgery PCL to the excised cylinder
Tumor Size	s_1 s_2 s_3	Categorical Ordinal	100 010 001	Defines the size of tumor (5%, 7.5%, or 10% of total breast volume)
Breast Laterality	R L	Categorical Nominal	1 0	Indicates the laterality of breast (right or left)
Breast Density	A B C D	Categorical Ordinal	1000 0100 0010 0001	Determines breast density level (A, B, C, or D)
Tumor Region	R_1 R_2 R_3 R_4	Categorical Nominal	1000 0100 0010 0001	Specifies the region of breast with the tumor (UOQ,UIQ, LOQ, or LIQ)

where P^{pre} is pre-surgery PCL, F is the feature list per instances (pre-surgery points), f is the demanded regression model, and finally $disp^{pre \rightarrow post}$ expresses the required displacements to convert pre-surgery PCL to post-surgery. Having predicted the displacement, predicted breast

shape (P^{pred}) is attainable via Equation 6.2:

$$P^{pre} + disp^{\,pre \rightarrow post} = P^{pred} \tag{6.2}$$

Looking back to the objective of predicting breast shape after BCS, the expected prediction should be performed considering the points of both pre- and post-surgery models, together with clinical features. Therefore, the possible learning approach to be proposed must be able to deal with a large number of inputs (points) and correlate them with the features (clinical features). In ensemble learning the key idea is that different algorithms explore different search spaces and hypotheses, so composite systems could outperform single ones [194]. The strategy of exploiting ensemble learning methodology assures to gain improvement of not only the robustness but also the performance of the learners via combining the votes of stronger single regressors combined to build the prediction model. As an ensemble learning approach, tree-based learners provide an appropriate framework (both in time and performance evaluations) to take part in training with a large number of inputs. Therefore, within this research, tree-based learning methodologies are taken into consideration to perform the required regression in finding the predicted coordinate of breast shape.

Regression methods also can be categorized based on the number of their outputs. While single output regression is the most used ones, the internal correlation between their voters can be set such that they can generate multiple outputs. Therefore, taking the problem of predicting breast shape into account, regressors can be categorized into the two types of Multiple Input Single Output (MISO), or Multiple Input Multiple Output (MIMO). Both types of the aforesaid regressors are studied and evaluated in this work.

6.3.2.1 Random Forests

Depending on the goal whether to decrease bias error and overfitting or to decrease both bias and variance, bagging and boosting are generally used, respectively. Concentrating in the bagging, unstable models, i.e. models whose performance is sensitive to small perturbations of the training set, are trained with different replicas of the training set, obtained with replacement to keep the same number of examples (bootstrap aggregation). Then, new examples are predicted by uniform voting between the regressors trained with different dataset replicas. A special variant of bagging applied to decision trees results in the RF method, which operates by constructing multiple decision trees with bagging and random selection of features at each split of each tree. This mechanism assures that the constructed trees become correlated with one or more features which are strong predictors [85].

In this study, the use of bagging is exploited by learning RF models. This method requires the optimization of the number of trees to use as forest, as well as the number of features considered during the construction of trees.

6.3.2.2 Gradient Boosting Regression

The algorithm for Gradient Boosting Regression (GBR) is a recast adaptation of AdaBoost that employs boosting methods in regression trees [23]. The general idea is to compute a sequence of simple trees, where each successive tree is constructed for the prediction residuals of the preceding tree [23]. Minimization of the loss (residuals) of the model (or regressor) is pursued by adding weak learners using a gradient descent procedure. Therefore, three elements are considered directly in developing a regressor with gradient boosting: a loss function, a weak learner, and finally an additive model to add weak learners to minimize the loss function. Considering decision trees as the weak learner, they are added one at the time, while the existing trees are kept unchanged. To ensure the simplicity of the learned trees, it is common to assign specific constraints to control the growth of trees, for instance, defining a maximum limit for depth, or the number of leaf nodes.

The capability of optimization is granted to the trees since they are constructed with parameters to be modified in direction of reducing the total loss function of the regressor. A tree which reduces the total loss is added to the existing sequence of trees [40, 128].

As a greedy algorithm, gradient boosting has overfitting potential in training data, quickly. Therefore, common techniques such as regularization assist the performance of prediction by penalizing various parts of the algorithm. The discussed constraints on tree construction is an example of the regularization methods to control the greediness of gradient boosting [62].

6.3.2.3 Multi-Output Regression

Regression models are normally characterized by only one output; however, taken into consideration the problem here presented, it makes sense to think in a strategy based in MIMO regressors. In order to predict more than one output, it can be simply considered a regressor for each output, by concatenating several MISO regressors [21]; however, ignoring possible relationship among the constructed models could result in a drawback for the solution. A smarter solution is also suggested to construct several regressors not only by the input training data but also by the possible internal relationships between them. In particular, this solution takes the advantage of constructing a MIMO regressor which is smaller than the size of those MISO regressors. It should be noted that the discussed solution leads to better predictions when there is a strong correlation between the features and the targets.

6.3.3 Summary of Regression Methodologies

Through a comprehensive study between the pre- and post-surgery PCLs, the influence of each breast and tumor characteristics features were determined. Aligned with the objective of the current research to predict the shape of the breast after surgery, regression was taken into consideration as the main solution. Further discussions unveiled that the tree-based methodologies are capable enough to satisfy the input/output demands of the solution.

6.4 Results

The definition of training and testing sets is carried out with a careful approach, in which a patient leave-one-patient-out (LOPO) strategy is advised to obtain test and train subsets. In each split, all example data generated from the same input patient would be used for testing, and the remaining patient's data would compose the training subset. In the particular case of having 6 patients, the LOPO strategy is followed to prevent overfitting, due to the similarities between the PCLs of a single patient. To assess the model performance through LOPO strategy and tuning parameters at the same time, a cross-validation approach was used in order to find the parameters' which presents the best configuration of the model.

As there is a deterministic correspondence between the points of the predicted (as the source) and the post-surgery PCL (as the target) for each patient, the evaluation metric can be defined by the Euclidean *point-wise distance (p2p)*. Denoted in Equation 6.3, the point-wise distance evaluates the performance of the regression model, since it measures the amount of displacement of each pair of points regardless of the total PCL displacements. Less distance means the regression model predicted the coordinate of each point closer to its expected location.

$$D^{p2p} = \frac{1}{N}\sum_{i=1}^{N} d(P_i^{\,source}, P_i^{\,target}), \tag{6.3}$$

where N and d denote the number of points and Euclidean distance, respectively, and P_i^{source} is the corresponding point of P_i^{target}. Not only point-wise but also *global distance* can be calculated, as well. Unlike the point-wise, the global distance appraises the displacement between the two comparing sets in whole. That means the discussed metric gives an overview of the similarities between the source set with the target. The global measurement of the distance results in reporting two distances: from the source to target PCL and from the target PCL to the source. Closer reported distances signify the more similarity between the two PCLs.

$$\begin{cases} D^{\,global}_{source \rightarrow target} = \frac{1}{N}\sum_{i=1}^{N} \min_j d(P_i^{\,source}, P_j^{\,target}) \\ D^{\,global}_{target \rightarrow source} = \frac{1}{N}\sum_{i=1}^{N} \min_j d(P_i^{\,target}, P_j^{\,source}) \end{cases}, \tag{6.4}$$

where the P_j is the nearest point to P_i.

Since the breast deformation is correlated with both internal and surface tissue (described in Section 6.2.1.3), both so-called points are considered during the training stage; however, numerical evaluation only comprises the analysis of the surface points.

Note that for the both presented metrics, the mean distance (μ), the standard deviation from the mean (σ) and the maximum distance (Max) between the comparing sets are reported as well. The maximum distance expresses the furthest distance between two corresponding points of the predicted and pre-surgery PCLs. Also, *pre* and *post* symbols stand for pre- and post-surgery PCLs and *pred* denotes the predicted breast PCL (wherever it is needed the predictions are also compared visually with the post-surgery models).

Finally, the ML implementations for RF and GBT were accomplished in python 3, by using *scikit-learn* package [148] on a machine powered by intel® Core i7® at 3.2 GHz with 128 GB of memory (for cross validation). As long as the *scikit-learn* package includes multi-output regressor which is based on concatenation of individual regressors, the implementation of MOR was carried out with a package in *R*, called *Multivariate Random Forest* [117].

6.4.1 Random Forests

Following the approach of individual regressor for each axis, three RF regressors were trained. The cross-validation inner loop was set to optimize the number of estimators (trees), the maximum number of features in each tree and the leaf size is of those parameters through $\{5, 10, ..., 500\}$, $\{2, 3, ..., 23\}$, and $\{1, 2, ..., 5\}$, respectively.

The criterion to select the tuned parameters was chosen considering two objective functions (OF): the average, and the Hausdorff (maximum). Focusing on the average, the best set of tuned parameters are selected such that it minimizes the average distance between the predicted and the post-surgery models. The other OF which is based on the Hausdorff distance intends to decrease the maximum distance between the points in each set of comparison of predicted and post-surgery PCLs, although the average distance may increase.

6.4.1.1 PCL Sampling

Theoretically, in RF, the inclusion of more points (more sampling rate) is thought to increment the gain of the regressor by declining the average distance between the predictions and the target, though, not only the training time continues its incremental trend, but also the aforesaid slope of the distance decelerates [36]. In this regard, a comprehensive study was designed to find an optimized sampling rate in the range of $\{5, 10, ..., 100\}$, according to both distance error and training time. The timing complexity reported in Figure 6.18 depicts the aforesaid evolution as the training size set increases, as expected. Besides, shown in Figure 6.19(a), considering the average OF, the declining slope of the distance error decreases in defiance of the sampling rate until it reaches to 65%. Although the difference of the reported distances between the rates of 45% and 65% is less than 0.50 *mm*, to satisfy the condition of the OF, it was decided to use the sampling rate correlated with the global minimum distance (65%).

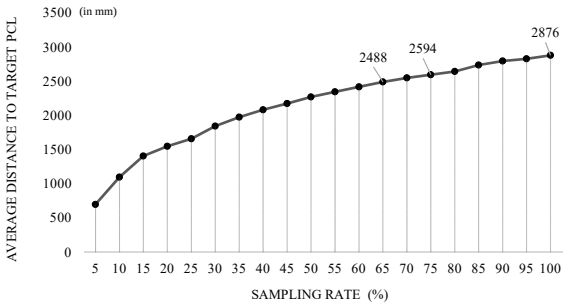

Figure 6.18: Impact of sampling breast PCL on the training time of RF

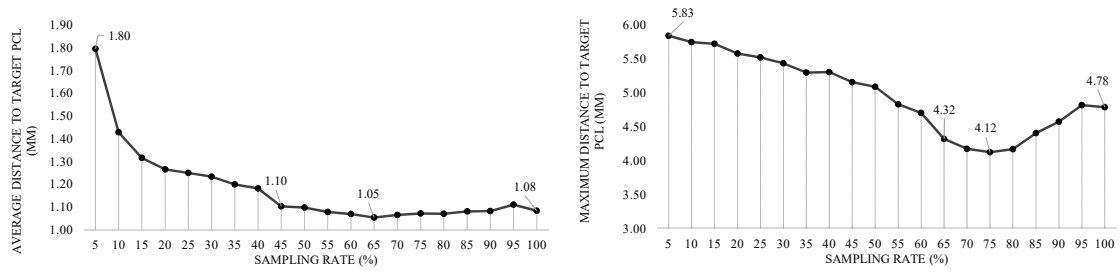

(a) (b)

Figure 6.19: Impact of sampling breast PCL on (a) the average, and (b) Hausdorff with respect to the pair-wise distances

With the same argument, and in accordance with the Hausdorff OF, the sampling rate of 75% was selected due to the least evaluated maximum distance, though the difference between the rates 75% and 65% is measured around 0.196 *mm*. Figure 6.19(b) depicts the evolution of maximum distance according to the Hausdorff OF. Considering the aforesaid sampling rates, numerical evaluations with respect to average and Hausdorff OFs are calculated and reported in Table 6.5 and Table 6.6, respectively. To evaluate the magnitude of the reported distances, an extra comparison is performed with the distance between the two comparing PCLs in case no method is applied (meaning that prediction data is exactly equal to the pre-surgery data). This comparison, so-called *baseline evaluation*, is reported in the last column of Table 6.5 and the last two columns of Table 6.6, for both the average and the Hausdorff OFs.

Table 6.5: Numerical evaluation: Pair-wise distance (in *mm*) based on both average and Hausdorff OFs for training set sampled with 65%, and 75%, respectively. Also, the last column denotes the evaluation of dummy method.

	Average-based OF	**Hausdorff-based OF**	**Baseline evaluation**
	D^{p2p}	D^{p2p}	D^{p2p}
μ	1.052	1.146	2.206
σ	0.920	0.934	1.920
Max	5.210	4.101	8.410

Table 6.6: Numerical evaluation: Global distance (in *mm*) based on both average and Hausdorff OFs for training set sampled with 65%, and 75%, respectively. The last two columns denote the evaluation of the dummy method.

	Average-based OF		**Hausdorff-based OF**		**Baseline evaluation**	
	$D^{global}_{pred\to post}$	$D^{global}_{post\to pred}$	$D^{global}_{pred\to post}$	$D^{global}_{post\to pred}$	$D^{global}_{pre\to post}$	$D^{global}_{post\to pre}$
μ	0.973	0.970	1.091	1.071	1.758	1.731
σ	0.787	0.748	0.825	0.761	1.333	1.277
Max	4.926	4.814	4.025	4.010	6.512	6.317

6.4.1.2 Assigning Weights

Deep investigation of the trained RF reveals that the nature of problem demands to define different weights for the points belonging to healthy or damaged tissue. In this work, a weight assigning strategy is followed in which the weights are initially assigned to the training instances and then they are updated iteratively in accordance with the distance from their correspondences in the target model. Thus, in each iteration, each point is assigned a weight that is proportional to the distance from its corresponding point of the target. This proposed iterative approach, called adaptive weighting, continues until either a fixed number of iteration is reached (in this case 100), or the OF is not satisfied within three consecutive iterations.

A glance at the results obtained in the previous section reveals that the distance for a point is near to 1 *mm* while the maximum distance is higher than 5 *mm*. Taken this in consideration we considered a weighting strategy by defining the values for the weights as the *ceiling* of the *point-wise distance (p2p)* in a range of 1 to 6, as shown in Figure 6.20.

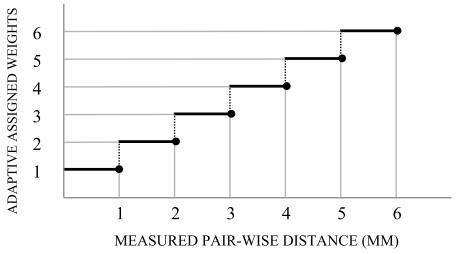

Figure 6.20: Assigning adaptive weight with respect to the range of the measured distances.

Obtained results from evaluation show an interesting trend in decreasing both average and Hausdorff distances. Table 6.7 and Table 6.8 express the numerical evaluation based on average and Hausdorff OFs, respectively. Comparing with the best set of results (obtained by using RF with 65% sampling), a slight improvement is observed (1.048 *mm* for weighted RF vs. 1.052 *mm* for weightless). Note that both regressors are built using a sampled dataset with the rate of 65%. The same decreasing trend is observed while the Hausdorff OF in considered (comparing 4.083 *mm* for weighted RF vs. 4.100 *mm* for weightless RF). This improvement certifies the assumption that the provision of a suitable weighting approach can lead the regression to predict post-surgery models with fewer distance evaluations. It should be noted that the weight assignment strategy has a significant impression to decrease the distance between predicted and post-surgery PCLs. Therefore, a new line of research is opened to investigate appropriate strategies to improve the prediction of breast shape using RF.

Besides the reported numerical evaluation, visual comparisons of three predicted breasts are depicted in Figure 6.21. The depicted predictions have been evaluated with average pair-wise distance of 1.62 *mm* (Figure 6.21(a)) as a poor prediction, 1.044 *mm* (Figure 6.21(b)) as a fair prediction, and 0.827 *mm* (Figure 6.21(c)) as a good prediction.

Table 6.7: Numerical evaluation: Pair-wise distance (in *mm*) between predicted PCLs and post-surgery models using RF with adaptive weights. The training set is sampled with rate of 65% and 75% due to average and Hausdorff OFs, respectively.

	Average-based OF	**Hausdorff-based OF**	**Baseline evaluation**
	D^{p2p}	D^{p2p}	D^{p2p}
μ	1.048	1.189	2.206
σ	0.905	0.981	1.920
Max	5.240	4.083	8.410

Table 6.8: Numerical evaluation: Global distance (in *mm*) between predicted PCLs and post-surgery models using RF with adaptive weights. The training set is sampled with rate of 65% and 75% due to average and Hausdorff OFs, respectively.

	Average-based OF		**Hausdorff-based OF**		**Baseline evaluation**	
	$D^{global}_{pred\to post}$	$D^{global}_{post\to pred}$	$D^{global}_{pred\to post}$	$D^{global}_{post\to pred}$	$D^{global}_{pre\to post}$	$D^{global}_{post\to pre}$
μ	0.961	0.951	1.124	1.094	1.758	1.731
σ	0.951	0.861	0.958	0.937	1.333	1.277
Max	5.182	5.178	4.022	3.980	6.512	6.317

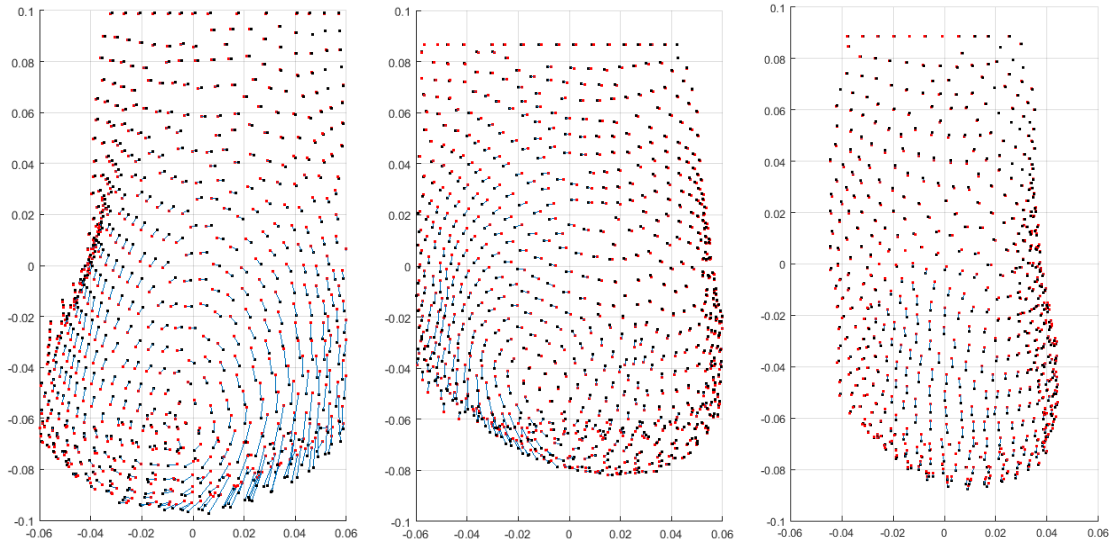

(a) (b) (c)

Figure 6.21: Visual evaluation of three PCLs from dataset with different prediction distances: (a) Poor prediction with $D_{pred\to post} = 1.624$ *mm*, (b) Fair prediction with $D_{pred\to post} = 1.044$ *mm*, and (c) Good prediction $D_{pred\to post} = 0.827$ *mm*. The post-surgery PCL is shown with red points while the predicted PCL is visualized with black points. The displacements between corresponding points are colored in blue.

6.4.1.3 Feature Importance

Although the points' displacement plays an important role in finding the regression, the used clinical features contribute in adjusting the amount of prediction required for each point of healthy or damaged region. The construction of trees in RF allows reporting the importance of each feature. In this regard, clinical studies can be accompanied by the resulted features' importance to highlight the ones which contribute more to the prediction. Based on the conducted analysis, the clinical features applied in the training procedure are studied to determine their level of importance to construct the regressor. Table 6.9 denotes the importance of features in percentage, for the regressors trained in each of the three axes. Additionally, for the features belonging to the same group, not only the individual importance but also the grouped importance (average of individuals) is reported, as well.

Table 6.9: Features' importance (both individual and grouped) measured in % for RF with adaptive weights.

Features	**ID**	**Trained Model for X**		**Trained Model for Y**		**Trained Model for Z**	
		Individual (%)	Group (%)	Individual (%)	Group (%)	Individual (%)	Group (%)
Points' coordinate	p_x	8.39	7.03	6.94	7.67	3.75	6.25
	p_y	7.46		8.37		6.93	
	p_z	5.25		7.68		8.08	
Coordinate difference to the excised cylinder	$disp_x$	1.17	1.73	0.90	1.19	1.37	1.75
	$disp_y$	1.46		1.25		1.57	
	$disp_z$	2.57		1.39		2.32	
Distance to the excised cylinder	$D_{x,y,z}$	8.23	8.23	8.09	8.09	8.00	8.00
Polar distance the the excised cylinder	ρ	0.11	0.42	0.04	0.47	0.29	0.70
	ψ	0.48		0.66		0.82	
	z	0.68		0.70		1.00	
Tumor Size	s_1	2.79	2.99	1.93	3.31	2.67	3.19
	s_2	3.03		2.21		3.21	
	s_3	3.16		5.79		3.69	
Breast Laterality	R	4.21	3.81	3.72	3.75	4.12	4.16
	L	3.42		3.79		4.19	
Breast Density	B_1	7.13	6.08	6.29	6.74	5.44	6.23
	B_2	7.00		7.30		6.35	
	B_3	5.10		6.51		6.44	
	B_4	5.11		6.87		6.69	
Tumor Region	R_1	4.77	5.95	4.44	5.81	5.97	5.76
	R_2	6.77		4.53		5.51	
	R_3	6.80		5.06		5.72	
	R_4	4.94		5.50		5.85	

From the obtained results it is observed that the points' coordinate has the most significant effect on prediction and as expected, each coordinate point, individually, contribute more in their own axis. The second remarkable feature is the distance to the tumor which reflects the Euclidean distance of each point to the tumor (represented as a cylinder). Such trait was also relevant to the features' behavior observed in the clinical analysis since points in larger distances from the tumor region are deformed less (see Section 6.3.1.2). Another interesting observed trend is the impression of the Z axis on the importance of the features. While the breast is more affected in the Z axis with respect to the tumor location (see Section 6.3.1), it is expected that features related with it, are more represented on that axis. Reported analysis of the two features, *coordinate difference to the excised cylinder* and *polar distance to the excised cylinder* satisfy the expected hypothesis. Far from expectations, it can be deduced that the tumor size feature not only influences the breast final deformation less than other clinical features but also shows an irrelevant behavior compared with the tumor region or the breast density features.

Additionally, to complete the investigation of features on the evaluation results, each clinical feature is assessed individually with respect to its impression of the best-obtained prediction. Table 6.10 reports the results of individual evaluations on the three studied clinical features including breast density, tumor size, and tumor region. By looking to the breast density, it is observed that the average distance error decreases with a direct relation to the amount of the adipose tissue (Table 6.10), as was previously observed in Section 6.3.1.1.It can be deduced, breasts with more fibro-glandular tissue, are less affected. The results reported in Table 6.9 signifies the weakest role of the tumor size among clinical features; however, the outcome presented in Table 6.10 provide more evidence to evaluate the contribution of this feature. It is observed that large tumors impose more deformation, which is also an expected result, based on the results obtained in Section 6.3.1.2. Regarding the tumor region, it is difficult to conclude anything relevant, since, by looking to the obtained results, the magnitude of the deformation seems independent on the quadrant.

Table 6.10: Individual evaluation of the clinical features (breast density, tumor size, and tumor region) with respect to the adaptive weight RF in scope of the average OF.

	Breast Density				**Tumor Size**			**Tumor Region**			
	A	B	C	D	S	M	L	UOQ	UIQ	LOQ	LIQ
μ	1.052	1.050	1.048	1.044	1.045	1.049	1.051	1.052	1.049	1.051	1.042
σ	0.931	0.910	0.890	0.891	0.900	0.905	0.911	0.920	0.901	0.910	0.891
Max	5.257	5.256	5.218	5.230	5.178	5.233	5.310	5.291	5.206	5.273	5.191

6.4.2 Gradient Boosting Regression

As in RF, in GBR a cross-validation is performed with LOPO strategy, the following range for each parameter of the model:the number of estimators (trees), in the rage of $\{5, 10, ..., 500\}$; the maximum number of features in each tree in $\{2, 3, ..., 23\}$; the leaf size in $\{1, 2, ..., 5\}$; and the

learning rate in the range of $\{0.01, 0.02, ..., 1\}$. Besides, the criterion which measures the quality of a split is set *Friedman MSE*. The numerical evaluation are reported in Table 6.11 and Table 6.12, for both the average and Hausdorff OFs.

Table 6.11: Numerical evaluation: Pair-wise distance (in *mm*) between predicted PCLs and post-surgery models using GBR. The training set is sampled with rate of 65% and 75% due to average and Hausdorff OFs, respectively.

	Average-based OF	**Hausdorff-based OF**	**Baseline evaluation**
	D^{p2p}	D^{p2p}	D^{p2p}
μ	1.326	1.631	2.206
σ	0.943	1.026	1.920
Max	5.933	5.564	8.410

Table 6.12: Numerical evaluation: Global distances (in *mm*) between predicted PCLs and post-surgery models using GBR. The training set is sampled with rate of 65% and 75% due to average and Hausdorff OFs, respectively.

	Average-based OF		**Hausdorff-based OF**		**Baseline evaluation**	
	$D^{global}_{pred \to post}$	$D^{global}_{post \to pred}$	$D^{global}_{pred \to post}$	$D^{global}_{post \to pred}$	$D^{global}_{pre \to post}$	$D^{global}_{post \to pre}$
μ	1.287	1.269	1.604	1.590	1.758	1.731
σ	0.928	0.906	0.985	0.972	1.333	1.277
Max	5.735	5.701	5.439	5.394	6.512	6.317

By comparing with results obtained with RF, GBR presented worse results. Numerical comparisons indicate that the average *pair-wise distance* obtained by GBR was 1.326 *mm* and 1.285 for the average *global distance*. The performance of GBR should be investigated through the definition of the learners. To keep the learners weak, constraints were imposed on the number of leaves and the depth of the trees. The assigned constraints to maintain the trees small have led to propagate error in the whole sequence of the model, which is noticeable through the increase of the errors in comparison with RF; however, more research could be performed in future in order to improve the understanding of this behavior.

6.4.3 Multi-Output Regression

Contrarily to expectations, Multi-Output Regression (MOR) presents poor results in both OF optimization, comparing to the RF. Numerical results of Table 6.13 and Table 6.14 express the performance of MOR with *pair-wise* and *global distances*.

Discussed in Section 6.4.1.3, some of the most important features, presents a high correlation of each individual axis with each specific direction. This fact might influence the MOR to present poor predictions. More experiments should be performed in the future, but by the obtained

Table 6.13: Numerical evaluation: Pair-wise distance (in *mm*) between predicted PCLs and post-surgery models using MOR. The training set is sampled with rate of 65% and 75% due to average and Hausdorff OFs, respectively.

	Average-based OF	**Hausdorff-based OF**	**Baseline evaluation**
	D^{p2p}	D^{p2p}	D^{p2p}
μ	1.173	1.330	2.206
σ	0.993	1.022	1.920
Max	5.746	4.738	8.410

Table 6.14: Numerical evaluation: Global distances (in *mm*) between predicted PCLs and post-surgery models using MOR. The training set is sampled with rate of 65% and 75% due to average and Hausdorff OFs, respectively.

	Average-based OF		**Hausdorff-based OF**		**Baseline evaluation**	
	$D^{global}_{pred\rightarrow post}$	$D^{global}_{post\rightarrow pred}$	$D^{global}_{pred\rightarrow post}$	$D^{global}_{post\rightarrow pred}$	$D^{global}_{pre\rightarrow post}$	$D^{global}_{post\rightarrow pre}$
μ	1.130	1.114	1.301	1.286	1.758	1.731
σ	0.935	0.903	0.983	0.966	1.333	1.277
Max	5.695	5.623	4.682	4.621	6.512	6.317

results we can say that the points' coordinate could play an independent role in predicting the displacement of each axis.

6.4.4 Summary

In this section two ML methodologies were studied; RF and GBR. The influence of sampling the data was studied taken into account the performance of the algorithm in terms of computational time and error of the prediction. Additionally, the use of adaptive weights was shown to have a positive influence on the prediction. In any case, it might be difficult to understand the magnitude of the error, due to the lack of comparative approach, which could lead to the weak understanding of the obtained results. For this reason, a Heuristic Model (HM) was designed, taken into account the feature analysis performed in Section 6.3.1. With this simple and heuristic method, we could understand how difficult is to achieve a good result without using complex models, taken into account only the knowledge of the problem.

The method comprises the computation of mean displacement (expressed in Equation 6.5) of each point in the PCL data. This is performed separately on each axis and in each quadrant independently.

$$\overline{disp}_{i\in\{x,y,z\}}^{\,q\in quadrants} = \frac{1}{n}\sum_{i=1}^{N}(P_i^{post} - P_i^{pre}) \tag{6.5}$$

where ${P_i}^{pre}$ and ${P_i}^{post}$ are corresponding points of pre- and post-surgery PCL, respectively, and N is the number of points in each PCL. The proposed HM follows the following strategy: the

displacement of each point belonging to the healthy quadrants is computed based on the average displacement of each specific quadrant; for the points belonging to the unhealthy quadrant, the displacement is computed taken into account the average displacement of that quadrant, but multiplied both by $\{4,3,2,1\}$ for the breast density ($\{A,B,C,D\}$, respectively), and by $\{3,2,1\}$ for tumor size ($\{L,M,S\}$, respectively), following the knowledge obtained in the Section 6.3.1 (see Equation 6.6):

$$P_i^{new} = \begin{cases} P_i + \overline{disp_i}^{\,q} & P_i \in \textit{healthy breast quadrants} \\ P_i + b \times s \times \overline{disp_i}^{\,q} & P_i \in \textit{quadrants which comprises the tumor} \end{cases}, \tag{6.6}$$

where b, s, and $\overline{disp_i}^{\,q}$ are breast density, tumor size, and displacement of the equivalent breast quadrant, respectively, and finally, p_i^{new} denotes the calculated post-surgery PCL. The presented results of Table 6.15 are obtained by this this approach.

Table 6.15: Numerical evaluation: Point-wise and global distance (in *mm*) between predicted and post-surgery PCLs using heuristic model. The training set is sampled with rate of 65%.

	Average OF		
	D^{p2p}	$D^{global}_{pred \to post}$	$D^{global}_{post \to pred}$
μ	1.634	1.522	1.503
σ	1.496	1.193	1.129
Max	5.763	5.326	5.136

By comparing this simple approach with the learning models presented previously, we can state that the magnitude of the error obtained with RF is acceptable. The framework designed in this work, composed by data, features, and models, presented some simplification regarding the reference framework from Vavourakis *et al.* [197], which could lead to some errors on the prediction, but with not so high influence in the visual aspect. Some new directions for this line of research are already planned to try to improve the obtained results, which will be presented in the Chapter 8.

6.5 Discussion

Considering the characteristics of the problem, such as the type of features, and the demanded output, RF based methodologies were primarily chosen as learning models for this problem. We started by studying the influence of data sampling for the performance of the model, and it was observed that less sampling generally leads to less errors on the prediction, but took to high computational time. Focusing on the *pair-wise distance*, the declining trend of errors stops when the sampling rate reaches to 65%. More sampling rates result in the errors oscillating in a the range of 0.1 *mm*. Although the difference errors between the distances in the range of 45% to 100% remains about 0.1 *mm*, the sampling rate with the minimum distance (1.048 *mm*) was chosen as

the final sampling rate (65%). Same argument has been carried out to select the sampling rate of 75% when the OF is set to be Hausdorff distance. The minimum distance with respect to the Hausdorff OF is reported near to 4.022 *mm*.

The influence of weighting was also taken into account. Following the strategy of adaptive weight assignment, the points on training data PCLs were weighted based on the errors to the corresponding point in the target PCL. It should be noted that the trained model in each iteration is evaluated to determine the new weights for the next iteration. The obtained results highlight the effectiveness of using an adaptive weighting function, obtaining better results, even they are not so significant. Additional investigation should be performed in this part, in order to find the most suitable weighting function for this problem.

RF was compared with GBR methodology. As previously discussed, learners of the GBR was kept weak intentionally to refrain the greedy growth of the methodology. The imposed constraints kept the learner leaves less (or equal) than 3, and the depth of the learners less (or equal) than 5. Therefore, in both lines of OF, an increase of the distances was observed. However, it should be mentioned that the current strategy to consider the aforementioned constraints, limited the range of reported distances, in which the average and maximum distance in the two OFs approached to each other.

A MOR approach was also taken into consideration. Although the results showed that it fell behind the single output RF, this weak result might lay in the facts that not only the MOR trainer was unable to find a correlation between the points' displacements of multiple coordinates, but also the features of different coordinates intruded the learner such that they cancel the impression of each other. The aforementioned hypothesis needs to be investigated more to determine the weak performance of MIMO methodology.

Finally, to close the discussion, it should be noted that all the regressors were trained with the same sampling rate. The RF with adaptive weights outperforms the other regressors with 1.048 *mm* and 4.083 *mm* for the average and the Hausdorff optimization, respectively. In the second rank, RF without consideration of adaptive weights stands with an average distance of 1.052 *mm* and maximum distance of 4.101 *mm*. Third and forth ranks were obtained by MOR (with average of 1.173 *mm*, and Hausdorff of 4.738 *mm*), and GBT (with average of 1.326 *mm*, and Hausdorff of 5.564 *mm*).

6.6 Summary

In this chapter, the use of ML techniques to predict the breast deformation after BCS is developed to use real MRI data of patients without depending on the knowledge of physical equations to describe the deformations.

To overcome the nonexistence of dataset suited for learning breast healing deformations, an in-house dataset was generated using MRI data from real patients combined with a multi-scale biomechanical and biochemical models to simulate post-surgical breast shape. Several clinical

features that might impact breast healing deformations, including breast density, tumor region, and tumor size, were considered in the creation of the dataset.

The learning process was divided into two main tasks: feature inspection and model selection. In the first task, the complex interplay of clinical features for conditioning the breast shape after surgery healing was untangled by comparing the influence of different sets of features in the deformed breast after resulted from BCS. Here, it was concluded that breast density had the highest impact on the breast displacements while the quadrant where comprises the tumor was determined to predict the directions of shape adjustments. Further analyses of features' importance resulted from learning process reinforced the experimental findings. In the model selection task, several regression methodologies, including Random Forest, Gradient Boosting Regression, and Multi-Output Regression were studied. Besides the learning model, a heuristic model was also proposed to validate the veracity of learning methodologies and understand the magnitude of the distances. Additional investigations were conducted with respect to sample PCL data, as well as a complementary study to assign different weights to the training instances, which resulted in predictions with slightly better evaluations. The numerical evaluations with the pair-wise and global distances indicated that the RF regressor constructed with the adaptive weighted training set outperformed MOR and GBR in both lines of average and Hausdorff OFs.

Chapter 7

Designing a Planning Demonstration for BCS

The proposed methodologies in Chapter 3 to Chapter 6 have been implemented to provide the aimed planning tool for BCS within three demonstrations. The aforesaid planning demonstrations consist of three applications dealing with 3D reconstructing patient torso and segmenting breast completely, generating parametric model for patient's breast, and predicting breast shape after BCS. In addition, proper Graphical User Interfaces (GUI) have been designed to facilitate user interaction. It should be noted that since the implemented demonstrations have only been tested with our clinical partners, they are not a medically validated widespread.

In the following section, first, the shared developing framework between the implemented demonstrations will be explained. Then, detailed description of each of them will be discussed including the functional requirements (i.e. actors, use cases and user stories) of the demonstrations are explained as well as the non-functional requirements (i.e. design and application flow).

7.1 Shared Developing Framework

To use the potential of a fast data passing between the implanted demonstrations, the same developing framework (the core programming language, the dependencies, and the GUI designing tool) was employed.

7.1.1 Functional Requirements

Functional requirements are defined based on the expectations motivated by the development of each demonstration. In further sections where the demonstrations are individually explained, the functional requirements will be stated in details.

7.1.2 Non-functional Requirements

Although non-functional requirements are not crucial for normal performance of each demonstration, their main responsibility involves facilitating the interaction with user. Non-functional requirements are mostly consist of the implementation of interface, the maintenance strategies, and the provision of proper plans for further developments. The shared non-functional requirements between the demonstrations are briefly explained in the following.

7.1.2.1 Interface

The user interface must be intuitive, allowing users to access all the functionalities with the minimal interaction in a logical way. To enhance this process, many of the functionalities are enabled (or become visible) as soon as the proper data are loaded. Hence, the flow of the demonstration is designed to inform the user in the best way to provide the required data before the required process is performed.

7.1.2.2 Maintenance

The demonstrations were developed in a way to easily modify the implemented functionalities. Employing both object-oriented and structured programming make the detection of possible bugs feasible in the level of maintenance. Besides, the demonstrations are designed to keep track of actions through standard log recording. These logs can be retrieved to track possible either application's malfunction, or data corruption.

7.1.2.3 Further Development

The demonstrations were developed in a way to easily extend or add additional functionalities. As the development was done with respect to object oriented programming, improving the demonstrations is feasible by either adding or changing some of the functions.

7.1.3 Development Framework

All the three aforesaid demonstrations have been implemented in the same framework to increase the development potentials, as well as to ease the maintenance. In the following, the used frameworks and required dependencies are explained.

7.1.3.1 C++

The code of the demonstrations, including the registration and segmentation, the parametric model generation, and the the breast shape prediction, have been written using *C++* version 11. They have been developed in Microsoft Visual Studio 2012 Enterprise Edition, and have been compiled with the commercial compiler provided in the same package. To increase both the readability and the maintenance, they are all written with respect to structured programming in *.cpp* files, benefiting from defining objects in corresponding header files ending at *.h*.

The codes have been written clearly with appropriate *object names* and *function calls* to increase the readability of each them. Additionally, comments were used alongside the main code to clarify the definition of variables or explanation of functions.

7.1.3.2 Qt

While Qt[1] allows to develop multi-platform applications, it has been used to design GUI of all the demonstrations. Using standard Graphical Objects, user interfaces were developed and presented in *.ui* files.

7.1.3.3 VTK

The Visualization Toolkit[2] (VTK) is an open-source software system used for 3D computer graphics, image processing, and visualization. It comprises several objects and functions library to deal with the visualization of 2D and 3D data.

Not only the visualization, VTK is integrated to manipulate pointclouds with embedded function, hence calling the provided local function increases the performance of the application whenever it is required to perform specific manipulations on 3D models. This facility makes VTK a good option to be used for the development of the aforesaid demonstrations. In the current implementations, VTK library version 6.2 was used with the purpose of both visualization and interaction with 3D pointclouds and meshes.

7.1.3.4 OpenCV

OpenCV[3] (Open Source Computer Vision Library) is an open source library for computer vision and machine learning processing. Similar to VTK, it has been provided in multiple platforms; hence and with respect to the chosen coding language, C++ implementation has been taken into consideration. It should be noted that OpenCV 2.3 has been used for the implementations.

7.1.3.5 Boost Library

Boost library is a set of libraries implemented in C++ that allows an easy utilization of linear algebra, image processing and multi-threading. These libraries were required for the utilization of VTK and Qt frameworks. In addition, to speed up the computation required for 3D visualization, multi-threading functionality Boost was exploited as well.

7.2 3D Reconstruction of Torso and Complete Breast Segmentation

The first chain in the pipeline of the proposed BCS planning approach is the reconstruction of patient's 3D torso. It is achieved by registering three depth views captured by Microsoft Kinect from

[1] http://doc.qt.io/
[2] https://www.vtk.org/
[3] https://opencv.org/

different angles. Discussed in Chapter 3, the reconstruction was performed in three steps comprising coarse, fine, and non-rigid registration. Besides, since the color quality of the reconstructed model is influenced by the changes of torso illumination during data acquisition, an additional step is considered to enhance the color of the reconstructed model by using a frontal image of the patient captured by a high quality camera via image processing techniques.

7.2.1 Functional Requirements

The functional requirements of the aforesaid demonstration, such as the actors, and the way to interact with the system, are explained in the following.

7.2.1.1 Actors

Both surgeons and radiologists are considered as health professionals and are allowed to perform any of the functionalities presented in the demonstration.

7.2.1.2 Functionalities

The developed application comprises the following functionalities:

- Loading RGB and depth data from acquisition
- Loading a high-quality image taken by camera
- Loading the annotated pectoral muscle obtained from MRI data
- Changing the automatically selected views
- Visualizing 3D reconstructed torso
  - Zooming model
  - Changing model point size
- Extracting 3D models in PLY format
- Visualizing exterior breast contour (2D visualization)
- Visualizing breast complete contour (3D visualization)
  - Zooming model
  - Changing model point size
- Extracting breast complete contour in PLY format
- Reset

7.2.1.3 User Stories

The demonstration is developed to fulfill the user stories described in Table 7.1.

Table 7.1: Different user stories for 3D reconstruction

ID	Name	Priority	Description
UR001	Load data	High	The user wants to load depth data to generate 3D model. The annotated MRI data and the frontal HQ image are loaded as well.
UR002	Data Visualization	High	The user may want to see the loaded images, and data.
UR003	3D registered model visualization	High	The user may want to check the registered model of patient torso.
UR004	Changing automatic selected views	Medium	The user may want to change the view selected for registration with the purpose of obtaining correct 3D reconstruction in case the automatic registration is failed.
UR005	Zoom in/out	Medium	The user may want to zoom in/out reconstructed models.
UR006	Rotate	Medium	The user may want to check the reconstructed models from different angles.
UR007	Visualize breast exterior contour	Medium	The user may want to visualize the detected exterior contour of breast
UR008	Visualize breast complete contour	Medium	The user may want to see breast complete contour segmented from patient's 3D reconstructed torso.
UR009	Export 3D model	High	The user may want to export either patient 3D model, segmented breast, or patient torso without breast.

7.2.1.4 Use Cases

Figure 7.1 describes possible interactions that a user can have in the demonstration. Note that simple interactions were ignored.

7.2.2 Application Flow

The flow presented in Figure 7.2 shows the required steps to perform the reconstruction of patient's torso.

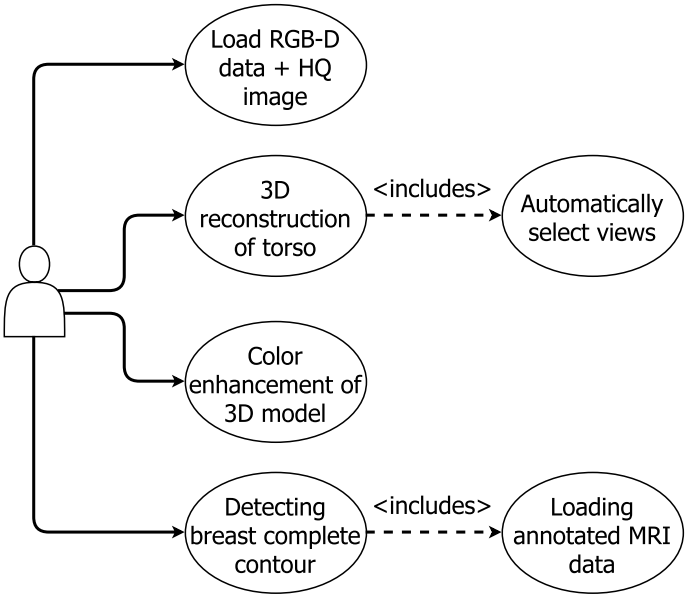

(a)

Figure 7.1: Use cases for the 3D reconstruction and breast segmentation application

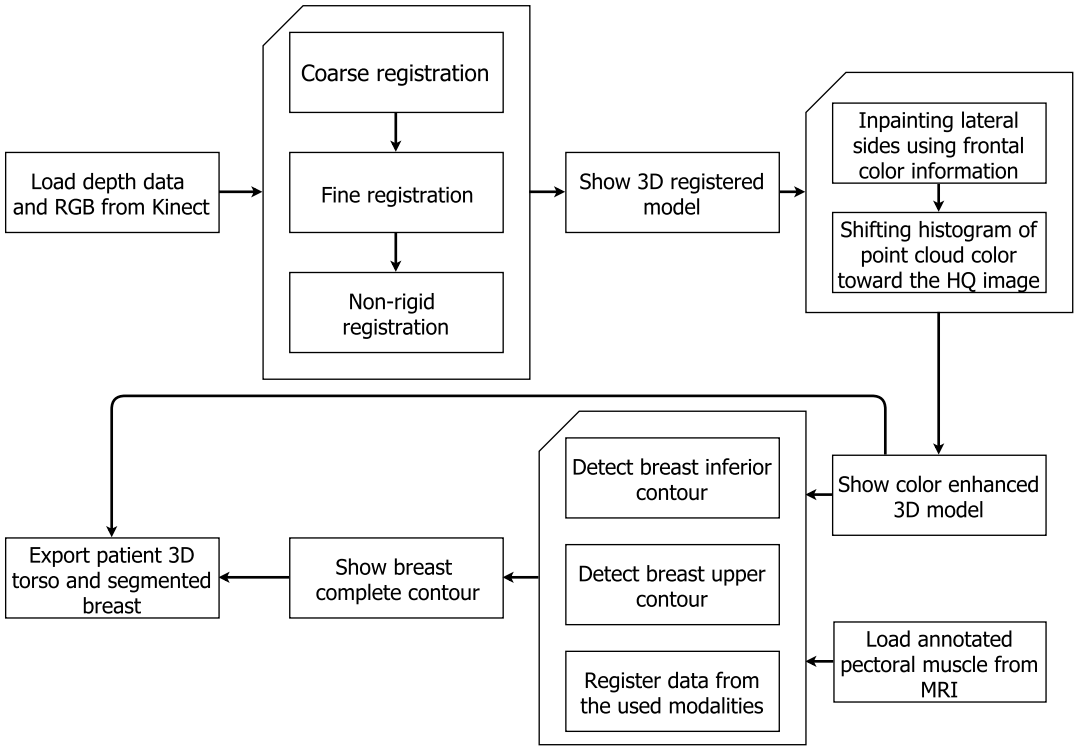

Figure 7.2: The flow of the reconstruction application

7.2.3 Interface

Different stages of the 3D reconstruction and segmentation demonstration are depicted in Figure 7.3(a), and Figure 7.3(b). The application is developed in a tabular design corresponding to each stage to be performed in order to obtain 3D reconstructions. The application is launched in the first tab demanding the user to select the directory containing patient's data. By choosing the directory, the view selection is performed automatically and then they are shown to the user for confirmation. Not only the selected views, the frontal high-quality image captured for the purpose of color enhancement (Figure 7.3(b)) is shown as well.

The reconstruction is performed in the second tab, as it is depicted in Figure 7.3(c). However, since the color quality of the output is influenced by the changes of the illumination, an extra step is required to improve the color of the 3D model.

The final tab is developed to segment breast from the reconstructed torso, based on the methodology presented in Chapter 4. The output is then visualized to the user while it can be exported in 3D format. Figure 7.3(d) illustrates the Segmentation tab.

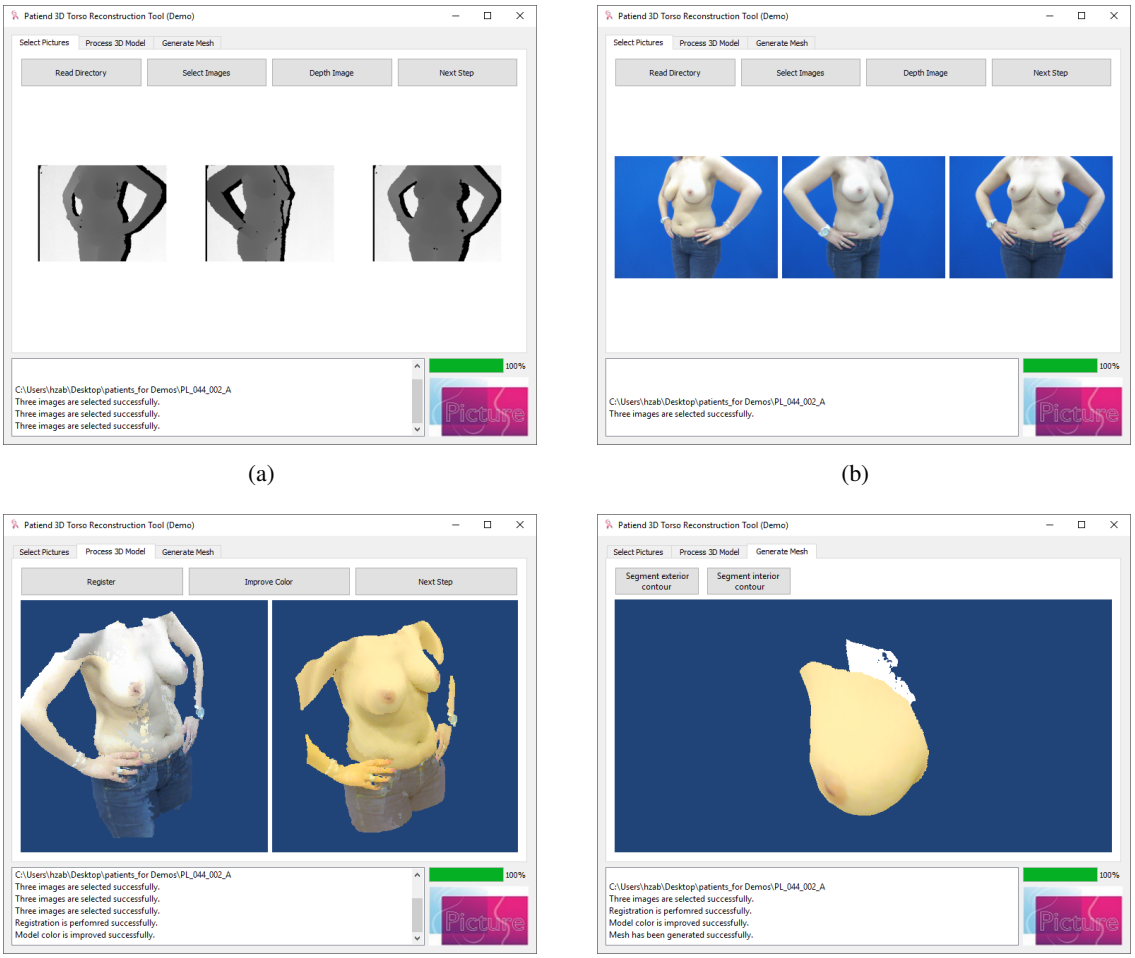

Figure 7.3: Interface of the 3D reconstruction and segmentation of Breast demonstration, (a) loading depth data, (b) loading Kinect RGB data, (c) 3D reconstruction of patient's torso and color enhancement, (d) breast segmentation

7.3 Parametric Model Generation

Discussed in Chapter 5, the parametric model is generated with the intention of providing a deformable breast model for physicians to impose possible deformations on patient's 3D model of the breast.

7.3.1 Functional Requirements

The functional requirements describing the parametric model generation demonstration and its components such as the actors, and the way to interact with the system, are explained in the following:

7.3.1.1 Actors

Physicians are considered as health professionals and they are allowed to perform any of the functionalities presented in the demonstration during the consultations with patients.

7.3.1.2 Functionalities

The developed application comprises the following functionalities:

- Loading 3D breast data
- Loading patient 3D torso
- Selecting breast laterality
- Defining initial model of parametric model
- Defining quantity of control points in each axis
- Generating parametric model of breast
- Superimposing the parametric model over the loaded patient torso
  - Zooming
  - Rotating
  - Changing model point size
- Imposing breast deformation by selecting a point on the parametric models and dragging it
- Extracting deformed breast model in PLY format
- Extracting deformed breast superimposed on the model of patient's torso in PLY format
- Undo
- Reset

7.3.1.3 User Stories

Concerning the application of breast parametric model generation, different user stories are analyzed and reported in Table 7.2.

7.3.1.4 Use Cases

Figure 7.4 describes possible interactions that a user can have in the application. Note that the simple interactions are ignored.

Table 7.2: Different user stories for the parametric model generation demonstration

ID	Name	Priority	Description
UP001	Load 3D breast	High	The user have to select a patient directory including breast 3D model and 3D torso without breast.
UP002	Define initial model	High	The user have to select the initial model required to generate parametric model.
UP003	Define quantity of control points	High	The user may want to define the number of required control points in each axis.
UP004	Visualize parametric model	High	The user may want to see the generated parametric model not only in individual view, but also superimposed on patient's 3D reconstructed torso.
UP005	Impose deformation	High	The user may want to deform the parametric model by selecting a model point and dragging it.
UP006	Zoom in/out	Medium	The user may want to zoom in/out the parametric model, or patient torso for better visualization.
UP007	Rotate	Medium	The user may want to rotate the parametric model, or patient torso for better visualization.
UP008	Export	Medium	The user may want to export the deformed breast (individually or superimposed on patient torso) in PLY format.
UP009	Undo	Medium	The user may want to cancel the most recent deformation and restore the model's previous shape.
UP010	Reset	Medium	The user may want to restore the initial state with purpose of loading new data.

7.3.1.5 Functional Constraints

The developed application has some constraints which should be considered while it is being used. Those constraints are presented below:

- There are no defined physiological constraints for the imposed deformations; therefore, unnatural breast shapes can result in the interaction.
- Theoretically, control points can be defined in any quantity; however, due to memory constraints, the quantity is limited up to 15 in each axis.

7.3.2 Application Flow

Figure 7.5 illustrates the application flow of the parametric model generation demonstration.

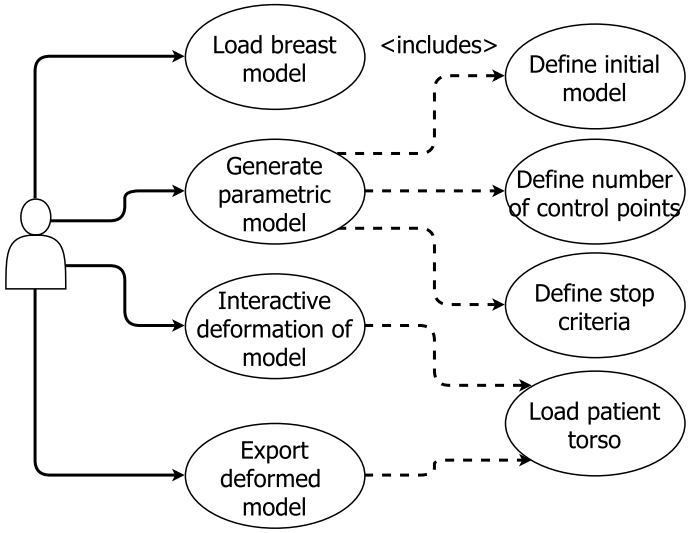

(a)

Figure 7.4: Use cases for the parametric generation demonstration

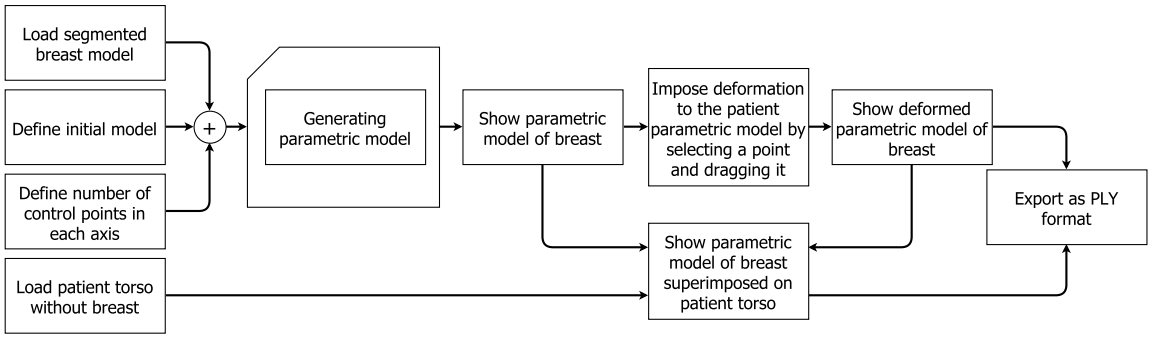

Figure 7.5: The flow of the parametric model generation demonstration

7.3.3 Interface

The interface of parametric model generation demonstration is depicted in Figure 7.6. As the application is launched, the user has to select the directory where patient's 3D data are stored. As soon as the segmented breasts and the patient torso is loaded to the application, the user is guided to select the breast laterality in order to generate the parametric model for that. The next step is followed by choosing the initial model from the two predefined ones: plane and superellipsoid. Besides, the user must define the number of control points in each direction used to generate the parametric model.

To control the iterations of the parametric model generation two stop criterion are considered with respect to either distance toward the segmented breast, or the number of performed iterations. Total time required to reconstruct a parametric model, considering $7 \times 7 \times 1$ control points and superellipsoid initial model, is measured to be less than 117 s. The stop criteria were set to be distance-based less than 0.5 mm.

The details have been previously explained in Chapter 5. Final parametric model is illustrated in the two visualizers, individual breast model is the right, and the breast model superimposed on patient's torso in the left visualizer. While left mouse click is associated to rotate the models, middle mouse button can be used to pan the visualizer, and the right mouse button is configured to drag the points of the model and impose user deformations. Finally, either the deformed breast model or the breast superimposed on the patient's torso can be exported, in standard 3D file formats.

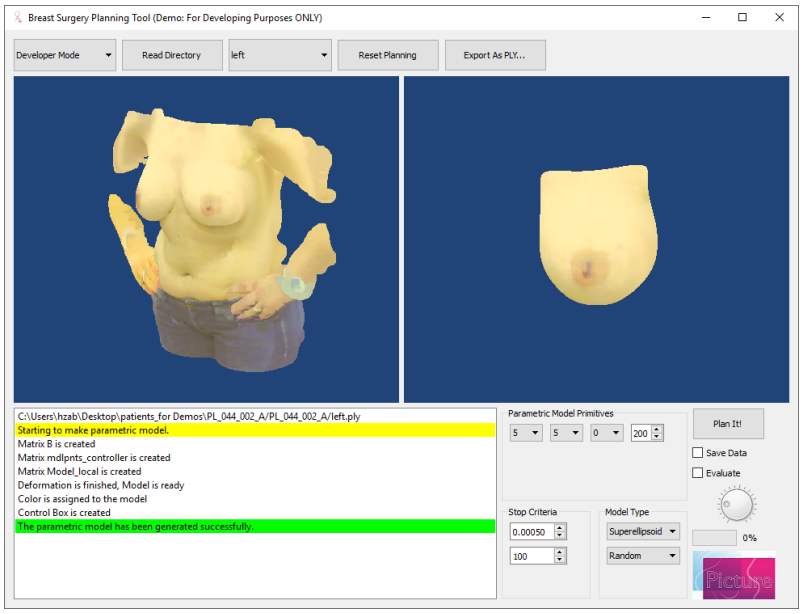

(a)

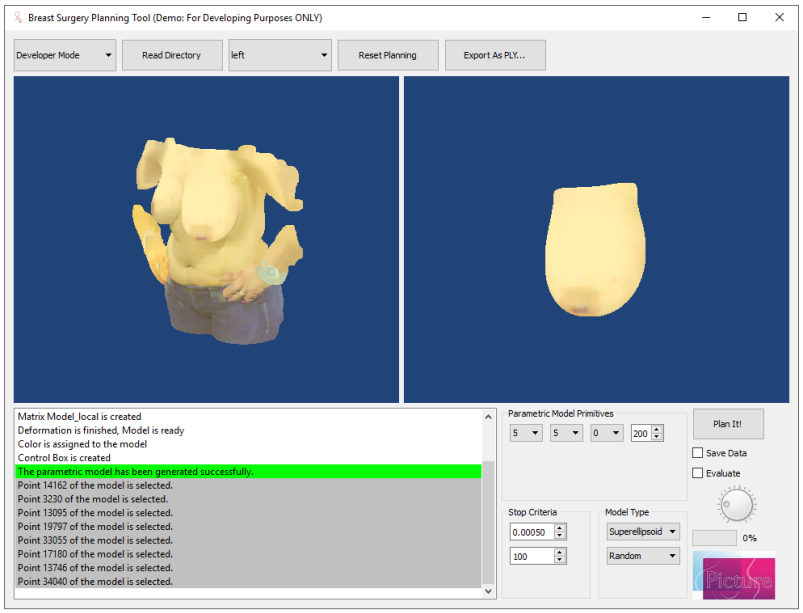

(b)

Figure 7.6: Interface of breast parametric model generator; (a) generating breast parametric model, and (b) imposing deformation interactively by mouse dragging

7.4 Breast Shape Prediction After BCS

The breast shape prediction demonstration is aimed to assist health professionals to understand the surgical outcome of breast shape resulted from tumor resection surgery. In this regard, the 3D model of a breast reconstructed from MRI data must be loaded while the tumor is inserted and configured, as well as the patient's physiological characteristics. The further step is followed by loading a previously trained model to simulate the healing process of the breast after removing the inserted tumor. The simulated shape of the breast is the predicted shape of the breast after the healing. The details of both tumor insertion and training of ML model have been discussed in Chapter 6.

Not only prediction, but also the designed application can be used to generate the dataset of breast models by varying the physiological properties of patient's breast, and tumor characteristics. The details of generating such dataset used to train the applied machine learning model was discussed in Chapter 6.

7.4.1 Functional Requirements

7.4.1.1 Actors

Surgeons are the main contributors of the breast prediction demonstration; however, physicians can benefit from this demonstration during the consultations with patients.

7.4.1.2 Functionalities

The developed application consists of the following functionalities:

- Loading Breast Model
- Loading tumor characteristics
  - Tumor size
  - Tumor location (either random definition for dataset construction, or exact location for simulation)
- Loading patient characteristics
  - Breast density
- Visualizing 3D model
  - Rotating
  - Zooming
  - Changing point size
- Locating the position of nipple

- Showing/hiding breast regions (quadrants)
- Visualizing information
  - Tumor position – quadrants
  - Breast laterality
  - Breast volume
  - Tumor size (dimensions, radius)
  - Tumor volume
  - Excision volume
- Undo
- Redo
- Reset

7.4.1.3 User Stories

Table 7.3 reports variety of user stories while using the breast shape prediction demonstration after BCS.

7.4.1.4 Use Cases

Figure 7.7 describes the possible interactions that a user can have in the demonstration. Note that simple interactions were ignored.

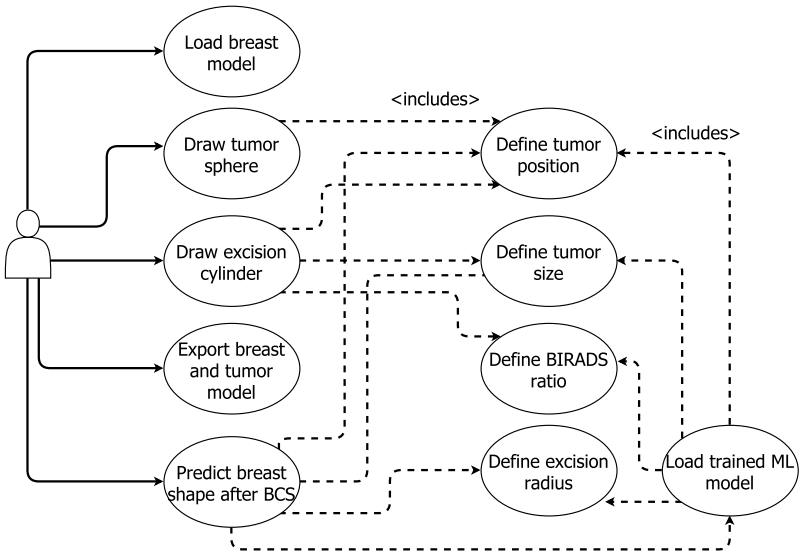

(a)

Figure 7.7: Use cases for the breast shape prediction demonstration

Table 7.3: Different user stories for the breast shape prediction after BCS demonstration

ID	Name	Priority	Description
US001	Load model	High	The user may want to load a specific breast's model of a patient.
US002	Model visualization	High	The user may want to rotate, zoom or pan the loaded model for visualization.
US003	Change orthogonal view	High	The user may want to visualize the breast model on an orthogonal view (front, top, bottom, back, lateral).
US004	Define nipple position	High	The user have to define the nipple position on the point cloud.
US005	Zoom in/out	Medium	The user may want to zoom the breast model in or out for better visualization.
US006	Change point size	Medium	The user may want to change the model point size for better visualization.
US007	Define BIRADS	High	The user may want to define the ratio of fibroglandular and adipose of the patient's breast.
US008	Define tumor position	High	The user may want to define the tumor's position, either by picking a point or choose a random location within the defined quadrant.
US009	Define tumor size	High	The user may want to define the tumor's size (small, medium, large, that are 5%, 7.5%, and 10% of breast total volume, respectively)
US010	Visualize tumor sphere	High	The user may want to see the tumor drawn with with a sphere within the breast's point cloud.
US011	Visualize excised cylinder	High	The user may want to see the excised cylinder passes through the breast from the skin toward the pectoral muscle.
US012	View breast volume	High	The user may want to be informed about the volume of the loaded breast.
US013	View excised volume	High	The user may want to know excision volume, including the tumor and surrounding tissue (excised cylinder).
US014	Export tumor	High	The user may want to export the model of breast with defined tumor and BIRADS ratio.
US015	Visualize deformed breast	High	The user may want to see the deformed breast after the simulated BCS.
US016	Reset	Medium	The user may want to restore the application to the initial configuration to load new data.

7.4.1.5 Functional Constraints

The developed application has some constraints to represent the breast model as a point cloud. These constraints are presented as follows:

- The selected points for the nipple the tumor position must be a point of the model's point-cloud;

- The calculated volumes of the breast, the tumor, and the excised cylinder are estimated through approximations;
- The breast boundaries are not taken into account When the tumor's sphere and the excised cylinder are defined. In this way, the polygon which visualizes the excised cylinder might exceed the breast boundaries.

7.4.2 Application Flow

The flow presented in Figure 7.8 shows the required steps to perform the BCS planning.

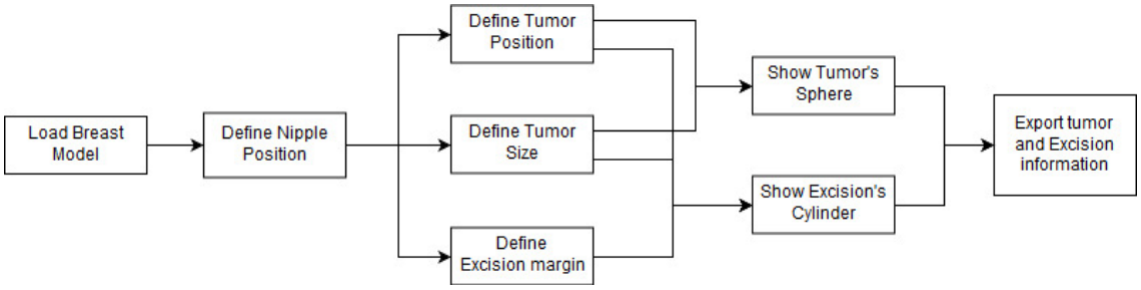

Figure 7.8: Prediction demonstration flow with the required steps to perform the BCS planning

7.4.3 Interface

Figure 7.9 shows the interface of the main functionalities of the application. When launching the tool, the initial window will be displayed, where it is only possible to load a breast point cloud. After loading the breast model, the nipple position has to be located by the user, via the left mouse click on a possible point of the model. Definition of the nipple position is followed by visualizing breast quadrants. This can be seen through planes drawn over the breast. In order to do the tumor definition, tumor position has to be selected as well as a tumor size. Completing all the required fields (indicating tumor size, and breast laterality), a sphere is represented as the inserted tumor within the breast. Finally, when selecting an excision margin, the excision's cylinder is drawn.

Regarding the interface, this was created considering the target group and adapted according to the application's purpose. One of the aspects that were taken into consideration was the used icons. Due to the lack of material's guidelines and icons to represent some of the intended actions, some icons used in the application were designed in order to overcome that lack and the ones that already existed were adjusted to provide an overall consistency among all the demonstrations. Other human-computer iteration principles were considered as the representation of already clicked buttons, and the pop-up of warning and dialog messages to inform the user of any error or task completion. The interface of the prediction demonstration is illustrated in Figure 7.10, where the interaction panels are delimited and coupled with a label.

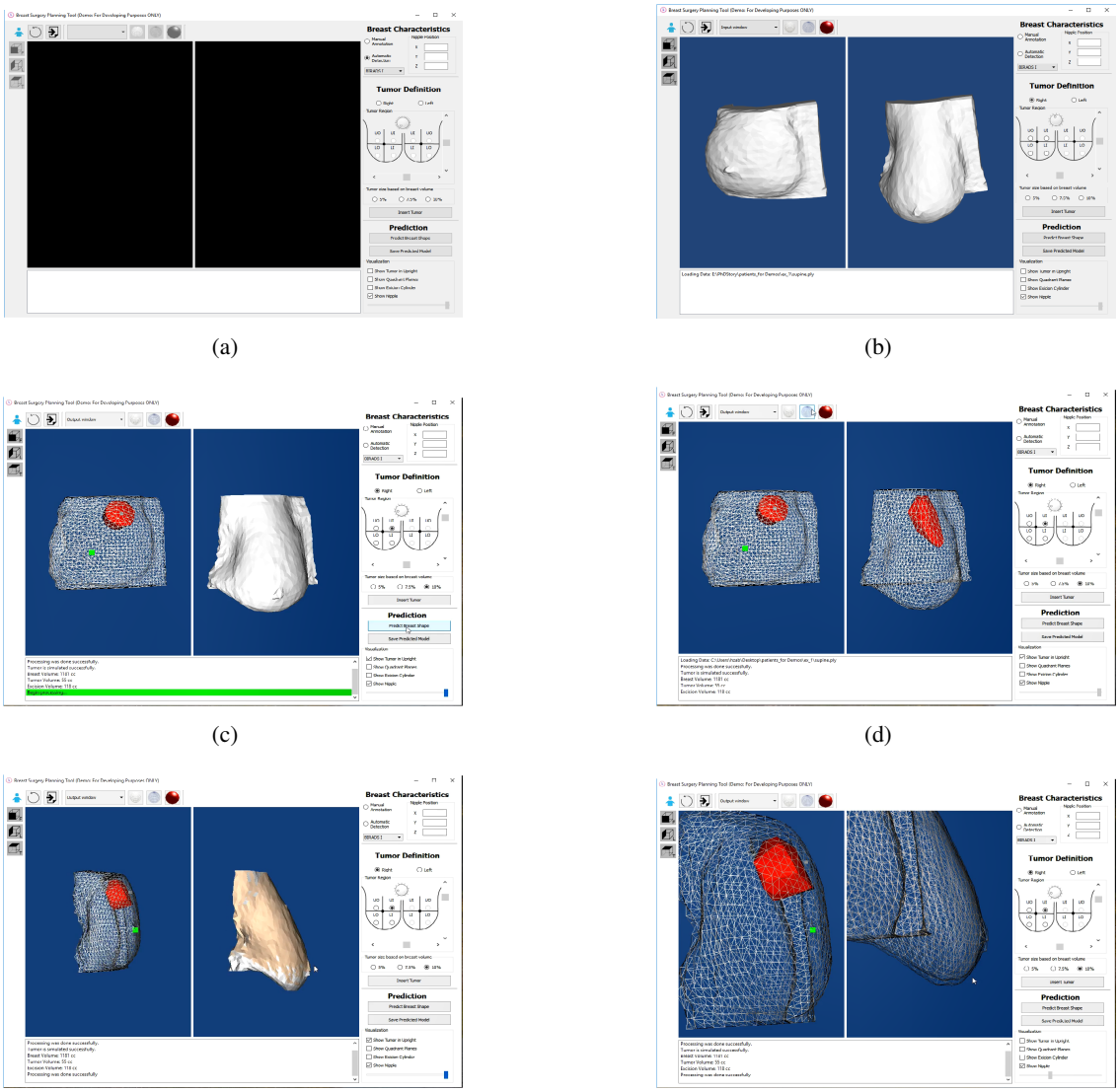

Figure 7.9: Interface of the breast shape prediction demonstration; (a) launching the demonstration, (b) loading patient' data, (c) locating tumor in supine position, (d) visualization of tumor in upright position, (e) prediction of the breast shape after removing the tumor (colored in gold), and (f) contraction of breast after the BCS prediction

7.5 Summary

In this chapter, three demonstrations were implemented with respect to the demands of a previously discussed planning approach for BCS. The first demonstration was responsible for the 3D reconstruction of patient's torso from RGB-D data acquired by Kinect. In addition, it was also responsible to segment breast completely using multi-modal data. The output of the first demonstration can be fed to the second one in order to generate a parametric model used to freely deform patient's own 3D model of the breast. This functionality provides a previously demanded framework for physicians to fill the gap having better communication with patients during the

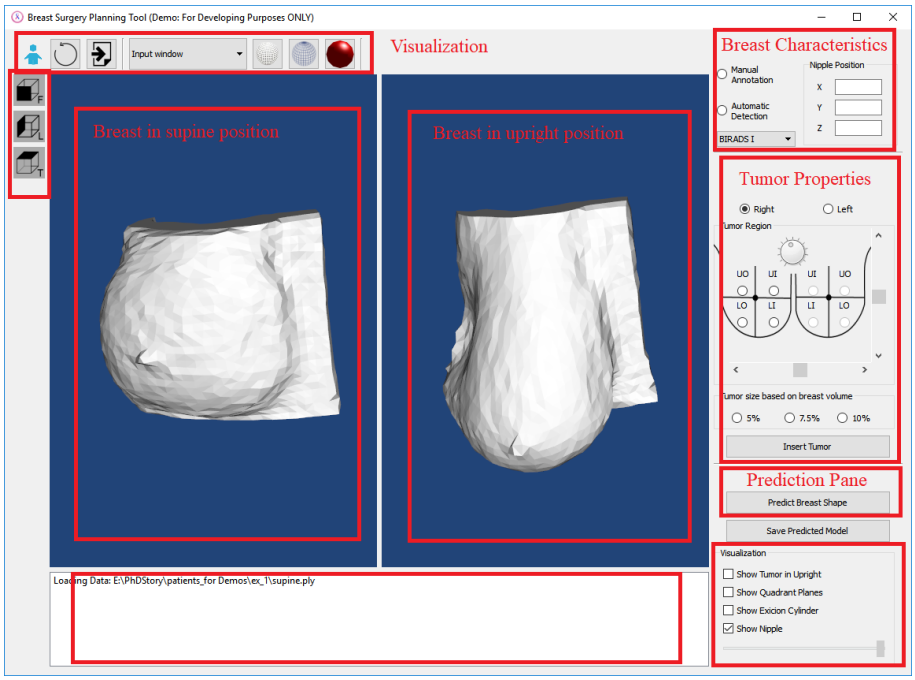

Figure 7.10: Breast shape prediction demonstration UI

consultations. Finally, with the last demonstration, the breast shape prediction demonstration, it is possible to model both the tumor and patient's own breast to have predicted breast shape after BCS wound healing.

To facilitate the development, and ease the maintenance procedure, all the demonstrations have been implemented in the same implementation framework. Considering C++ as the implementation language, Qt was contributed for designing GUI, Boost library was used for fast mathematical implementations, and VTK carried out the task of 3D visualization. Besides, OpenCV was used to speed up the mathematical operations as well. Finally, to provide a widespread planning approach, the GUI should be clear, intuitive, and simple; hence it was tried to design the demonstrations to increase the usability while keeping them easy to be followed.

Chapter 8

Conclusions

As one of the most important symbols of feminine, breasts are deformable organs located in front of the torso, that their responsibilities include children nourishment, and sexual attraction as well. Consisting mainly of adipose and fibroglandular tissue, they are highly deformable to either any imposed internal or external stresses, or physiological alterations (age, pregnancy, and menstrual cycle).

Breast cancer treatment that is mostly followed by invasive treatments, comprises tumor resection which deforms breast shape permanently. Nowadays, with widespread of screening, breast cancer is diagnosed in earlier stages with less tumor size, so that surgical treatments result in the better aesthetic outcome; however, breast deformation is still the main reason influencing patient's Quality of Life. Several studies have addressed the harmful influences of breast deformation resulted after breast cancer treatment on the psychosocial health of patients, mostly losing self-esteem, impairing sexual activities, and disliking towards their bodies. In addition, detailed investigations revealed that the aforesaid influences are directly related to the fact that patients are less satisfied with the shape of the treated breast. Comparisons with objective assessment show that a small portion of surgeries (6%) resulted in poor aesthetic outcomes. This fact highlights the gap between patient's expectation of surgery from one side, and surgeon's ability to describe the deformed breast shape to the patient from the other side.

While communication between patient and physician plays an important role to improve patient's understandings about surgery aftermath, current approaches studied in Chapter 4 were shown to be inefficient. Consultations before BCS are mainly focused to describe breast shape after imposed deformations by using pen and paper, or to draw on patient's body. However, using 2D approaches might not be appropriate enough to illustrate 3D breast shape. Though availability of methodologies to provide breast shape after breast augmentation surgeries, yet there has been no applicable approach satisfying such demand for BCS. Provision of a planning approach (aligned with the aforesaid demands) not only facilitates physician/patients communication to have a common understanding of breast shape after surgery but also elevates surgeons expertise in their performance.

Within the context of this research, it has been attempted to propose a planning approach

for BCS, considering the objective of improving pre-surgery consultations. Using the 3D model of patient's breast, physicians are able to illustrate the deformations resulted after BCS, while patients can have a better outlook on their body. The provision of the aimed planning approach involves several stages consisting of 3D reconstruction of patient's body, segmentation of breast from the 3D model automatically, generation of the parametric model from the 3D model for more interaction, and finally, prediction of breast shape after surgery.

Described in Chapter 3, the first chain in the pipeline of the BCS planning approach is the provision of patient's 3D model. Considering the available methodologies and sensors for 3D reconstruction, Microsoft Kinect was chosen to acquire raw data. With a defined protocol, patients were rotating in front of Kinect, and multiple views were captured. Three views containing one frontal and two laterals were automatically selected then and stitched via rigid registration. Since the patient was moving during data acquisition, a non-rigid registration stage was performed to compensate the movement's artifacts. Notwithstanding the two-stage registration, the reconstructed model presents unacceptable color quality, resulted from changes of illumination whilst the patient was rotating. Hence, the 3D model color was enhanced in two steps; first by relying more on the color of frontal views, and second by improving the color histogram of 3D model based on the image taken with a high-quality camera mounted over Kinect. The evaluations comprising rigid, nonrigid and color enhancement showed that the reconstructed model has enough details to be used for medical purposes.

Focusing on the planning approach for BCS, the 3D reconstructed model of patients should be segmented to have the breasts as the region of interest. While the state-of-the-art methodologies segmented only the inferior contour of the breast, the proposed methodology in this research performed a complete segmentation of both inferior and upper contours. Additionally, since the segmentation was done in 3D, the interior contour was defined through the annotated pectoral muscle in patient's MRI data. Using the proposed multi-modal approach, it is assured that a closed pointcloud surface was obtained after segmentation. Since the proposed approach to detect the inferior breast contour was inspired by a baseline methodology, evaluations revealed a similar detection. In addition, although the superior region of the breast is known to be featureless for contour detection, the proposed methodology detected the contour in an acceptable range. Finally, in absence of a standard method for numerical assessment, visual evaluations were conducted alone to assure the correctness of the pectoral muscle that had been transferred from MRI modality to 3D reconstructed data.

The presence of a parametric model of the patient breast is an important step in providing a planning approach since the physicians can interactively deform breast model generated from 3D reconstructed pipeline. The segmented 3D model of breasts still cannot be used in the proposed planning approach, as they were a set of individual scattered points. Unless they are not mathematically connected, the movement of a point does not distribute naturally among all the model. Such behavior prevents interaction with the breast model as a tissue with interconnected points. The procedure to create a mathematical model for segmented breast data was performed by using FFD approach. Besides, two suggestions were proposed not only to save time but also to improve

the similarity between the parametric models and 3D segmented breast. Numerical evaluations certified that the generated parametric model resembled the breast segmented data in a reasonable range for medical usages.

Provision of a parametric model to be deformed by physicians manually is a necessary part of a planning approach, but it is not sufficient enough since surgeons cannot assure to generate deterministic breast shapes for patients with different tumor characteristics. Hence, a methodology is developed to model breast with emphasizing breast shape prediction. In this way, machine learning techniques were utilized to predict breast shape encompassing patient clinical properties, such as breast model, and breast density, together with tumor region and size. The application of machine learning techniques was chosen to speed up the prediction procedure (comparing with previous FEM based approaches), and also to decrease the complexities which were required for 3D model preparation. Notably, the application of machine learning demands to provide a training set with sufficient variety of breast entities. Hence, the MRI model of six patients was extended by consideration of 3 sizes for tumor size, 4 categories for breast densities, and 4 regions for tumor location. It should be noted that since tumor characteristics are not present in 3D reconstructed models, only MRI data were used in this specific part of the research. The total dataset was then used to train a Random Forest regressor with Leave-one Patient Out strategy, leading to predict the shape of the breast with average distance near to 1 *mm*, and the maximum distance of 4 *mm* from the ground-truth data.

Last but not least, the proposed methodologies were implemented consisting of three main demonstrations listed as follows:

- **Registration demonstration**, to get the depth views from Kinect, a frontal high-quality image from camera, and annotated MRI data determining pectoral muscle designed to reconstruct 3D model of patient, and the segment the breast complete contour
- **Parametric model generation demonstration**, to generate parametric model from breast 3D model, and to provide a platform to ease the interaction with the model
- **Breast shape prediction after BCS demonstration**, which is fed by segmented breast from MRI data, with the aim of inserting the tumor with variety of sizes, and determining breast density in order to provide the prediction of breast post-surgery shape

Finally, some parts of this dissertation (including 3D reconstruction and parametric modeling) were performed in the same direction of a European project, PICTURE – Patient Information for the Combined Assessment of Specific Surgical Outcomes in breast cancer. The project combined the analysis of 3D models with routine medical examinations which, together, will make it possible to develop techniques for biomechanically modeling the anatomy of the breast, and to understand the effect that the surgery to remove cancerous tissue can have on the patient. With these demonstrations, it will be possible to explore new alternative strategies and to evaluate the consequences of the options available, always respecting the appearance of the breast. It was a three-year project developed in partnership with Philips, the University College London (UK), the

Academisch Ziekenhuis Leiden - Leids Universitais Medisch Centrum (the Netherlands) and the Institut National de la Santŕ et de la Recherce Medicale (France).

In addition, the conducted research in this dissertation was part of the national project 3d BCT – 3D Models for Aesthetic Evaluation and Prediction of Breast Cancer Interventions, (including 3D reconstruction), as well as the project BCCT.plan – a 3D tool for planning breast cancer conservative treatment (including prediction of breast shape after BCS).

8.1 Future Work

Perhaps the most important future work can be defined with respect to utilizing 3D reconstruction models in breast shape prediction. This suggestion comprises the transformation between the two modalities used in this work: 3D reconstruction, and MRI. While the modality of 3D reconstruction provides color information, it lacks to express the tumor characteristics. Contrarily, MRI data provide tumor information, but they cannot be used when color reconstruction is intended. Considering the protocols through scanning (such as breast compression and patient pose), it will be worth to convert them into each other. In addition to prediction, even breast segmentation will be benefited as well, since the annotated pectoral muscle in MRI data will be located more accurately from one modality to another.

In this research, MRI data from 6 patients were extended to generate the dataset used for training. As a future work, it is intended to use more MRI data to increase dataset entities, as well as to consider more variations of breast size, breast density, and tumor location. The extended dataset will be used either to enhance the current learned model or train new models using other training approaches such as deep learning.

While MRI is known as an expensive acquisition device, an investigation can be performed to replace MRI data with mammogram images. In addition, surface reconstructed models resulted form Kinect can be used instead to provide the data for the demanded prediction purposes.

Taking parametric modeling in mind, the proposed methodology generated unconstrained deformation of a breast. An interesting future work can be proposed to embed breast specific deformation while limiting the unnatural breast shapes resulted in FFD.

Finally, with widespread of using augmented reality devices in medical applications, it is suggested to set a milestone in accordance to detach the 3D models from computer screens to put them in the world of augmented reality.

References

[1] L. Aerts, M. Christiaens, P. Enzlin, P. Neven, and F. Amant. Sexual functioning in women after mastectomy versus breast conserving therapy for early-stage breast cancer: A prospective controlled study. *The Breast*, 23(5):629–636, Oct 2014.

[2] D. Aiger, N. J. Mitra, and D. Cohen-Or. 4-points congruent sets for robust surface registration. *ACM Transactions on Graphics*, 27(3):#85, 1–10, Aug 2008.

[3] K. Aitpayev and J. Gaber. Creation of 3d human avatar using kinect. *Asian Transactions on Fundamentals of Electronics Communication & Multimedia*, 1(5):12–24, Jun 2012.

[4] S. Al-Ghazal, R. Blamey, J. Stewart, and A. Morgan. The cosmetic outcome in early breast cancer treated with breast conservation. *European Journal of Surgical Oncology (EJSO)*, 25(6):566–570, Dec 1999.

[5] S. K. Al-Ghazal and R. Blamey. Cosmetic assessment of breast-conserving surgery for primary breast cancer. *The Breast*, 8(4):162–168, Aug 1999.

[6] B. Allen, B. Curless, and Z. Popović. The space of human body shapes. In *Proceeding of ACM Special Interest Group on Computer GRAPHics and Interactive Techniques (SIGGRAPH)*, pages 587–594. ACM Press, Jul 2003.

[7] B. Amberg, S. Romdhani, and T. Vetter. Optimal step nonrigid ICP algorithms for surface registration. In *Proceeding of IEEE Conference on Computer Vision and Pattern Recognition*. IEEE, Jun 2007.

[8] American Cancer Society. Breast cancer detailed guide. Technical report, American Cancer Society, 2014.

[9] D. Anguelov, P. Srinivasan, D. Koller, S. Thrun, J. Rodgers, and J. Davis. Scape: Shape completion and animation of people. *ACM Trans. Graph.*, 24(3):408–416, Jul 2005.

[10] M. J. ao Cardoso. Is three better than two? the use of 3d scanners in the assessment of aesthetic results in local breast cancer treatment. *The Breast*, 21(3):227–228, Jun 2012.

[11] K. S. Asgeirsson, T. Rasheed, S. J. McCulley, and R. D. Macmillan. Oncological and cosmetic outcomes of oncoplastic breast conserving surgery. *European Journal of Surgical Oncology*, 31(8):817–823, Oct 2005.

[12] B. Aubert, C. Vergari, B. Ilharreborde, A. Courvoisier, and W. Skalli. 3d reconstruction of rib cage geometry from biplanar radiographs using a statistical parametric model approach. *Computer Methods in Biomechanics and Biomedical Engineering: Imaging & Visualization*, 4(5):281–295, May 2014.

[13] F. S. Azar, D. N. Metaxas, and M. D. Schnall. A deformable finite element model of the breast for predicting mechanical deformations under external perturbations. *Academic Radiology*, 8(10):965–975, Oct 2001.

[14] M. Bačák, R. Bergmann, G. Steidl, and A. Weinmann. A second order nonsmooth variational model for restoring manifold-valued images. *SIAM Journal on Scientific Computing*, 38(1):A567–A597, Jan 2016.

[15] R. Balaniuk, I. Costa, and J. Mello. Cosmetic breast surgery simulation. In *Proceeding of 8th Symposium on Virtual Reality*, pages 387–396, Jan 2006.

[16] E. Bardinet, L. D. Cohen, and N. Ayache. A parametric deformable model to fit unstructured 3d data. *Computer Vision and Image Understanding*, 71(1):39–54, Jul 1995.

[17] G. Berglund, C. Bolund, T. Fornander, L. E. Rutqvist, and P.-O. Sjödén. Late effects of adjuvant chemotherapy and postoperative radiotherapy on quality of life among breast cancer patients. *European Journal of Cancer and Clinical Oncology*, 27(9):1075 – 1081, Sep 1991.

[18] F. Bernardini, J. Mittleman, H. Rushmeier, C. Silva, and G. Taubin. The ball-pivoting algorithm for surface reconstruction. *IEEE Transactions on Visualization and Computer Graphics*, 5(4):349–359, Oct 1999.

[19] C. Bert, K. G. Metheany, K. Doppke, and G. T. Y. Chen. A phantom evaluation of a stereovision surface imaging system for radiotherapy patient setup. *Medical Physics*, 32(9):2753–2762, Aug 2005.

[20] P. Besl and N. D. McKay. A method for registration of 3-d shapes. *IEEE Transactions on Pattern Analysis and Machine Intelligence*, 14(2):239–256, Feb 1992.

[21] H. Borchani, G. Varando, C. Bielza, and P. Larrañaga. A survey on multi-output regression. *Wiley Interdisciplinary Reviews: Data Mining and Knowledge Discovery*, 5(5):216–233, Jul 2015.

[22] J.-Y. Bouguet and P. Perona. 3d photography on your desk. In *Proceefind of 6th IEEE International Conference on Computer Vision*. Narosa Publishing House, Jan 1998.

[23] L. Breiman. Prediction games and arcing algorithms. *Neural Computation*, 11(7):1493–1517, Oct 1999.

[24] M. L. Brutto and M. G. Spera. Image-based and range-based 3d modeling of archaeological cultural heritage: The telamon of the temple of olympian zeus in agrigento (italy). *ISPRS - International Archives of the Photogrammetry, Remote Sensing and Spatial Information Sciences*, XXXVIII-5/W16:515–522, Sep 2012.

[25] P. Buyssens, M. Daisy, D. Tschumperlé, and O. Lézoray. Superpixel-based depth map inpainting for rgb-d view synthesis. In *Proceeding of IEEE International Conference on Image Processing*, pages 4332–4336, Sep 2015.

[26] Z. Bylinskii, T. Judd, A. Oliva, A. Torralba, and F. Durand. What do different evaluation metrics tell us about saliency models? *arXiv preprint arXiv:1604.03605*, Apr 2016.

[27] D. H. C., J. Kannala, and J. Heikkilä. Accurate and practical calibration of a depth and color camera pair. In *Computer Analysis of Images and Patterns*, pages 437–445. Springer Berlin Heidelberg, Aug 2011.

[28] J. S. Cardoso and M. J. Cardoso. Breast contour detection for the aesthetic evaluation of breast cancer conservative treatment. In *Advances in Soft Computing*, pages 518–525. Springer Berlin Heidelberg, Feb 2007.

[29] J. S. Cardoso and M. J. Cardoso. Towards an intelligent medical system for the aesthetic evaluation of breast cancer conservative treatment. *Artificial Intelligence in Medicine*, 40(2):115 – 126, Jun 2007.

[30] J. S. Cardoso, R. Sousa, L. F. Teixeira, and M. J. Cardoso. Breast contour detection with stable paths. In *Biomedical Engineering Systems and Technologies*, pages 439–452. Springer Berlin Heidelberg, Jan 2008.

[31] M. J. Cardoso, J. Cardoso, A. C. Santos, H. Barros, and M. C. de Oliveira. Interobserver agreement and consensus over the esthetic evaluation of conservative treatment for breast cancer. *The Breast*, 15(1):2–57, Feb 2006.

[32] M. J. Cardoso, J. S. Cardoso, C. Vrieling, D. Macmillan, D. Rainsbury, J. Heil, E. Hau, and M. Keshtgar. Recommendations for the aesthetic evaluation of breast cancer conservative treatment. *Breast Cancer Research and Treatment*, 137:629–637, Feb 2012.

[33] M. J. a. Cardoso, H. P. Oliveira, and J. S. Cardoso. Assessing cosmetic results after breast conserving surgery. *Journal of Surgical Oncology*, 110(1):37–44, Mar 2014.

[34] T. J. Carter. *Biomechanical Modelling of the Breast for Image-Guided Surgery*. PhD thesis, University of London, May 2009.

[35] T. J. Carter, C. Tanner, W. Crum, N. Beechey-Newman, and D. Hawkes. A framework for image-guided breast surgery. In *International Workshop on Medical Imaging and Augmented Reality (MIAR)*, volume 4091 of *Lecture Notes in Computer Science*, pages 203–210. Springer Berlin Heidelberg, Aug 2006.

[36] J. C.-W. Chan and D. Paelinckx. Evaluation of random forest and adaboost tree-based ensemble classification and spectral band selection for ecotope mapping using airborne hyperspectral imagery. *Remote Sensing of Environment*, 112(6):2999 – 3011, Jun 2008.

[37] W. Chang and M. Zwicker. Automatic registration for articulated shapes. *Computer Graphics Forum*, 27(5):1459–1468, Jul 2008.

[38] D. T. Chen, I. A. Kakadiaris, M. J. Miller, R. B. Loftin, and C. Patrick. Modeling for plastic and reconstructive breast surgery. In *Proceeding of Medical Image Computing and Computer-Assisted Intervention (MICCAI)*, pages 1040–1050. Springer Berlin Heidelberg, Oct 2000.

[39] S. Chen, Y. F. Li, J. Zhang, and W. Wang, editors. *Active sensor planning for multiview vision tasks*. Springer Berlin Heidelberg, 2008.

[40] T. Chen and C. Guestrin. Xgboost: A scalable tree boosting system. *CoRR*, abs/1603.02754, 2016.

[41] D. R. H. Christie, M.-Y. O'Brien, J. A. Christie, T. Kron, S. A. Ferguson, C. S. Hamilton, and J. W. Denham. A comparison of methods of cosmetic assessment in breast conservation treatment. *Breast*, 5:358–367, Oct 1996.

[42] D. H. Chung, I. D. Yun, and S. U. Lee. Registration of multiple-range views using the reverse-calibration technique. *Pattern Recognition*, 31(4):457–464, Apr 1998.

[43] J. H. Chung, V. Rajagopal, P. M. F. Nielsen, and M. P. Nash. A biomechanical model of mammographic compressions. *Biomechanics and Modeling in Mechanobiology*, 7(1):43–52, Feb 2008.

[44] P. Cignoni, M. Callieri, M. Corsini, M. Dellepiane, F. Ganovelli, and G. Ranzuglia. MeshLab: an open-Source mesh processing tool. In V. S. Erra, R. D. Chiara, and Ugo, editors, *Eurographics Italian Chapter Conference*. The Eurographics Association, Jul 2008.

[45] D. Clarke, A. Martinez, and R. S. Cox. Analysis of cosmetic results and complications in patients with stage i and ii breast cancer treated by biopsy and irradiation. *International Journal of Radiation Oncology Biology Physics*, 9(12):1807–1813, Dec 1983.

[46] F. J. J. Clarke, R. McDonald, and B. Rigg. Modification to the jpc79 colour–difference formula. *Journal of the Society of Dyers and Colourists*, 100(4):128–132, Oct 1984.

[47] K. B. Clough, G. J. Kaufman, C. Nos, I. Buccimazza, and I. M. Sarfati. Improving breast cancer surgery: A classification and quadrant per quadrant atlas for oncoplastic surgery. *Annals of surgical oncology*, 17(5):1375–1391, Sep 2010.

[48] P. Costa, J. P. Monteiro, H. Zolfagharnasab, and H. P. Oliveira. Tessellation-based coarse registration method for 3d reconstruction of the female torso. In *Proceeding of International Conference on Bioinformatics and Biomedicine (BIBM)*, pages 301–306, Nov 2014.

[49] P. Costa, H. Zolfagharnasab, J. ao P. Monteiro, J. S. Cardoso, and H. P. Oliveira. 3d reconstruction of body parts using RGB-d sensors: Challenges from a biomedical perspective. In *Proceedings of 5th International Conference on 3D Body Scanning Technologies*. Hometrica Consulting - Dr. Nicola D'Apuzzo, Oct 2014.

[50] Y. Cui, S. Schuon, D. Chan, S. Thrun, and C. Theobalt. 3d shape scanning with a time-of-flight camera. In *Proceeding of IEEE Computer Society Conference on Computer Vision and Pattern Recognition*. IEEE, Jun 2010.

[51] P. de Heras Ciechomski, M. Constantinescu, J. Garcia, R. Olariu, I. Dindoyal, S. Le Huu, and M. Reyes. Development and implementation of a web-enabled 3D consultation tool for breast augmentation surgery based on 3D-image reconstruction of 2D pictures. *Journal of Medical Internet Research*, 14(1):e21, Feb 2012.

[52] A. de la Rochefordiere, A. L. Abner, B. Silver, F. Vicini, A. Recht, and J. R. Harris. Are cosmetic results following conservative surgery and radiation therapy for early breast cancer dependent on technique? *International Journal of Radiation Oncology Biology Physics*, 23(5):925–931, Jan 1992.

[53] A. P. del Palomar, B. Calvo, J. Herrero, J. López, and M. Doblaré. A finite element model to accurately predict real deformations of the breast. *Medical Engineering & Physics*, 30(9):1089–1097, Nov 2008.

[54] C. E. DeSantis, J. Ma, A. Goding Sauer, L. A. Newman, and A. Jemal. Breast cancer statistics, 2017, racial disparity in mortality by state. *CA: A Cancer Journal for Clinicians*, 67(6):439–448, Oct 2017.

[55] C. J. D'Orsi, E. A. Sickles, E. B. Mendelson, and E. Morris. *ACR BI-RADS Atlas: Breast imaging reporting and data system*. American College of Radiology, 2013.

[56] M. Eder, S. Raith, J. Jalali, A. Volf, M. Settles, H.-G. Machens, and L. Kovacs. Comparison of different material models to simulate 3-d breast deformations using finite element analysis. *Annals of Biomedical Engineering*, 42(4):843–857, Dec 2013.

[57] B. Eiben, L. Han, J. Hipwell, T. Mertzanidou, S. Kabus, T. Buelow, C. Lorenz, G. M. Newstead, H. Abe, M. Keshtgar, S. Ourselin, and D. J. Hawkes. Biomechanically guided prone-to-supine image registration of breast mri using an estimated reference state. *Proceedings of the International Symposium on Biomedical Imaging*, pages 214–217, Apr 2013.

[58] A. Elmoataz, F. Lozes, and M. Toutain. Nonlocal PDEs on graphs: From tug-of-war games to unified interpolation on images and point clouds. *Journal of Mathematical Imaging and Vision*, 57(3):381–401, Sep 2016.

[59] P. Faria. Predicting breast healing deformation after cancer conservative treatment. Master's thesis, Universidade do Porto, Faculdade de Engenharia, September 2017.

[60] F. Fitzal, W. Krois, H. Trischler, L. Wutzel, O. Riedl, U. Kuhbelbock, B. Wintersteiner, M. Cardoso, P. Dubsky, M. Gnant, R. Jakesz, and T. Wild. The use of a breast symmetry index for objective evaluation of breast cosmesis. *The Breast*, 16(4):429–435, Aug 2007.

[61] E. Foersterling, M. Golatta, A. Hennigs, S. Schulz, G. Rauch, S. Schott, C. Domschke, F. Schuetz, C. Sohn, and J. Heil. Predictors of early poor aesthetic outcome after breast-conserving surgery in patients with breast cancer: Initial results of a prospective cohort study at a single institution. *Journal of Surgical Oncology*, 110(7):801–806, Aug 2014.

[62] J. H. Friedman. Greedy function approximation: A gradient boosting machine. *The Annals of Statistics*, 29(5):1189–1232, Oct 2001.

[63] G. Gallo, G. C. Guarnera, and G. Catanuto. Human breast shape analysis using pca. In *Proceedings of the Third International Conference on Bio-inspired Systems and Signal Processing, BIOSIGNALS*, pages 163–167, Jan 2010.

[64] G. Gallo, G. C. Guarnera, F. Milanese, D. Modica, G. Catanuto, and F. Pane. Parametric representation of human breast shapes. In *IEEE International Workshop on Medical Measurements and Applications*. IEEE, May 2009.

[65] V. Gandhi, J. Cech, and R. Horaud. High-resolution depth maps based on TOF-stereo fusion. In *Proceeding of IEEE International Conference on Robotics and Automation*. IEEE, May 2012.

[66] M. Garbey, B. L. Bass, and S. Berceli. Multiscale mechanobiology modeling for surgery assessment. *Acta Mechanica Sinica*, 28(4):1186–1202, Aug 2012.

[67] M. Garbey, R. Salmon, D. Thanoon, and B. Bass. Multiscale modeling and distributed computing to predict cosmesis outcome after a lumpectomy. *Journal of Computational Physics*, 244:321–335, Jul 2013.

[68] M. Garbey, D. Thanoon, and B. Bass. Multiscale modeling in computational surgery: Application to breast conservative therapy. *Journal of the Serbian Society for Computational Mechanics*, 5(1):81–89, May 2011.

[69] D. Garcia. Robust smoothing of gridded data in one and higher dimensions with missing values. *Computational Statistics & Data Analysis*, 54(4):1167–1178, Apr 2010.

[70] J. Geng. Structured-light 3d surface imaging: a tutorial. *Adv. Opt. Photon.*, 3(2):128–160, Jun 2011.

[71] P. George and H. Borouchaki. *Delaunay triangulation and meshing: Application to finite elements*. Butterworth-Heinemann, 1998.

[72] J. Georgii, M. Eder, K. Bürger, S. Klotz, F. Ferstl, L. Kovacs, and R. Westermann. A computational tool for preoperative breast augmentation planning in aesthetic plastic surgery. *IEEE Journal of Biomedical and Health Informatics*, 18(3):907–919, May 2014.

[73] C. Geuzaine and J.-F. Remacle. Gmsh: A 3-d finite element mesh generator with built-in pre- and post-processing facilities. *International Journal for Numerical Methods in Engineering*, 79(11):1309–1331, Sep 2009.

[74] N. S. Gomes and S. R. d. Silva. Avaliação da autoestima de mulheres submetidas á cirurgia oncológica mamária. *Text Context Nursing*, 22(2):509–516, Jun 2013.

[75] C. Guillemot and O. L. Meur. Image inpainting: Overview and recent advances. *IEEE Signal Processing Magazine*, 31(1):127–144, Jan 2014.

[76] J. Han, L. Shao, D. Xu, and J. Shotton. Enhanced computer vision with microsoft kinect sensor: A review. *IEEE Transactions on Cybernetics*, 43(5):1318–1334, Oct 2013.

[77] L. Han, J. H. Hipwell, B. Eiben, D. Barratt, M. Modat, S. Ourselin, and D. J. Hawkes. A nonlinear biomechanical model based registration method for aligning prone and supine mr breast images. *IEEE Transactions on Medical Imaging*, 33(3):682–694, Mar 2014.

[78] J. Hansen and F. Netter. *Netter's clinical anatomy*. Saunders/Elsevier, 2014.

[79] J. R. Harris, M. B. Levene, G. Svensson, and S. Hellman. Analysis of cosmetic results following primary radiation therapy for stages i and ii carcinoma of the breast. *International Journal of Radiation Oncology Biology Physics*, 5(2):257 – 261, Feb 1979.

[80] H. Henseler, B. Khambay, A. Bowman, J. Smith, J. Siebert, S. Oehler, X. Ju, A. Ayoub, and A. Ray. Investigation into accuracy and reproducibility of a 3d breast imaging system using multiple stereo cameras. *Journal of Plastic, Reconstructive and Aesthetic Surgery*, 64(5):577–582, May 2011.

[81] H. Henseler, A. Kuznetsova, P. Vogt, and B. Rosenhahn. Validation of the kinect device as a new portable imaging system for three-dimensional breast assessment. *Journal of Plastic, Reconstructive & Aesthetic Surgery*, 67(4):483 – 488, Apr 2014.

[82] C. E. Hill-Kayser, C. Vachani, M. K. Hampshire, G. A. D. Lullo, and J. M. Metz. Cosmetic outcomes and complications reported by patients having undergone breast-conserving treatment. *International Journal of Radiation Oncology Biology Physics*, 83(3):839 – 844, Jul 2012.

[83] A. Hilton, D. Beresford, T. Gentils, R. Smith, W. Sun, and J. Illingworth. Whole-body modelling of people from multiview images to populate virtual worlds. *The Visual Computer*, 16(7):411–436, Nov 2000.

[84] J. H. Hipwell, V. Vavourakis, L. Han, T. Mertzanidou, B. Eiben, and D. J. Hawkes. A review of biomechanically informed breast image registration. *Physics in medicine and biology*, 61(2):R1–R31, Jan 2016.

[85] T. K. Ho. A data complexity analysis of comparative advantages of decision forest constructors. *Pattern Analysis and Applications*, 5(2):102–112, Jun 2002.

[86] T. Hopp, M. Dietzel, P. A. Baltzer, P. Kreisel, W. A. Kaiser, H. Gemmeke, and N. V. Ruiter. Automatic multimodal 2d/3d breast image registration using biomechanical fem models and intensity-based optimization. *Medical Image Analysis*, 17(2):209–218, Feb 2013.

[87] P. Huang, L. Gu, J. Yan, H. Xu, J. Dong, W. Chen, J. Liu, J. Zhang, J. Song, X. Yu, L. Zhang, and H. Zhou. Virtual surgery planning of breast reconstruction using deformation modeling and curve shape approximation. In *Proceeding of 6th International Special Topic Conference on Information Technology Applications in Biomedicine*, pages 127–130, Nov 2007.

[88] Q.-X. Huang, B. Adams, M. Wicke, and L. J. Guibas. Non-rigid registration under isometric deformations. *Computer Graphics Forum*, 27(5):1449–1457, Jul 2008.

[89] L. Itti, C. Koch, and E. Niebur. A model of saliency-based visual attention for rapid scene analysis. *IEEE Transactions on Pattern Analysis and Machine Intelligence*, 20(11):1254–1259, Nov 1998.

[90] S. Izadi, A. Davison, A. Fitzgibbon, D. Kim, O. Hilliges, D. Molyneaux, R. Newcombe, P. Kohli, J. Shotton, S. Hodges, and D. Freeman. KinectFusion. In *Proceedings of 24th annual ACM symposium on User interface software and technology (UIST)*, pages 559–568. ACM Press, Oct 2011.

[91] N. K. Janz, M. Mujahid, P. M. Lantz, A. Fagerlin, B. Salem, M. Morrow, D. Deapen, and S. J. Katz. Population-based study of the relationship of treatment and sociodemographics on quality of life for early stage breast cancer. *Quality of Life Research*, 6(14):1467–1479, Aug 2005.

[92] A. Jennifer, M. D. Harvey, and E. B. Viktor. Quantitative assessment of mammographic breast density: Relationship with breast cancer risk. *Radiology*, 230(1):29–41, Jan 2004.

[93] M. Jiang, S. Huang, J. Duan, and Q. Zhao. SALICON: Saliency in context. In *Proceeding of IEEE Conference on Computer Vision and Pattern Recognition (CVPR)*. IEEE, Jun 2015.

[94] Y. Jiang, L. Cao, R. Sankreacha, and J. Pignol. Software tool for breast cancer brachytherapy planning using vtk. In *Proceeding of 6th IEEE International Conference on Cognitive Informatics*, pages 381–384, Aug 2007.

[95] Y. R. Jiang and E. R. Sykes. A 3d computer-assisted treatment planning system for breast cancer brachytherapy treatment. *International Journal of Computer Assisted Radiology and Surgery*, 10(4):373–381, Jul 2014.

[96] A. Johnson. *Spin-images: A representation for 3-D surface matching*. PhD thesis, Robotics Institute, Carnegie Mellon University, August 1997.

[97] A. Johnson. 3d surface matching from range images using multiscale local features. Master's thesis, School of Electrical and Electronic Engineering, The University of Adelaide, December 2009.

[98] G. M. Johnson and M. D. Fairchild. A top down description of s-CIELAB and CIEDE2000. *Color Research & Application*, 28(6):425–435, Oct 2003.

[99] D. Kamath, S. Kamath, K. Prasad, and K. V. Rajagopal. Segmentation of breast thermogram images for the detection of breast cancer – a projection profile approach. *Journal of Image and Graphics*, 3(1), Jan 2015.

[100] K. Khoshelham and S. O. Elberink. Accuracy and resolution of kinect depth data for indoor mapping applications. *Sensors*, 12(12):1437–1454, Feb 2012.

[101] M. K. Kim, T. Kim, H. G. Moon, U. S. Jin, K. Kim, J. Kim, J. W. Lee, J. Kim, E. Lee, T. K. Yoo, D.-Y. Noh, K. W. Minn, and W. Han. Effect of cosmetic outcome on quality of life after breast cancer surgery. *European Journal of Surgical Oncology (EJSO)*, 41(3):426–432, Mar 2015.

[102] Y. Kim, K. Lee, and W. Kim. 3d virtual simulator for breast plastic surgery. *Computer Animation and Virtual Worlds*, 19(3–4):515–526, Aug 2008.

[103] L. Kovacs, M. Eder, R. Hallweck, A. Zimmermann, M. Settles, A. Schneider, K. Udosic, K. Schwenzer-Zimmerer, N. A. Papadopulos, and E. Biemer. New aspects of breast volume measurement using 3-dimensional surface imaging. *Annals of Plastic Surgery*, 57(6):602–610, Apr 2006.

[104] L. Kovacs, M. Eder, R. Hollweck, A. Zimmermann, M. Settles, A. Schneider, M. Endlich, A. Mueller, K. Schwenzer-Zimmerer, N. A. Papadopulos, and E. Biemer. Comparison between breast volume measurement using 3d surface imaging and classical techniques. *The Breast*, 16(2):137–145, Apr 2007.

[105] L. Kovacs, A. Yassouridis, A. Zimmermann, G. Brockmann, A. Wohnl, M. Blaschke, M. Eder, K. Schwenzer-Zimmerer, R. Rosenberg, N. A. Papadopulos, and E. Biemer. Optimization of 3-dimensional imaging of the breast region with 3-dimensional laser scanners. *Annals of Plastic Surgery*, 56(3):229–236, Mar 2006.

[106] K. Krafka, A. Khosla, P. Kellnhofer, H. Kannan, S. Bhandarkar, W. Matusik, and A. Torralba. Eye tracking for everyone. In *2016 IEEE Conference on Computer Vision and Pattern Recognition (CVPR)*. IEEE, Jun 2016.

[107] W. Krois, A. K. Romar, T. Wild, P. Dubsky, R. Exner, P. Panhofer, R. Jakesz, M. Gnant, and F. Fitzal. Objective breast symmetry analysis with the breast analyzing tool (BAT): Improved tool for clinical trials. *Breast Cancer Research and Treatment*, 164(2):421–427, May 2017.

[108] M. Kümmerer, T. S. A. Wallis, and M. Bethge. Information-theoretic model comparison unifies saliency metrics. *Proceedings of the National Academy of Sciences*, 112(52):16054–16059, Dec 2015.

[109] M. Kümmerer, T. Wallis, and M. Bethge. How close are we to understanding image-based saliency? *arXiv*, Sep 2014.

[110] R. M. Lacher, J. H. Hipwell, N. R. Williams, M. R. S. Keshtgar, D. J. Hawkes, and D. Stoyanov. Low-cost surface reconstruction for aesthetic results assessment and prediction in breast cancer surgery. In *Proceedings of 37th Annual International Conference of the IEEE Engineering in Medicine and Biology Society (EMBC)*. IEEE, Aug 2015.

[111] R. M. Lacher, F. Vasconcelos, D. Bishop, N. R. Williams, M. Keshtgar, D. J. Hawkes, J. H. Hipwell, and D. Stoyanov. A comparative study of breast surface reconstruction for aesthetic outcome assessment. In *Proceeding of 20th Medical Image Computing and Computer Assisted Interventions Conference (MICCAI)*, pages 514–522, Sep 2017.

[112] A. Lapuebla-Ferri, A. P. del Palomar, J. Herrero, and A. J. Jiménez-Mocholí. A patient-specific fe-based methodology to simulate prosthesis insertion during an augmentation mammoplasty. *Medical Engineering & Physics*, 33(9):1094 – 1102, Nov 2011.

[113] A. W. C. Lee, J. A. Schnabel, V. Rajagopal, P. M. F. Nielsen, and M. P. Nash. Breast image registration by combining finite elements and free-form deformations. In *Digital Mammography*, pages 736–743. Springer Berlin Heidelberg, Jun 2010.

[114] J. Lee, G. S. Muralidhar, G. P. Reece, and M. K. Markey. A shape constrained parametric active contour model for breast contour detection. In *2012 Annual International Conference of the IEEE Engineering in Medicine and Biology Society*, pages 4450–4453, Aug 2012.

[115] D. Li, A. Cheong, G. P. Reece, M. A. Crosby, M. C. Fingeret, and F. A. Merchant. Computation of breast ptosis from 3d surface scans of the female torso. *Computers in Biology and Medicine*, 78(Supplement C):18 – 28, 2016.

[116] H. Li, E. Vouga, A. Gudym, L. Luo, J. T. Barron, and G. Gusev. 3d self-portraits. *ACM Transactions on Graphics*, 32(6):1–9, Nov 2013.

[117] A. Liaw and M. Wiener. Classification and regression by randomforest. *R News*, 2(3):18–22, 2002.

[118] G. Liljegren, L. Holmberg, and G. Westman. The cosmetic outcome in early breast cancer treated with sector resection with or without radiotherapy. *European Journal of Cancer*, 29(15):2083–2089, Jan 1993.

[119] E. V. Limbergen, A. Rijnders, E. V. Schueren, T. Lerut, and R. Christiaens. Cosmetic evaluation of breast conserving treatment for mammary cancer. 2. a quantitative analysis of the influence of radiation dose, fractionation schedules and surgical treatment techniques on cosmetic results. *Radiotherapy and Oncology*, 16(4):253–267, Dec 1989.

[120] I. Lissner and P. Urban. Toward a unified color space for perception-based image processing. *IEEE Transactions on Image Processing*, 21(3):1153–1168, Mar 2012.

[121] A. Losken, I. Fishman, D. D. Denson, H. R. Moyer, and G. W. Carlson. An objective evaluation of breast symmetry and shape differences using 3-dimensional images. *Annals of Plastic Surgery*, 55(6):571–575, Dec 2005.

[122] A. Losken, H. Seify, D. D. Denson, A. A. Paredes, and G. W. Carlson. Validating three-dimensional imaging of the breast. *Annals of Plastic Surgery*, 54(5):471–476, May 2005.

[123] F. Lozes, A. Elmoataz, and O. Lezoray. Morphological PDEs on graphs for filtering and inpainting of point clouds. In *Proceeding of 8th International Symposium on Image and Signal Processing and Analysis (ISPA)*. IEEE, Sep 2013.

[124] J. Ma, J. Zhao, and A. L. Yuille. Non-rigid point set registration by preserving global and local structures. *IEEE Transactions on Image Processing*, 25(1):53–64, Jan 2016.

[125] M. Mahy, L. Van Eycken, and A. Oosterlinck. Evaluation of uniform color spaces developed after the adoption of cielab and cieluv. *Color Research & Application*, 19(2):105–121, Jan 1994.

[126] T. Mallick, P. P. Das, and A. K. Majumdar. Characterizations of noise in kinect depth images: A review. *IEEE Sensors Journal*, 14(6):1731–1740, Jun 2014.

[127] F. Martínez-Martínez, M. Rupérez-Moreno, M. Martínez-Sober, J. Solves-Llorens, D. Lorente, A. Serrano-López, S. Martínez-Sanchis, C. Monserrat, and J. Martín-Guerrero. A finite element-based machine learning approach for modeling the mechanical behavior of the breast tissues under compression in real-time. *Computers in Biology and Medicine*, 90:116–124, Nov 2017.

[128] L. Mason, J. Baxter, P. Bartlett, and M. Frean. Boosting algorithms as gradient descent. In *Proceedings of 12th International Conference on Neural Information Processing Systems (NIPS)*, pages 512–518. MIT Press, 1999.

[129] L. McMillan and S. Gortler. Image-based rendering. *ACM Special Interest Group on Computer GRAPHics and Interactive Techniques (SIGGRAPH)*, 33(4):61–64, Nov 1999.

[130] T. Mertzanidou, J. Hipwell, S. Johnsen, L. Han, B. Eiben, Z. Taylor, S. Ourselin, H. Huisman, R. Mann, U. Bick, N. Karssemeijer, and D. Hawkes. Mri to x-ray mammography intensity-based registration with simultaneous optimisation of pose and biomechanical transformation parameters. *Medical Image Analysis*, 18(4):674–683, May 2014.

[131] W. S. Mokrzycki and M. Tatol. Colour difference δe – a survey. *Machine Graphics and Vision*, 20(4):383–411, Jan 2011.

[132] J. P. Monteiro, H. Zolfagharnasab, and H. Oliveira. Enhancing color quality of 3d reconstructed pointclouds using multiple views captured by kinect. *To be Submitted*, Jun 2018.

[133] H. R. Moyer, G. W. Carlson, T. M. Styblo, and A. Losken. Three-dimensional digital evaluation of breast symmetry after breast conservation therapy. *Journal of the American College of Surgeons*, 207(2):227–232, Aug 2008.

[134] A. Narvaez and E. Ramirez. A simple 3d scanner based on passive vision for geometry reconstruction. *IEEE Latin America Transactions*, 10(5):2125–2131, Sep 2012.

[135] H. Nassar, T. Wallis, A. Andea, J. Dey, V. Adsay, and D. Visscher. Clinicopathologic analysis of invasive micropapillary differentiation in breast carcinoma. *Modern Pathology*, 14(9):836–841, Sep 2001.

[136] S. Nayar, M. Watanabe, and M. Noguchi. Real-time focus range sensor. *IEEE Transactions on Pattern Analysis and Machine Intelligence*, 18(12):1186–1198, Dec 1996.

[137] R. A. Newcombe, A. J. Davison, S. Izadi, P. Kohli, O. Hilliges, J. Shotton, D. Molyneaux, S. Hodges, D. Kim, and A. Fitzgibbon. KinectFusion: Real-time dense surface mapping and tracking. In *Proceeding of 10th IEEE International Symposium on Mixed and Augmented Reality*. IEEE, Oct 2011.

[138] N. nez Benjumea Francisco J., S. Carmen, and A. B. na. Automatic landmarks detection in breast reconstruction aesthetic assessment. *Studies in Health Technology and Informatics*, 210(Digital Healthcare Empowering Europeans):399–403, 2015.

[139] M. Noguchi, Y. Saito, Y. Mizukami, A. Nonomura, N. Ohta, N. Koyasaki, T. Taniya, and I. Miyazaki. Breast deformity, its correction, and assessment of breast conserving surgery. *Breast Cancer Research and Treatment*, 18(2):111–118, May 1991.

[140] R. L. O'Connell, R. Di Micco, K. Khabra, L. Wolf, N. deSouza, N. Roche, P. A. Barry, A. M. Kirby, and J. E. Rusby. The potential role of three-dimensional surface imaging as a tool to evaluate aesthetic outcome after breast conserving therapy (bct). *Breast Cancer Research and Treatment*, 164(2):385–393, Jul 2017.

[141] H. P. Oliveira. *An affordable and practical 3D solution for the aesthetic evaluation of breast cancer conservative treatment*. PhD thesis, Faculty of Engineering, University of Porto, 2013.

[142] H. P. Oliveira, J. S. Cardoso, A. Magalhães, and M. J. Cardoso. Methods for the aesthetic evaluation of breast cancer conservation treatment: A technological review. *Current Medical Imaging Reviews*, 9(1):32–46, Apr 2013.

[143] H. P. Oliveira, J. S. Cardoso, A. T. Magalhães, and M. J. Cardoso. A 3d low-cost solution for the aesthetic evaluation of breast cancer conservative treatment. *Computer Methods in Biomechanics and Biomedical Engineering: Imaging & Visualization*, 2(2):90–106, 2014.

[144] H. P. Oliveira, P. Patete, G. Baroni, and J. S. Cardoso. Development of a bcct quantitative 3d evaluation system through low-cost solutions. In *Proceedings of the 2nd International Conference on 3D Body Scanning Technologies*, pages 16–27, Oct 2011.

[145] M. R. Oswald. Concurrent stereo reconstruction. Master's thesis, Technische Universität Dresden, Germany, June 2007.

[146] J. Pan, C. Canton, K. McGuinness, N. E. O'Connor, J. Torres, E. Sayrol, and X. a. Giro-i Nieto. Salgan: Visual saliency prediction with generative adversarial networks. In *arXiv*, Jan 2017.

[147] P. Patete, M. I. Iacono, M. F. Spadea, G. Trecate, D. Vergnaghi, L. T. Mainardi, and G. Baroni. A multi-tissue mass-spring model for computer assisted breast surgery. *Medical Engineering & Physics*, 35(1):47–53, Jan 2013.

[148] F. Pedregosa, G. Varoquaux, A. Gramfort, V. Michel, B. Thirion, O. Grisel, M. Blondel, P. Prettenhofer, R. Weiss, V. Dubourg, J. Vanderplas, A. Passos, D. Cournapeau, M. Brucher, M. Perrot, and E. Duchesnay. Scikit-learn: Machine learning in python. *Journal of Machine Learning Research*, 12:2825–2830, 2011.

[149] D. Pernes, J. S. Cardoso, and H. P. Oliveira. Fitting of superquadrics for breast modelling by geometric distance minimization. In *Proceedings of IEEE International Conference on Bioinformatics and Biomedicine, (BIBM)*, pages 293–296, Nov 2014.

[150] R. D. Pezner, J. A. Lipsett, N. L. Vora, and K. R. Desai. Limited usefulness of observer-based cosmesis scales employed to evaluate patients treated conservatively for breast cancer. *International Journal of Radiation Oncology Biology Physics*, 11(6):1117–1119, Jun 1985.

[151] R. D. Pezner, M. P. Patterson, L. R. Hill, N. Vora, K. R. Desai, J. O. Archambeau, and J. A. Lipsett. Breast retraction assessment: An objective evaluation of cosmetic results of patients treated conservatively for breast cancer. *International Journal of Radiation Oncology Biology Physics*, 11(3):575–578, Mar 1985.

[152] S. T. Pöhlmann, E. Harkness, C. J. Taylor, A. Gandhi, and S. M. Astley. Preoperative implant selection for unilateral breast reconstruction using 3d imaging with the microsoft kinect sensor. *Journal of Plastic, Reconstructive & Aesthetic Surgery*, 70(8):1059–1067, Aug 2017.

[153] N. Qian. Binocular disparity and the perception of depth. *Neuron*, 18(3):359–368, Mar 1997.

[154] V. Rajagopal. *Modelling breast tissue mechanics under gravity loading*. PhD thesis, University of Auckland, Jan 2007.

[155] V. Rajagopal, P. M. F. Nielsen, and M. P. Nash. Modeling breast biomechanics for multimodal image analysis-successes and challenges. *Wiley Interdisciplinary Reviews: Systems Biology and Medicine*, 2(3):293–304, Oct 2010.

[156] N. G. Ramião, P. S. Martins, R. Rynkevic, A. A. Fernandes, M. Barroso, and D. C. Santos. Biomechanical properties of breast tissue, a state-of-the-art review. *Biomechanics and Modeling in Mechanobiology*, 15(5):1307–1323, Feb 2016.

[157] G. R. Ray and V. J. Fish. Biopsy and definitive radiation therapy in stage i and ii adenocarcinoma of the female breast: Analysis of cosmesis and the role of electron beam supplementation. *International Journal of Radiation Oncology Biology Physics*, 9(6):813–818, Jun 1983.

[158] E. Reinhard, M. Adhikhmin, B. Gooch, and P. Shirley. Color transfer between images. *IEEE Computer Graphics and Applications*, 21(4):34–41, Sep 2001.

[159] F. Remondino and S. El-Hakim. Image-based 3d modelling: A review. *The Photogrammetric Record*, 21(115):269–291, Aug 2006.

[160] C. Rother, V. Kolmogorov, and A. Blake. "GrabCut". In *ACM SIGGRAPH 2004 Papers on - SIGGRAPH*. ACM Press, Aug 2004.

[161] Y. Rubner, C. Tomasi, and L. J. Guibas. The earth mover's distance as a metric for image retrieval. *International Journal of Computer Vision*, 40:2000, Nov 2000.

[162] D. Rueckert, L. Sonoda, C. Hayes, D. Hill, M. Leach, and D. Hawkes. Nonrigid registration using free-form deformations: Application to breast MR images. *IEEE Transactions on Medical Imaging*, 18(8):712–721, Aug 1999.

[163] O. Ruiz, S. Arroyave, and D. Acosta. Fitting of analytic surfaces to noisy point clouds. *American Journal of Computational Mathematics*, 03(01):18–26, Apr 2013.

[164] R. B. Rusu, N. Blodow, and M. Beetz. Fast point feature histograms (FPFH) for 3d registration. In *Proceeding of IEEE International Conference on Robotics and Automation*. IEEE, May 2009.

[165] J. Salvi, C. Matabosch, D. Fofi, and J. Forest. A review of recent range image registration methods with accuracy evaluation. *Image and Vision Computing*, 25(5):578–596, May 2007.

[166] G. Sansoni, M. Trebeschi, and F. Docchio. State-of-the-art and applications of 3d imaging sensors in industry, cultural heritage, medicine, and criminal investigation. *Sensors*, 9(1):568–601, Jan 2009.

[167] M. Schmeing and X. Jiang. Edge-aware depth image filtering using color segmentation. *Pattern Recognition Letters*, 50:63–71, Dec 2014.

[168] S. Schuon, C. Theobalt, J. Davis, and S. Thrun. LidarBoost: Depth superresolution for ToF 3d shape scanning. In *Proceeding of IEEE Conference on Computer Vision and Pattern Recognition*. IEEE, Jun 2009.

[169] H. Seo, F. Cordier, and K. Hong. A breast modeler based on analysis of breast scans. *Computer Animation and Virtual Worlds*, 18(2):141–151, May 2007.

[170] T.-c. Shih, J.-h. Chen, D. Liu, K. Nie, L. Sun, M. Lin, D. Chang, O. Nalcioglu, and M.-y. Su. Computational simulation of breast compression based on segmented breast and fibroglandular tissues on magnetic resonance images. *Physics in Medicine and Biology*, 55(14):4153–4168, Jul 2010.

[171] R. L. Siegel, K. D. Miller, and A. Jemal. Cancer statistics, 2016. *CA: A Cancer Journal for Clinicians*, 66(1):7–30, Jan 2016.

[172] A. Siu and R. Lau. Image registration for image-based rendering. *IEEE Transactions on Image Processing*, 14(2):241–252, Feb 2005.

[173] S. L. Spear, J. H. Boehmler, and M. W. Clemens. Augmentation/mastopexy: A 3-year review of a single surgeon's practice. *Plastic and Reconstructive Surgery*, 118(Supplement):136S–147S, Dec 2006.

[174] M. Strickland, J. Tremaine, G. Brigley, and C. Law. Using a depth-sensing infrared camera system to access and manipulate medical imaging from within the sterile operating field. *Canadian Journal of Surgery*, 56(3):E1–E6, Jun 2013.

[175] G. M. Sturgeon, N. Kiarashi, J. Y. Lo, E. Samei, and W. P. Segars. Finite-element modeling of compression and gravity on a population of breast phantoms for multimodality imaging simulation. *Medical Physics*, 43(5):2207–2217, Apr 2016.

[176] J. Suckling, J. Parker, D. Dance, S. Astley, I. Hutt, C. Boggis, I. Ricketts, E. Stamatakis, N. Cerneaz, S. Kok, P. Taylor, D. Betal, and J. Savage. The mammographic images analysis society digital mammogram database. *Experta Medica International Congress Series*, 1069:375–378, 1994.

[177] R. W. Sumner, J. Schmid, and M. Pauly. Embedded deformation for shape manipulation. In *Proceeding of ACM Special Interest Group on Computer GRAPHics and Interactive Techniques (SIGGRAPH)*. ACM, Jul 2007.

[178] J. Sun, M. Ovsjanikov, and L. Guibas. A concise and provably informative multi-scale signature based on heat diffusion. *Computer Graphics Forum*, 28(5):1383–1392, Jul 2009.

[179] S. P. Sun, J. S. Chen, and B. C. Yuan. The planning system for breast augmentation with implant pocket region indices. In *Proceeding of 4th International Congress on Image and Signal Processing*, volume 4, pages 2138–2142, Oct 2011.

[180] J. Süssmuth, M. Winter, and G. Greiner. Reconstructing animated meshes from time-varying point clouds. In *Proceedings of the Symposium on Geometry Processing*, pages 1469–1476. Eurographics Association, 2008.

[181] M. J. Swain and D. H. Ballard. Color indexing. *International Journal of Computer Vision*, 7(1):11–32, Nov 1991.

[182] G. K. L. Tam, Z.-Q. Cheng, Y.-K. Lai, F. C. Langbein, Y. Liu, D. Marshall, R. R. Martin, X.-F. Sun, and P. L. Rosin. Registration of 3d point clouds and meshes: A survey from rigid to nonrigid. *IEEE Transactions on Visualization and Computer Graphics*, 19(7):1199–1217, Jul 2013.

[183] H. R. Tavakoli, A. Borji, J. Laaksonen, and E. Rahtu. Exploiting inter-image similarity and ensemble of extreme learners for fixation prediction using deep features. *Neurocomputing*, 244:10–18, Jun 2017.

[184] M. E. Taylor, C. A. Perez, K. J. Halverson, R. R. Kuske, G. W. Philpott, D. M. Garcia, J. E. Mortimer, R. J. Myerson, D. Radford, and C. Rush. Factors influencing cosmetic results after conservation therapy for breast cancer. *International Journal of Radiation Oncology Biology Physics*, 31(4):753–764, Feb 1995.

[185] O. M. Tepper, N. S. Karp, K. Small, J. Unger, L. Rudolph, A. Pritchard, and M. Choi. Three-dimensional imaging provides valuable clinical data to aid in unilateral tissue expander-implant breast reconstruction. *The Breast Journal*, 14(6):543–50, Nov 2008.

[186] O. M. Tepper, K. Small, L. Rudolph, M. Choi, and N. Karp. Virtual 3-dimensional modeling as a valuable adjunct to aesthetic and reconstructive breast surgery. *The American Journal of Surgery*, 192(4):548–551, Nov 2006.

[187] O. M. Tepper, J. G. Unger, K. H. Small, D. Feldman, N. Kumar, M. Choi, and N. S. Karp. Mammometrics: The standardization of aesthetic and reconstructive breast surgery. *Plastic and Reconstructive Surgery*, 125(1):393–400, Jan 2010.

[188] D. Terzopoulos and D. Metaxas. Dynamic 3d models with local and global deformations: deformable superquadrics. In *Proceedings of 3rd International Conference on Computer Vision*, pages 703–714. IEEE Computer Society Press, Jul 1990.

[189] D. Thanoon, M. Garbey, and B. L. Bass. Computational modeling of breast conserving surgery (bcs) starting from mri imaging. In *Computational Surgery and Dual Training*, pages 67–86. Springer New York, Nov 2014.

[190] T. Tőkés, L. Torgyík, G. Szentmártoni, K. Somlai, A. Tóth, J. Kulka, and M. Dank. Primary systemic therapy for breast cancer: Does the patient's involvement in decision-making create a new future? *Patient Education and Counseling*, 98(6):695–703, Jun 2015.

[191] R. Toldo, A. Beinat, and F. Crosilla. Global registration of multiple point clouds embedding the generalized procrustes analysis into an icp framework. In *Proceedings of 3D Data Processing, Visualization, and Transmission (3DPTV)*, 2010.

[192] C. Tomasi and R. Manduchi. Bilateral filtering for gray and color images. In *Proceeding of 6th International Conference on Computer Vision*, pages 839–846. Narosa Publishing House, Jan 1998.

[193] J. Tong, J. Zhou, L. Liu, Z. Pan, and H. Yan. Scanning 3d full human bodies using kinects. *IEEE Transactions on Visualization and Computer Graphics*, 18(4):643–650, Apr 2012.

[194] C.-F. Tsai and J.-W. Wu. Using neural network ensembles for bankruptcy prediction and credit scoring. *Expert systems with applications*, 34(4):2639–2649, May 2008.

[195] P. Vangorp, G. Chaurasia, P.-Y. Laffont, R. W. Fleming, and G. Drettakis. Perception of visual artifacts in image-based rendering of façades. *Computer Graphics Forum*, 30(4):1241–1250, Jun 2011.

[196] T. Várady, R. R. Martin, and J. Cox. Reverse engineering of geometric models—an introduction. *Computer-Aided Design*, 29(4):255–268, Apr 1997.

[197] V. Vavourakis, B. Eiben, J. H. Hipwell, N. R. Williams, M. Keshtgar, and D. J. Hawkes. Multiscale mechano-biological finite element modelling of oncoplastic breast surgery—numerical study towards surgical planning and cosmetic outcome prediction. *PLOS ONE*, 11(7):e0159766, Jul 2016.

[198] U. Veronesi, N. Cascinelli, L. Mariani, M. Greco, R. Saccozzi, A. Luini, M. Aguilar, and E. Marubini. Twenty-year follow-up of a randomized study comparing breast-conserving surgery with radical mastectomy for early breast cancer. *New England Journal of Medicine*, 347(16):1227–1232, Oct 2002.

[199] C. Vrieling, L. Collette, A. Fourquet, W. J. Hoogenraad, J.-C. Horiot, J. J. Jager, M. Pierart, P. M. Poortmans, H. Struikmans, B. Maat, E. V. Limbergen, and H. Bartelink. The influence of patient, tumor and treatment factors on the cosmetic results after breast-conserving therapy in the EORTC 'boost vs. no boost' trial. *Radiotherapy and Oncology*, 55(3):219–232, Jun 2000.

[200] M. Wand, B. Adams, M. Ovsjanikov, A. Berner, M. Bokeloh, P. Jenke, L. Guibas, H.-P. Seidel, and A. Schilling. Efficient reconstruction of nonrigid shape and motion from real-time 3d scanner data. *ACM Transactions on Graphics*, 28(2):1–15, May 2009.

[201] M. Wand, P. Jenke, Q. Huang, M. Bokeloh, L. Guibas, and A. Schilling. Reconstruction of deforming geometry from time-varying point clouds. In *Proceedings of 5th Eurographics Symposium on Geometry Processing*, SGP '07, pages 49–58. Eurographics Association, 2007.

[202] G. Wang, D. Garcia, Y. Liu, R. de Jeu, and A. J. Dolman. A three-dimensional gap filling method for large geophysical datasets: Application to global satellite soil moisture observations. *Environmental Modelling & Software*, 30:139–142, Apr 2012.

[203] R. Wang, J. Choi, and G. Medioni. Accurate full body scanning from a single fixed 3d camera. In *Proceeding of 2nd International Conference on 3D Imaging, Modeling, Processing, Visualization & Transmission*. IEEE, Oct 2012.

[204] A. Weiss, D. Hirshberg, and M. J. Black. Home 3d body scans from noisy image and range data. In *2011 International Conference on Computer Vision*. IEEE, Nov 2011.

[205] J. Wheat, S. Choppin, and A. Goyal. Development and assessment of a microsoft kinect based system for imaging the breast in three dimensions. *Medical Engineering & Physics*, 36(6):732 – 738, Jun 2014.

[206] C. Zhang and Z. Zhang. Calibration between depth and color sensors for commodity depth cameras. In *Proceeding of IEEE International Conference on Multimedia and Expo*, pages 1–6. IEEE, Jul 2011.

[207] L. Zhao, A. Cheong, G. P. Reece, M. C. Fingeret, S. K. Shah, and F. A. Merchant. Inferior breast-chest contour detection in 3-d images of the female torso. *IEEE Journal of Translational Engineering in Health and Medicine*, 4:1–10, Sep 2016.

[208] J. Zhu, L. Wang, R. Yang, J. E. Davis, and Z. Pan. Reliability fusion of time-of-flight depth and stereo geometry for high quality depth paps. *IEEE Transactions on Pattern Analysis and Machine Intelligence*, 33(7):1400–1414, Jul 2011.

[209] H. Zolfagharnasab, S. Bessa, S. Oliveira, P. Faria, J. Teixeira, J. Cardoso, and H. Oliveira. A regression model for predicting shape deformation after breast conserving surgery. *Sensors*, 18(1):167–193, Jan 2018.

[210] H. Zolfagharnasab, J. S. Cardoso, and H. P. Oliveira. Fitting of breast data using free form deformation technique. In *Proceeding of International Conference on Image Analysis and Recognition*, pages 608–615. Springer International Publishing, Jun 2016.

[211] H. Zolfagharnasab, J. P. Monteiro, J. F. Teixeira, F. Borlinhas, and H. P. Oliveira. Multimodal complete breast segmentation. In *Pattern Recognition and Image Analysis*, pages 519–527. Springer International Publishing, Jul 2017.